Locomotion and Control of Cnidarian-Inspired Robots

Gregory Michael Krummel

Dissertation submitted to the faculty of the Virginia Polytechnic Institute and State
University in fulfillment of the requirements for the degree of

Doctor of Philosophy
In
Mechanical Engineering

Shashank Priya, Chair
Danesh K. Tafti
John J. Socha
Rolf Mueller

December 5, 2018
Blacksburg, VA

Keywords: jellyfish, siphonophore, robot, control, locomotion

Locomotion and Control of Cnidarian-Inspired Robots

Gregory Michael Krummel

ABSTRACT

Effective locomotion and maneuvering in aquatic environments is important for survival for marine fauna. The ability to move quickly, change direction, and tune energy consumption for long migrations is critical for escape from predators and pursuit of prey. This controlled propulsion in terms of varying speed, turning rates, and actuation effort is of interest for the next generation of underwater vehicle design. Integration of biological functional simplicity, robustness, and superior performance enables robotic vehicles to successfully complete difficult and dynamic operational goals. Gelatinous animals known as Cnidarians employ a wide variety of propulsive methods, ranging from the simple but efficient propulsion of large jellyfish to the rapid and highly maneuverable multi-jet propulsion of colonial animals known as siphonophores. This dissertation studies how these two extremes of underwater soft body propulsion are able to achieve simple yet effective control and locomotion, and thus inform the design of effective vehicle propulsion control and actuation. Two large single bell jellyfish robots, Cyro 2 and Cyro 3, were designed and constructed to implement the simple body form and propulsive methods of large jellyfish to study the unique locomotive characteristics and fluid interactions that generate straight swimming and turning maneuvers. The other extreme of small soft-body colonies moving by multi-jet propulsion was subsequently investigated in-depth, starting with a characterization of the biological fluid jetting actions and gaits. The results of these performance capabilities were then applied to an experimental robotic model with bio-inspired construction and controls to verify an elegant but highly functional neurological control scheme and the kinematic capabilities from varying jetting gait patterns.

Locomotion and Control of Cnidarian-Inspired Robots

Gregory Michael Krummel

GENERAL AUDIENCE ABSTRACT

The ability to move rapidly in any direction is a primary characteristic of successful animal species. Evasion of predators, as well as pursuit of prey, is paramount for survival. Jellyfish are excellent examples of animals that have thrived for millions of years with varied methods of moving in their diverse environments. However, the propulsion methods of large jellyfish in straight swimming and turning have not been well understood until recent years. This dissertation focuses on the fundamental understanding of the locomotion and fluid interaction that jellyfish use for propulsion. A large jellyfish robot, named Cyro 2 ("Cy" for the species *Cyanea*, "ro" for robot, and the second generation of the design), was constructed to explore the role of various structural and fluidic parameters on the locomotion characteristics of the largest jellyfish species *Cyanea*. The successor Cyro 3 was designed to mimic the complex motions of large jellyfish during maneuvering. Motion tracking and fluid analysis of the robot during turning was utilized to explain how jellyfish dynamically control their orientation. These results inspired further study of a unique relative of jellyfish, the siphonophore, which can swim with a modular chain of soft pumping bodies that coordinate without a central nervous system. This unique control strategy and method of movement underwater was studied by analyzing specimens of the siphonophore *Nanomia*. Development and modeling of elegant control techniques inspired by this species is presented and implemented on an experimental model that uses this unique propulsion method to validate and expand upon observations of live specimens. Combined, the results obtained in this dissertation open the possibility of designing advanced underwater vehicles.

Acknowledgements

I would like to thank Dr. Shashank Priya for advising and supporting my research throughout my graduate career. His continuing support and encouragement has helped guide my research projects into rigorous, high-impact contributions to the fields of biomechanics, biomimetic robotics, and biomimetic control architectures.

I would also like to express gratitude towards Colin Stewart for his unwavering guidance and assistance on my research, and his willingness to collaborate and contribute time towards the mutual success of our research.

The completion of my advanced education would not have been possible without the continuing support of my parents. Their support during more than 20 years of education have been critical to my success and dedication to advancing my career.

This dissertation is dedicated to my late fiancée, Ella Mode. Her enthusiasm towards the life sciences, research, higher education, and the sharing of scientific information for the betterment of society continuously renewed my passion for the sciences. Her perpetual encouragement, support, and investment into my wellbeing, career, and future at large while exhibiting incredible strength and perseverance in the face of adversity inspired me to have the ambition to complete this dissertation.

Attributions

The research presented in Chapter 1 on Cyro 2 and Chapter 3 on siphonophore biomechanics were my contribution to collaborative efforts with Colin Stewart. His dissertation will cover the details of the simulation and further data analysis, particularly fluid flow imaging with PIV and dynamic fluid modeling.

Cyro 2 was initially developed by students in our lab, but major design changes and the final construction and experimental setup were my sole contribution. Testing and analysis were collaborative efforts with Colin, and will be included in both dissertations with weighting on our individual contributions.

Cyro 3 design, construction, kinematic testing and data processing, and PIV data collection and transect processing was my sole work. Colin provided some guidance on proper methods, and the PIV video processing for generating the flow field was his contribution.

Siphonophore video and biomechanics analysis were my sole contribution. Further preparation of this data for dynamic inputs based on fluid flow theory, as well as modeling of their resulting kinematics from varying biomechanics, was collaborative but primarily Colin's work. As before, this material will be jointly included in our dissertations, with heavy weighting on our individual contributions.

Siphonophore robot design, construction, and testing, as well as 2D optimization and dynamics modeling of the siphonophore robot, were completely my work. The fluid dynamic considerations for a 1D version of this model derived from the modeling work on biological siphonophores by Colin Stewart, but the 2D modeling was completely developed anew for my research and dissertation.

Videos utilized for siphonophore locomotion were provided by Jack Costello of Providence College and Brad Gemmell of the University of South Florida, as an ongoing collaboration on jellyfish and related projects.

Contents

List of Figures

List of Tables

1. Introduction, Motivation, and Background

Gelatinous zooplankton in the phylum Cnidaria exhibit multiple features that are attractive for biological and engineering studies. The encompassed species vary in body shape, from a single bell with varying fineness ratios for jellyfish to a colonial multi-body form found in siphonophores. This variability enables a wide variety of morphologies and functional capabilities, which open new opportunities in the design and development of robotic underwater systems. These various shapes are present in a span from millimeter to meter scale, from juvenile ephyra and jetting adult cnidarians to large oblate jellyfish such as *Cyanea capillata* (Costello et al., 2008; Dabiri et al., 2007; Dabiri et al., 2010; Gladfelter, 1972). This diversity also brings about changes in behavior, such as a tendency for oblate jellyfish to use 'rowing' propulsion by rolling and ejecting vortex rings to generate momentum and thrust while prolate body plans jet water from their bell and generate vortices in addition to a high velocity jet of water (Costello et al., 2008; Dabiri et al., 2007).

While these forms and functions have been studied in previous exploratory studies, multiple questions still remain unaddressed. In the case of *Cyanea capillata*, most specimens observed and analyzed in captivity were at the lower centimeter scale (Higgins et al., 2008). As the animal grows in size, especially to large adults in the upper centimeter and meter scale, their locomotion strategies, gait timing, and morphology has only been observed and analyzed from limited diver interactions and video footage (Higgins et al., 2008; Villanueva and Priya, 2014). The ability to analyze these gaits and maneuvering in a laboratory setting, equipped with high speed cameras and particle image velocimetry (PIV), will provide insight into fluid-structure interactions. This would extend our understanding of how large-scale jellyfish are able to move efficiently through the water (Dabiri et al., 2010; Gemmell et al., 2013).

While variability between local taxa and regions is expected for most species, cnidarians also encompass a broad range of drastically different body forms with specialized functional structures for locomotion and biological processes. Strictly within jellyfish the bell shape and locomotion strategies are diverse (Dabiri et al., 2010). As animals outside of single-bell jellyfish are explored, more complicated and unique biological systems can be found with desirable locomotive traits. One such taxa within

Cnidaria that exhibits more complicated morphologies is the order Siphonophora (Mackie et al., 1988). These organisms are truly colonial systems that utilize division and redundancy of labor between individual, loosely-connected units termed zooids (Mackie, 1964). In terms of propulsion, the highly mobile siphonophores in the group Physonectae utilize multiple jetting propulsors, called nectophores, aligned in a bilaterally symmetric serial chain to produce thrust at variable positions along the colony. While this body form and propulsion strategy has been studied in past publications, actual quantitative data and records of specific representative behavior, as well as local behavior of these jetting nectophores during varied propulsion modes, has yet to be comprehensively studied (Costello et al., 2015). For a type of organism that is so prevalent in the ecology and biodiversity of the oceans, the research in their behavior and biomechanics is lacking (Barham, 1963; Mapstone, 2014).

In addition, the architecture and behavior of the neural control of siphonophores and jellyfish maneuvering has been largely unquantified and unexplored (Satterlie, 2011). Recent studies, when coupled with past broad studies on various species, have exposed how oblate jellyfish are able to manipulate their vortex rings for propulsion during non-axial maneuvering (Gemmell et al., 2015). This has only been validated on the smaller species *Aurelia aurita*, so variation in maneuvering strategies across different body forms and scales is still widely unknown except for qualitative studies (Gladfelter, 1972).

For siphonophores, their ability to maneuver adeptly at high speeds while only loosely connected with simple neural pathways between individual neural networks opens questions about their control architecture (Grimmelikhuijzen et al., 1986; Mackie, 1964; Mackie, 1973). This high level of control with high resolution spatial and temporal adjustments is indicative of high computational complexity modern control algorithms and communication architectures. It has been discovered, however, that their loosely connected and simple nervous system relies on reduced order and structured hybrid control schemes. This natural solution to simplified control of complex coupled systems with minimal inter-unit communication requires further studies into the detailed software and hardware architecture of such a control system. In addition, the propulsion methods and planning for high speed maneuvering have only been studied in single-jet fixed pivot turning and axial motion. Although videos of their maneuverability are limited in spatial and temporal resolution and scale, being able to analyze, extrapolate, and validate their propulsion patterns in conjunction with simple control laws would enable the progression of knowledge on these critical yet widely unknown organisms. In addition, the technological developments needed to implement these system architectures and software would advance complicated high-speed temporal and spatial control of coupled systems.

This dissertation studies the locomotion of two species mentioned above - the large jellyfish *Cyanea* and the highly mobile serial chain colony *Nanomia*. The goal of these investigations is to provide system-level advancement in the understanding of underwater locomotion that is extremely involved yet structurally simple. The validation of the observed behaviors of these two species and extension to related species provides deeper understanding of the correlations between morphology and propulsive behaviors. Further decomposition and structured analysis of the internal control and mechanical structures behind various modes of locomotion will provide insight towards the role of anatomical features in governing motion. The advancements in the understanding of fluid-structure interactions of a controlled underwater mechanical system, as implemented on representative bio-inspired robots, will lead towards the design of novel locomotion strategies of soft underwater autonomous robots.

2. Design, fabrication and characterization of *Cyanea capillata* inspired model Cyro 2

2.1. *Introduction*

Initial investigations reported on the large *Cyanea*-inspired robot, Cyro, led to additional questions about large jellyfish locomotion and maneuvering. First, the gait of the robot, and thus the animal, had the potential to drastically modulate the efficiency, proficiency, thrust production, and overall power consumption during swimming. Therefore, the timing control of the gait phases – contraction, cruising while full contracted, relaxation, and stalling while fully relaxed – necessitated analysis for more intelligent experimental model design. This will help in gaining insight into the gait control space of large rowing jellyfish. Furthermore, an understanding of how these four factors scale over multiple experimental model and animal diameters can improve our ability of determining the factors governing the biomechanics and fluid dynamics of swimming.

In addition to scientific questions posed by our prior study of a *Cyanea*-inspired robot, the vehicle design itself left room for improvement in order to approach the predictions based on jellyfish morphology. The large scale of Cyro, while posing interesting insight into very large extremes of rowing jellyfish near 2 meters in diameter, was limited in testing due to the challenges of a standard laboratory water tank facility. For example, initial testing of thrust production was completed with one lobe of the bell, which represented one eighth of the total bell surface. Oblate rowing jellyfish utilize vortex rings to encapsulate a mass of water and eject the rotating fluid at a velocity to generate a momentum flux. Therefore, the assumption in the prior study that a single segment of the bell without any interaction with the adjacent segments will produce representative thrust of an axially symmetric system and fluid interaction was sufficient for simplifying large scale lab testing. However, it did not account for coupling effects that could change the magnitude of the thrust generated from the complete bell. The large scale of Cyro and the focus on biomechanics also led to the use of complicated solid aluminum linkages and large actuators to control each lobe. This resulted in the consumption of 70 W of average power and introduced significant additional mass to the design (Villanueva et al., 2013). A post-integration analysis found that the original actuator, when compared to the force requirement for a single lobe actuating underwater, had a safety factor for force output of

8.15, whereas an efficient motor design typically is specified at an operating torque of one quarter the motor stall torque and thus a smaller safety factor of 4. This high safety factor caused the actuators to perform in a suboptimal zone of their performance curve, which was propagated in the design eightfold for each actuator integrated for total bell motion. Natural *Cyanea* move using thin sheets of proximally concentric and distally radially aligned muscle in a gelatinous, fibrous matrix, termed mesoglea, with integrated soft joints created by strategically thinned linear portions in the gelatinous mesoglea material (Gladfelter, 1972). This natural design uses simple yet elegant materials, structures, and actuation mechanics to convert simple soft beam bending into a propulsion system. This disparity between previous designs and the features found in nature necessitated the design of a smaller and simpler *Cyanea*-inspired robot without sacrificing the integrity of the bio-inspired swimming mechanics.

A previous analysis of large *Cyanea* kinematics was conducted using a video of a 50 centimeter diameter specimen (Villanueva and Priya, 2014). At this scale a biomimetic robot would be able to fit inside of a tank equipped to perform planar PIV (Particle Image Velocimetry), as well as other kinematic and system performance measurements. While this size still limited the number of cycles that could be achieved by the robot in available water tanks, steady state swimming would be nearly achievable by a robot at a 50 cm diameter within the frame of two vertically stacked high speed cameras (Photron FastCam SA4) used for PIV. This was critical for capturing, in a quantitative velocity and vorticity field, the vortex ring and resulting wake produced by the robot during swimming. Since the size of actual *Cyanea* jellyfish examined in captivity tended to be below 10 cm in diameter, a large range of sizes that are present in nature had not been analyzed in controlled measurement environments (Higgins et al., 2008). These size scales could benefit from robotic studies of the fluid dynamics and swimming behavior, both for completeness and for further cataloguing of changes in swimming strategies and fluid interactions across multiple orders of magnitude in size. To resolve these design and experimental issues, a new *Cyanea*-inspired robot is proposed and developed. Comparisons with the initial design, further improvements, and test results on this robot are presented in subsequent sections.

2.2. ***Preliminary Biomimetic Design***

2.2.1. Mesoglea Bell Structure

The form of the mesoglea was determined by the morphological and kinematics studies detailed in the paper on the first Cyro robot and the video tracking of a 50 cm *Cyanea* specimen swimming in open water (Villanueva and Priya, 2014; Villanueva et al., 2013). As explained in the introduction, this size was determined to fit within the tank of the PIV system available in the laboratory for quantifying fluid interaction, kinematics, thrust, and electrical power. Therefore, the robot was designed to have the same 50cm bell diameter as the *Cyanea* tracked in the available video.

The measurements in the specimen kinematic study determined that the bell can be discretized into rigid sections and inflection points with specific degrees of deflection during contraction and relaxation. It was determined that the most representative number of inflection points was three major inflection points along the bell, as well as a high deflection area at the tip of the bell where the velar flaps are present. The bell segments were each designed with a tapered thickness seen in the cross section of *Cyanea* and other rowing jellyfish. To discretely include the inflection points with prescribed ranges of motion, as well as stiffen the regions between inflection points, dual ridges seen on the subumbrellar surface were included into the bell form. Each ridge integrated splits at the inflection points that were tapered to the prescribed maximum deflection angles at full contraction. When the bell contracted, these reduced sections would bend locally until the ridges contacted each other at the prescribed angle and stopped local motion. The split sections thus had thinner silicone cross sections, which simultaneously concentrated deflection and balanced stiffness for energy storage during forced contraction. This stored elastic energy was passively released under no external load to induce relaxation. The bell segments were tapered width wise as well to stiffen the center of the lobe and allow localized deflection between the lobes when folding occurred during contraction.

The eight individual segments were designed in 3D CAD, as shown below, and a negative mold for each segment was designed and printed on a Makerbot 2 fused deposition modeling 3D printer. This negative mold was filled with Ecoflex low-stiffness casting silicone, which was selected due to its low stiffness and density similar to that of water

(Villanueva et al., 2013). These properties were selected on Cyro due to these properties closely mimicking jellyfish bell mesoglea, and thus were selected again for this design. After eight identical silicone bell segments were cast, the cured segments were then fused with silicone to form an eight segment continuous bell. To mimic the velar region at the tip of the bell, thin silicone at the end of the bell casting was separated to form half of the velar flap and additional cast silicone of similar thickness was adhered with silicone to form the other half of the cleft velar flap.

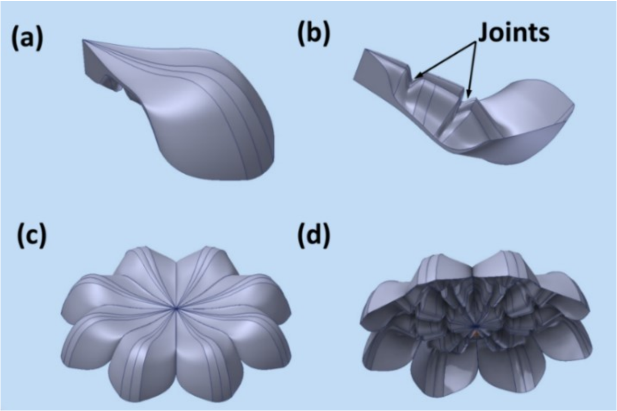

Figure 1 - CAD of Cyro 2 bell design. (a) Isometric view of a bell segment. (b) Under view of a bell segment showing joint locations. (c) Isometric view of the bell. (d) Under view of the bell.

2.2.2. Bell Actuation

Cyanea utilizes circumferential muscles for the contraction of the bell by folding inter-lobe thinned ridges, which fold similar to the membrane of a folding umbrella, while radial muscles are utilized for controlling the peripheral motion of the velar flaps and distal end of the lobes (Gladfelter, 1972). These radial muscles are localized to each lobe, similar to the individual actuation of Cyro. Circumferential contraction is prohibitively complicated and inefficient for a mechanical actuator since a reduction in circumference reduces diameter of the actuated section proportionally but the directed force is tangential to the direction of radially controlled stiffness. Since radial actuation was needed for peripheral portions of the bell, and the prescribed angles of the bell were relative to the radial planes, the bell actuation was determined to be initiated with radial elements to cause localized beam bending. By routing a cable through the stiffening ridges, fixing the cable just before the velar region of the bell, and reducing the length, a force was applied at a distance far below the neutral axis of the bell and bending is induced. In addition to reduced stiffness, this distance from the neutral axis was maximum at the splits in the stiffening ridges, initiating bending locally and mostly eliminating bending at the stiffened sections. In order to ensure a balanced bending towards the central axis of the bell and eliminate lateral bending along the radial centerline of each segment, the stiffening ridges were implemented in pairs. To reduce frictional losses in the cable system through these ridges, the cable pathways were lined with PTFE tubing that monofilament cables would run through with minimal friction, even under side load during contracted poses.

Individual control of each lobe, as implemented in Cyro, is energetically expensive and complicated due to the number of lobes, needing to balance actuation, and the multiplicity of maximizing efficiency under the expected load range. Swimming in the axial direction of the bell is initiated with radially symmetric contraction, so actuating this motion with redundant motions only increases the chance of ineffective operation due to actuator fault and resulting axial asymmetry in thrust production. In order to improve reliability while eliminating unnecessary redundancy, the motion for each lobe was combined to a synchronous, centralized, radially inward and downward motion prescribed by a waterproof servo motor (Savox SW-1210SG). The servo motor, fixed in a mating 3D printed housing that kept it open to the water for cooling, was connected through its output spline shaft to a threaded rod and jam nuts that were threaded into a winch and epoxied into mating rigid surfaces. The winch was sized to allow full contraction within the 180 degree range of the servo motor. This winch was attached to two monofilament fishing line cables for each lobe, and the cables were routed through the PTFE channels in the lobe stiffening ridges. The far end of the cable was anchored to the distal end of the lobe before the velar region using silicone and plastic plates. These plates included holes for tying down the cable and flanges to prevent pulling through the silicone bell when under load. When the winch moved to a prescribed position, the cable would go under tension to apply a radial force inward. As the cable wrapped around or unwound from the winch, the cable within the bell increased or decreased in length and in turn reduced the angle at the lobe inflection points uniformly across all lobes. When the inflection points each reached the locally prescribed contracted angle, the stiffening ridges would interfere and contraction at the inflection point would stop. Full contraction was determined as when the inflection points were all at the maximum prescribed deflection. When the winch was run in reverse to elongate the cables, tension was released and stored elastic energy in the silicone of the bell would passively relax the bell. Full relaxation was determined as when the cable had zero tension and the elastic energy in the bell was depleted.

2.2.3. Electronics and Control

Since the integration of electronics underwater for motion control was difficult due to the complexity of waterproofing custom designed housings, robots being developed at the time in BMDL were tethered to outside of the water. This tether, which on the robot attached to the power, ground, and PWM signal line of the servo, went to a benchtop power supply and a Pololu Micro Maestro servo motor controller. The cable was chosen to be a low diameter to minimize cable tension and drag in the water, which would place external loading on the robot during swimming and may have affected swimming performance.

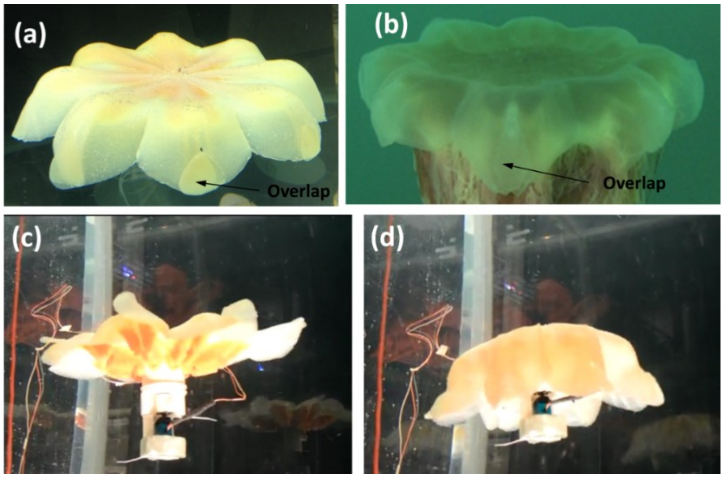

Figure 2 - Initial design and planned swimming of Cyro 2. (a) Cyro 2 in water. (b) *Cyanea capillata* showing the overlap of a bell segment. (Villanueva and Priya, 2014) (c) Cyro 2 fully relaxed in a swimming sequence. (d) Cyro 2 Fully contracted in a swimming sequence.

2.3. ***Design Improvements***

2.3.1. Mesoglea Bell Structure

After initial testing of the bell motion under servo actuation, it was found that the bell readily tore along the seams and delaminated from the central column that housed the winch. Therefore the bell was reinforced at these potential tearing points with silicone adhesive of similar durometer to the bell silicone. The adhesive improved adhesion between the housing plastic and cast silicone, and additional adhesive was added to bridge the portion of the bell near the central column to holes at the top of the column housing. This additional material pulled the bell inwards and held the adhesive joints in compression, reducing the load on the interfaces and therefore avoiding further tearing damage.

The PTFE tubes, while low in friction to reduce cable frictional resistance and induced motion errors, tended to migrate within the channels of the stiffening ridges. This can be attributed to some cable friction under high side loading during contraction, which bent the cables across edges of the tubing, as well as silicone compression and expansion at the ridges during the contraction cycle that acted as a peristaltic force. When the tubes moved within the channels, they would block the deflection of the splits in the ridges and hence cause inaccurate bell deflection. These tubes would also go into the winch housing, which had openings to allow cable entry, and would wedge into the spinning mechanism. If the tube moved away from the cable in the channels, the cable would directly abrade the silicone and break out of the stiffening ridges. Adhesion between the channels and the tubes was attempted with adhesive silicone to allow flexion and mate with silicone, which in itself is hard to bond, but the low surface energy and chemical resistance of PTFE eliminated any adhesion. In order to repair the damaged channels and reinforce the existing pathways for the cables, large diameter polyolefin heat shrink tubing was used. Polyolefin plastic typically exhibits low friction, and the large diameter with thin and flexible walls allowed the tube to be split lengthwise, wrapped around the cable, wrapped to multiple layers until the diameter of the original channel inner diameter, and adhered into the ridges with silicone adhesive.

2.3.2. Bell Actuation

The reliability of the cable system was found to be suboptimal after extended testing, so multiple changes were implemented. The monofilament cable was originally chosen due to its low cost and low expected friction. However, even high strength monofilament cables are susceptible to small damage that initiates necking under tension and repeated loading of the cable. This led to repeated breakage of the cables after extended testing. Therefore, braided filament cable of similar diameter was chosen to exhibit similar flexibility but increased strength due to redundant fibers that would not completely fail with small defects under load. The braided cables are wound tight and are intended for heavier loads and smooth winding on fishing reel spools, so the friction of the cable was not compromised while reliability was increased drastically. This reliability was further improved by replacing the plastic flanged pieces, which had a tendency to pull out or detach from the cable, with long set screws. This allowed a broad surface to resist pulling out, a rounded surface to distribute load and eliminate progressive pulling out under repeated load due to stress concentrations on the surrounding material, and fine threads that allowed multiple turns of the cable to be wrapped around, tied off, and epoxied onto the screw. This screw was inserted into the cavity of the original flanged plates, adhered and sealed into the cavity with silicone adhesive, and the cable was routed back into the housing and clipped to length. In order to improve predictability of cable winding, the cables were elongated and wrapped a quarter turn around the spindle before exiting the housing. While the old design's cable attachment was directly in line with the hole at full relaxation and only bent the cable initially and took a portion of a turn to start wrapping the cable around the spindle, the pre-wrapping ensured that as the spindle turned the change in length was proportional to the spindle's angular rotation.

The housing around the winch that supported the cables, supported the winch shaft, and provided an attachment point for the bell exhibited faults during extended testing. The housing included slits at each cable entry point to allow the cable to be slid into place during assembly, and when combined with a thin wall thickness the sections that fit over the motor housing were fragile cantilevered beams. This, as well as the 3D printed layers being aligned normal to the bending forces with limited tensile strength at the layer interface, resulted in frequent fractures that made repair unsustainable over the long term. The vertical slits for cable entry also resulted in the cable slipping down during contraction, contributing more to actuation inaccuracy and housing loading that led to fractures. An early improved design included thickened walls with rounded features to reduce stress concentrations at the base of the cantilevered elements. The housing wall thickness was varied along its length to taper the housing and reduce both material and potential drag losses during swimming. The slits were initially rerouted to enter in parallel to the outlet holes in the housing and then drop down into the outlet holes from above to eliminate cable migration downwards when under tension. However, this design complicated the cleaning of these nonlinear slots after printing, and the plastic parts were still cantilevered and thus prone to fracture. The final version of this housing had no slots, and the cable was routed through during assembly with the bell held so that the cable tension was released. The housing thickness and form was further refined for strength and reduction in drag.

The shaft of the spindle was originally supported by a bearing in the center of the top face of the housing, preventing bending and lateral displacement from side loads from dynamic asymmetry in cable tension. This bearing was a standard steel ball bearing with no shielding or sealing, and as can be expected the bearing rusted and seized. The bearing was also not sized to mate with the shaft, which was a threaded rod and not appropriate for precision bearing surfaces, so the coarse thread freely moved laterally within the bearing bore. In order to improve support, simplify assembly, and eliminate additional frictional losses from corroded surfaces, the new housing design included a reinforced hole that was bored smooth and sized to mate with the shaft with a close slip fit. The hole was recessed and fixed with washers and lock nuts to improve axial support, which was an improvement over the previous standard steel nut and no washer.

The housing also did not include mounts for attaching sting assemblies for static testing and peripheral accessories, such as flotation and weighting material for buoyancy and balancing control, and the few holes at the top were not deep enough to support a threaded mount under dynamic loading. The improved spindle housing included threaded posts that projected above the housing but ended deep inside the upper layer of the part. These posts later allowed for sting mounts for static tests and the attachment of foam, weights, and lights for free-swimming tests.

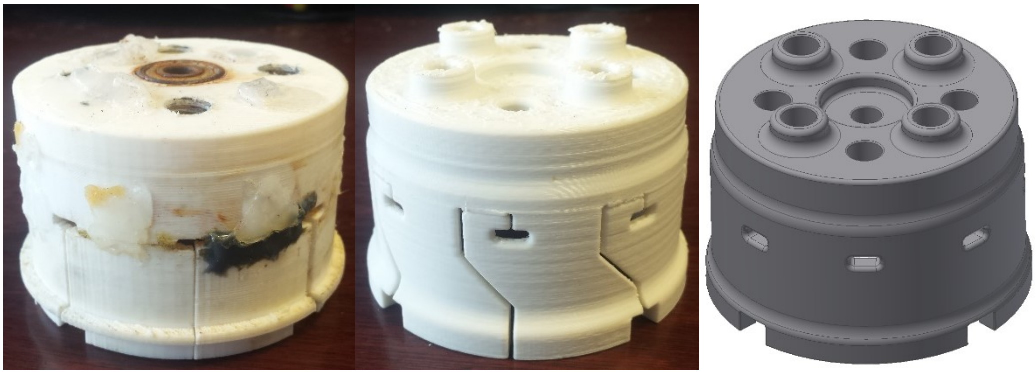

Figure 3 - Progression of spindle housing design. Initial design (left) exhibited structural failures and faulty cable, shaft, and accessory support surfaces. The improved version (middle) eliminated support surface problems, but still had occasional fractures. The final version (right) resolved all present issues.

The fully relaxed and contracted positions of the winch were previously not inherent to the design. To identify and fix the range of the spindle, it was detached from the servo then rotated and fixed relative to the servo output to have full relaxation at one extreme of rotation. This also maximized the potential range of the winch, which was critical to maximizing the available range when empirically finding the fully contracted position. The position for full contraction was empirically determined and fixed. Knowing this position eliminated the possibility of commanding a position too far past full contraction, which would introduce delays and stalled position holds that result in erroneous gait timing and induce additional load on the motor. During contraction the position moved from full relaxation to full contraction with a prescribed time, and the velocity was tuned on the servo controller to allow full travel in the expected time. Acceleration of the servo was also tuned to allow soft start and stop, which reduced motor wear, stopping and starting power spikes, and therefore prolonged the life of the servo motor during oscillatory motion. The relaxation, although passively driven from elastic energy stored in the bell from bending, was position and velocity controlled by slowly changing the unspooled cable length to maintain tension while releasing stress stored in the bell until the predetermined fully relaxed position was reached. As with contraction, the velocity inputs were empirically determined whenever the timing was changed during cycle variation to maintain a consistent velocity profile with soft starting and stopping. The servo motor position, speed, and acceleration control during the contraction, cruise, relaxation, and stall phases were commanded with a servo motor controller (Pololu Micro

Maestro). While the control architecture of this controller is unknown, it is expected that without the internal position feedback on the servo that the controller prescribes positions in a controlled manner with the assumption that the servo will reach the commanded position as long as the commands are within the speed and torque constraints. With prescribed endpoints, forced slopes, and forced ramping, the controller works well enough for prescribed motions used during the testing. However, appropriate tuning of values was critical for ensuring the accurate operation of this controller.

2.3.3. Electronics and Control

The updated electronics comprised of three primary segments – the control of the servo motor position and kinematics, the delivery of constant voltage and variable current to the motor, and the measurement of power consumption and phase during the gait cycle.

The robot position and kinematics were still controlled by the Pololu Maestro servo controller, and tuning of the input for proper actuation was detailed in the previous subsection. However, the controller was mounted onboard to eliminate command errors to the servo due to long cable resistive losses. The power to the board is monitored by the on board microcontroller, so local voltage fluctuations to the servo are sensed and error protected by the board.

The power to the board, and then to the servo motor, was redesigned to eliminate transmission resistive losses and improve measurement accuracy. The previous design's tether input was built with a small gauge wire, which introduced a small resistance in series with the robot. According to Ohm's laws, this small resistance in series with a varying load would have little impact on system performance under low current conditions. However, the servo motor was approaching the max torque load and hence the stall current of 4 A. This small resistance, under large current, would introduce a voltage drop across the cable and reduce voltage when the motor instead needed additional power. For these electromagnetic motors, dropping the voltage also reduces the mechanical output range and thus the power draw under peak conditions, so a small voltage drop constricts the mechanical power production capacity of the motor in two separate ways. If the current and voltage were to be measured from the end of the cable this resistive loss would have been difficult to isolate, and the power input measurement would be artificially high due to more voltage before the cable and a potentially different current draw across the system.

Two potential solutions for improving power delivery and measurement integrity were identified. An initial design included battery power from a NiMH or LiPo battery positioned on the robot. This would deliver local power, but the loss of access to the power draw of the remote system was unacceptable. In addition, battery voltage drops under increased loads and during long term testing, so the local power would not improve any of the existing restrictions. Therefore the other solution of a well-designed power and measurement tether that enabled rapid code changes and repeatable testing was determined to be the best option.

The power for the controller and servo motor was provided by an external power supply through a 16.5 foot, 16 AWG gauge tether. The flexibility of the power cable jacket and the stranded internal conductor was selected specifically to reduce external loading on the robot from cable bending and movement. The power supply for power delivery into the tether was initially a 5A supply (Agilent E3648A), but with regulation, additional circuitry, and cable losses the power supply fluctuated in voltage at high frequency. This level of fluctuation, which introduces measurement noise and occasional brown-outs of the onboard electronics, was unacceptable, and the supply was replaced with a higher power supply with 36 A maximum current (Keithley 2260B-80-13). The cable gauge and length was parametrically iterated to minimize current losses at maximum load to less than 1 V, so the distal power delivery would stay within the intended motor operational range of 5 V and 6 V.

The resulting cable had 0.187 Ohms of internal resistance, and at the maximum motor current of 4A the voltage to the robot would drop 0.784 V. Since the operating range of the motor is from 4.8 V to 6 V, this decrease in voltage would account for 65.33% of the operating range and hence a significant reduction in speed and torque output. To stabilize this power signal, switching voltage converters were implemented on the robot to give a known input voltage to the motor despite current draw and tether voltage drop. Initially a step-up, step-down converter and then a step-up converter were utilized, but the response time and current supply was not satisfactory during sudden spikes in current at high load. Switching converters, as with the switching power supplies, can drop out at near-overload conditions, introduce noise to the power supply signal, and reduce output or lag in response to high current draws due to additional load on the switching circuitry. These errors can interact with the power and control circuitry integral to the servo motor, introducing audible whine and twitching at high loads.

In order to reduce the strain on the converter, supply a higher voltage and lower current through the tether to limit resistive changes in voltage, and reduce the current draw of the motor at lower voltages, the final design used in this study sent the power from the tether to a 5V 5A step-down switching voltage converter. The voltage into the tether was set at 7V with the high current power supply to stay above the converter's input voltage threshold and eliminate residual high frequency stepping effects from the power supply. The voltage at the output of the converter was verified to be consistent during the gait cycle of the robot, but a tap line of the voltage was installed on the tether to send feedback of the true motor voltage to a power measurement DAQ for power calculations. The converter output power was distributed by the motor controller to the servo motor, and the controller was powered off of the 5V output as well.

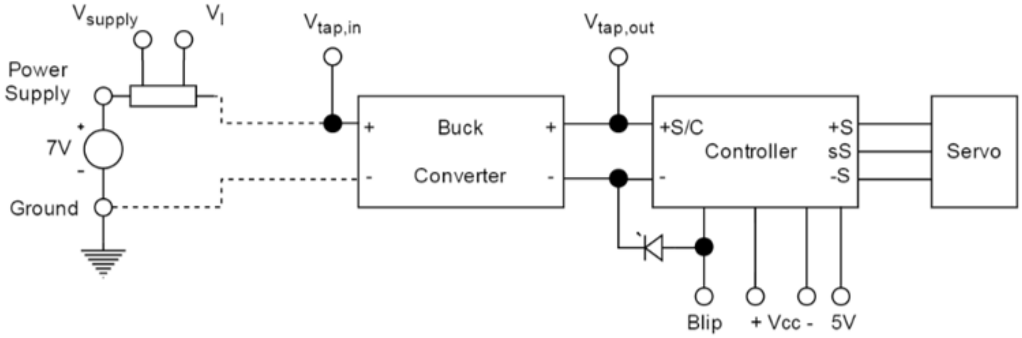

Figure 4 - Electrical systems diagram, including power transmission from the power supply, through the tether, converted in the buck converter to 5V, and distributed by the controller to the servo motor. $V_{tap,in}$ represents the voltage tap of the voltage given to the converter, while $V_{tap,out}$ is the voltage tap of the voltage to the servo and controller.

In order to access the program on the robot for cycle timing changes, as well as measure the power draw of the robot, the tether port was designed to use a sealed D-sub connector with 9 pins. The USB input to the servo motor controller were broken out into four pins, and a D-sub to USB connector converted the pins back to the USB standard for connection to a laptop port for monitoring and code changes. Three small gauge cables, which exhibited minimal losses due to the high input resistance of the DAQ, ran from the robot to the DAQ: local voltage into the converter ($V_{tap,in}$) and into the motor and motor controller ($V_{tap,out}$), and a pulsed 5 V output line that indicated the phase of the gait that the robot was executing (Blip). The blip signal was continuously on for contraction, continuously low for relaxation, and pulsed quickly for the cruise phase. Signaling the start of a stall phase at the end of relaxation was not needed since the final code did not utilize a prescribed stall period. The entire robot was grounded together, so all of the measurements were able to be derived from the ground of the power input. At the far end of the tether near the DAQ, a 0.1 Ohm 1% tolerance power resistor was put in series with the positive power side of the tether. Alternative current measurement devices, such as coil-based sensors, were considered and tested, but the complexity and problems with the reliability of these sensors ruled them out for the final design. Shunt resistors are used widely in industry for current measurement, so we decided to use the simple resistive current measurement. The voltage before and after the resistor, which was selected for minimum voltage drop but sufficient dV/dA for current measurement across the resistor and hence the system, was sent into the DAQ as well. The voltage drop across the small resistor was proportional to the current of the system, and since the cable resistance was in series the current into the cable was assumed to be equal to the current into the robot. The voltage drop across the cable, derived from the voltage before and after the cable, allowed for removal of cable losses from robot power measurements. The final form of the power equation was:

$$\begin{aligned}
P_{motor} &= V_{motor} I_{motor} = \epsilon_{converter} V_{in} I_{in} \\
&= \epsilon_{converter} \left(V_{supply} - I_{supply} R_{shunt} - I_{supply} R_{cable} \right) I_{supply} \\
&= \epsilon_{converter} P_{supply} - \epsilon_{converter} I_{supply}^2 R_{shunt} - \epsilon_{converter} I_{supply}^2 R_{shunt}
\end{aligned}$$

2.3.4. Electronics Housing

Since the electronics for control and power regulation were moved to be internal to the robot, a waterproof sealed housing was necessary to be added to the robot. For testing in the large PIV tank, the robot electronics had to stay waterproof for durations on the order of several hours at depths up to about 5 feet. The fluctuations in static and dynamic pressure during the swimming cycle required that the sealed housing be flexible, redundant, and reliable in aquatic applications. The initial actuator design and mechanisms took up a semicircular columnar space under the robot bell, so the electronics needed to be fit in a housing that was fit closely around the mechanisms to reduce cable power losses and complete the column shape for axisymmetry.

The housing was 3D printed on a CubePro Duo FDM printer out of ABS thermoplastic, with a lid that seated into a recessed ledge. Initial designs placed the NiMH and LiPo battery cells for onboard power in the deep well of the housing and the electronics in the well closer to the lid, with the lid adhered and sealed into place with solid silicone adhesive sealant. However, the silicone seals repeatedly failed underwater due to saturation of the adhesion interface, and the electronics were subsequently exposed to any leakage through the lid. Leakage also occurred through the sides of the housing walls due to microscopic separation between the fused deposition modeling layers. Any moisture into the housing, even in small amounts, accumulated and corroded electrical contacts.

The seal and housing designs were iterated to solve the individual problems until the final design, seen below, was determined as the optimal sealing solution. To integrate a physical pressurized seal into the lid, the lid fit into a recessed ledge and locked into place with ramped cams and slots when rotated. The lid seam was redundantly sealed with a cross O-ring under the lid, which sealed against three seam lines and two solid bodies when compressed by the locking lid, and E6800 high strength marine adhesive sealant deposited into the seam cavity between the housing ridge and the lid rim. The D-sub connector was sealed against the lid with threaded standoff fasteners and an integral O-ring, but the lid design also included a ridge behind and around the connector that was flooded with marine adhesive sealant after wiring. The entrance of the servo motor power and control cable into the housing stepped down towards a low-tolerance fit with the cable at a flange, and ribbed cavities along the length of the cable formed a labyrinth seal when flooded with marine adhesive sealant. To avoid moisture corrosion and moderate submersion in the case of a leak, each electronic board was coated in silicone after wiring to ensure all contacts would not come into direct contact with any water present. The coated boards were put into the cavity at the portion of the deep well furthest away from the lid so during upward swimming any leakage would fall towards the lid and pool away from the boards. The elevated boards were surrounded by desiccant crystals to absorb any ambient moisture, and the wires between the electronics and the lid were surrounded with highly absorptive cloth that would absorb and contain any water that leaked into the housing. This redundantly protected distance between the lid and electronics minimized the possibility of exposure to leaks, and the elevation of the electronics relative to the sealed ports when the robot is swimming in the upright position allowed gravity and the absorptive materials to pull leakage away from the electronics. The sealed housing was then attached to the existing mechanical housing of the robot with silicone adhesive, with gaps between the housings to avoid cable crimping near the servo and promote water submersion around the motor for cooling at the heat sink. The outside of the electronics housing was coated in silicone to fill gaps in the fused deposited housing layers. With this added volume of air at the rear of the robot, the large volume with minimal density caused positive buoyancy and an inverting stabilizing moment. An aluminum ballast mass, which was near the housing diameter and tapered to reduce additional flow disturbances by entrainment and drag, was machined and attached around the electronics housing to move the center of mass below the center of buoyancy and stabilize the robot during swimming, as well as adding some additional mass to make the robot closer to neutral buoyancy.

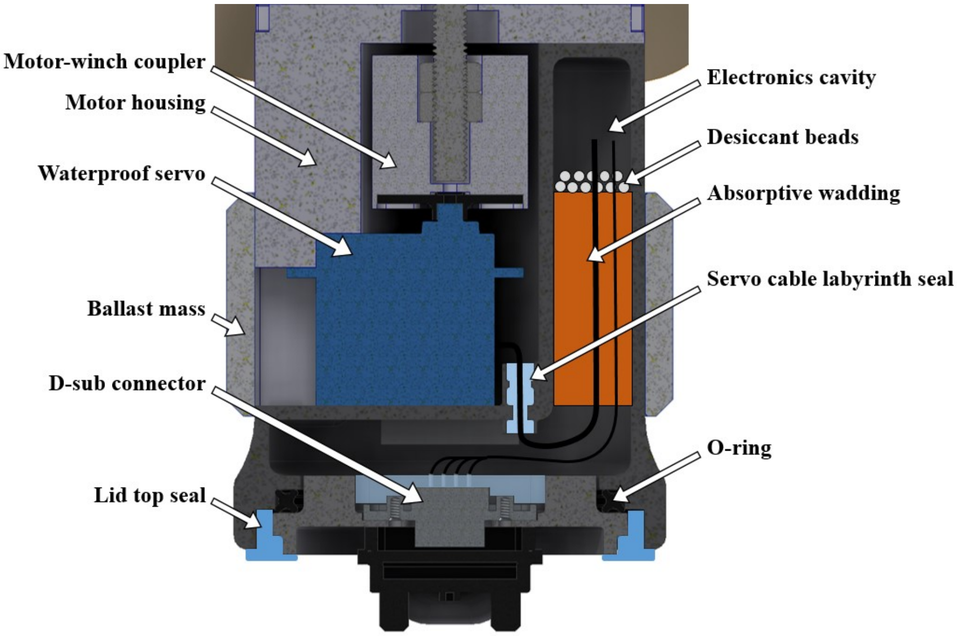

Figure 5 - Close up of the electronics containment unit, with its position and internal components shown relative to the servo motor and surrounding structures.

2.4. ***Testing and Validation of Robot Performance***

2.4.1. Kinematics Measurements

To identify the shape motion profile of the bell for a comparison to the motion of *Cyanea* and Cyro, the bell needed to be marked with visible markers and optically tracked. Multiple markers and contrasting backgrounds behind the clear tank walls were tested for their ease of attachment, low cost, and ease of being tracked. 3D printed ABS red balls were manufactured and tested against a dark black felt background, but the size and matte surface did not appear clearly against the background in the camera footage and the manufacturing was difficult due to the small size. Large metallic red and cyan colored beads were tested next, with them attached to the bell with steel wire pins and imaged in front of a dark background. These tracking balls, similar in relative size to those chosen for Cyro profile tracking, still did not contrast well with the dark background but did appear better than matte surfaced balls.

The final trackers chosen for the robot were green metallic pins, with the end of the pins inserted into the bell until flush with the surface and then backed on the underside of the bell with earring caps to hold them in place during silicone flexure. These pins were placed along the centerline of a single lobe at the inflection points of the bell, points in between the inflection points, and two distal points on the velar flap. A single green ball and an LED turned on by the blip phase signal were attached to the centerline of the robot as a reference. The robot was attached to a solid sting mount threaded into the top of the robot with four threaded rods. These rods were inserted into a solid aluminum plate and fixed rigidly to a 3D printed custom bracket, which mated with an aluminum 80-20 crossbar along the major horizontal centerline of the tank at the top of the tank. The sting and fixed robot were aligned with the center of the tank to eliminate unbalanced fluid interactions and reflections. The back of the tank was covered with a white felt fabric to isolate the colored balls, and the backdrop and pins were lit using a 400W halogen spotlight (Hamilton Technology). As the robot moved through the contraction cycle at steady state, the robot was imaged over time using a Sony NEX 6 digital camera (60 fps, 1080p). The frame was optically zoomed in to capture the full stroke of the robot in frame, and the frame was positioned on the half of the robot with the tracking balls with the tracked lobe parallel to the camera plane. The resulting video was imported into Adobe After Effects, and the individual points were tracked over time using the built-in motion tracking toolbox. The motion tracking algorithm was set to RGB channel tracking and inertial interpolation to achieve reliable tracking despite rapid point motion and occasional occlusion. The data was calculated to be relative to the centerline point, and the normalized motion track of each point over the cycle was plotted relative to the motion tracking data of *Cyanea* and Cyro.

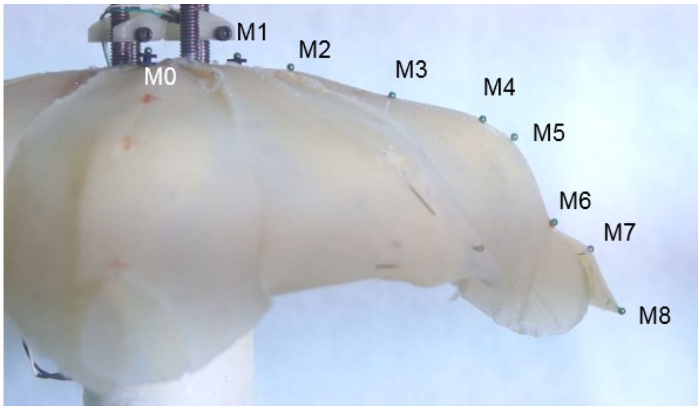

Figure 6 - Locations of the nine tracking markers M0-M8 used to measure swimming kinematics. The lobe in front of the measured lobe had a pinned back velum to avoid occlusion.

2.4.2. Velocity Measurements

Using the same camera and tracking ball setup as the kinematics measurements, the robot was allowed to swim vertically in the tank while being imaged. The frame was zoomed out so the robot could be seen from the start at the bottom of the tank to the end at the top of the tank. Similar to the kinematics tracking, the light at the top of the robot indicated the timing of the phases of the gait, while the tracking ball on the top of the robot indicated the centerline and a constant position reference. Polystyrene foam disks were attached to the top of the robot using the mounting threads to keep the robot near neutral buoyancy but very slightly biased to negative buoyancy. This balance allowed the robot to produce sufficient thrust to exceed the buoyancy force threshold, similar to the neutral buoyancy of jellyfish and their thrust exceeding inertial resistance, drag, and buoyancy. Eleven trials were captured, and each trial was tracked using After Effects and the same settings as the kinematics measurements. As with thrust measurements, the velocity measurements over time were ensemble averaged and statistically analyzed to determine variation in the data. The scale of the measurements was collected using a metric ruler imaged in the plane of the robot at the same magnification and focal length.

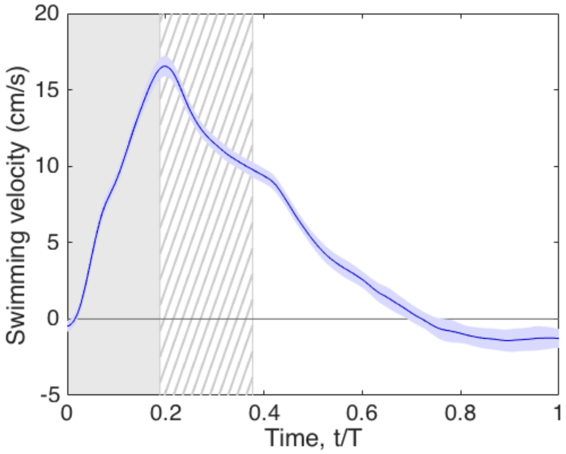

Figure 7 - Forward swimming velocity during one swimming cycle. The contraction, cruise, and relaxation phases of the swimming gait are denoted by the shaded, crosshatched, and white backgrounds, respectively. Trend line is the ensemble average of the last cycle in 11 tests and red shaded regions represent one standard deviation.

2.4.3. Gait Cycle Timing

The controlled position gait was prescribed based on measurements of the *Cyanea* gait timing in videos. The original gait timing from the biological data had a contraction period of 5.4s, with a contraction for 2s, a fully contracted delay for 1s to cruise using inertia and limited drag, and 2.4s to relax slowly with minimal backwards progress due to induced drag (Villanueva and Priya, 2014). Once the position was set for the fully contracted and relaxed state, static testing of the bell kinematics during the cycle was used to determine the speed settings during each phase of the gait. The motor velocity was reduced such that the movement would not reach the endpoint and wait until the completion of that gait phase, but not too much such that the movement was too slow and did not complete in the intended time frame. The motor acceleration was limited to reduce sudden movements at the start and end of motions and prolong the life of the motor gearing and electronics, but not reduced so much that the velocity was impacted during the middle of the cycle phases.

The swimming gait of oblate rowing jellyfish like *Cyanea* is comprised of three phases: contraction, cruise with fully contracted shape held, and relaxation (Figure 8). We measured the duration of these phases for specimens of various sizes ranging from 2.6 cm to 50 cm to develop a generalized, natural gait to test on the robot (Table 1). We found that contraction, cruise, and relaxation last for 31%, 19%, and 47% of the cycle on average, respectively. Sometimes a delay was observed at the end of the cycle but on average only lasted 7% of the total cycle and was therefore neglected when testing the robot. Relative to the original biological timing of the 50cm specimen at 37% contraction time, 18.5% cruise time, and 44.4% relaxation time, this gait was kept as a starting point during testing.

Table 1 - Gait timings for *Cyanea capillata* specimens ranging from 2.6 cm to 50 cm. Data sourced from Higgins (Higgins et al., 2008), Villanueva (Villanueva and Priya, 2014), or measured for this study at the National Aquarium in Baltimore. Data collected in collaboration with Colin Stewart.

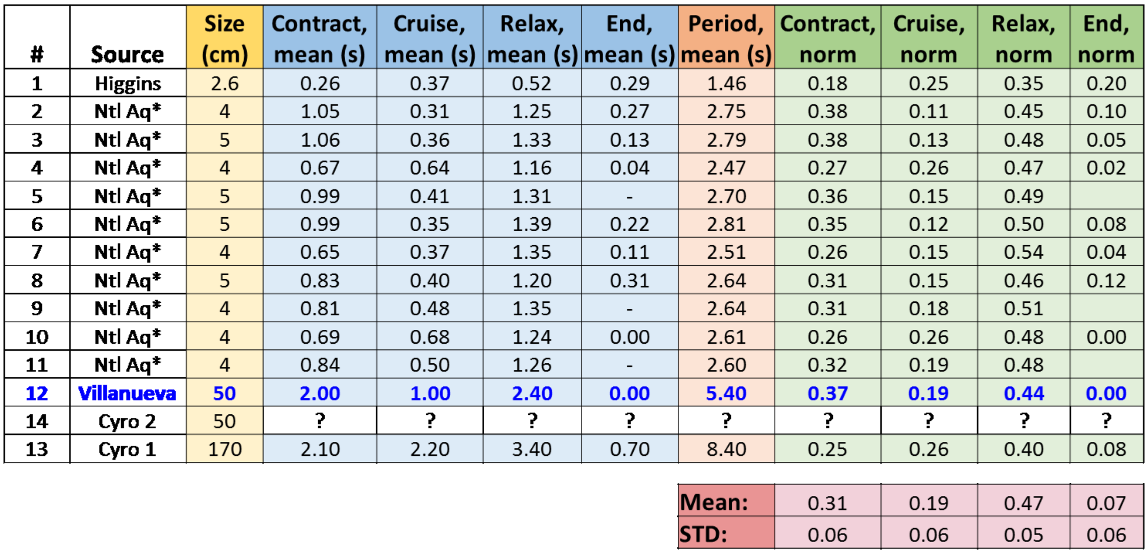

#	Source	Size (cm)	Contract, mean (s)	Cruise, mean (s)	Relax, mean (s)	End, mean (s)	Period, mean (s)	Contract, norm	Cruise, norm	Relax, norm	End, norm
1	Higgins	2.6	0.26	0.37	0.52	0.29	1.46	0.18	0.25	0.35	0.20
2	Ntl Aq*	4	1.05	0.31	1.25	0.27	2.75	0.38	0.11	0.45	0.10
3	Ntl Aq*	5	1.06	0.36	1.33	0.13	2.79	0.38	0.13	0.48	0.05
4	Ntl Aq*	4	0.67	0.64	1.16	0.04	2.47	0.27	0.26	0.47	0.02
5	Ntl Aq*	5	0.99	0.41	1.31	-	2.70	0.36	0.15	0.49	
6	Ntl Aq*	5	0.99	0.35	1.39	0.22	2.81	0.35	0.12	0.50	0.08
7	Ntl Aq*	4	0.65	0.37	1.35	0.11	2.51	0.26	0.15	0.54	0.04
8	Ntl Aq*	5	0.83	0.40	1.20	0.31	2.64	0.31	0.15	0.46	0.12
9	Ntl Aq*	4	0.81	0.48	1.35	-	2.64	0.31	0.18	0.51	
10	Ntl Aq*	4	0.69	0.68	1.24	0.00	2.61	0.26	0.26	0.48	0.00
11	Ntl Aq*	4	0.84	0.50	1.26	-	2.60	0.32	0.19	0.48	
12	**Villanueva**	**50**	**2.00**	**1.00**	**2.40**	**0.00**	**5.40**	**0.37**	**0.19**	**0.44**	**0.00**
14	Cyro 2	50	?	?	?	?	?	?	?	?	?
13	Cyro 1	170	2.10	2.20	3.40	0.70	8.40	0.25	0.26	0.40	0.08

	Contract, norm	Cruise, norm	Relax, norm	End, norm
Mean:	0.31	0.19	0.47	0.07
STD:	0.06	0.06	0.05	0.06

Since the gait measurements were taken from steady swimming of one specimen, modifications of the gait during testing were performed to collect thrust, power, and velocity measurements with dependencies on gait timing. The natural gait utilizes a slow contraction cycle to produce more steady and prolonged thrust. Therefore, we tested the effects of varying the contraction speed to half (4s), 1.5 times (1.33s), and double (1s) the original duration to impart a more steady thrust output or a more impulsive thrust on the robot, respectively. To find similar effects on the sought variables, we varied relaxation as a velocity controlled 2.4 s with cables limiting the relaxation amount and a zero velocity control, fully passive high speed relaxation where the bell opens as fast as the refilling flow, gravity, and elasticity will force. We also varied the 1s delay duration of the original gait to occur after contraction to act as a cruise time for maximizing inertial thrust, after relaxation to allow for full passive relaxation and steady the flow around the robot, and no delay to measure the direct effects and interactions of the contraction and relaxation phases.

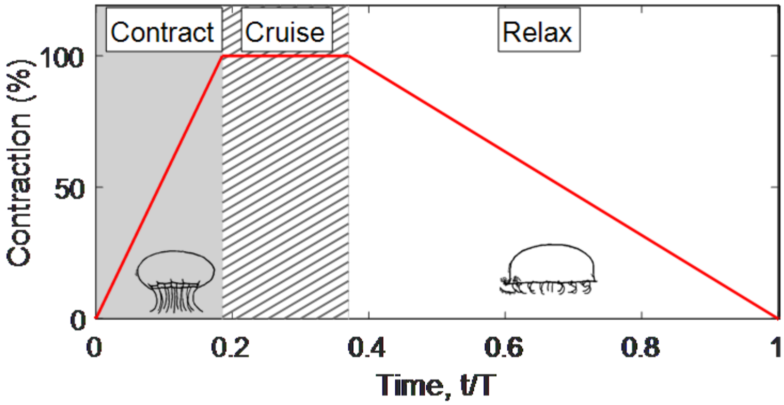

Figure 8 - The swimming gait consists of three phases corresponding to the motion of the bell (body): thrust-producing contraction, holding the contracted shape to cruise forward, and relaxation back to the starting, natural shape. The specific timing shown here for one non-dimensional cycle was used on Cyro 2.

To measure the phase of the gait, the controller output a characteristic square wave to a tap line connected to the DAQ for digital acquisition and to a high intensity white LED for optical acquisition and synchronization during kinematics measurements. During all of the varied gait tests, the 'blip' signal and LED were illuminated during contraction and off during relaxation. With no delay and delay after relaxation, the LED would stay off during relaxation. For the gait with a cruise time delay after contraction, the LED would turn off during cruise time, send a 100ms pulse to indicate the start of relaxation, and turn back off during the remainder of the relaxation period.

2.4.4. Static Thrust Measurements

Since directly measuring thrust force during swimming is impractical, two indirect methods for estimating thrust were utilized. The first method measured thrust using a 10 pound load cell (Transducer Techniques MLP-10) in compression and tension during the swimming cycle that was sampled at 10 kHz by a National Instruments DAQ (NI USB-6002). The load cell was attached to an amplifier box to increase the amplitude of the load cell output, and the signal was balanced to zero voltage at zero load using the amplifier bias potentiometer. Since the signal could not be completely zeroed by the bias adjustment, a summation resistive operational amplifier circuit was placed in series with the amplifier output and a DC bias was applied to the amplifier by the DAQ card to completely zero the signal at zero load. The resulting sensor system was calibrated using masses ranging from 0 to 10 pounds that were hung from the load cell in compression and tension configurations. The resulting calibration curve was a linear fit across the full compression and tension region, with an R^2 of 0.9997.

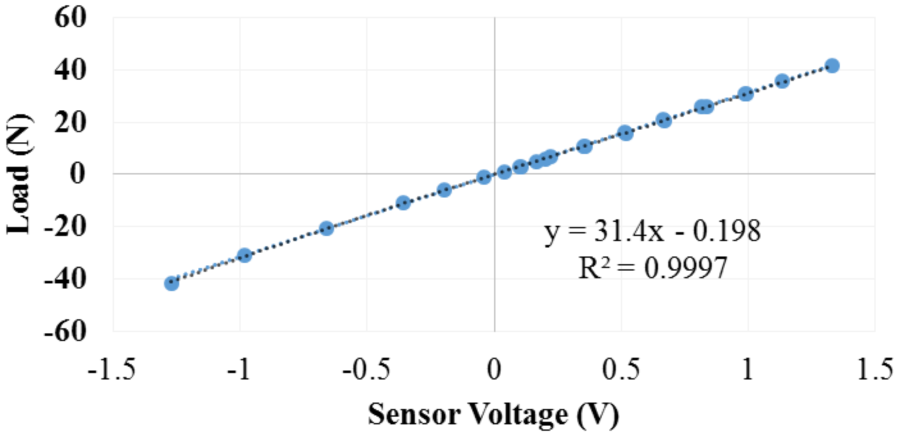

Figure 9 - Load cell calibration for thrust measurement stand

Since the load cell needed to be out of the water, the robot was fastened to the load cell via a sting composed of four 7/16 inch threaded rods, which were threaded into reinforced holes at the top of the robot and constrained to a 1/2 inch thick aluminum adapter with through holes and locking nuts. This aluminum plate was screwed into one end of the load cell. The other end of the load cell was threaded into a ball and socket adapter, which kept the robot axially aligned with the load cell without sideways loading and despite lateral movements. The ball and socket adapter was then threaded into the center of an 80-20 extruded aluminum bar, which was attached to the 80-20 aluminum cross bar across the center of the tank using 90 degree flanges that rigidly constrained one side of the ball and socket adapter. The threaded rods were adjusted so the robot was axially aligned with the load cell and centered in the depth of the tank. The tank size was 172.72 cm x 81.28 cm x 142.24 cm., which is greater than the diameter of the bell in the lateral dimensions (1.626:1 width, 3.454:1 length at maximum diameter) and the height of the robot in the depth direction (7.175:1 depth). Since most of the fluid interactions occur in the depth direction and near the margin of the bell, wall interactions were not expected to be significant.

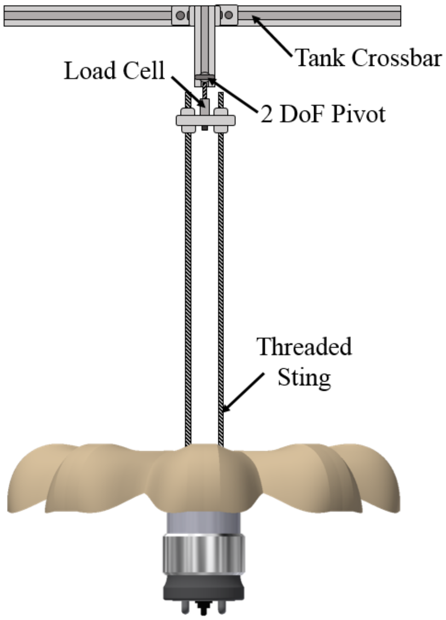

Figure 10 - Sting mount arrangement for load cell static thrust testing

To measure the thrust from the robot, a static measurement of the load without movement was taken before each trial set to provide a baseline to compensate for robot and sting assembly weight and buoyancy at that time of day. For each contraction cycle timing, data collection was started and then the robot was turned on to start the gait cycle. The first pulse always started as a sudden contraction when the controller sent an initial clipped signal, and the next two cycles were determined to still be not indicative of steady state since the water in the tank was still relatively static. Therefore, thirteen or more contraction cycles were collected to allow ten or more complete steady state cycles with reliable thrust measurements after the first three contraction cycles were removed. Ten trials of thirteen contractions were collected per contraction cycle timing, with each trial starting with the robot turning on after the robot had been turned off for two minutes to allow the fluid movement to stabilize. The average of the static load measurement was subtracted from each data set, and the gait cycles were split into individual cycle thrust measurements over time based on the gait phase signal. The one hundred measurement cycles were filtered for 60Hz noise and ensemble averaged at each time step to get the expected representative thrust output curve, and the range and standard deviation was calculated to determine the variation in the data and identify possible experimental errors or reliability issues.

2.4.5. Power Measurements

The current draw of the motor was calculated with Ohm's Law by measuring voltage across an external 0.1 Ohm, 1%, 10W resistor in series with the robot tether. The robot power was determined as the power going into the buck converter, which was the measured current combined with the tapped voltage measurement of the input to the buck converter. The previous calculations formulated during the electronics design required an accurate measurement of the cable resistance and converter efficiency to achieve motor and controller power draw. While the power to the motor and controller is slightly less due to losses in the buck converter, directly measuring current in the robot was sensitive to moisture and the converter efficiency varied from about 90-95% in the operating range, so this measurement is taken as a slightly conservative estimate. In addition, it can be assumed that since the power converter is integral to the proper regulation of the input into the motor over variable input voltage and variable current draw, and since there should be a converter and/or regulation component with similar efficiency between any power supply and the actuators, controllers, and sensors, this small power increase was considered part of total robot power draw. Using the power tap from on the robot and before the regulator included the power fluctuations under load due to cable resistive losses, and hence results in a simple Ohm's Law calculation for power that is more reliable than a multi-measurement calculation that can accumulate error.

During each free swimming and static measurement, the current and voltage over time was collected. As with the thrust measurements, the steady state cycles were isolated, split into cycles based on the timing signal, and ensemble averaged and statistically analyzed to determine variation.

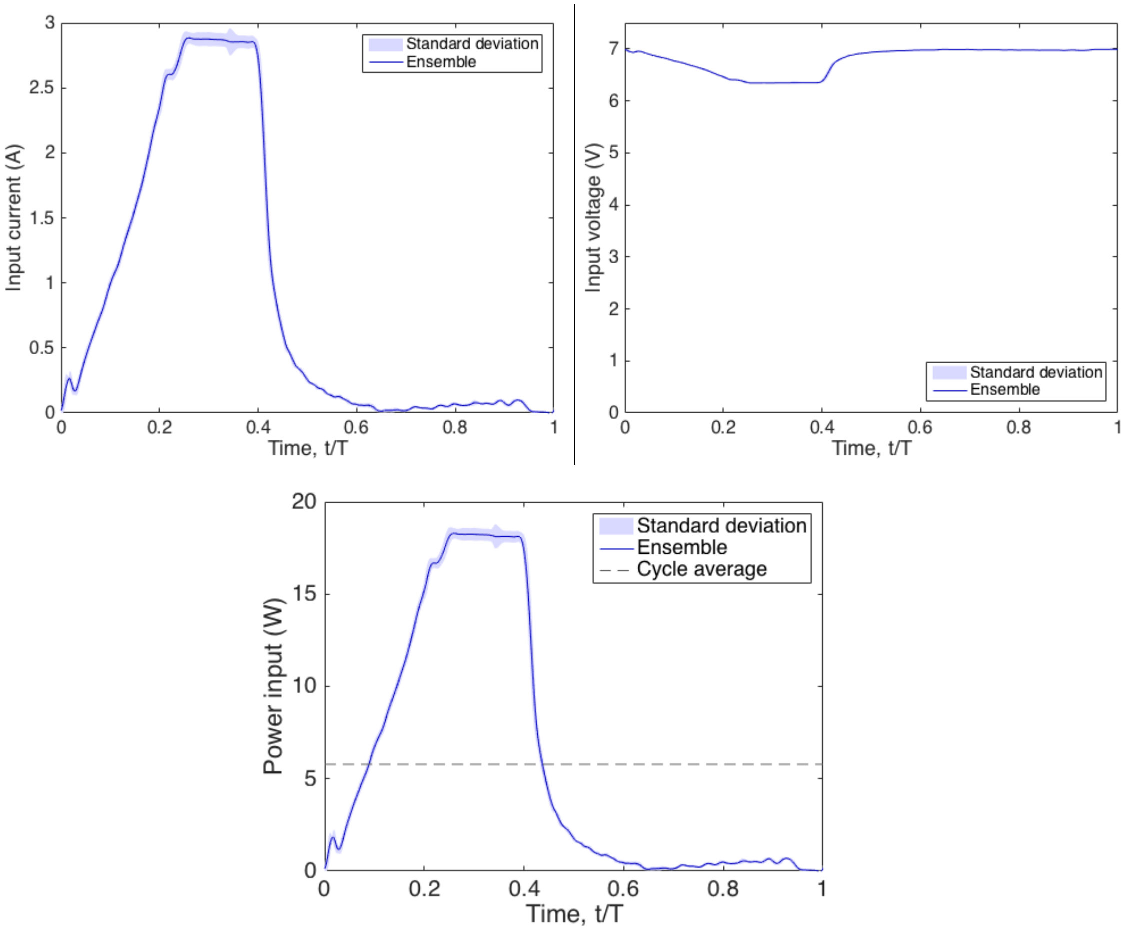

Figure 11 - Full cycle voltage, current, and power draw. The solid blue curves show the representative data (ensemble average of 137 cycles), while the shaded area shows one standard deviation. The cycle average power of 5.7 Watts is shown on the power plot.

2.5. ***Conclusions***

2.5.1. Kinematics Measurements

The initial goal of this robot was to mimic the kinematics of *Cyanea* closely to enable the study of the fluid interactions and expand the current knowledge of large jellyfish locomotion. Unfortunately, this preliminary effort to match kinematics and material properties with limited reference images of a static and relaxed bell resulted in kinematics that deviated from the natural kinematics tracked for a specimen of similar size (Villanueva and Priya, 2014). Since the bell form was originally based on multiple pictures where *Cyanea* was at the end of the relaxation part of the swimming cycle but still moving, the drag on the bell caused downward deflection and the fully relaxed position was artificially placed low. The low rest position, as well as the low stiffness silicone chosen to closely mimic the mesoglea of a jellyfish, also reduced the stored elastic energy in the bell. Since the relaxation was completely passive and relied on this stored energy, limited stiffness and pre-deflection of the bell greatly reduced the capability of the bell to relax to the range and hence at the speed observed in nature. This resulted in reduced stroke length, which was limited to the lower part of the cycle and hence at the portion that produced the least thrust. This drastically limited the cost of transport and efficiency expected from a *Cyanea* inspired robot.

In addition to the limited stroke, the trace of the velar tip was seen to form a figure eight instead of an oblong round path characteristic of *Cyanea* jellyfish of similar size. This resulted from the casting form of the velum as well as potentially some testing setup limitations. During the contraction phase, the velum was expected to bend far outwards during the start of the contraction, stay bent outwards during the contraction, and settle back in line with the bell surface as the contraction slowed and the cruise phase was initiated. It can be seen in the comparison between the robot tracking in (a) and the animal tracking in (b) below that the velum had a starting shape that was pre-deformed upward and cupped to trap the flow even more. As the robot contracted, the cup flattened out and the bending at the base increased even more, excessively deflecting the velum upwards. As the bell slowed down the velum seemed to re-form the cupping prematurely, further distorting the path. During relaxation the bell should fold strongly inwards to reduce the bell diameter and deform under drag, as seen in the red dotted lines in (b). However, the shape of the velum almost kept its no-load shape the entire relaxation motion. This was expected to be in part an artifact of a slowed controlled relaxation on the robot, as well as less flow over the bell during static tracking and hence less drag and inertia induced deformation. A more significant factor was the overlapping lobes that were intentionally added to the casting form. While these are seen in reference images of *Cyanea*, the images used as a reference were during relaxation. The folding of the velum inwards should cause some overlapping, but this does not necessarily assume that the fully relaxed form should overlap. In other images of full relaxation, the velar flaps clearly have distinct cleft halves per segment that do not overlap until relaxation and full contraction. This stiffened the velum during relaxation and locked at least half of each cleft velar flap pair in place, while the entirety of the velum on each lobe was free to move and flex further outwards during contraction. In order to revise the casting and kinematic errors, improvements in the stiffness of the bell and casted form for further relaxation and proper velar deflection were necessary. This also required revisions in the spindle and cable design due to additional cable travel that was needed for the upper section of the full stroke.

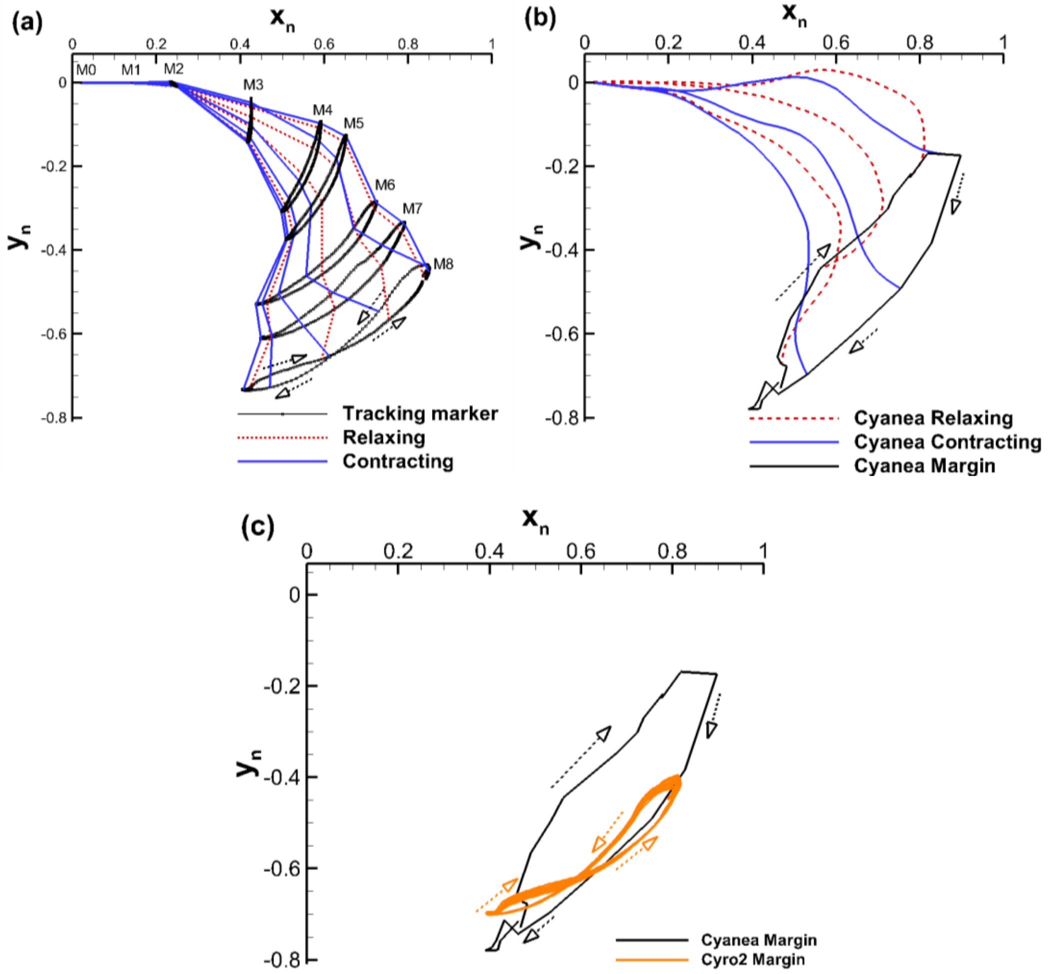

Figure 12 - Reconstructed half bell profiles of (a) Cyro 2, (b) a 50cm *Cyanea capillata* specimen, and (c) a comparison of the paths traveled by their marginal tip points during swimming. Axes are normalized by the center axis to velar tip arc length.

2.5.2. Velocity Measurements

Cyro 2 achieved a maximum velocity of 16.6 cm/s and an average velocity of 5.0 cm/s. When compared to Cyro, which achieved a maximum velocity of 25.5 cm/s and an average velocity of 7.3 cm/s, the performance of Cyro 2 was impressive at 65.1% the max velocity and 68.5% the mean velocity at a diameter reduction to 25%. As can be expected, the proficiency of Cyro 2 was better at 0.36 max and 0.11 average than Cyro's proficiency of 0.15 max and 0.04 average. Small biological samples (3.5 cm – 5.6 cm) in videos provided by Jack Costello had a max proficiency from 0.61 to 1.04 and an average proficiency from 0.16 to 0.38. The 50cm specimen that the robot was based on had an average proficiency of 0.3. Therefore, compared to known specimens, Cyro 2 was less proficient on average but near the expected range at some points in the cycle. Proficiency at the same robot scale can be achieved by increasing the velocity of locomotion, which would be a result of improving the bell range of motion to produce significantly more thrust and improving the velar deflection at relaxation to reduce deceleration due to drag at the periphery of the bell.

2.5.3. Swimming Cycle Timing

The final gait timing used by the robot maintained the 5.4 second total cycle time, as well as no stall time after relaxation and before contraction. However, the original timing of 2 seconds contraction, 1 second cruise, and 2.4 seconds relaxation resulted in too much deceleration and induced drag during the relaxation phase, as well as too little thrust production during the slow contraction. Reducing the contraction time improved thrust production since the gradual ejection of the fluid, which relied on a long time duration of low thrust for acceleration, was changed into a short burst of high momentum flux and thus thrust that achieved rapid acceleration to move the robot to a high forward velocity. This method utilized the inertia of the system and the reduced frontal profile of the bell at full contraction during late contraction and a cruise period to augment pure thrust production for additional forward progress. Increasing the relaxation time slowed down the movement of the bell against the direction of movement, thus reducing high pressure on the front of the robot and low pressure under the bell. Therefore the final timing was increased to 3.4 seconds for relaxation to balance the 1 second reduction in contraction time. Adding a stall time at the end of the cycle only extended the relaxation, and hence did not appreciably introduce a benefit over extending the relaxation time. Increasing the cruise time past the 1 second setting allowed the robot to enter a fully contracted but no forward velocity state and subsequently allow stopping due to drag or sinking in reverse, so the cruise time was kept the same. Integrating a controlled release of the relaxation, instead of immediately releasing the spindle and allowing free relaxation, helped make the relaxation time and stroke more prescribed and predictable. The highly controlled position and velocity also avoided a fast early relaxation and slow final relaxation with oscillations at the end of the relaxation as seen with free relaxation, which served to induce even more drag at the same relaxation time.

Due to this sensitivity to variation in parameters, the final gait was found to be the only gait that worked for upward free swimming. Improving the stroke length of the bell in a new design would allow a total increase in the contraction time while producing more total thrust and similar transient thrust, which could allow a longer and thus more biomimetic contraction time. For example, since the stroke is about half of the actual full stroke observed in nature, doubling both the travel and time should not change tip velocity and hence would still apply a large spike in thrust but with an intermediate flat band thrust region. Improving the velar flap deflection would reduce drag in the relaxation phase, and hence a slightly faster relaxation could be effective since the frontal area would be reduced while velocity could be slightly increased, which would cause even more area reduction with a faster movement inducing more drag-induced bending of the velum.

2.5.4. Static Thrust Measurements

As expected, positive thrust was generated during contraction and negative thrust was generated during relaxation when fluid is being drawn in to refill the bell (Figure 13). The peak thrust during the cycle was 6.17 N, the average thrust during contraction was 3.68 N, and the average thrust was 0.22 N, roughly indicating that the robot was capable of forward locomotion. However, the thrust of the robot still had potential for improvement. For vertical swimming the thrust just had to produce enough force to cancel and exceed the slightly negative buoyant force on the robot. However, this acceptance of any thrust that breaks the buoyancy threshold as good for swimming was faulty in its broad practicality. If the robot were to swim in any direction except vertically, the strong buoyant force currently on the robot is stabilizing and would force the robot to swim vertically again. In addition, buoyancy cannot help bias the thrust towards good performance in non-vertical directions, so balancing resistive forces while ensuring stability to hold a direction was much more difficult and could require more force to maintain a heading against gravity and buoyancy. Therefore the actual thrust production should be more critically analyzed. The average thrust was a good indicator as holistic performance.

During the primary stage of contraction, the thrust was an impulse loading on the fluid and hence an impulse reaction on the robot. However, this waveform took extra energy and rapid motion to produce this forceful impulse thrust, and this impulse only had as average thrust of about 60% the peak thrust. Therefore it would be beneficial to explore more gradual contraction with a longer stroke length to generate more magnitude thrust over a longer period of time, thus increasing the average of that phase and reducing the energy required to shove the water away from the bell as opposed to elegantly manipulating the water.

During the cruise time and relaxation, as the impulse tapered off the robot experienced negative thrust of a non-negligible amount relative to the thrust produced during contraction. While some negative thrust can be expected, this negative thrust could be decreased by adjusting the form of the robot. As mentioned during kinematics, the lack of velar flexion during relaxation maintained a broad surface area to impart drag. Improving flap flexion to match the biological kinematics that reduce frontal area and deforms more under faster relaxations would enable a more natural gait, less drag resistive forces, and hence further increase the average thrust.

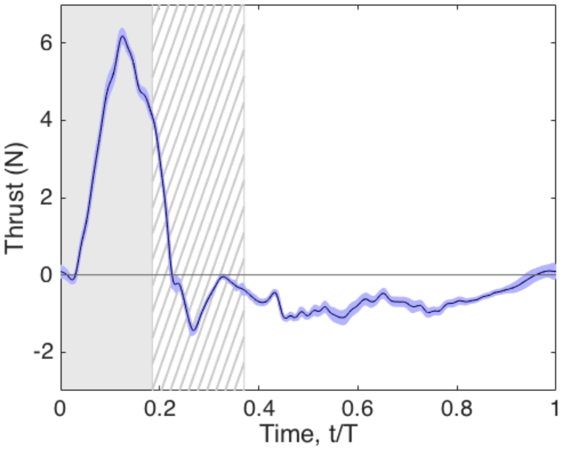

Figure 13 - Thrust during one swimming cycle. The contraction, cruise, and relaxation phases of the swimming gait are denoted by the shaded, crosshatched, and white backgrounds, respectively. Trend lines are the ensemble average of 137 cycles and red shaded regions represent one standard deviation.

It should be said that this test of thrust forces from a device on a sting mounted to a load cell far outside of the fluid flow is a common practice in engineering for reliable and consistent results. However, for a system that manipulates the fluid both below the bell and flowing over the bell during free swimming, an inherently dynamic system may have over-estimated thrust when measured on a static sting. Flow over the bell would induce additional drag on the bell since bell local movement is added to bulk movement through the water. The fluid under the bell that is rolled into an ejected vortex ring mass is also known to stack to improve efficiency of movement (Dabiri et al., 2005). Pushing a mass of water against a moving fluid and dynamic wake does reduce the potential thrust of the system, while pushing off against slow-moving and mostly static fluid during the sting tests would artificially increase the measured thrust. While a direct method of quantifying thrust is still a significant problem for dynamic systems, modeling can be used to derive thrust from wake energy and bulk kinematics. This method has inherent problems, such as assumptions of form that feed into the calculation of drag and added mass, and could produce erroneous estimations, but as long as the wake is resolved reliably with PIV and the velocity measurements are accurately imaged and tracked this could provide a more ‘true’ thrust measurement. The intricacies and methods of this estimation were based on Daniel’s model of motion, and will be explored and detailed in Colin Stewart’s dissertation (Daniel, 1983).

In addition to thrust measurements for the final working gait, thrust measurements for variations in the gait were observed. These were also collected during static tests, which were collected regardless of no successful swimming since the identification of gait sensitivity was critical to further understanding of swimming performance. As can be seen in the comparison, average thrust was higher for no delay and end delay for controlled relaxation as opposed to free relaxation. End delay adds additional time to relax the bell to increase stroke and slow down the fluid around the body to increase thrust, while no delay increases interactions between the relaxation and contraction phase by eliminating stagnation in flow or motion during a delay period. While the swimming case of cruise delay appears to have limited thrust, the no delay case and end delay case limited forward travel during the cruise period. This cruise advancement is critical since the contraction phase used an impulse thrust with small duration, so the contraction induced enough acceleration for the jellyfish to coast at minimal frontal area during the cruise phase but not induce significant forward travel during the contraction phase. No delay resulted in limited time for deceleration but also limited time for forward advancement, and the end delay resulted in not enough time to advance forward but too much time to drift backwards in the water column. End delay and no delay induced minimal drag due to minimal forward velocity and limited forward travel time during the cycle at free swimming, and hence the thrust was large but not indicative of positive progress in the bulk kinematics. The cruise delay appears to have lower average thrust for controlled relaxation since the negative thrust was large but rapid for free relaxation, while controlling the relaxation resulted in less deceleration impulse thrust but over a longer duration that reduced the cycle average. This timing effect on the average thrust value also accounts for the increase in the no delay case, due to limited stall or cruise time to encounter negative or reduced thrust and thus a higher time average value.

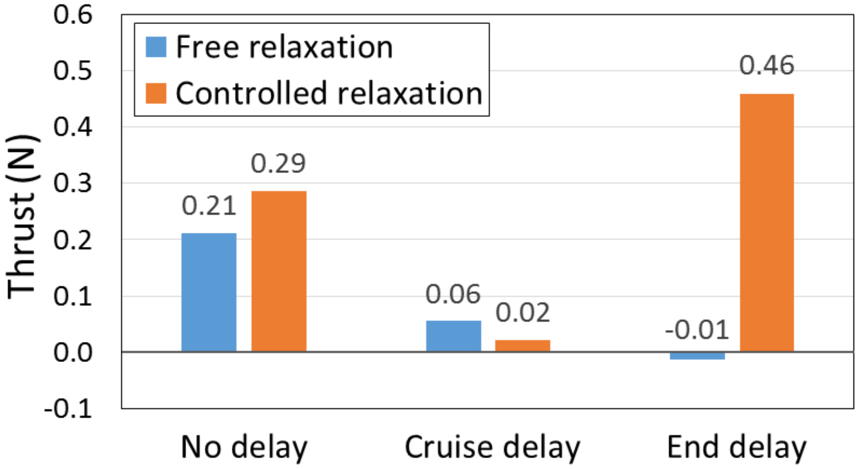

Figure 14 - Thrust production based on delay timing and relaxation speed

For varied contraction timing with a controlled relaxation, the biological contraction time of 2 seconds with a relaxation time of 2.4 seconds and cruise time of 1 second resulted in an average thrust of 0.02 Newtons, while the faster contraction of 1 second and a slower relaxation of 3.4 seconds, with the same 1 second cruise time, resulted in an average thrust of 0.22 Newtons. The cycle average time was the same, while negative thrust was minimized by a slower relaxation and the contraction thrust was increased due to a short duration impulse as opposed to a long duration, low thrust period with small overall thrust production and a resultantly lower cycle average thrust. This profile was expected to, and experimentally did, swim the best due to the correct balance of fast acceleration to high speeds, long duration at these high speeds and minimal surface area to achieve forward travel, and minimal drag resistance to forward progress or induced downward drift.

2.5.5. Power Measurements

Input power also peaked during contraction and average power consumption was 5.7 Watts, which was substantially lower than our previous jellyfish robots. For a comparison, Cyro consumed a cycle average of 70 Watts, which means Cyro 2 consumed 8.1% the power of Cyro while only scaling to 25% of the diameter. This could also be in part due to the mass of the robot, which for Cyro 2 was 4.3% of the Cyro mass. However, the cubic reduction in three dimensional size expected that Cyro 2 should be 1.6% the mass of Cyro. Bell density was constant between robots, but the density and size of actuation, balance, and control elements relative to the robot scale led to the change in proportional mass.

To non-dimensionalize these potentially interconnected parameters for equal comparison, one common method used for biological propulsion is the cost of transport. This metric measures the power consumed vs the mass and velocity of the system. Although it was expected that cost of transport decreased roughly linearly with the mass of the system on a log-log plot, this was usually seen over orders of magnitude and not as a significant difference in cost of transport over a little over one order of magnitude (Cyro at 76 kg, Cyro 2 at 3.28 kg) (Villanueva et al., 2013). Cyro 2 had a cost of transport of 35.2 $\frac{W}{kg\frac{m}{s}}$, while Cyro had a lower overall cost of transport of 12.7 $\frac{W}{kg\frac{m}{s}}$. In order to reduce the cost of transport three methods can be used. The power of the system can be reduced to improve cost of transport and overall efficiency. As can be seen in the power plot, reproduced and phase-aligned below, the cruise phase consumed as much power as the entire rest of the cycle while not actively adding to robot movement. If the actuation was considered as an analog of muscles in the jellyfish, muscle does consume energy to hold a load at a fixed position (He et al., 2000; Koerhuis et al., 2003). However, in terms of useful energy on a robot it can be seen as ‘wasted’ energy, and removal of this load using latching mechanisms would reduce power by half to reduce the cost of transport to 17.6 Watts. For comparison, Cyro had significant wasted energy in over-safe actuator selection, so it is unknown if power reduction alone would improve relative performance.

An increase in mass could improve cost of transport, but the ballast masses and foam already added excessive mass to the system and inertially limited the swimming velocity. This non-dimensional measure also canceled proportional increases in velocity from decreases in mass, so changing mass alone is not as effective. Therefore the second practical method for improving cost of transport would be to increase the velocity of travel. As seen in the thrust, kinematics, and cycle timing sections, increasing the total stroke length of the bell and velar flap deflection during relaxation would increase acceleration and reduce drag-based deceleration. This would increase average velocity without significant mass changes, and this improvement paired with power optimization would drastically improve the cost of transport and overall system efficiency.

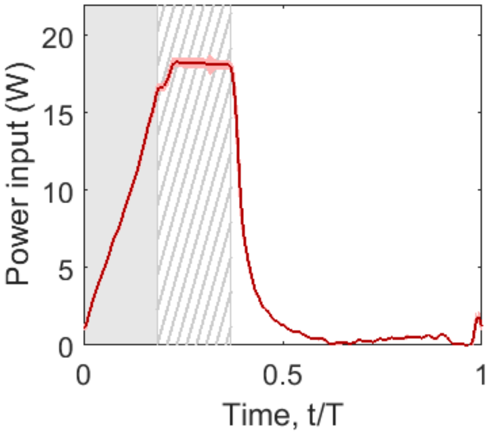

Figure 15 - Power input during one swimming cycle, split into the three stages of the cycle. The contraction, cruise, and relaxation phases of the swimming gait are denoted by the shaded, crosshatched, and white backgrounds, respectively. Trend lines are the ensemble average of 137 cycles and red shaded regions represent one standard deviation.

During relaxation speed and delay timing variation, the cruise delay induced additional power draw as seen above and hence had a higher average power. The no delay eliminated this high power draw phase, effectively reducing the average cycle power, and the end delay had additional low power consumption time, which resulted in a further reduced average power draw. Free and controlled relaxation were close in power draw since the relaxation time was equal and little power was consumed regardless of the relaxation speed.

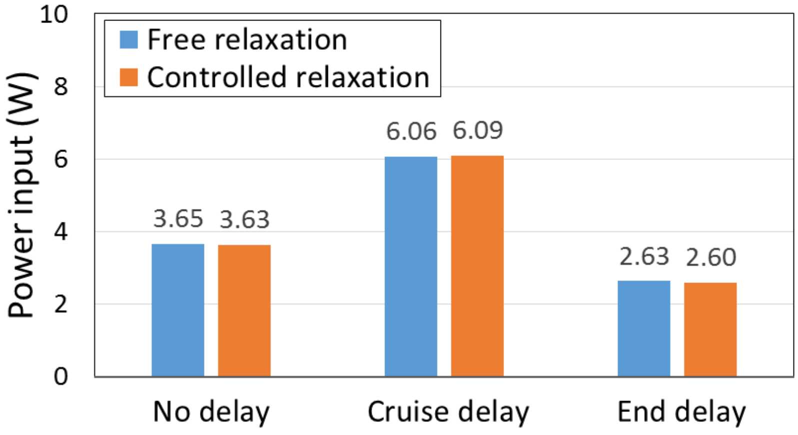

Figure 16 - Power consumption based on relaxation speed and delay timing

For the biological contraction of 2 seconds versus the impulse contraction of 1 second, average power was roughly the same at 6.09 Watts for slow contraction and 5.78 Watts for fast contraction. The longer duration contraction period reduced motor impulse loading and thus instantaneous power consumption, but the high-load period was resultantly longer and the low power relaxation period was lower by 1 second relative to the fast contraction phase. Therefore short duration loading, long duration minimal load provided a small 5% decrease in power consumption.

2.5.6. Performance Scaling Relative to Biology

Although the performance of *Cyanea* jellyfish has not been characterized in large numbers, the specimens that are available can be used to determine whether Cyro 2 had scaled appropriately. This determined not just whether the robot was an appropriate representation of the animal in terms of overall performance, but also provided a limited insight into how *Cyanea* and other rowing jellyfish scale over several orders of magnitude using Cyro and Cyro 2 as proxy representations of biological data. Existing data used included four specimen videos provided by Dr. Jack Costello, as well as two data points from specimens tabulated in a previous study (Acuna et al., 2011).

In terms of kinematics, average velocity though the cycle was found to scale logarithmically relative to diameter and mass. As can be expected, the slope of the log of the diameter was 2.48 times the slope for log of mass due to the cubic relationship between mass and diameter. The less than cubic relationship can be a representation of less trailing structure growth relative to bell diameter. In biological specimens the trailing structures are small for small sizes, then suddenly grow as the specimens enter adult stage and grow extremely long for the largest of sizes. Since the robots did not maintain a long central mass proportional to that of the animal's growth, this scaling property was indicative of a discrepancy when considering the mass basis of growth. In addition, the robot central columns were usually variable density volumes, so the composition of the depth direction was inconsistent with neutrally buoyant and near equal density tissues. Therefore, additional data would be needed for a comprehensive mass basis scaling law.

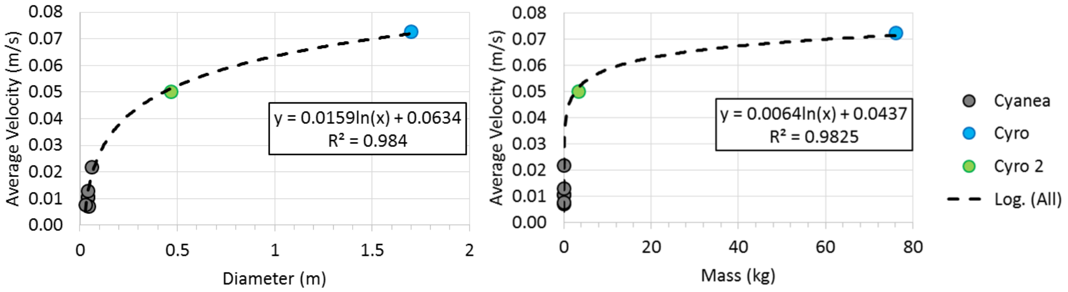

Figure 17 – Scaling of average velocity relative to mass and diameter scale for biological specimens of *Cyanea* and existing robot platforms.

Scaling of the average proficiency, defined as average velocity divided by bell diameter, had an inverse log relationship with a less than perfect fit due to the spread of proficiencies for the biological examples. This showed that while proficiency can be a good measure, similarity with nature when it inherently included broad variation between 0.16 to 0.34 Hz cycle time was not a good measure for robot platforms. It did show that, despite the spread of the data, the proficiency of the robots and animals decreased with diameter. This was due to the increased inertia and drag, reducing the ability to accelerate relative to the absolute size of the animal. This was also seen in effect from the velocity curve where, despite an increase, the tapering from size indicated difficulty in achieving proportional speed.

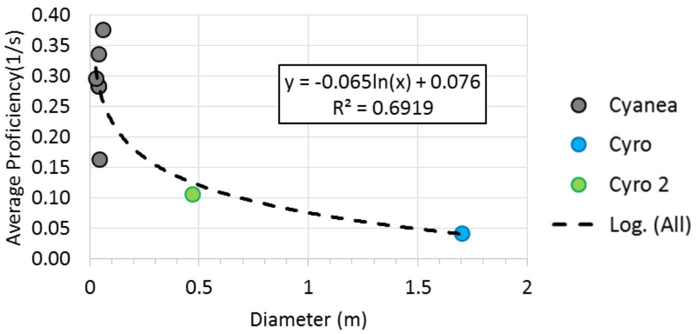

Figure 18 – Scaling of average proficiency relative to diameter for biological specimens of *Cyanea* and existing robot platforms.

Another necessary analysis when considering the efficiency and necessary effort to generate the propulsion for forward swimming was the power input relative to mass. The biological data was clustered on the lower end, so for both the limited biological data and existing robot data it was seen that power consumption increased at a roughly linear rate to mass (nearly a 1:1 ratio at 0.9154). This sharp increase in scale was an even better fit using the frontal area of the bell, showing that the depth contribution to mass that was not consistent across all scales reduced the consistency of the data. In addition, while mass changed the power requirement for acceleration, the frontal area encompassed the drag on the robot and resistance to moving the bell through the water under actuation. These were the primary effects on power consumption besides actuator efficiency, which we can assume was tuned as well as possible for these designs. Therefore, we can see that robot design should scale actuator effort linear to frontal area. Additional data is needed for a true biological trend of metabolic input, as well as separate effects of total system, power conversion, actuation, and hydrodynamic efficiency on power consumption.

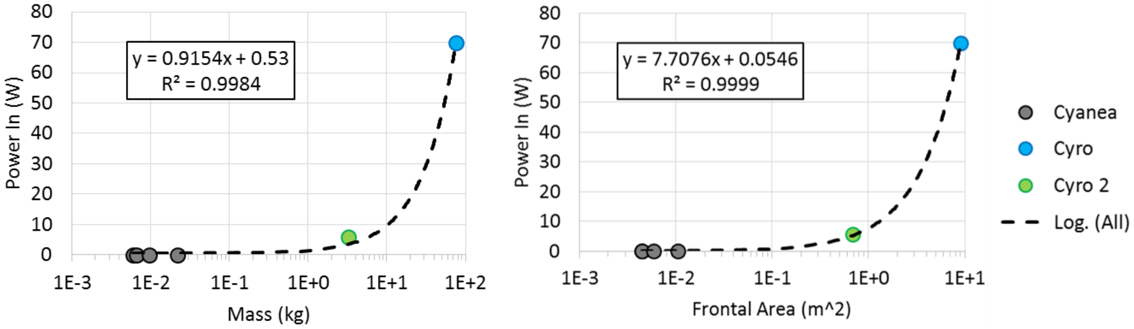

Figure 19 - Power consumption based on relaxation speed and delay timing

3. Decomposition of factors utilized for *Cyanea* maneuvering

3.1. ***Introduction***

3.1.1. Motivation from Cyro 2 Results

After the development of Cyro 2 to more closely mimic *Cyanea* forward swimming with efficient actuation, multiple design limitations relative to the locomotion capabilities of *Cyanea* were uncovered. As an intended mimic of the *Cyanea* swimming kinematics, the kinematics of the bell shape were designed to closely follow the tracked bell kinematics of a *Cyanea* of equal size. However, the compromise of actuation resistance from material stiffness during contraction and recovered spring energy for relaxation led to the selection of a very low stiffness silicone. This selection reduced the stroke length of the swimming cycle due to sagging of the bell under its own weight. In addition, references for bell shape mostly show the form during coaxial flow and with deformation due to gravity acting on the low stiffness mesoglea. Therefore, the references for the shape included naturally loaded deflection in the original shape, which further lowered the relaxed position and reduced the upper portion of the stroke. Since the bell form and kinematics are imperative to the method of locomotion by jellyfish, these limitations reduced the possible swimming performance as well as the generalizability of the gathered dynamics metrics and trends.

While the simple design of Cyro 2 was an effective approach of integrating the simplicity in form and function of jellyfish at a scale that would normally require increased system complexity and power consumption, the simplicity inherently limited the propulsive capabilities. The single motor construction reduced the swimming kinematics of rowing jellyfish to the radially symmetric actuation for axial movement, and decreased the power consumption needed for individual lobe control. However, having the load of eight bell segments on one motor increased the per-motor load, and since the load was observed to be near stall torque at full contraction the actuation efficiency of the motor was low. Since servo motors have internal PID feedback loops consisting of a potentiometer feedback on the output shaft, as well as mechanical stops on the motor output to prevent sensor damage, travel on the motor and kinematic control of the motor was limited. Using the servo controller to control kinematics was effective, but the means and limitations of this control were further hidden from the user. Under persistent and increasing or decreasing load, the motor position output was not consistent and manual tuning was needed to get the kinematics to match the desired states as close as possible. Any change in the timing of the swimming cycle required extensive tuning of speed settings to get the timing under load to match. In addition, error tended to accumulate as the motor failed to reach a final position, causing the true motion of the motor during the cycle to vary within the envelope of the desired motion path. This periodic error introduced problems with consistency of robot kinematics. When cycle timing and kinematics were found to be extremely sensitive, and small changes made the robot fail to achieve the easiest case of upward buoyancy-balanced swimming, reliability and consistency was a critical focus for future robot mechanical designs and control architectures.

For power management and predictability, the single motor architecture was originally tethered to power supplies and data acquisition cards out of the testing tank for power monitoring and control. Since power measurements outside of the tank do not account for cable resistance, and the power delivered to the robot strongly varied based on load, this architecture required additional cables and measurement points to properly characterize local robot power and cable losses. This further required additional electronics to be placed on the robot in a sealed enclosure, which had to conform to a predetermined design and required additional development time to seal against water ingress. This housing added more mass and sealed off air to the robot, which induced changes in both the center of mass and buoyancy that required additional external features to control the stability and buoyancy balance of the robot. In addition, the cable tether was designed to minimize resistive losses that altered the power delivered to the onboard components, thus requiring a low gauge, high diameter wire to increase the current carrying area and reduce destructive and wasteful heating. Although the cable diameter and stiffness was minimized as much as possible through selection of high flexibility conductor architectures and jacket materials, the large cable still disrupted flow around the robot during PIV measurements. Although attempts were made to mask the disrupted flow and appearance of the cable in the frame, including coloring of the cable with colored tape to improve visibility for automatic masking, the cable motion and size persisted to cause difficulties in masking. The most significant problem was the effect of the cable on swimming repeatability and reliability.

Since the cable added an additional force vector from bending and weight, which varied depending on the cable orientation and increased length carried with the robot off the bottom of the tank, the robot tended to drift in the tank and disrupt the assumed planar motion required for PIV measurements. These sub-optimal design features, as well as limited kinematic capabilities, necessitated a significant improvement in robot design for future iterations that could be considered biologically accurate and viable for measurement.

3.1.2. Motivation and Background of Jellyfish Turning

Finely controlled maneuvering is a functional necessity for underwater animals that are escaping predators or unfavorable environmental factors, pursuing or station keeping for prey capture, and migrating over long distances (Fish et al., 2018). These maneuvers require that asymmetry is introduced into typically straight swimming from balanced fluid interactions, either through additional modes of thrust production or manipulation of the straight swimming kinematics. Rowing jellyfish such as *Aurelia* have been observed turning via a combination of asymmetric contraction timing, such that the inside lobes of the bell in the plane of the turn contract before the outside lobes of the bell, and asymmetric bell margin stiffness, where the inside lobe stiffens the marginal flap and the outside loosens the marginal flap (Gemmell et al., 2015). However, the gradation of the turning based on these features, as well as the individual contribution of the stiffness and timing on the turning magnitude, has not been explored. In addition, the relaxation phase of the turn has not been discussed in previous studies due to the widespread focus on the contraction phase, since it has been expected that the primary forces are generated through thrust during the contraction phase of the cycle. While additional experiments with specimens in a lab environment could elucidate this control space of jellyfish turning, large jellyfish such as *Cyanea* have only been observed in their natural environment to have induced asymmetric timing (Gladfelter, 1972). The sketches by Gladfelter could indicate changes in contraction timing and speed with marginal stiffness, but the impact of these factors on *Cyanea* has not been explored.

Therefore, the implementation of asymmetric timing control on the bell of a new robot, Cyro 3, would enable a kinematic and fluid dynamic parametric study of the graded response, as well as contributing component isolation, to explore the factors that impact large rowing jellyfish maneuvering and broadly expand the observations to all rowing jellyfish. This chapter outlines the improvements of actuation, structure, and control over previous jellyfish robot designs, implementation of turning kinematics on a mobile robot, and the resulting turning kinematics and fluid interactions that provide insight into the physical reasoning and graded effects of these contributing locomotion methods.

3.2. ***Biomimetic Design and Manufacturing***

3.2.1. Mesoglea Bell Structure

3.2.1.1. Bell Design

As mentioned in the Cyro 2 results and conclusions, the design of the bell is the single most critical component of robot performance effectiveness. Jellyfish locomotion is purely the cyclic contraction and relaxation of the bell, and the body mass of most rowing jellyfish is primarily comprised of the bell. Other structures of the jellyfish body, such as tentacles and oral arms, could be considered as simply supporting the life cycle of the bell musculature and form. Therefore, the design of the bell has been a primary point of focus for this project.

The driving factor for the bell design has been the mimicry of the bell form, in particular at the uppermost extreme of the bell stroke. This region was not reachable on the past robot, and this region of motion contributes a large amount of thrust due to the most axial displacement of fluid per bending amount. Reference images were found online, and the bell form was modeled based on the intricacies of the bell rounding, clefts between and bisecting the eight individual segments, and the variation in thickness. Getting the thickness correct contributes to the amount of velar deflection and the stiffness of the bell, which are critical to the deforming bell shape during swimming. As found for *Aurelia*, the velum was tapered in a spline curve to gradually adjust the deflection amount along the length of the velar flap (Villanueva et al., 2014). This tapering can be seen along the length of the bell in reference pictures, particularly in cross sections of the bell (Gladfelter, 1972). The bell was therefore constructed by two primary cross sections – the profile along the centerline of the bell, which was well documented in *Cyanea* kinematics profiles, and the profile between the eight bell sectors that kept the tapered form but caused a reduced radial profile. These cross sections were then lofted along a profile that would give the characteristic outline of the bell between the profiles, and the profiles and outlines were iterated until it closely mimicked the reference material. The bell was formed by individual segments, but the bulk shape when combined together was also considered since the reference images showed the full bell. The bell halves were symmetric, and the cleft down the centerline of the bell was a simple rectangular removal symmetric to the centerline, with the distance and width iterated to match reference images. It should be stated that the velum lobes are non-overlapping when fully relaxed, and contrary to the original Cyro 2 design they should not be cast to overlap but expected to potentially overlap when the bell is fully contracted and the individual segments are compressed radially and laterally. Reference images show some downward sloping along the width of the bell, so multiple images were consulted to isolate what was integral deflection and which was just deflection due to the effect of gravity, small amounts of drag, and inter-lobe compression. Further profile shaping and rounding helped define the final shape.

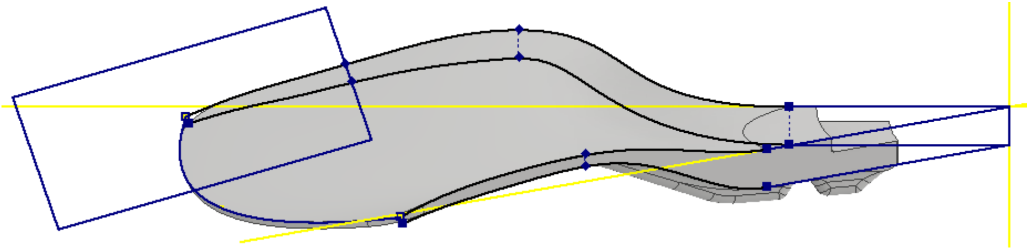

Figure 20 - Two intermediate profiles and lofting curvature used for formation of the half of a laterally symmetric bell segment

In order to guide the cables and constrain the angles of deflection during contraction, stiffening ridges with localized inflection points, where the ridge thickness was reduced with the opening tapered to act as an angular stop during contraction, were integrated as on Cyro 2. However, the original bell angles at the inflection points appeared to not be coherent with the documented angles for a four-segment case in the kinematic study of *Cyanea* (Villanueva and Priya, 2014). These angles were then re-determined to be 17.5, 42, and 12 degrees at the inflection points of 0%, 26%, and 60% exumbrellar arc length, respectively. An additional inflection point is designed to occur when the velar region starts at the 80% exumbrellar arc length position. The velar region was documented to be from 80-88% exumbrellar arc length, but as for Robojelly the velar region was maximized to allow for additional deflection at the tip (Villanueva et al., 2014). The inflection point at the base of the bell was constrained to be 2.85 cm away from the centerline since the electronics and cable housing was that diameter, and thus the inflection point angle was scaled to be 32.16 degrees to proportionally allow the same amount of segment axial deflection. To allow for more than a full range of motion, with some additional upper and lower range, each inflection point angle was multiplied by 1.5 and the bell elevation at full relaxation was increased. The control system and assembly of the cable system set the fully relaxed and fully contracted positions to obtain a full range of motion without gravitational, stiffness, or structural limitations to reduce the range of motion.

According to the previous studies on bell form and kinematics, the total bell diameter, in radial horizontal distance, should be between about 85-90% the exumbrellar arc length, but the arc length was difficult to estimate in the design. In addition, the aligned distance from base to tip has been determined to be about 98% that of arc length, even with significant arc curvature around this linear estimate. Each segment of the bell between inflection points was roughly linear, the aligned arc distance between two inflection points was slightly higher than the pure aligned linear distance, and the segmented analysis inflection points were slight underestimates of the biological expected inflection points based on anatomy. Therefore, each inflection point position was estimated as the respective percentage of the 25cm radius in an aligned distance along the subumbrellar surface, with any variation acceptable within published analytical method error and anatomical variation in nature.

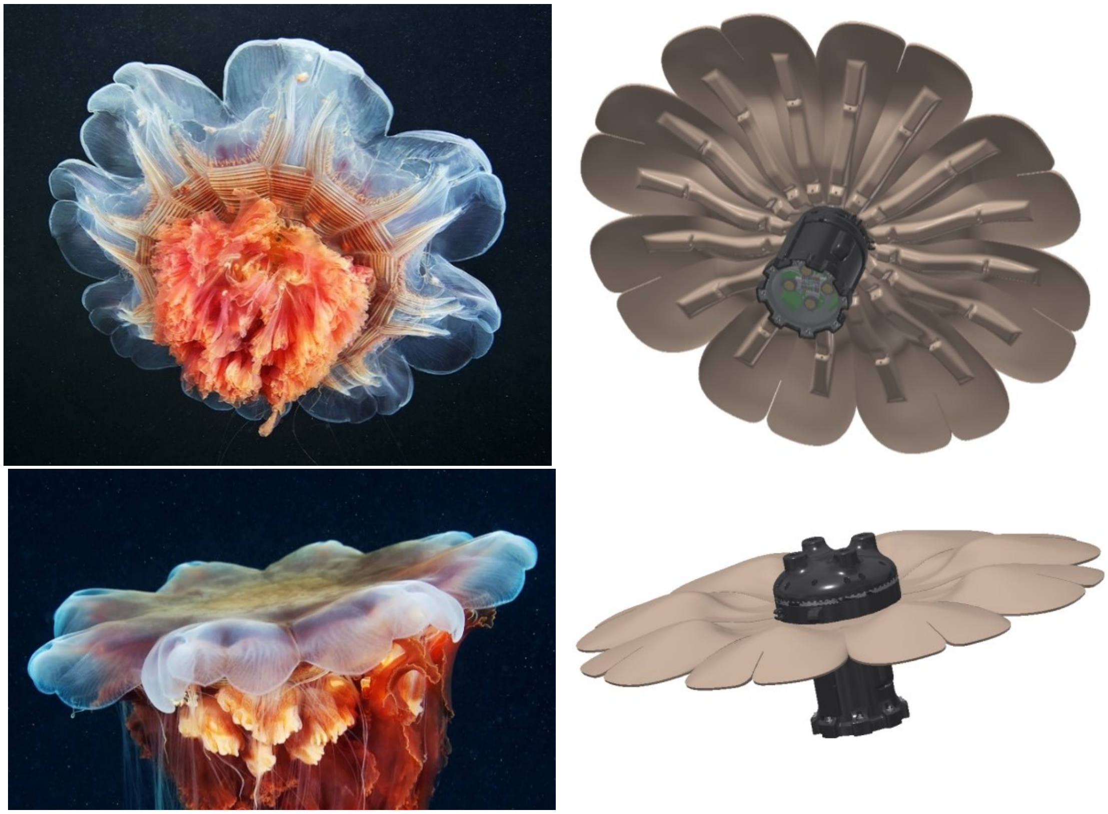

Figure 21 - Final bell form (right) relative to reference images of the bell (left). Reference images used with permission by Alexander Semenov / Aquatilis Expedition.

3.2.1.2. Bell Manufacturing

Once this complicated form for a single segment was designed, eight identical silicone segments needed to be cast separately and then patched together. The bell segments of Cyro 2 were cast out of Ecoflex low-durometer silicone in a 3D printed negative mold. This mold, however, had ridges that were captured in the casting and took up a significant amount of material to manufacture. This new bell is also flatter than the Cyro 2 bell, which resulted in a prohibitively larger and flatter mold. Since FDM printers tended to not complete flat molds due to long layer deposition times and significant warping from differential cooling, this was also difficult to make on the cheaper FDM machines and would cost too much to produce on the higher quality polyjet printer in BMDL. An FDM mold negative was attempted, but the multi-part construction and low lamination strength caused the mold life to be extremely limited to a single attempt.

Therefore, a lower-cost and more traditional solution was to 3D print a bell positive that would form the cavity of an externally cast negative mold. Dragon Skin platinum cure casting silicone was found to be of sufficient strength, and was known to be compatible with other platinum cure silicones that the bell could have been cast with during the molding process. The 3D printed model was elevated in a containment box, and the silicone was mixed, degassed, and poured around the mold. In order to save on material, some volume-filling blocks were inserted into the boundary around the positive, and at the top of the mold partially-cured silicone that was of higher viscosity was piled on top of the upper ridge of the bell segment to remove the need for a high mold with a lot of wasted material near the periphery at the top. Once cured, the mold was cut along the edge of the plastic form with a zig-zag pattern to allow repeatable mold indexing on each face, and the plastic form was removed. Holes for the guidance tubes were perforated to allow the passage of a negative of the channels for the integrated guidance tubes. The top and bottom of the mold were covered with 10lb FoamIt polyurethane foam to rigidize thin faces and allow even pressure during mold compression during casting.

Before casting the form, accessory features were added to the mold. Through the perforations in the silicone, the PTFE tubing used on Cyro 2 was routed to form the channels for the tubing in the bell. The lack of adhesion with this tubing was utilized in this case to ease removal from the mold during demolding of the cast form. Since the tubing would not always match the profile of the channels and occasionally caused defects in the molded parts, thin wire forms were added to the inside of the mold that could be pulled out as the cast form was removed from the mold without causing visible voids in the cast part. The inside of the mold was then covered in liquid or aerosol EaseRelease release agent to avoid silicone-silicone bonding, and the mold was then filled with the casting silicone. The casting was completed in two stages because of the complexity of the part. The bottom of the mold with the ridges were first cast with 125 grams of each resin (250 grams of total silicone), and once cured the top of the form that the silicone did not fill was filled with more casting silicone to cure and finish the part.

To match the stiffness required to maintain the passive shape of a *Cyanea* bell lobe without the gravitational displacement from the softer Ecoflex used on Cyro 2, two alternatives were considered. The mold had attachment sites for the insertion of spring steel, which was cut and pre-bent over a form that matched the centerline of the bell segment on each side along the ridges. This added additional stiffness to the Ecoflex form.

However, the inflection points were then too stiff to deform locally, the velum was excessively flexible and did not match the documented profile of the bell during contraction, and the spring steel was exceedingly difficult to position in the mold without breaching out of the part. Therefore, the stiffer silicone Dragon Skin was selected as the final material. With higher stiffness but still a soft durometer, the bell was able to deflect locally but quickly relax due to additional stored strain energy at the inflection points during deflection. In addition, the stiffness of the tip of the bell matched the profile that had been documented for *Cyanea* (Gladfelter, 1972; Villanueva and Priya, 2014). During swimming the tip of the bell had been documented to flex more or less depending on the timing of the contraction (Gemmell et al., 2015). This could have been due to a differential material stiffness or muscular control of the velum. However, the stiffness of Dragon Skin allowed the margin to proportionally deflect relative to the speed of the bell contraction and thus drag, hence reducing another potentially controlled turning mechanism to a passive response. During slow contraction on the inside of a turn the bell margin stayed relatively tangent to the bell, while the bell margin deflected inward and outward during a faster contraction and relaxation elsewhere on the bell.

As can be expected from a flexible mold, some slight variation in thickness between lobes was found during robot testing. Lobes with excessive thickness were found to hold the opened flat form even during contraction, so cuts along the inside midline of the bell thinned out the centerline thickness and appropriately tapered the surrounding bell thickness for smooth transitions and durability. Lobes with reduced thickness were augmented with additional silicone to introduce additional stiffness along the centerline to reduce deflection. After this iterative augmentation, it resulted that each lobe was thinned at their centerline to promote localized bending as found in *Cyanea* mesoglea (Gladfelter, 1972). Inter-lobe stiffness was critical for proper bending, so additional silicone was added to stiffen sections to hold a desired form while allowing localized folding inwards during contraction. This balance ensured the designed bio-mimetic deflection, as seen in Figure 21, which resulted in a nearly smooth or slightly creased inner portion of the bell before the second joint, and then sharp lateral folding of lobes past that joint such that the lobe centerline extended outward and the inter-lobe line creased inwards.

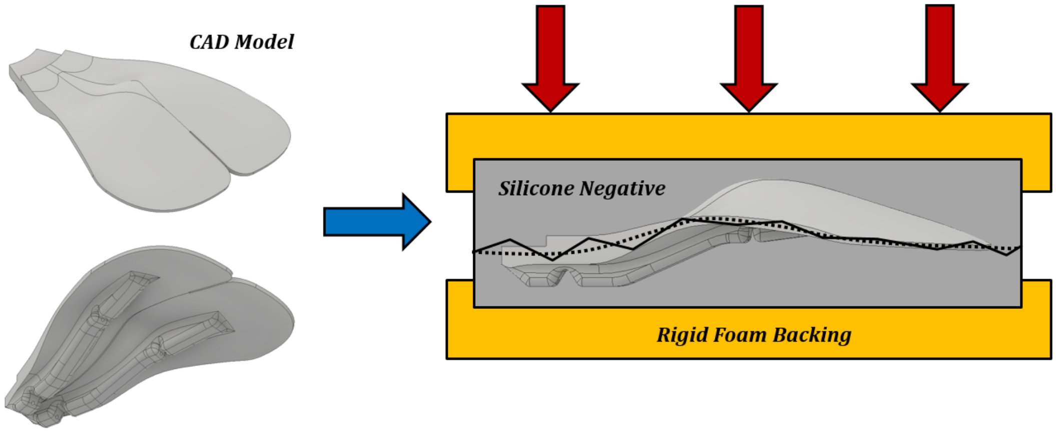

Figure 22 - Bell segment manufacturing plan. A 3D printed positive of the bell form was used to cast a silicone negative, which was then reinforced by a rigid foam backing. The bell positive was removed, accessory features such as channels were inserted into the mold, and degassed silicone was then poured into the mold cavity. Once cured and formed completely, the accessory features were removed and the bell form was separated from the mold. Defects and waste material were then trimmed and patched with additional silicone.

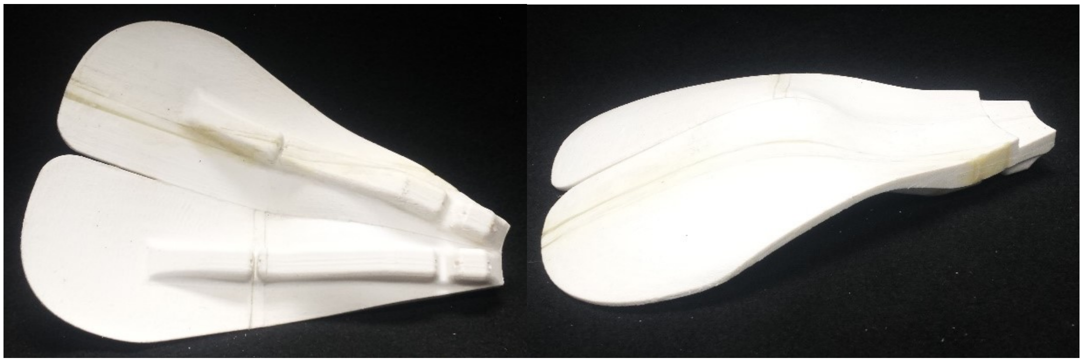

Figure 23 - Final 3D printed PLA positive of bell segment. Patching of the print where delamination occurred or partially printed segments were joined was completed with plastic bonding epoxy, and the final mold and patches were sanded smooth and continuous.

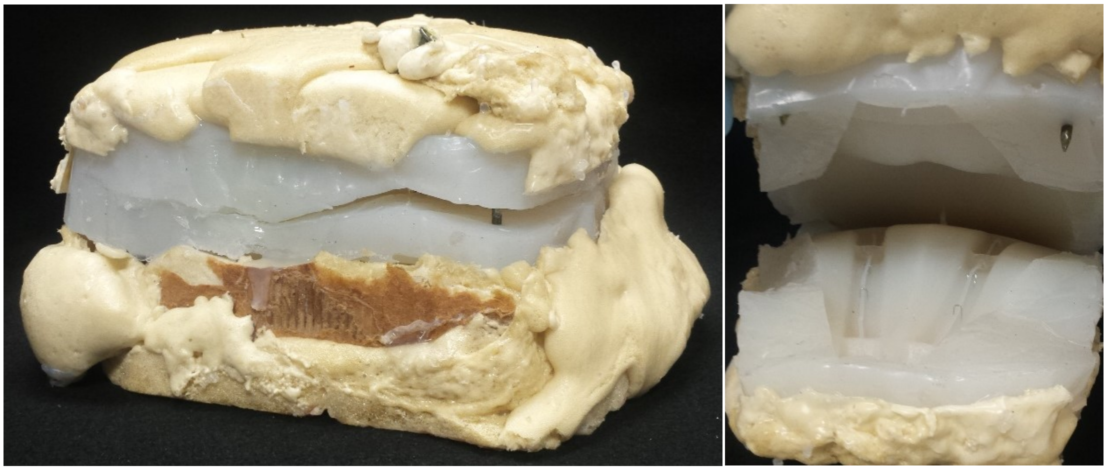

Figure 24 - Final silicone and foam-reinforced mold form, with pins to improved adhesion to foam backing. External view (left) and internal view of part cavity (right)

Figure 25 - Cable guide channel negative (thin tubing down channels negative) with support wires. Complex upper and lower support wires (left) worked well but caused some damage on removal. Simple linear or slightly formed guide wires (right) improved ease of removal while minimizing damage.

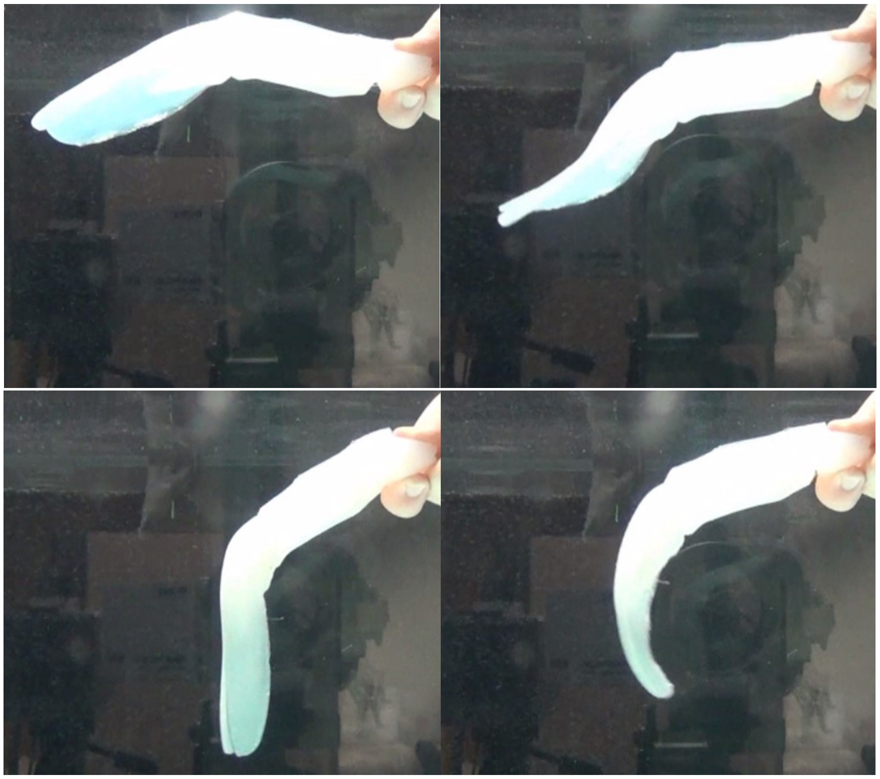

Figure 26 - Initial manual testing results of contraction range. Without any forward or reverse motion, the bell velar deflection varied from fully relaxed (upper left), mid-contraction (upper right), fully contracted (lower left), and mid-relaxation (lower right).

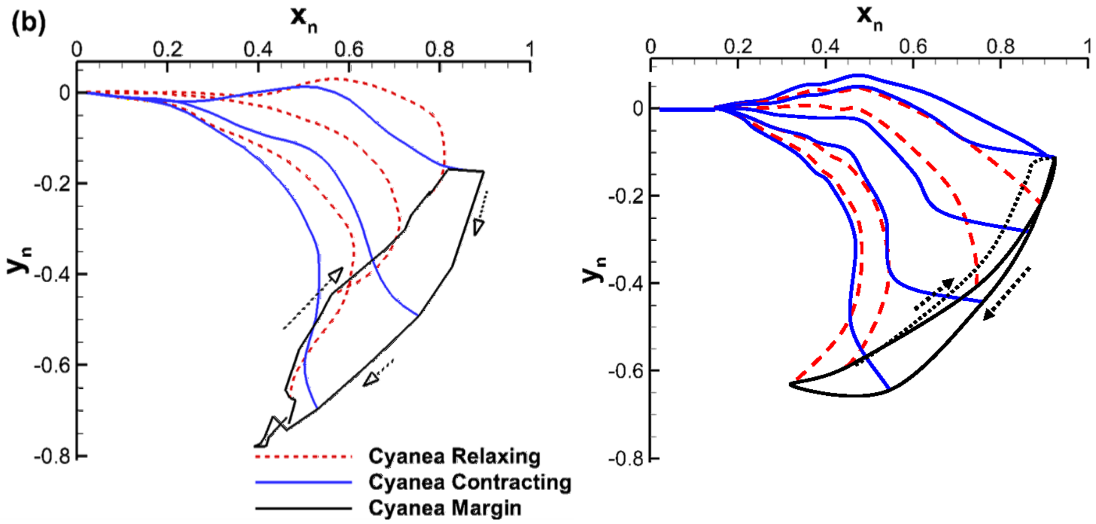

Figure 27 – Motion tracking of initial manual testing results of contraction range (right) compared with a natural 50cm *Cyanea* specimen (left).

3.2.2. Actuation Design

3.2.2.1. Motor Selection

Since the torque loading of the bell deflection was difficult to estimate, the torque needed for the full bell deflection was estimated to be the max torque output at full bell deflection by Cyro 2. Since the max rated torque, max rated current, and max current input at full deformation were known, and torque is roughly proportional to current at a known voltage, these parameters were used to scale the rated torque to the max used torque. The angular velocity of the motor was also estimated from one second for 1.5 inches of circumferential rotation of the spindle on Cyro 2, which was the max speed for contraction and still twice as fast as the biological example. This amount of turning required was doubled to account for more stroke length, which resulted in a doubly fast speed for the baseline motor specification. The continuous load for a DC electric gearmotor was advised to be below 20-30% stall torque by motor manufacturers, so the peak load point was estimated during the design to land at the 75% speed, 25% torque output, and thus the rated stall torque requirement for the motors was based on four times the max torque output. A calculation of the power requirements, assuming linear trends of current, speed, and torque from the specified extremes, provided an efficient point for the first selected gearmotor to be 23.75% torque, 76.25% speed, so this estimation for specifications was appropriate and within reasonable constraints for motor manufacturing and variance due to electrical and mechanical wear. This also allowed a large factor of safety for additional loading or reduced loading during contraction, ensuring near-optimal performance and no stalling of the motor. Since this resulting torque was for eight lobes of the bell, and the minimal number of motors for two planar, non-axial turning was four to control two lobes per motor, the required torque was thus a quarter of the specified optimal torque requirement. Since spindle size also changed the speed and torque requirement, a table of potential spindle sizes and the resulting optimal scaled torque and angular velocity requirements for full contraction was used to select candidate motors. Since four motors were needed with positional awareness, the size of the required spindle and mode of position measurement were both taken into account to identify the selected motor. The system power for all four motors at max output was also considered, since the optimal goal for the system power of a mobile robot was to minimize power consumption without reducing the motor performance below the design requirements.

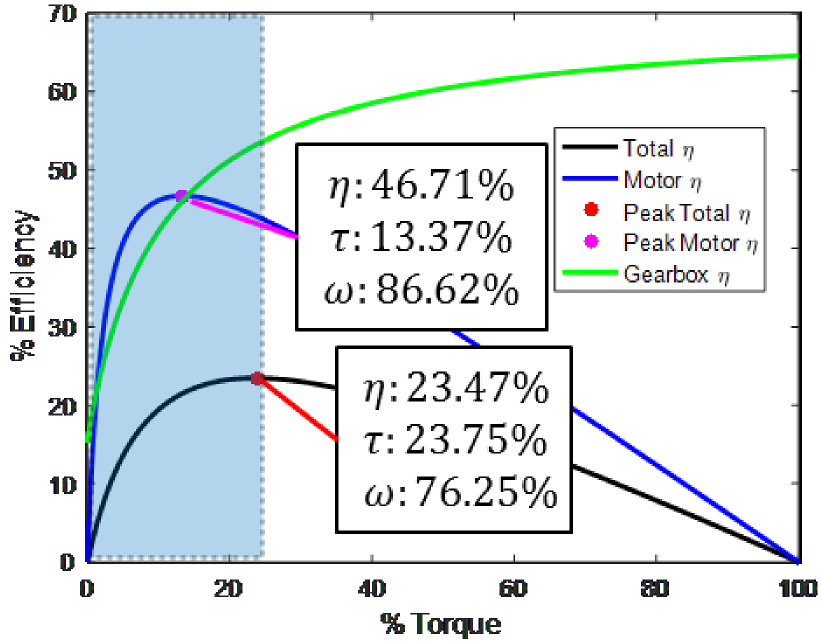

Figure 28 - Efficient points for initial selected motor. The highlighted region indicates the expected operation region (at or below 25% torque).

The first motor selected was a ‘47:1 Metal Gearmotor 25Dx52L mm MP 12V with 48 CPR Encoder’ from Pololu. This motor had a safety factor of specified vs required torque at the optimal point of 1.37, and the resulting spindle size was a radius of 0.2387 inches. After the initial implementation of this motor selection, it was found that the true cable tension requirement for contraction was between 39.24 to 58.86 Newtons. This tension requirement depended on the orientation of the robot relative to gravity since the bell weight was directly supported by cable tension in an inverted state. For the original spindle radius, this resulted in a 33.70 to 50.54 ounce-inch torque requirement, doubled for two lobes per motor to 67.4 to 101.08 ounce-inch torque. The originally specified motor had a stall torque of 85 ounce inches, which was exceeded by the upper limit and only moderately higher than the lower limit specification. This close a max torque to the lower limit of static torque requirements was suboptimal for motor performance, and the additional loading from a dynamic load of a nonlinear stiffness and inertia added additional torque to the static estimation. This increase in the specification, which was derived from the Cyro 2 design results, was due to the increase in stiffness with the increased durometer from Ecoflex in Cyro 2 to DragonSkin for Cyro 3. A new spindle and motor selection was completed, with an additional safety factor allowed for other unexpected factors. The second selected motor was the ‘Metal DC Geared Motor w/Encoder - 12V 122RPM 38Kg.cm’ from DFRobot, which had a broad safe and efficient operating range for the required torque and speed for each pair of lobes. The spindle size could have had a radius from 0.623 inches to 0.313 inches, but to allow a range of safety in the speed and torque output while also maintaining limited increases in the motor housing size the final spindle radius was selected at 0.468 inches. This motor was found to have a total efficient peak of 38.12% at 18.03% torque and 81.97% speed, which was a lower peak percent torque than previously estimated but still within a reasonable estimate of the 25% torque operating region. The average pulley diameter used for this design required the motor to operate at a maximum of 18.77% torque, which was close to the expected efficiency peak operation.

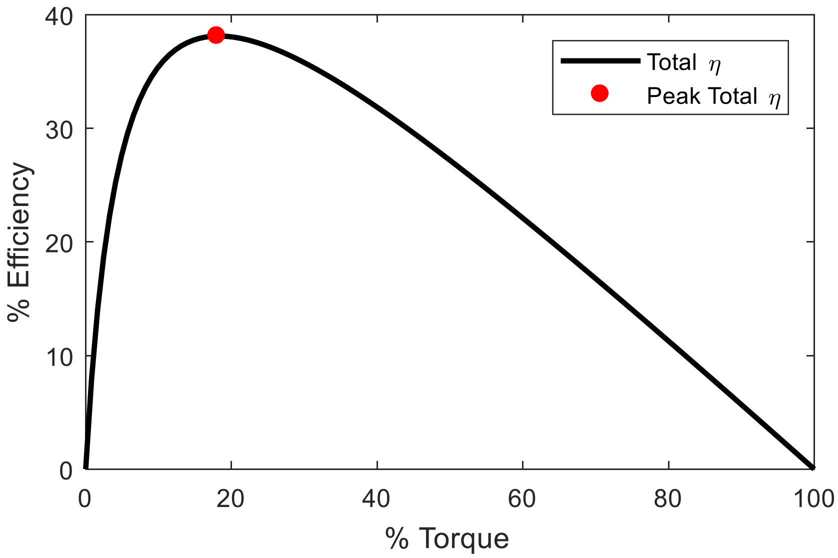

Figure 29 - Final motor selection efficiency curve, indicating efficient peak

Implementation and testing of these motors showed appropriate power output for the robot contraction and relaxation motions. However, high power draw and faulty internal components caused mechanical and electrical fatigue failures that were likely inevitable with similar motor products that were commercially available. In order to rectify this supply-side issue, waterproof servo motors were selected due to integrated motion control circuits, sufficient torque and speed, reduced power requirements, and internal controls for power reduction at stall and adaptive PID control parameters. The reduced stroke range to 180 degrees, as well as a measured 48% reduced range of motion needed to full contraction, resulted in further changes in spindle design to meet the required torque, speed, and rotary motion range. The final motor selected was the Hitec D-840WP, which integrated a broad range of power input and outputs up to 30 kgcm (418.91 ozin) at a speed of 0.11 seconds to travel 60 degrees. While the power draw was high at 1.6A running current and 9A stall current, the range of motion on the motors was optimized to achieve the required kinematics without running into the built in angle-limiting stops and pulling stall current. Since this motor was also selected with the 25% torque optimized point in mind, with some additional safety factor possible due to the reduced required stroke, the power draw had been reduced relative to the comparable DC brushed motors. In addition, these motors were programmed to include a 20% reduction in power at stall to prevent burnouts, increased range for full 180 degree or greater stroke, adaptive PID gains to improve performance while cyclically moving, and a tuned neutral position to correct for manufacturing variation without additional programmed inputs in the control code.

3.2.2.2. Cable Guidance and Actuation

The design of the bell of Cyro 2 explored valuable conceptual design elements that were fully executed and tuned in the design of Cyro 3. The cable guidance through the ridges of the bell inside of a low-friction flexible tubing was carried over into this design, with the low surface energy PTFE tubing changed to HDPE tubing for increased adhesion with cyanoacrylate glue, improved flexibility, and maintained low cable friction and wear resistance while under side loading during tension and bending. Since the polyethylene tubing was slightly larger in diameter than the PTFE tubing, the channel cast into the bell helped hold the tubing in place with both adhesive bonding and compression onto the tubing. This tubing had exhibited a tendency to migrate through the silicone as contraction and expansion occurred locally along the bell during the cycle and induced a peristaltic progression. Therefore, the current design used cyanoacrylate glue to successfully stabilize the tubing along the length of the cast channel. Future design exploration could look into other cable guide designs, such as integral ridges in the silicone and tubing, to maintain and improve these properties without interfering with locally induced bending positions, resistance, and range.

The spindle design was iterated through the different motor selections to match the required kinematics, as well as improve on durability and ease of maintenance. Early version of the spindles were 3D printed to match the D-shaft output geometry of the motors. However, single set screws and the brittle spindle material, as well as the small flats on the motors, led to frequent loosening of the spindle on the shaft. In addition, cables were tied down to cleat-like posts, but the brittle printed material frequently fractured and lost hold of the cables on the spindle. Cyanoacrylate glue helped aid in the holding power around the posts and along the length of the cable along the spindle. However, the brittleness of the printed material (VeroClear, Objet Eden 260V), as well as the integrated forms that could not be repaired, led to frequent failures and necessitated further improvements.

The second spindle design had three major upgraded features. The primary form material was changed to nylon, which could be machined on the lathe to form the spindle while greatly improving the durability of the spindle over time. The cable tie downs were changed to binding screws, which could easily loosen to allow tuning and tightened to hold down the cables with friction. Cyanoacrylate glue was also used to further improve the hold as before. The addition of larger set screws in a pair along the shaft length further improved holding power and eliminated the loosening of the spindles. While these spindles were drastic improvements in durability and ease of tuning and repair, the machining on the lathe did take a significant amount of time to complete each spindle.

The final design combined the successful features of the previous designs, while allowing integration on the newly integrated servo motors. The mating of the spindle to the motor was no longer an integrated form to mate the shaft, but rather an integrated form that mated with a nylon servo horn that was included with the motor and cut to the spindle size. This allowed quick replacement and repair as needed, as well as a positive registration to a broader force transferring surface that could be screw-tightened in place. The cable tie downs continued to consist of tapped holes with binding head screws and cyanoacrylate reinforcement. These spindles were printed out of a softer material used for the Formlabs Form 1+ stereolithography printer, which was sufficiently durable and allowed for more rapid manufacturing. The softer material could benefit from an upgrade as more resins become available to improve tapped hole integrity and reduce cracking or fracture failures at thin features.

Since each of the spindle designs needed to handle four cables, with two from each lobe and two lobes per spindle, in close proximity, the arrangement of the cables to actuate equally was critical to design success and repeatability. The two cables from the left of the two lobes wrapped tangentially to the left side of the spindle, wrapped a half turn around the spindle to ensure consistent spindle hold, and routed up through a hole to the tie-down point where the cables were fixed in position. The second cable pair from the right lobe wrapped also to the left of the spindle, wrapped a quarter turn and routed to a similar anchoring point. The cables would then be wrapped by the appropriate turn of the motor to achieve a contraction motion, and then the equal but opposite directional motion to unwrap the cables for relaxation. The initial design for the spindle used a 180-degree offset between anchors and 3D printed tie-down points. The cable holes and mounting points were shifted to be 90 degrees apart to equalize the wrapping distance and thus the cable lengths needed in the design.

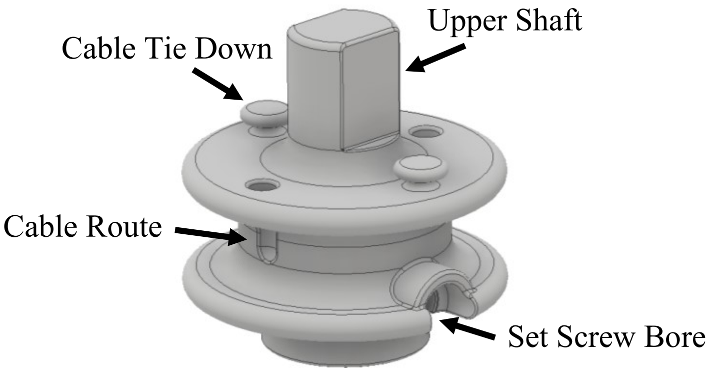

Figure 30 – First Spindle Design, 3D Printed Photopolymer

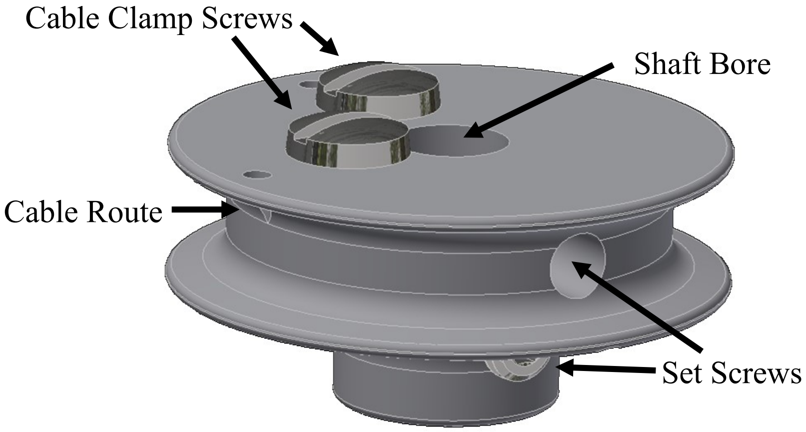

Figure 31 – Second Spindle Design, Lathe Machined Nylon

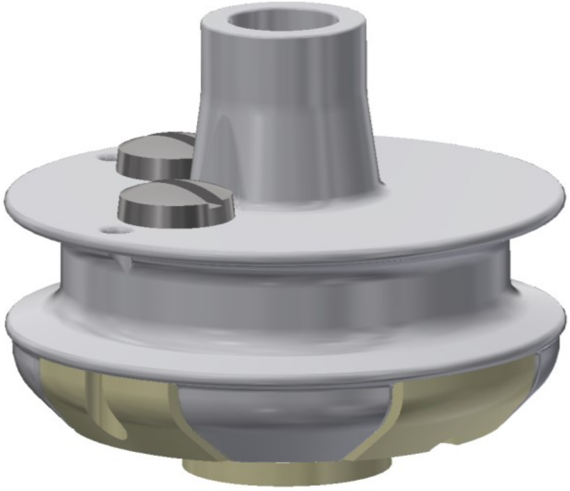

Figure 32 – Final Spindle Design, 3D Printed Soft Polymer with Nylon Insert

Since power consumption of the motor while holding a position under load was a consideration for improving this design over Cyro 2, two major considerations were taken into account. First, the ease of back driving the servo motor in Cyro 2, compounded by the large spindle that handled sixteen tensioned cables at a large diameter, inevitably caused a significant amount of load on the motor that required position correction as the motor slipped. Therefore, the smaller spindle and separation of the cables among the motors reduced the load on the motor. The spindle size alone, which was reduced from a radius of 0.75 inches to 0.2387 inches for the first motor design, 0.468 inches for the second motor design, and 0.5 inches for the servo motor design, reduced the moment arm of the cable tensions by 68.2%, 37.6%, and 33%, respectively. The motor was scaled with the amount of expected torque and a reduction based on separation of load was not expected to be significant. By manual inspection, the static resistance to turning without an electrical load for each of the selected motors, which was both by motor internal resistance and gearbox friction multiplied by the gearbox ratio, were significantly higher than the servo motor on Cyro 2 and thus held the position just by internal resistance.

For additional mechanical support under load, the first spindle design had a partially rounded shaft that ran inside inserts that were 3D printed partially hollow, secondary bored closely to the spindle shaft diameter, and vacuum infused with mineral oil to aid in lubrication. If the holding torque and resistive torque of the motor was not enough to hold the motor position, the circular bore insert could have been replaced with an insert that included a detent profile and a detent spring could have been inserted over the flat-indexed upper shaft. This could provide a small amount of holding power that should not cause significant moving resistance but would allow holding resistance during position holds. This detent shape was tuned for this balance between holding power and ease of moving smoothly, and the inserts and spring were once again either laser cut out of polypropylene or 3D printed for ease of iteration as well as accuracy and ease of deburring for the custom shapes in a small profile. The latest spindle designs did not include a detent design due to the additional complexity and machining required from including features for the detent or other locking mechanisms. Since the motor static holding power increased as the size and power was increased, resistance based static holding was considered sufficient. Additional efficiency improvements, such as a detent with a tuned preload or braking from a locking pin or frictional pad at the end points of motor travel initiated by a mechanical cam, could be implemented with an extended spindle design and additional machined features with increased manufacturing complexity. However, reliability and repeatability during maneuvers was of higher primary importance, while efficiency and design tuning is a secondary goal in the future.

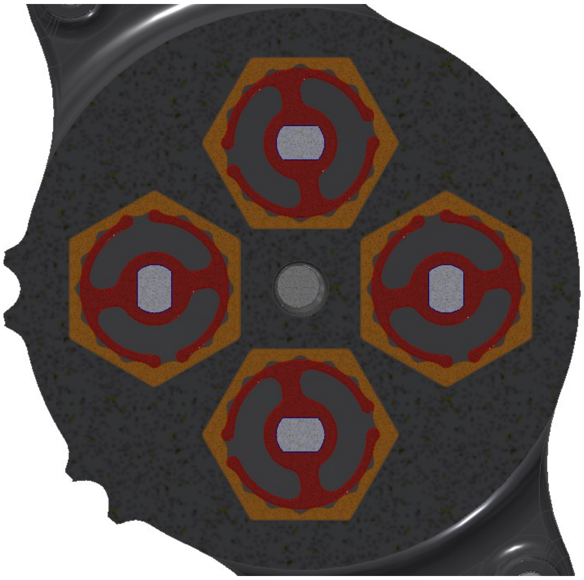

Figure 33 – Spindle detent springs (red) inserted into detent races (orange) on the spindle shaft (light gray) and inserted into the spindle cover housing.

3.2.3. Electronics and Control Design

3.2.3.1. Control Architecture

In order to control four motors simultaneously to follow prescribed position paths, two separate operational goals were required for the control architecture: motion control of each motor based on position feedback relative to a desired position, and coordination of the motions of each motor relative to the current system state and desired cycle motion. Traditional control architectures for large robot systems utilize a high powered central controller for all operations, often with multiple threads for each operation or a fast enough clock speed to maintain synchronization between motions despite complex control algorithms. However, smaller scale systems with portable power were limited to microcontrollers, with desired operational complexity, power supply criteria, and size limiting the microcontroller architectures utilized. Since the robot design aims to minimize electronics size and power consumption while prioritizing motion control and coordination, an individual microcontroller would not sufficiently fit within these criteria. Taking inspiration from the distributed control of each lobe by neural networks in jellyfish that respond and coordinate motion and stimuli, the architecture selected for this robot was a combined centralized and decentralized control. The decentralized control utilized individual microcontrollers for each pair of motors and thus a pair of quadrants of the robot, prioritizing control accuracy through time using a tuned PID controller to take current motor position and desired position to output a motor effort through voltage control. The centralized control component simultaneously calculated the motion waveform for each lobe and sent the command to each lobe controller, prioritizing temporal accuracy at a system scale. This formed a fast centralized and distributed hybrid control network that relied on role specialization to optimize the control system goals.

3.2.3.2. Motor Motion Control

For the motion control, the desired position was in the form of a trapezoidal periodic signal consisting of the fully contracted and relaxed position points determined at the predetermined swimming cycle timing points. These points in time were linearly connected, forming a ramp type input to the system. In order to achieve zero steady state error, a ramp input requires at least two poles in the system. Since a motor was considered to include an integrator in the system transfer function, a single integrator controller was needed to drive the system to zero steady state error. Therefore, a pure proportional-integrator controller was chosen for this system. The proportional gain was used to handle response speed, and the integrator gain was used to stabilize error over time.

To read in encoder position, an interrupt was needed to update the motor position at a rate faster than the main loop update. However, on the selected A-Star 32U4 Micro microcontroller the interrupts were limited, and only two viable interrupts INT0 and INT1 were left after INT3 and INT2 were reserved for serial communication for USB reprogramming. Other pin change interrupts and one more standard interrupt INT6 were available, but the interrupt architecture for this controller needed to be the same for each motor, ruling out the one INT6 left, and the pin change interrupt service routine fires globally and ambiguously whenever a pin change interrupt is triggered. The initially selected motor encoder also updated, with both interrupt pins measured, at 2248.86 level changes per revolution of the output shaft. Therefore, it was decided that only one encoder output with the interrupt triggering on both rising and falling edge state changes would be used, dropping the rotational resolution to a still highly accurate 1124.43 counts per revolution. A full contraction was two turns of the initial spindle specification, resulting in the full contraction position at 2248.86 state change counts, rounded to 2249 counts so it can be stored as a precompiler macro to save space over a floating point global variable (which resulted in only an additional 0.0448 degree increase on the output shaft). When the state was triggered, the level of the interrupt-linked encoder output as well as the second encoder output, read in as a simple digital I/O signal, were compared to determine direction. If both pins matched state at the state change then the motor was rotating counter clockwise and hence initiating relaxation with a decrementing position counter, and non-matching pin states indicated clockwise rotation and hence contraction and an increasing position counter.

Once the motor position was read in, the desired position of the motor was compared and fed into the PI controller. This input was position error, and controller output was a 20 kHz velocity PWM value to the motor controller with a value between 0 and 400 for zero and full duty cycle, respectively. The controller was placed into the main loop of the program since the update rate was sufficient for the program, the position was updated as soon as a change triggered the interrupt, and the integrator measured the current and past time to form a right-hand rectangular integration, which had sufficient time resolution to not induce noticeable error, to account for small variation in timing. The sampling rate averaged at 396.32 Hz, with a minimum frequency of 250 Hz and maximum of 500 Hz at a standard deviation of 87.1336 Hz. This was measured by printing out the target and current positions, error, integrative error, and output speed signal to the serial communication to the serial monitor on the Arduino IDE on a laptop, so communication time added additional reduction and variation in processing speed. With empirical variation of the K_P and K_I gains in the controller to eliminate ringing at steady state and oscillation during the position response, the best gains were determined to be a K_P of 8 and a K_I of 6.

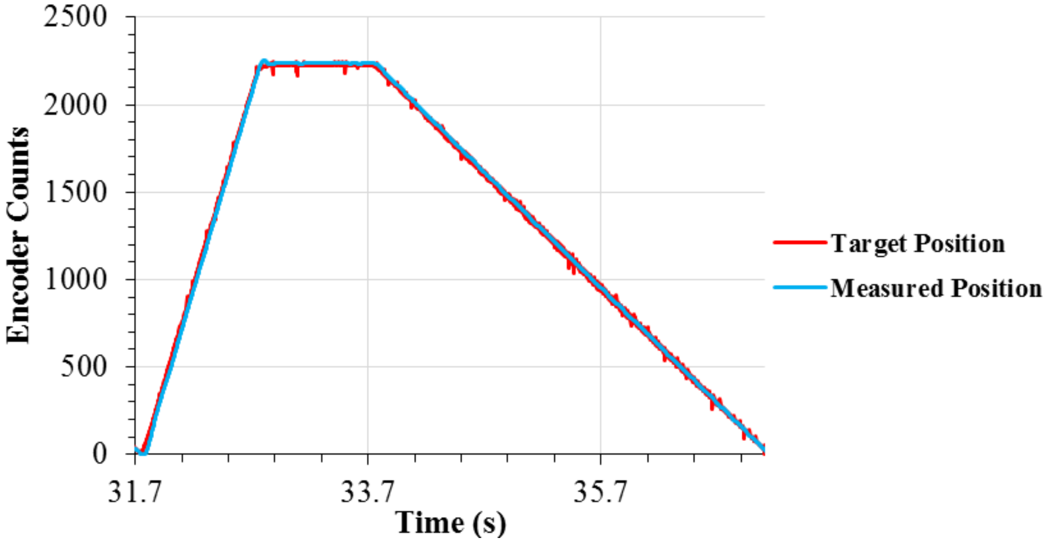

Figure 34 - Controller performance with proportional gain of 8 and integrator gain of 6. Time started when a representative steady state controller response was reached. Steady state was quickly reached within a cycle.

The second motor configuration with the larger motors but the same control architecture maintained the same PI gains due to locally accurate and low flutter position control. Additional gain combinations were attempted, but the same results from the smaller motor configuration were obtained due to the same software implementation on a sufficiently fast motor to match position commands. The new specified encoder revolution was 1440 counts per revolution, and the motor specification for speed and torque allowed a range of supported spindle and contraction position configurations. The final control design resulted in a spindle set for 367.28 degrees per contraction, resulting in 1469.12 counts per contraction. This specification was found to be about half the needed encoder counts for the desired turn, so the rotation count was increased accordingly to 2898 and tuned to avoid over-contraction during experimentation by reducing the contraction motion encoder count to 1500.

The decision to change to servo motors for actuation kept this architecture, but changed the form of the controllers. Instead of manually tuning the controllers for each motor to get the desired output position through an input from the central controller, the onboard PID controller of the servo motors took a position command and directly controlled the output of the servo from an internal potentiometer sensor. As mentioned in the actuator selection section, settings on the motor controller were tuned via a Hitec programming interface (DPC-11 Programming Interface for Hitec Servos) to improve motor performance and stability.

3.2.3.3. Swimming Cycle Gait Generation and Communication

Since the central planning controller needed to communicate desired positions to four motors, an analog signal was selected to use the analog input pins and minimize use of digital I/O pins to keep them open for position control of the motor drivers. The analog input of the A-Star microcontroller had 1024 possible analog levels, allowing high precision and speed of the motor position command. Since microcontrollers of this size do not have an analog output, a simple analog output was derived via a PWM output by the central microcontroller for each motor position, encoded to have full contraction as full duty cycle and full relaxation at zero duty cycle. This output was sent as 490Hz pulses with a value of 0 to 255, giving a resolution of 0.39% of a contraction, and filtered with a low pass RC filter to turn the pulsed signal into an analog variation in average voltage across the pulse cycle. The resistive and capacitive components were chosen with a MATLAB script, which iterated through common resistive and capacitive component values and calculated the resulting bandwidth, RMS error, phase lag, and a composite figure of merit that found the root square sum of the bandwidth and RMS error. The final configuration chosen for the filter was a resistive value of 2.7 kΩ and a capacitive value of 10 μF, providing a bandwidth of 5.8946 Hz, RMS error of 0.0705, and a phase lag of 0.0278 seconds. While this wasn't the least error or lag, nor maximal bandwidth, the response had a low ripple and consisted of components readily available with reasonably small components that could be packaged into small serial units between microcontrollers. Tuning of the contraction amount during the cycle was accomplished by either the more invasive and permanent adjustments for the endpoint positions on the local motion controllers, or a rapidly tunable method of adjusting the input waveform from the central controller. While reducing the maximum and minimum limits of the waveform reduced the percent contraction resolution, filtering and high starting resolution allow for a reasonable reduction for minor tuning.

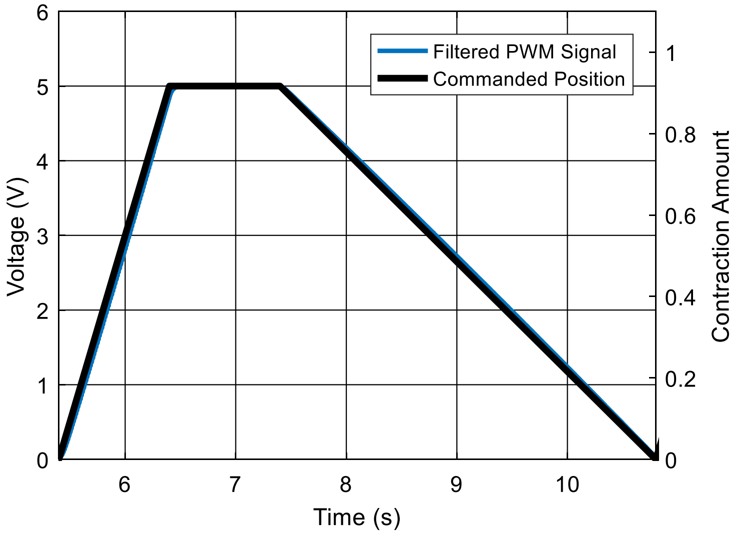

Figure 35 - Filtered PWM signal vs the desired commanded position signal. This response exhibited exceptional accuracy with very limited ripple and phase lag.

When the actuators were migrated to servo motors, the input to the onboard motion controller per servo was still a PWM signal representing the position, but with a specific duty cycle and frequency for the motor controller. The absolute limits of the motors were tuned to reduce power consumption and increase the total usable range of motion.

The turning motion of *Cyanea* and other rowing jellyfish is induced by two primary mechanisms: a time difference such that the inside lobe of the body in the plane of the turn contracts sooner than the outside lobe, and an increased marginal flap stiffness of the inside lobe with a reduced marginal flap stiffness on the outside lobe (Gemmell et al., 2015). Lobe margin stiffness affected the deflection of the flap, where the flexible lobe rolled up a clear rotational region that ejected mass to impart momentum while the inside stiff margin acted as a braking section with little to no mass ejection. The degree of stiffness difference from passive effects, since the deflection could also be relative to drag on the margin due to tip velocity, versus active material property changes and muscular action had yet to be studied since the study on *Aurelia* showed this difference in all turns. Therefore, we tested each gait with a symmetrically flexible bell margin to test for passive stiffness differences, as well as a stiffened margin for the inner quadrant through plastic plates stitched to the bell margin to allow hinging at the margin but not flexible bending.

The differential contraction raised questions about proportionality of speed and timing. From the study by Gemmell and sketches by Gladfelter, the relative speed of each side and contraction timing cannot be determined, and the contraction profile of the lobes out of plane had not been discussed. Time lapse images of *Aurelia* turning in the study by Gemmell showed that the inside and outside contraction was approximately symmetric in timing, but with a time lag on the outside of the turn of about 50% of the total contraction time (Gemmell et al., 2015). The sketches by Gladfelter of *Cyanea* turning indicated a similar symmetric contraction time, with about a delay of 25% of the total contraction time (Gladfelter, 1972). Upon inspection of video footage of small *Cyanea* captured at the National Aquarium in Baltimore, as well as corroborating these observations with papers by Gladfelter and Gemmell, the bell margins did exhibit differential marginal deflections and delayed contraction times, with the delay of the outside contraction start after the inside contraction constituted between about 10% to 40%, with a mean delay of both size groups around a quarter of the cycle time. This data clearly indicated an ability to finely tune the turning amount via delay time within a range of about 0% contraction duration of delay for straight swimming and 50% delay for a strong turn. Therefore, the gradation of the turning delay times relative to turning amount was necessary to form a control space for turning. In addition, relaxation time had not been determined to have a delay or a symmetric timing, although Gladfelter and Gemmell images indicated symmetric relaxation times. An additional study of whether the rotation and translation of the fluid from a symmetric and asymmetric relaxation start time was needed to complete the picture and determine if a delay can boost or reduce turning amount per cycle. Since contraction and relaxation times were symmetric despite asymmetric start times, and neither side relaxed until contraction was complete and vice versa, the gait timing was treated as a sliding window within each gait period. The total contraction time was used for straight swimming with no delay, denoted as 0% delay. Any induced delay resulted in the same total contraction time, but the individual quadrant contraction time is adjusted to

$$t_{contraction,lobe=} (1 - \%delay) * t_{contraction,total}$$

such that the inside lobe started contraction at the start of the total contraction phase and ended the delay amount before total contraction ended, while the outside lobe held the relaxed position until the delay time had elapsed, and then contracted until the end of the total contraction time. A similar sliding window approach was applied for relaxation, though a fixed value of 25% appeared to have the most effect over symmetric relaxation. Contraction was varied from 0% to 50% delay in 10% increments, with the range iterated for a symmetric lobe stiffness as well as a stiffened inner lobe. At 50% contraction delay and stiff or natural marginal flexibility, the 25% relaxation was also induced.

While previous gait studies with Cyro 2 showed that the best straight swimming gait was a 2 second contraction, 1 second cruise, 2.4 second relaxation, and no stall period, this gait was best for only straight vertical swimming with only forward progress as the metric for success. Since the cycle timing required changes for the balance and structure of a new robot, as well as adding the criteria of progress during the turn, the contraction of Cyro 3 was reduced to 1 second to increase the turning amount due to increased momentum flux, the cruise time was reduced to a quarter of the original to 0.25 seconds to allow the momentum to carry through the turn without sinking back into a stable position of drag or balance, and the relaxation time was also reduced to a quarter to 0.6 seconds to maintain the momentum of the turn without sinking or stabilization. Slower gaits were tested with the robot, but reliable turning was best with this selected faster gait and other gaits had trouble with generating or persisting the turn during a maneuver. In order to ensure successful turning without reducing the robot ability to swim straight the motors were balanced on both the top and bottom of the robot to maximize symmetry, and the combination of the total mass and buoyancy as well as relative positions of the center of mass and buoyancy were tuned with foam and small magnetic masses to ensure near neutral buoyancy and overlapping centers of mass and buoyancy to avoid stability aided or attenuated turning. Since perfect balance could not be achieved due to small changes in buoyancy throughout the robot over time, the robot was soaked to minimize saturation changes during testing, buoyancy was selected to be slightly negative if necessary, and balance was chosen to not favor an upright or inverted orientation nor a tilt in the plane of tested turning. Therefore, the stable position was favored to be a slight tilt out of plane if exact stability was not possible.

Table 2 - Gait delay timings for *Cyanea capillata* specimens during turning maneuvers, ranging from 4 cm to 5 cm in diameter. Data measured for this study at the National Aquarium in Baltimore, as well as reproduced data from a previous study of *Aurelia* turning (Gemmell et al., 2015). Timing in proportion of contraction cycle time (delay time / total contraction period, 0 = no delay)

	5cm *Cyanea* (N=20)	**4cm *Cyanea* (N=5)**	**3-4cm *Aurelia* (N=12) (Gemmell, 2015)**
Mean	0.2506	0.2808	0.097
Range Max	0.4	0.3867	0.5
Range Min	0.0967	0.2103	-
Range Max Delta	0.1494	0.1059	-
Range Min Delta	0.1540	0.0706	-
+1 Std Dev	0.3224	0.3614	-
-1 Std Dev	0.1789	0.2003	-

Since the bell of jellyfish is controlled by a neural ring with nodes that command local musculature, and the stimulation cascades through this net around the bell, a smooth propagation of the contraction and relaxation signals was expected (Satterlie, 2011). However, due to the coupling of the bell, ambiguity in biological footage of intermediate lobe timing, as well as an observed improvement in turning when the intermediate lobes were left flexible and synchronized with the outside quadrant, the gait timing made the intermediate lobes always move with the outside lobe during all phases of the gait cycle. Further studies of the intermediate lobe kinematics may aid in the bell coupled dynamics and turning effects of out of plane motion. It can be expected that this additional motion did not act in plane, but spreads the rotation from the outside lobe from what would likely be a tubular vortex into a partial vortex ring. The resulting effect of this in biological specimens can be seen with the crescent shape of the vortex ring for *Aurelia*, which extended in a range from the outside lobe only to three quarters of the way around the body axis (Gemmell et al., 2015).

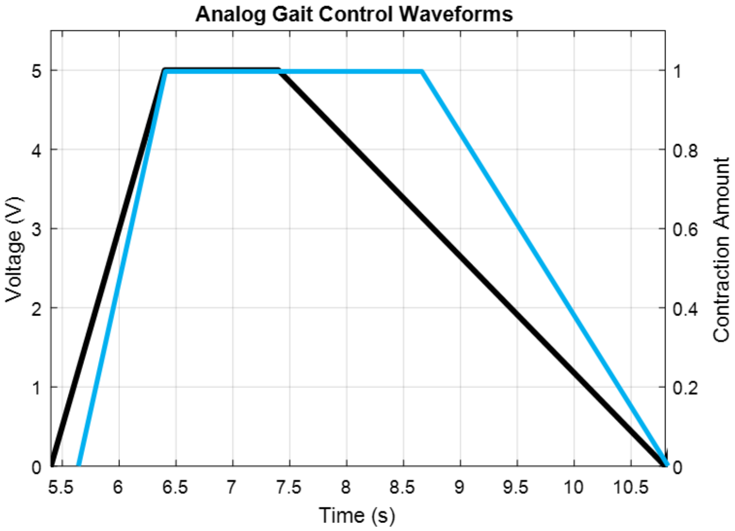

Figure 36 – The gait waveform initially implemented on the robot. The primary central gait was the black line, while the contraction- and relaxation-delayed waveform was superimposed in blue. The cycle form was extracted from a continuous waveform for simulating the system response, so the time started at an arbitrary point at the beginning of a cycle. However, this shape shows a change in speed to create the timing instead of a sliding window control profile.

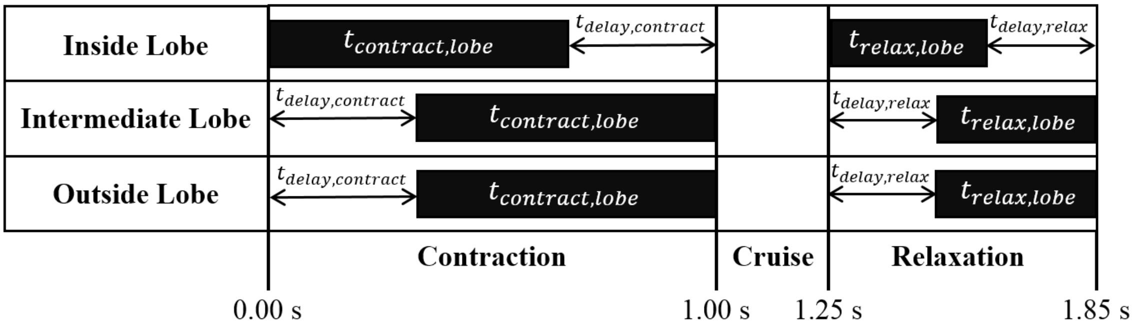

Figure 37 – Final timing architecture for delayed contraction and relaxation moves within sliding window of global cycle timing.

As with the measurements of Cyro 2, the power consumption and gait phase needed to be sent externally to a digital acquisition card for sampling and storage during initial testing. However, the measurements should not affect the performance of the robot and hence subsequent measurements, such as PIV or motion tracking. Initial tests indicated that a power delivery tether was unreliable for high powered robots in high sensitivity measurement environments. Therefore, as opposed to the thick and stiff multi-conductor cable used for Cyro 2, small 24 gauge cables with sufficient flexibility but limited diameter and thus minimal fluid interaction extend from the robot to the DAQ card for each of the onboard measurements. These cables were also used as an activation switch for the robot, allowing power to be delivered to the robot but the control circuit to be disabled to enter a low power mode and restart the gait cycles. The enabling circuit consisted of a simple tactile switch in series with a 1kΩ resistor, with one end connected to a 5v power supply grounded with the robot and the other end connected to a digital interrupt pin on the robot controller. The high 10 GΩ input resistance of the DAQ enabled reliable voltage measurements at low current draw, and thus extremely low resistive voltage losses. For the initial design with onboard power, two external port cables that were waterproofed both during and outside of monitoring with an O-ring seal were used to charge the batteries and monitor power consumption with an onboard 0.1Ω shunt resistor and voltage reference taps before and after the resistor. The power of the robot was solved with a simple derivation:

$$P = IV = \left(\frac{\Delta V_{resistor}}{R_{resistor}}\right)\left(V_{battery}\right) = \left(\frac{V_{battery} - V_{post-resistor}}{R_{resistor}}\right)\left(V_{battery}\right)$$

The updated designs with larger motors required higher power delivery, so a tether was utilized to deliver higher voltage to a step down converter only during power measurements. This high power also exceeded the wattage of previous shunt current measurement setups, so a 100W 0.1Ω shunt resistor was used for current measurement and was attached to a heatsink consisting of thermal interface paste, a 1/8 inch copper interface plate, and a large 1/4 in aluminum plate for dissipation and stable resistance values. By taking the voltage drop across the resistor, as well as the voltage tap at the robot side with a voltage divider that reduced the voltage to a third of the true value (voltage drop across one of three series arranged 20kΩ 0.1% tolerance 1/4 watt resistors) to allow DAQ collection, the power consumption was calculated as

$$P = IV = \left(\frac{\Delta V_{resistor}}{R_{resistor}}\right)\left(V_{battery}\right) = \left(\frac{\Delta V_{resistor}}{0.1\Omega}\right)\left(3 * V_{tap\ divider}\right)$$

The phase of the robot actuation was also tapped out as a digitally pulsed signal. High voltage, low voltage, and different single pulses were used before on Cyro 2, but discerning the pulse and changing this architecture for different gait organizations was less than optimal during experimentation and data analysis. Analog signals could be used, but the filtered PWM output required more complexity onboard in limited space, as well as limited resolution and induced noise that could complicate state detection. In addition, for a phase measurement the inclusion of an additional phase lag from filtering was unadvisable. Therefore, the signal was simply a PWM signal that was full duty cycle during baseline contraction, two-thirds duty cycle during cruise, one-third duty cycle at relaxation, and zero duty cycle at stall. The pulses were read into the DAQ, the high and low states were resolved to a normalized binary value. This cleaned signal was processed using a forward-scanning window of 1 ms (due to a 980 Hz PWM signal), and the window values were averaged to find the instantaneous value that was matched to one of the four cycle states. The minimum pulse was 0.34 ms for the one-third relaxation gait state, which was readable on the analog I/O of the DAQ. The analog signal was then rounded to zero or five volts in the MATLAB analysis code to indicate the digital states.

Power switching was accomplished by a hardware and software switch pair. The hardware switch utilized a low voltage trigger, high power transistor switch attached to a reed switch adhered inside the robot body (Pololu “Mini MOSFET Slide Switch with Reverse Voltage Protection, SV”, Littelfuse MDCG-4-12-23 “SWITCH REED SPST-NO 350MA 140V”). This triggered the on-off of the power, and during experimentation the switch was left on with the power supply for the tether accomplishing power delivery. The software switch was achieved by a 5V digital line attached to a state-change interrupt on the central microcontroller. When the line was set low, the robot would return to and hold the fully relaxed position for all lobes. When the line was set high, the program would operate normally through the contraction cycle. This pulse was delivered by an additional power supply with the power switch acting as the enabling controller, but a constant 5v voltage with a trigger switch was eventually used as an enable switch for experimental ease when a single operator was running experiments.

Gait and parameter variation during parametric study of the gait was required to be rapid and easy. Previous communications with the jellyfish robots for gait changes either required the controller to be held out of the water and tethered to the robot, which induced cable resistance and voltage losses under high current draws, or the robot to be removed from the water, have the electronics enclosure seal broken to access the electronics, and resealing of the electronics enclosure. These methods either resulted in unrepresentative swimming performance or long waiting times between gait iterations, usually spanning from one day to an entire week to wait for the sealant to cure. Cyro 2 improved this with a custom cable that mated with the multi-purpose D-sub access port, but gait changes still required removing the robot from the water and re-establishing the proper buoyancy for the robot, again taking time on the scale of several hours per code change. Therefore, Cyro 3 has been programmed with two rapid update methods. The central controller was equipped with a SparkFun Bluetooth Mate Silver Bluetooth serial link. This serial link enabled external communication with the data collection laptop without removing the robot from the water. With a 10 meter range, even when enclosed in a plastic battery housing or sealant, the link was able to be communicated with to change the central microcontroller code and parameters when the robot was surfaced. Since the distance between the robot and the laptop in the tank was low, only surfacing the robot was needed to reliably establish a link.

The Bluetooth link acted as a serial programmer, which enabled a port to communicate with the microcontroller in the Arduino IDE. However, this module required modification to enable this behavior. The TX and RX communication was valid since the programming was a simple serial communication. To enable access to the code on the board, the microcontroller needed to be reset and the code needed to be downloaded before the board initiated program execution. The Arduino IDE handled this by sending a pulsed reset signal at upload to automate the code downloading and timing (Arduino Playground - ArduinoReset). However, this mode was disabled on the Bluetooth module and did not send the pulse (Lortie, 2012). To enable the module, a direct link needed to be established, and once connected the command mode needed to be enabled using the '$$$' command in the serial monitor. When a confirmation message was received that the mode was initialized, the code 'SU, 57.6' was used to set the baud rate to the typical programmer baud of 57600. The command 'S~,3' initiated MDM mode which enabled remote pin I/O on the board. These changes were verified with the 'D' command in the serial window. Next, the surface mounted pin 33 on the Bluetooth board, which correlated to the PIO10, needed to be broken out to access the DTR/RTS (Data Terminal Ready, or Request to Send) digital pulse to indicate that the data was ready to send to the board. The DTR signal dropped to ground on transmission, while the microcontroller required a ground to initiate the reset and then a change to the high state to start the reset process (Arduino Playground - ArduinoReset). Therefore, it was convention to include a 0.1 μF capacitor in series to form a high-pass filter that converted the low level drop to a pulse that initiates the program access (Fried, 2015).

Since this connectivity was required for the central gait control, a compatible microcontroller was required. While the A-Star was of appropriate scale and functionality, and would ease supply chain and compatibility issues with the motion control microcontrollers, the external Bluetooth programmer was not compatible with the ATmega32u4 microcontroller on the A-Star board. Therefore, the slightly larger but small scale Arduino Pro Mini 328 5V with the built in serial communication header and compatible architecture was chosen. This was due to the ATmega328 typically requiring a separate onboard USB to serial converter, which was bypassed for the Bluetooth communication and even completely absent on the Mini board due to its integrated FTDI headers, and the ATmega32u4 having an integrated USB to serial converter that could not be directly bypassed for code changing (Fried, 2015).

During later testing some long term water ingress or moisture caused the serial link to fault intermittently, so the FTDI interface of the Bluetooth to the card was changed to routing the FTDI signal lines into a waterproof connector, which mated with a waterproof plug connected to a USB to FTDI adapter to enable programming when fully or even partially surfaced during testing.

The central microcontroller also had access to a Pololu MinIMU-9 v5 six degree of freedom IMU for monitoring the turning and translation of the robot during maneuvers. This can be used in the future for closed-loop control of the turning towards a target. This sensor was initially integrated but not part of the control system, since the exploration of gait dependent maneuvering was paramount and the true movement was more reliable to track with high speed or standard digital cameras than with an onboard sensor with implementation complexities.

3.2.3.4. Power Supply and Regulation Architecture

Power delivery to the robot has been accomplished via two primary means – off-board continuous tethered power, and onboard rechargeable stored power. The previous large robot Cyro 1 had sufficient space in the electronics enclosure to hold banks of batteries for portable power. Due to a decreased size, Cyro 2 utilized tether power for more continuous measurements and long term power delivery without adding additional mass or space on the robot, at the tradeoff of fluctuating voltage and interference in fluid measurements and free swimming consistency. Therefore, Cyro 3 sought reliability in swimming during maneuvers with limited external forces, but high power consumption also necessitated continuous power delivery with limited effects of reduced battery power delivery.

The initial design with smaller motors opted for on board power due to the early limited power requirements. Therefore, this robot was integrated with four Lithium Ion batteries from Adafruit, with a 2200mAh capacity at a nominal voltage of 3.7V and a maximum voltage of 4.2V. These cells each had a mass of 46 grams, including charge and discharge fault circuitry that prevented excessive or abnormal cell behavior or power draw. The high voltage density, with four series cells providing a maximum of 16.8V and a minimum of 11V, exceeded the voltage density of Nickle Metal Hydride cell batteries at the expense of some robustness under heavy use, hence the fault protection. The cells were tapped out to the upper two waterproof cables, with one four-pin cable providing the positive voltage of each cell and the other cable giving a full voltage and ground tap. This allowed balanced charging with a custom balance cable that could charge the robot when surfaced without concern of shorting in the water at the waterproof contacts.

In order to deliver the appropriate power levels to the electronics from the high voltage bank of batteries, while also reducing current draw from the LiPo cells, stages of stepping boost and buck converters were integrated in the system. In the battery housing the Bluetooth was powered by a 5V buck converter (D24V10F5, Pololu), and this power was delivered to the main housing via the four-pin waterproof communication cable. The 5V line was used to power the motor drivers' logic circuits, as well as a 5V to 9V boost converter (U3V12F9, Pololu), which achieved the appropriate voltage at low current consumption for the three microcontrollers. In the main power cable, voltage from the batteries after the current-sensing circuit was sent with the global ground, as well as the phase and trigger lines integrated into the battery housing. This main voltage was then sent through a 12 volt buck converter (D24V22F12, Pololu) to power the motors via the motor drivers. In addition to the external stepping converters for high efficiency, the microcontrollers each had linear regulators to drop the input 9V power to the logic levels of 5V and 3.3V. The 3.3V line was used to power the IMU (MinIMU-9, Pololu) since it consumed sufficiently low power. While this additional step used an inefficient conversion method, the power draw through the controllers for logic and peripheral powering was low and thus the waste power was low. In addition, the boards were not suggested to be powered directly with the 5V pin since it bypassed the voltage regulator and induced a voltage to the regulator output with no input voltage, potentially inducing a reverse power flow with potentially noisy and fluctuating input that could damage the microcontroller and the on-board regulator (Arduino Board Uno; ON Semiconductor, 2017). This regulator and board were similar to the A-Star and Arduino Pro Mini boards, and while those boards' regulators do not mention reverse bias protection it was decided to avoid complications or delayed faults. While a 5V input to the USB line would bypass the converter without causing the reverse biasing issue, as would be found with a USB connection during programming and monitoring, integrating a USB Micro male connector would have taken up a relatively large amount of space in the already compact motor and electronics housing.

To verify appropriate power draw from each converter and load, the range of performance was calculated and compared to the system and battery requirements. For the 12V buck converter, the voltage input range varied from 12.9V to 36V with a maximum output current of 2.2A. The maximum input current for this peak output occurred at the full battery charge, with the equivalent current at a 95% expected efficiency reaching 1.65A. The minimum input current for this peak output occurred at the 12.9V input voltage, which resulted in 2.15A input. The peak total current of the motors, estimated at the max efficient torque for each motor, was 0.38A per motor and thus a system total of 1.54A at a system power of 18.44W. This was comparable, and even slightly lower, power draw than the single motor solution of Cyro 2. At this peak total current, the equivalent peak converter input would be 1.51A, which was safely below the cell max continuous battery draw of

4.4A from the datasheet and close to the expected protected constant current draw of 1.1A, as well as below the peak output current for the voltage converter. The datasheet standard continuous current was at 0.44A, which for the majority of the cycle was expected to be a safe current draw.

This power draw was expected to result in a 1.43 hour battery lifetime at the peak current, and 2.86 hours at the half peak. Since the average power draw of Cyro 2 was 30.68% of the peak current, and eliminating the position hold current would half the average to 15.34% the peak current, the expected design battery lifetime would have been about 6.52 times the peak current lifetime and hence about 9.32 hours. This was sufficient lifetime for testing, as well as sufficient lifetime for autonomous performance with solar cell charging and power draw optimization during path planning. It should be noted that the 12.9V input cutoff was higher and hence premature relative to the cell stack minimum voltage of 11V. At a peak discharge of about 1.5A, or about 0.68C capacity current draw, the 3.225V cell voltage was reached at approximately 92.5% the rated cell capacity discharged. At peak current the cell capacity dropped to about 97.5% rated capacity, and hence the minimum voltage was truly the 94.9% capacity of the cell discharged. This occurred at the end of the capacity where voltage dropped off rapidly, and lower current draw during the cycle resulted in a larger capacity at the cutoff voltage and an even smaller difference between minimum cell voltage and minimum converted voltage. Below the converter minimum voltage the converter either shut off or delivered a slightly reduced voltage, which at worst would reduce motor performance slightly. Therefore, this loss in performance range was not expected to be significant.

To improve the performance life of the robot during testing, as well as a way to stop performance and all power draw during storage, a switch was integrated directly after the battery stack output. The switch was a transistor mounted on a prefabricated board (Pololu "Mini MOSFET Slide Switch with Reverse Voltage Protection, SV"), and the transistor was switched by a reed switch closing a contact to the trigger line. The reed switch was placed at the top of the battery housing cavity, allowing close contact with the magnet and easy access from a surfaced position. This ensured waterproof switching for main power that was easy to quickly access.

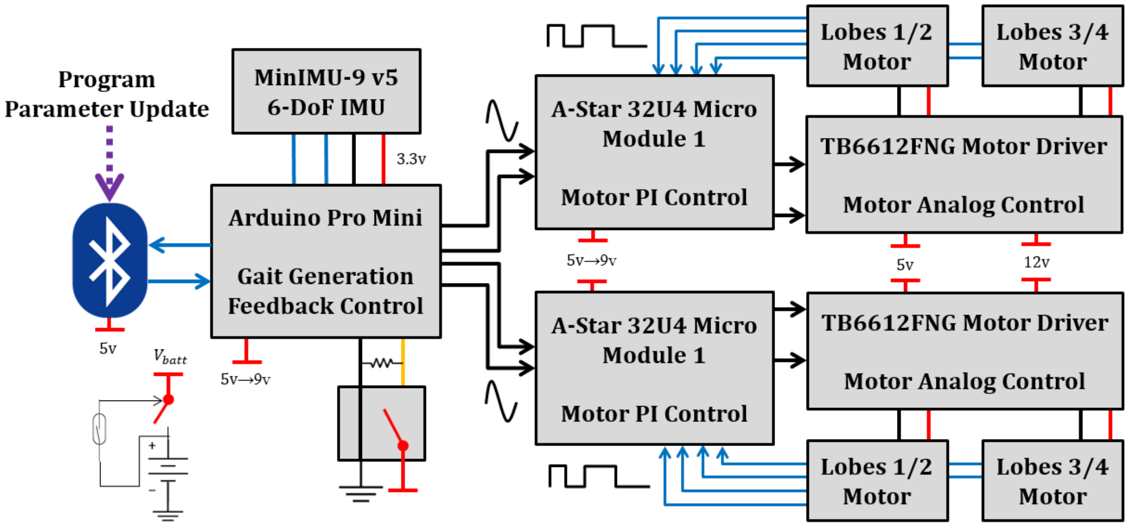

Figure 38 - Full control and power management system diagram for initial Cyro 3 design

After design validation was completed for the small motor design, it was found that the motors consumed significantly higher power and could not sustain the torque needed to actuate the bell lobes. As previously mentioned, this was due to the change in durometer of the bell material. Therefore, the larger motors were integrated to handle the torque loading, initially DC gearmotors and finally DC servomotors. These required actuators consumed significantly higher power, and therefore efficiency of the design was a significant consideration but the electromechanical efficiency was inherently low and thus not a major design feature. To characterize the power and deliver significant consistent power for water testing, initial design validation was completed with a tether cable to isolate power delivery from performance, as well as accommodate quickly changing power requirements from design iterations. The cable consisted of four flexible 20 gauge wires in a rubber jacket for the power and ground delivery, phase signal, and trigger signal, with two 24 gauge stranded wires attached for voltage and ground measurement in the robot. Once out of the tank, the 20 gauge wires were stepped up to 16 gauge to reduce losses from the tank to the power supplies and data acquisition hardware. The total cable length was designed to extend 20 feet, with 2/3 of the cable in the tank or coiled outside the tank for tuning of the in-tank slack. As found before, any data or low current signals were not expected to have any resistive losses in the cable. The power delivery was expected to reach a maximum of 9 Amps from desktop experiments, and the input voltage was selected at 15 volts such that the voltage drop across the cable, as well as the dropout voltage of the power converter, still ensured sufficient power delivery to the actuators.

However, it was found that the swimming thrust and turning torque generated by the iterated kinematics were not sufficient to overcome external forces from the cable tension and torsion. Therefore, a two cell 7.4V Lithium Polymer battery with a hard-shell case (Dynamite Speedpack Li-PO Silver Series 5000mAh 20C) was selected to deliver power on the robot due to the appropriate size and voltage level for the servo motors, and the hard-shell case allowed easy waterproofing with a marine sealant around the seams and cable ports (Loctite PL Marine). The battery was strapped onto the robot via the buoyancy adjustment foam at the rear of the robot, and four conductor waterproof cables were used to transfer power to the motors and electronics underwater. Due to the limited power rating on each conductor, the balance port was split between the conductors on each cable but the power and ground was sent in separate cables across all four conductors. This allowed consistent power delivery to the robot without external tether forces, and during testing the power was monitored to stay well above the nominal voltage of 7.4 volts (the cells were stable over a long period at nominal voltage, and charged to a maximum of 8.4 volts, so the power was maintained to above 8 volts during testing). Also, since the microcontrollers regulated the voltage down to 5 volts via on-board regulators and the servos were made to operate across the full range of a LiPo battery, this battery configuration was ideal for this size of robot in terms of low weight, optimal power capacity and voltage, size within the profile of the central column, and ease of waterproofing.

Initial power testing of the final robot design over a tether, using a localized voltage tap on the robot and an off board shunt resistor, found that power consumption of straight swimming was 34.92 Watts on average, with a cycle maximum of 85.75 Watts and minimum of 6.61 Watts. With asymmetric lobe movement, such as the 45% case shown below, power consumption was reduced on average since the movement time during the cycle was reduced in total. However, faster movement did marginally increase the peak power draw. The 45% test case averaged at 30.84 Watts, while the peak was at 91.00 Watts and minimum power draw at 2.44 Watts. Therefore total power consumption per cycle dropped with turning gaits, but only by about 4.53 Watts, or 13%, at a 45% contraction delay turning gait. Initial testing also indicated that, for a 7.5 Volt drop-down voltage converter (Pololu D24V150F7) supplied with a 12 Volt tether line input, the high power consumption period induced a drop in line voltage due to cable resistance and power supply rebound below the drop-out threshold of the converter, further motivating the use of batteries with high wire gauge supply lines for reliable constant power instead of a long tether to an external power supply.

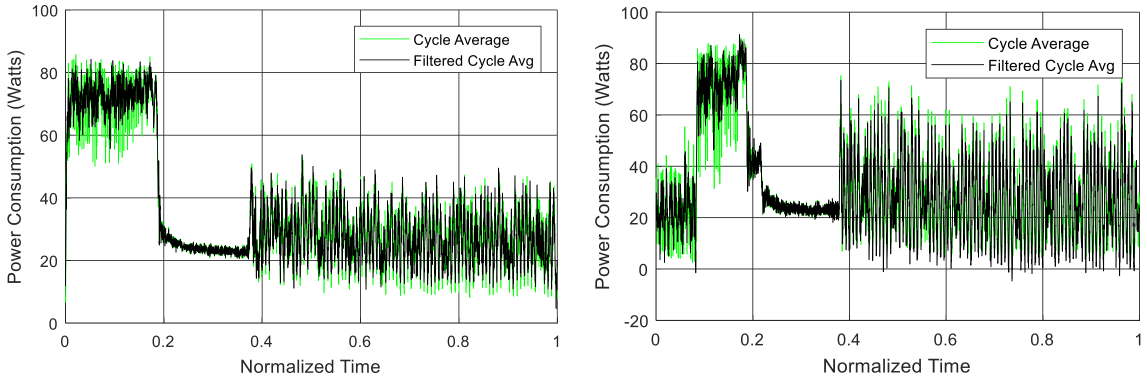

Figure 39 – Power consumption of final design of Cyro 3 from straight swimming (left) and a 45% contraction delay cycle (right). Filtered results were processed with a notched 50Hz filter to remove the major effects of a carrier wave in the servo motion controller.

3.2.4. Housings, Assembly, and Waterproofing

3.2.4.1. Initial Design Housings – Small DC Gearmotor

3.2.4.1.1. Battery Housing

The topside housing of the robot, which extended above the bell to balance the mass of the motor enclosure on the underside of the robot and locate the center of mass in the middle of the bell, contained the primary power supply and rapid-access controls for the robot. The housing consisted of two 3D printed halves, which were screwed together against a laser cut nitrile rubber gasket to form an evenly distributed seal that could be removed for repairs but still reliable and sufficiently thick to ensure a long lifetime seal. Screw holes and hexagonal nut holes were integrated into the top and bottom housings such that the seal contained the hardware, the fasteners were moved into the housing profile to not disturb surface flow, and the screw length was standardized in the design to reduce part costs. The bottom of the housing included ridged holders to locate and support the lithium ion batteries. The batteries were wired in series, with taps at each connection and the distal ends to enable voltage balancing and power delivery. The power lines then went to a switch actuated by a peripheral reed switch, which along with the Bluetooth module were positioned and adhered close to the lid of the housing to minimize material separation and thus improve magnetic and wireless signal transmission. Where the switch was adhered on the inside of the housing lid, the exterior had two short carbon steel round stock pieces to allow a small cylindrical magnet to seat and stay at the correct position and orientation to always actuate the switch. Two cables exited the housing for upwards access – one for power and phase monitoring, and one for balanced charging. These two cables exited the housing, routed through integrated clips, and fit into press-fit sockets to hold the ends in place and allow a solid flat interface for the cable O-rings to seal against to keep water out of the pin and socket terminals. Two other cables exited the housing posteriorly to carry power, control logic, and programming logic and power to the control and actuation electronics in the main housing. Two small-gauge wires also exited the housing through a small slot to provide the input and ground reference for the enabling switch to trigger the robot, and the wires ran vertically in the water to be out of the wake structures and provide minimal tension interference to the robot motion. The cables ran through a separate cavity between the spliced connections and the housing exit holes, where the wires were flooded with epoxy to act as moisture- and leak-resistant potting. The 5V regulator also fit in the housing to power the Bluetooth module. For attachment to the rest of the robot, the assembled housing sat into a recess in the cast bell and bolted on to the lower housing assembly. The topside of the battery housing also had four 7/16”-14 threaded holes, which were flanged, embedded deep in the housing with significant surrounding material, and threaded to the bottom of the hole for accessory and sting attachment for measurements and buoyancy control.

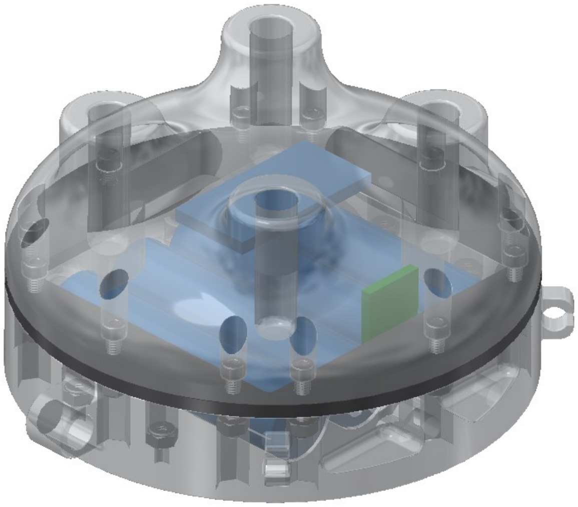

Figure 40 - First Housing Design, Battery housing structure and assembly CAD Model

3.2.4.1.2. Motor and Electronics Housing

The upper section of the main housing enclosed the detent springs and spindles for cable actuation. The upper flange provided a broad surface for the bell and battery housing to rest on, and the flanges included recessed screws that attached to four lock nuts embedded into the battery housing to draw the upper half of the robot together. In the center of the upper section, a single 1/4”-20 screw was embedded that screwed into the main actuation housing to ensure proper separation and support for the two halves around the spindles, which was critical for reliable spindle performance under load. While this screw ensured axial locating and centering, a flange around the base of this housing included cutouts to index the spindle housing rotationally and concentrically to the lower main actuation and electronics housing. Where the cables entered the central column to attach to the spindles for actuation, elongated and filleted holes were included for each lobe for routing with reduced friction and constrained lateral cable travel. Since the housing needed to be open for cable entry and no critical water-sensitive components were enclosed, this section of the robot was flooded with water.

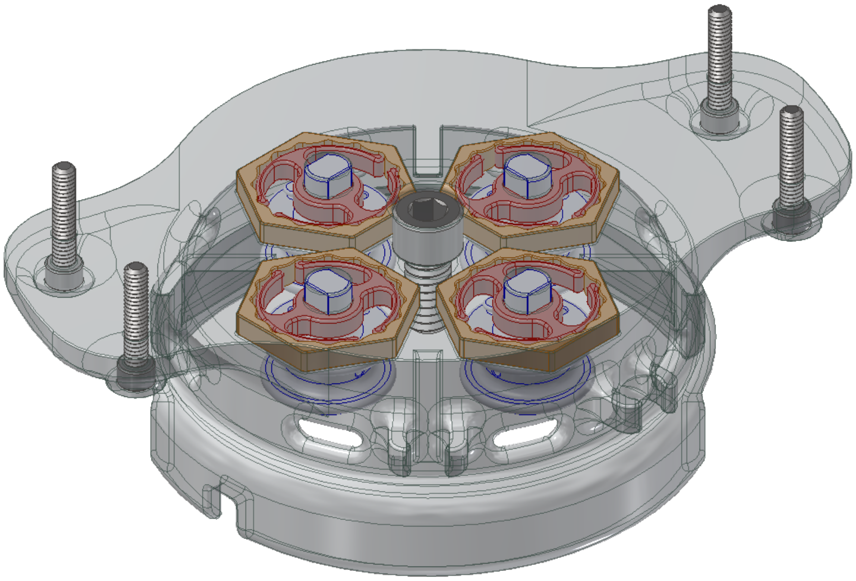

Figure 41 – First Housing Design, Upper Main Housing, which contained the spindle and cable assemblies

The lower housing body contained the control, power management, sensor, and actuator electronics for the primary functions of the robot. The main housing was 3D printed, with a labyrinth seal entry for the two power and communication waterproof cables to enter the housing and be surrounded with waterproof sealant. The motors were arranged radially in close proximity at the center of the housing, and the electronics were embedded into peripheral recesses in the housing walls. The motors were connected to the housing via low profile socket hex screws, which had laser cut nitrile seals at the socket head and the motor threaded hole to form a redundant seal when the motor was affixed to the housing upper plane. The motor shaft also had a 1/32 inch thick laser cut nitrile seal around the shaft that was clamped between the housing and the bushing for the motor, and it had an undersized inner diameter to promote shaft sealing when the clamping force of the screws caused transverse expansion towards the shaft. Wires and small electronics not embedded in the walls were distributed around the motors and electronics, with placement of each component and wire route selected to minimize excessive cable strain that caused contact failure and avoid interference with the spinning of the encoder disc on the lower end of the motor. The housing had eight circumferentially evenly distributed Nyloc nuts embedded into flanges around the periphery of the housing at the base, and a 1/4 inch thick laser cut acrylic plate was screwed on with socket head machine screws. To form the bottom seal, the plate compressed a laser cut 1/8 inch rubber gasket that was recessed into a lip to constrain transverse deflection under clamping load. Since the air-filled electronics housing for Cyro 2 was found to negatively affect buoyancy, this housing was initially flooded with mineral oil. This was intended to bring the density of the robot body to closer to water, and the mineral oil was expected to simultaneously improve heat distribution and cooling, lubrication of moving parts, and form an oil film around the gaskets and moving parts to repel water and improve seal continuity where small gaps would otherwise allow water entry. These seals were tested to successfully prevent oil escape beyond a slight oil film where intended. However, this oil flooding was found to reduce motor performance likely due to viscous damping of the rotational components and dielectric insulation of the arc gap of the motor brushes, and a simple air containment was selected for the iterated design with a grease layer between gaskets and the walls to eliminate air gaps.

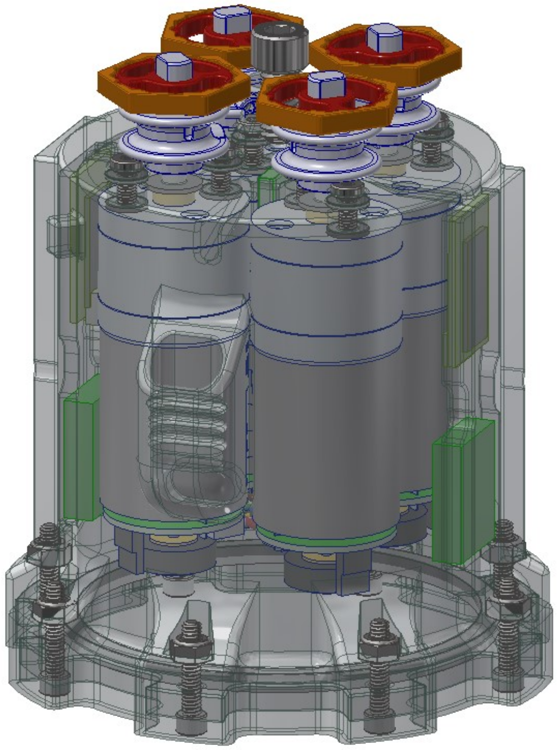

Figure 42 – First Housing Design, Main electronics and motor housing

3.2.4.2. Second Design Housing – Large DC Gearmotors

The inclusion of larger DC gearmotors to meet the updated torque requirements for a bell constructed with DragonSkin silicone necessitated an updated enclosure design. This design focused on ease of manufacture and flexibility for future iterations. The bell was attached to a laser cut circular acrylic plate with elliptical cutouts around the periphery, with silicone adhesive used to glue the bell around the perimeter of the plate as well as extend into the cutouts to reduce the chance of tensile or shear failure at the plate and bell interface. This plate was screwed in via threaded spacers into a larger laser cut acrylic plate, which the motors were attached to via screw points and a nitrile rubber seal between the motor and the acrylic plate. The nylon spindles attached to the motor shafts, as detailed in the spindle design section, with clearance between the upper extent of the spindle assembly and the topmost plate. The electronics were adhered to the motors around the outside perimeter, and wires routed around and between the motors to maintain a compact enclosure. The enclosure then consisted of a cast silicone form that surrounded the electronics and flared at the top to mate with the large acrylic plate. An additional laser cut split ring was made to clamp around the underside of the flared silicone, and the plate and ring were screwed together with nylon screws and nuts to compress the silicone flange to form a seal. This design was found to be mostly waterproof, and the flange seal and screw holes were covered further with a marine adhesive sealant (Loctite PL Marine) to cover any potential voids between the silicone and the acrylic. In addition, the motor and electronics assembly was wrapped with absorbent fiber towels to absorb any leaked water and hold any moisture at the periphery away from any sensitive components. This formed a better waterproof enclosure than the previous 3D printed enclosures due to no leakage due to printed layer porosity and unevenness at seal interfaces. In addition, since this design utilized a tether cable to deliver power, the housing only included small holes in the large acrylic plate for cables to enter. These holes were sealed with epoxy and an extra layer of the marine adhesive sealant to block water ingress.

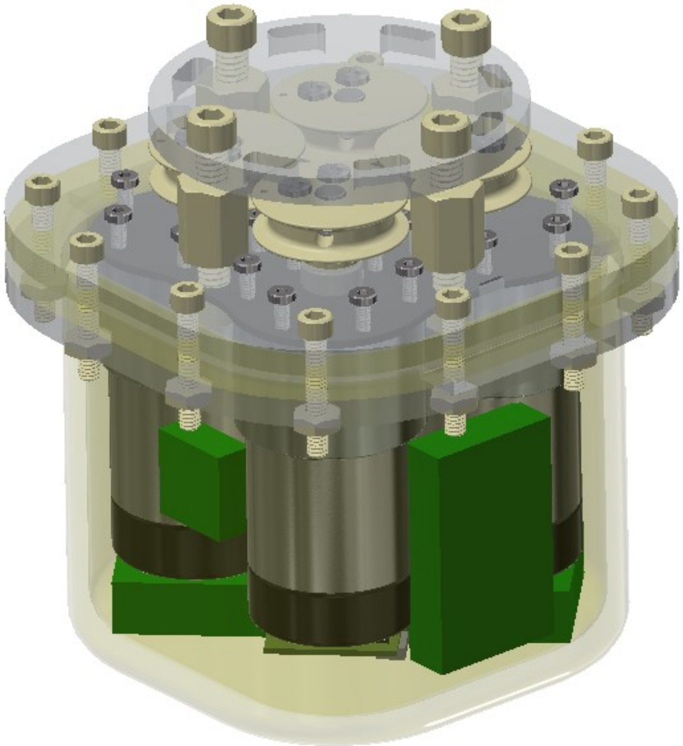

Figure 43 – Second Housing Design, Main electronics and motor housing

3.2.4.3. Final Design Housing – DC Servo Motors

The final design that utilized servo motors took a minimalist approach to waterproofing and structures. The bell was still adhered to a laser cut acrylic plate with peripheral attachment points for additional support, and monofilament fishing line was used to stitch the bell to the plate for even more physical support via forced compression on the silicone. The spindles were suspended between the bell plate and a secondary laser cut acrylic plate, with the underside of the servo horn and the cylindrical protrusion on top of the spindle seating into circular cutouts on each plate. These two plates were screwed into 3D printed spacers that fit between the spindles around the periphery while allowing sufficient clearance for the spindles and cables. The motors were then mounted on the top and bottom in pairs, with a laser cut acrylic plate sliding over the back of the motor pairs to seat at the motor's mounting flange. The circular and motor plates were screwed together to position and clamp the motor to the spindle assembly, with a rectangular 3D printed spacer in between the plates and servos to keep the motors parallel and maintain the proper spacing between the plates when in compression. The electronics were coated with the marine adhesive sealant (Loctite PL Marine), and once dry adhered to the back of the motors with the same adhesive. Tests found that exposing the electronics to open water with a complete coverage seal using the adhesive sealant allowed for sufficient cooling for high power components while minimizing moisture and water ingress failures. Repairs and troubleshooting were easiest with this design, and wires were routed freely around components and contained using Velcro tie downs and additional adhesive sealant spot tacking. The buoyancy foam was cut from 2 inch thick rigid housing insulation, and the forms either conformed around the motors with Velcro ties holding them firmly to the body or were placed at the backs of the motors with screws holding them into the circumscribing foam rings. The tether cables, and eventually the battery cables, were routed into the space at the center of the motors, adhered into place with the adhesive sealant, and then routed out of the surrounding foam for access and external routing between the top and bottom of the robot. Cable routes through the bell were achieved with small incisions in the bell silicone near the center of the bell and re-sealed with adhesive sealant. The battery was attached to the bottom of the robot using steel wire bent to conform to the battery enclosure, routed into the foam, and bent over to keep the wire from pulling out under tension. Additional foam placed at the bottom was then shaped to support the battery via sections cut to shape and screwed into foam between the battery and the motors.

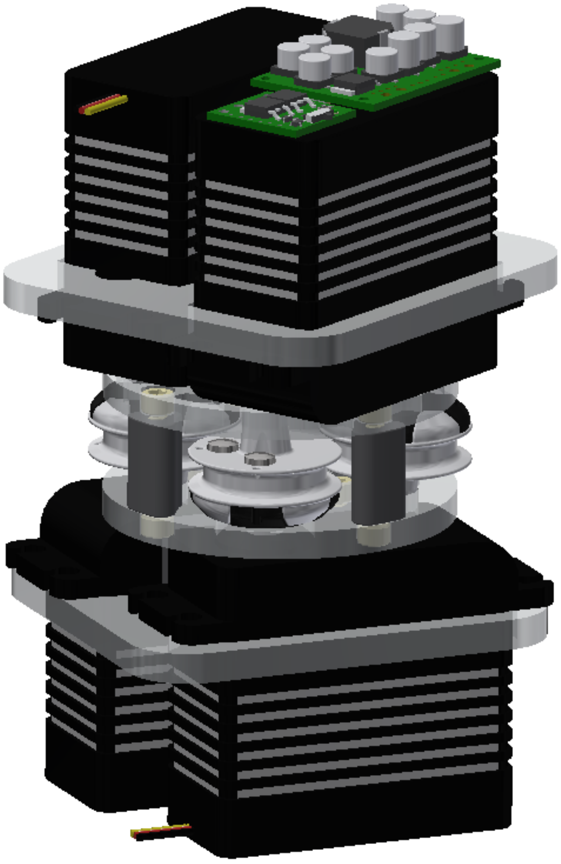

Figure 44 – Final Housing Design, Minimalist spindle housing and motor support

3.3. ***Parametric Study of Maneuvering Gaits***

The study that indicated that rowing jellyfish achieve turning from a combination of asymmetric contraction timing and local stiffness control of the bell margin opened three primary questions (Gemmell et al., 2015). First, the degree of influence on turning amount from timing and stiffness, individually, was ambiguous from previous studies since the effects are combined in natural swimming motions. While marginal stiffness changes were likely a combination of muscular control and structural features that allowed variable stiffness in the margin, the additional mechanical benefit from muscular effort and energy input could have been either significant and worth the extra energy expenditure or insignificant and wasteful or only worth passive effects. With this proposed decomposition problem, the second question was how the timing effects scaled between straight swimming and turning. The previous paper separated the behaviors, but data from *Cyanea* and observations of turning behavior from multiple rowing species has shown a continuous spectrum of turning amounts from varying amounts of asymmetric timing. The study of the kinematic effects of varied timing provided an understanding of the control space of rowing jellyfish maneuverability. The jellyfish turning study, as with many jellyfish swimming research, also focused solely on the contraction period of the turning. However, the cycle portion where the bell refills entails a significant effect on the effectiveness of the fluid motion and thus thrust from contraction, both due to changes in induced drag and augmenting thrust due to impingement and vortex formation. A third focus of this study looked at the variable relaxation timing and its effect on the turning of the robot, and thus rowing jellyfish. These parametric studies looked at both the kinematic evidence of the turning from motion tracking and the fluid interactions and structures from PIV during turning.

For all testing, the robot was set to neutral buoyancy in the water. Foam was added to the top and bottom of the robot to increase buoyancy and move the center of buoyancy closer to the center of mass, while small magnetic weights attached to screws holding the foam together were used to fine tune the magnitude and center position of the robot mass. Since the mass and buoyancy of the robot was transient during long periods of testing due to saturation of the foam and robot materials, the buoyancy was monitored throughout testing and adjusted to maintain balance and neutral buoyancy. Since exact adjustment was not always possible through trial and error, the buoyancy would be slightly negative if not exactly neutral. In addition, if orientation instability of the robot was not achieved through moving the center of mass and buoyancy, the stable position was selected such that in the plane of turning the robot did not prefer an orientation and was as close to unstable as possible. Any stability was selected out of plane, so the robot would only prefer a stable position out of plane and not either augment or attenuate in plane motion. This was monitored and tuned between trials to ensure dynamic consistency, including throwing away trials that resulted in significant out of plane drift during the maneuver such that the angular measurement tracking and fluid motion was occluded or not aligned in plane.

3.3.1. Parametric Testing Kinematics

For each iteration, 20 trials were collected with at least four turning cycles in plane with the camera view. Pins with pearlized cylindrical heads were attached to the robot at four spots on the top of the robot on the foam (left and right, above and to the side of the foam) in plane with the turning and camera view. These pins were illuminated with a 400 Watt 6500K metal halide lamp, which illuminated the pins without bloom to contrast against a black background. These white dots were then motion tracked in After Effects, with the tracking following the luminance channel with subpixel positioning and motion extrapolation. The track was monitored during processing, and any erroneous tracks were manually modified to be correct before continuing the automated tracking. These time histories of coupled position data was then processed in MATLAB to obtain the angle and angular rate through time. The average of the first, second, fourth, and all four cycles combined of each trial was found, and the average across all trials was found for each combination of cycles. This data was then processed in Minitab through the linear modeling ANOVA with the factors of percent contraction delay (0%-50% in 10% intervals), margin stiffness on the inside quadrant (stiff, loose), and relaxation delay (0%, 25%).

As seen in the plot of the average of the first four cycles, then averaged across trials to find the typical average turning rate for the first four turning cycles, each effect of increased inner marginal flap stiffness, increased contraction delay, and increased relaxation delay augment the average turning rate across four cycles. Across the first four cycles, it was found that the stiffened turning quickly reached the maximum turning rate and tended to taper in turning rate as gravity changed its orientation on the body, despite still achieving orientation changes on the fourth cycle. On the opposite case of a naturally flexible flap for all quadrants, the turning rate was reduced but the buildup of turning momentum across cycles was more pronounced such that a steady state or maximum was not reached by the fourth cycle. This upward trend and positive effect of each factors was present in each cycle, with the first cycle showing a more pronounced turning at the 30% case likely due the moderate force on the fluid coupled with a moderate flow disturbance from rest that would otherwise require a steady state to produce stable and consistent structures for momentum flux. The results of the ANOVA clearly showed that the three factors had a significant effect on turning ($p<0.05$), even when separating data based on collection times to remove batching effects on the data. While batching did affect the magnitude of the individual results, the impact of each of the effects were always statistically significant. The visualization of the effects show that while relaxation timing had a lesser effect, possibly due to only testing a 0% and 25% case due to an observed improvement of turning around that relaxation delay, stiffness and percent delay had about the same magnitude influence on the turning rate across the span of tested values. In addition, the interactions between contraction delay and stiffness and between relaxation delay and stiffness both were found to be statistically significant. There was not enough data to evaluate the effect of contraction delay and relaxation delay, since relaxation delay was only assessed at 50% contraction delay. This existed because a stiffened inside quadrant marginal flap increased the turning amount induced from contraction and relaxation delay. It should be noted that while stiffness control of the flaps augmented turning, the profile of the graded turning showed that the non-stiffened case had a nearly linear response to contraction delay while the stiffened cases exhibited a nearly constant turning rate relative to contraction delay. It can be recommended for vehicle design that stiffness only be used for strong turning, while graded turns would benefit in the breadth of the control space and reduced energy consumption from an equal stiffness marginal flap.

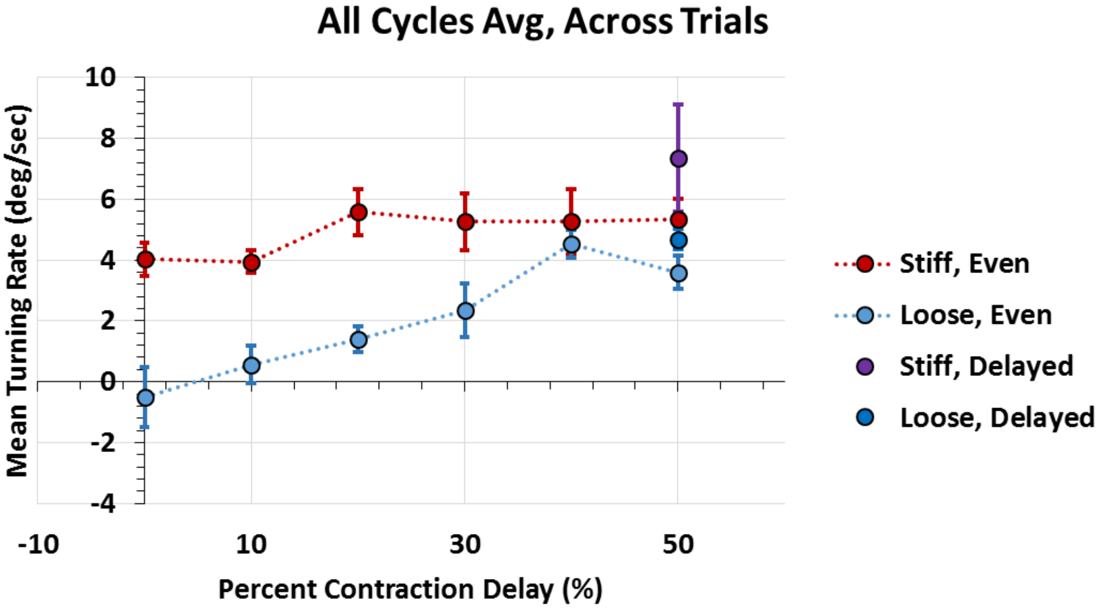

Figure 45 – Turning rate across contraction delay, relaxation delay, and marginal flap stiffness. Data represents average of 20 trials, each values of average turning rate across four turning cycles.

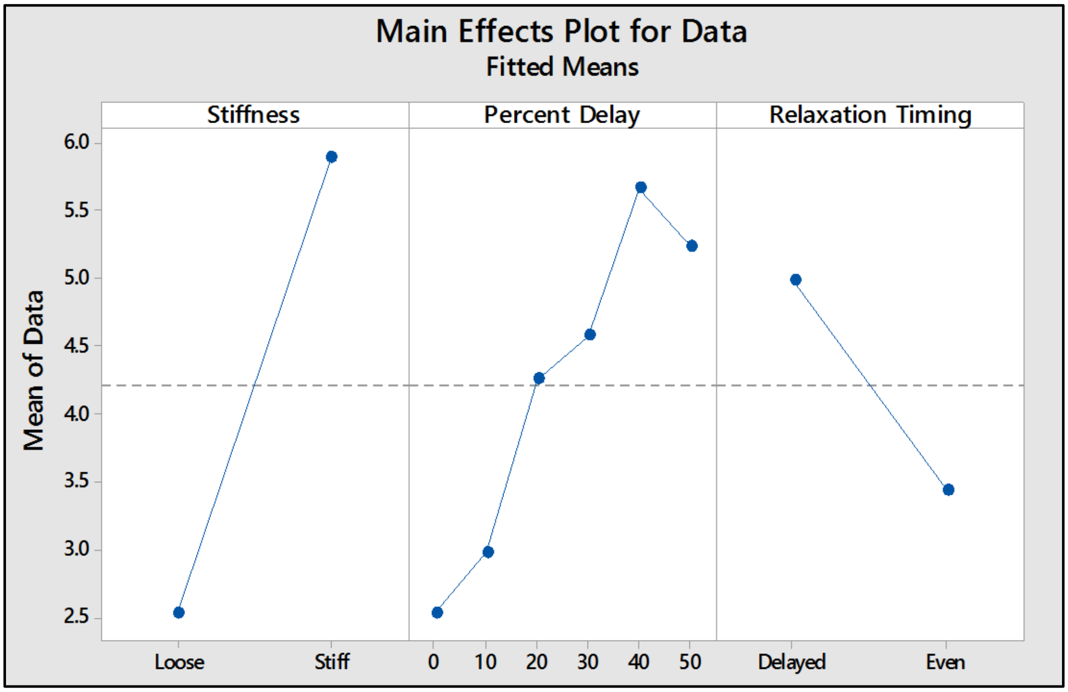

Figure 46 – Primary effects of stiffness, contraction percent delay, and relaxation percent delay on the magnitude of the turning rate.

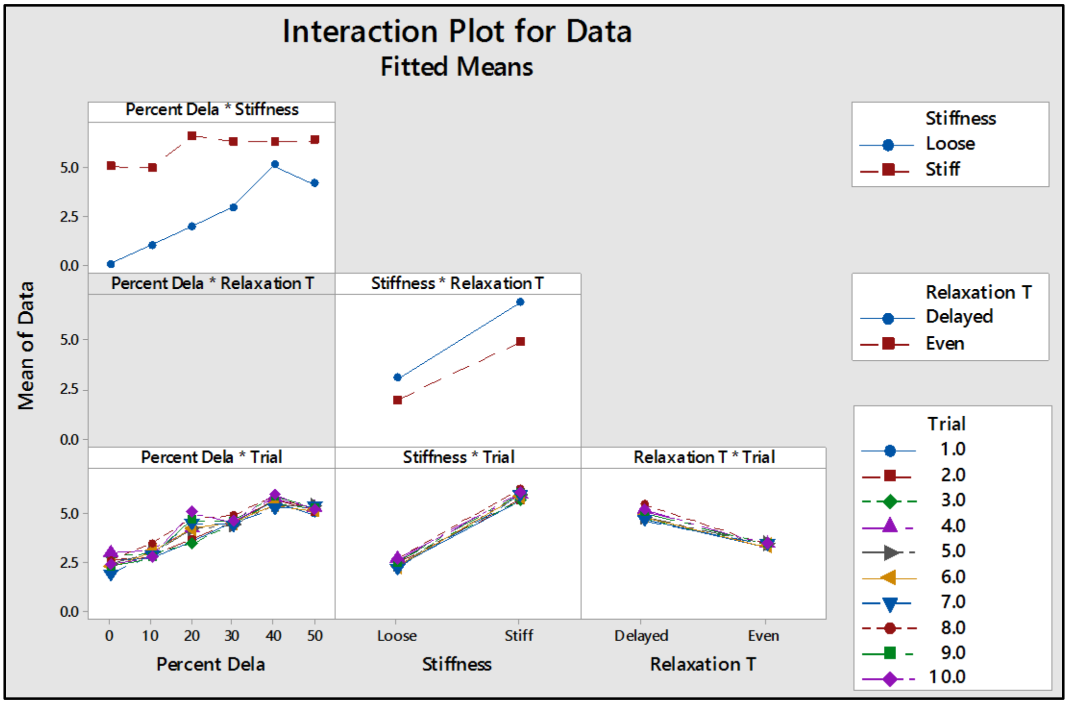

Figure 47 – Interaction effects between stiffness, contraction percent delay, and relaxation percent delay on the magnitude of the turning rate. Trial was also included to isolate the effects of data collection methods on results, which was found to be not influential on the significance of the factor effects on the data.

One interesting result uncovered from this study was that, when compared to other animals in nature, Cyro 3 and the rowing jellyfish data from the *Aurelia* study were found to turn with a turning rate characterized as stiff swimmers (Fish et al., 2018; Gemmell et al., 2015). While this was not intuitive, since jellyfish are the paragon of flexible animals as a pervasive gelatinous zooplankton, the broad surface of the bell combined by an inflexible central column to glide into the turn impeded the ability to turn as with rigid body animals like turtles. This non-intuitive result can also be seen for animals that use a flexible body for propulsion, such as rays and squid, and yet are still impeded by body shape or the mode of locomotion.

3.3.2. Turning PIV Fluid Interaction Analysis

Planar PIV measurements of six cases – 0% contraction delay with loose and stiff margins, and 50% contraction delay with loose and stiff margins as well as even and delayed relaxation – were conducted to find some correlation between fluid interaction and the augmented effects of stiffened bell margins on the internal quadrant and contraction and relaxation timing asymmetry.

The contraction delay introduced increased marginal velocity on both sides of the bell. This introduced a rapid contraction soon after relaxation on the inside of the bell, which interfered with the formation of a stopping vortex under the bell and thus reduced the amount and duration of inflow impingement at the end of relaxation. The inside also experienced mixing that broke up any rotational regions that could have been ejected for momentum flux, causing a streak of mixing fluid without uniform flow or rotation. This streak tended to trap any rotation generated by the margin, inducing a strong backwards flow at the margin that would increase drag along the bell. The outside of the bell experienced the opposite effect, with the delay in contraction prolonging the formation of the stopping vortex and thus increasing the duration and magnitude of impingement on the outside quadrant of the bell during the turn. This longer duration also allowed natural buildup and attenuation of rotation, producing a cleaner wake with discrete ejections of rotational mass. The additional marginal speed aided the size of the vortex and the ejection speed of the starting and stopping vortex pair, reducing marginal co-flow and increasing momentum flux on the outside.

The introduction of stiffness on the inside lobe approached flapping flat plate behavior. Instead of rolling up a strong vortex ring, the stiff flap induced strong co-flow that can cause additional drag on the inside quadrant of the bell. This also fought the formation of any inflow during relaxation, reducing impingement inflow on the underside of the inside quadrant of the bell. This flat plate effect also disrupted the flow on the inside quadrant, breaking up any rotational flow and creating a streak of mixing low velocity fluid that did not appreciably impart a momentum flux due to induced flow or mass ejection. During relaxation, any formation of a stopping vortex leaked into the mixing streak early in the relaxation portion of the cycle, further reducing impingement and any possible mass to eject for momentum flux. The starting vortex stayed proximal to the margin of the bell during contraction, failing to separate before dissipating in the mixing streak and being obliterated by the flat plate during relaxation. However, for the loose outside margin the vortices successfully formed and ejected one third to one half of a bell diameter before naturally dissipating, indicating successful momentum flux as stated before via both impingement from induced flow and ejection of the rotational mass. It should be stated that the loose bell margin cases, while able to turn with a contraction delay, typically had more forward translation during the turns than the stiff margin cases.

Asymmetry in the relaxation of the inner and outer quadrants of the bell provided an additional boost to the interacting fluid dynamics. The stopping vortex induced by the flexible outer bell quadrant was increased in size and strength, while the flow on the inside quadrant was almost entirely backwards on the robot. This increased impingement duration and magnitude on the outside while nearly eliminating impingement on the inside quadrant. The additional marginal tip velocity of the outside during refilling, followed by a period of no motion, increased the size and strength of the vortex rotation and formed the rotational regions sooner than the even relaxation cases.

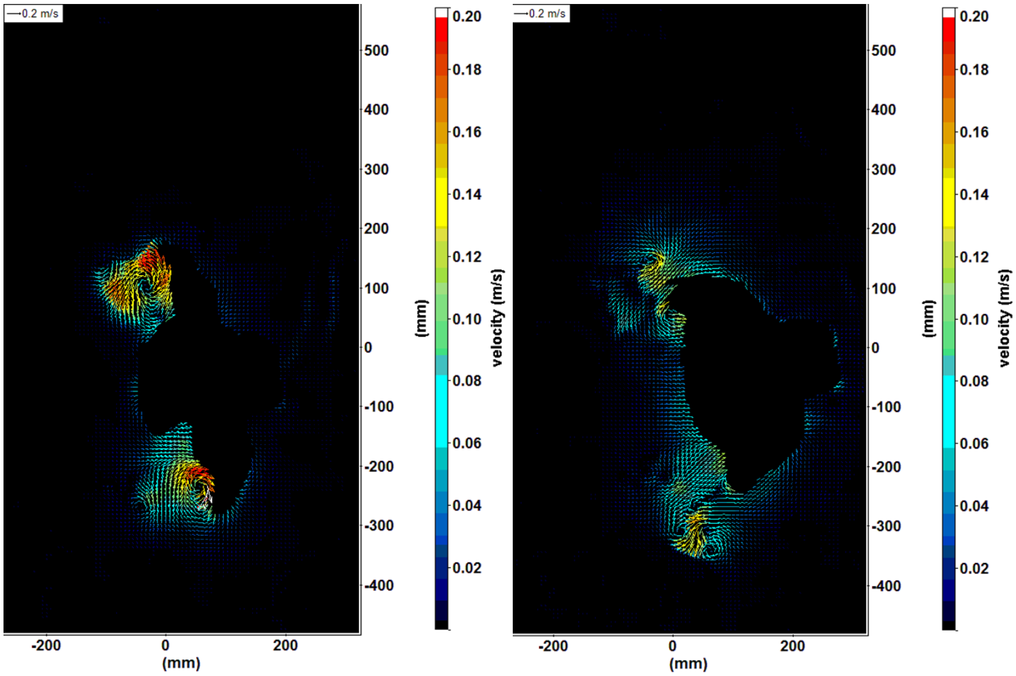

Figure 48 – Velocity field of Cyro 3 during symmetric contraction timing, symmetric relaxation timing, and symmetric marginal flap stiffness. Images show end of first cycle at fully relaxed (left) and full contraction of the second cycle (right).

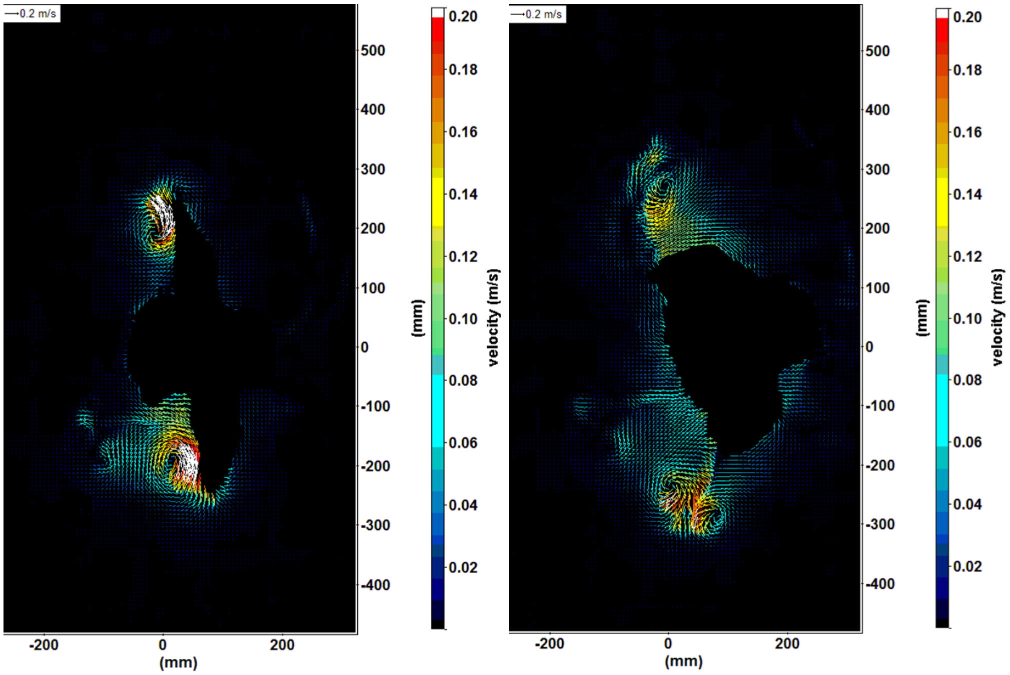

Figure 49 – Velocity field of Cyro 3 during symmetric contraction timing, symmetric relaxation timing, and a stiffened internal quadrant marginal flap. Images show end of first cycle at fully relaxed (left) and full contraction of the second cycle (right).

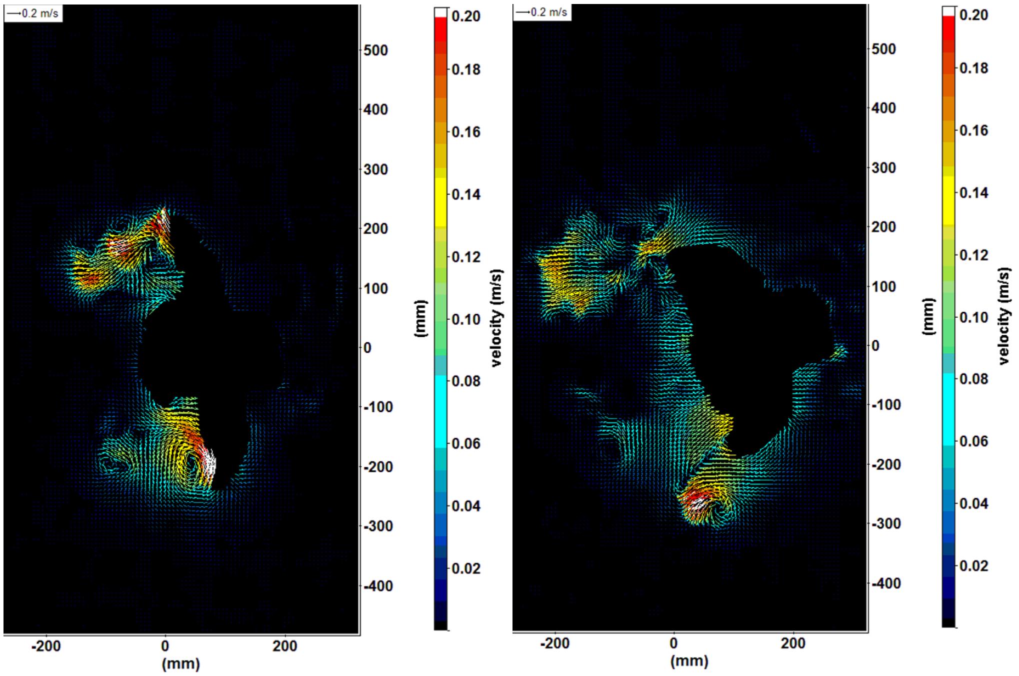

Figure 50 – Velocity field of Cyro 3 during asymmetric contraction timing (50% delay), symmetric relaxation timing, and symmetric marginal flap stiffness. Images show end of first cycle at fully relaxed (left) and full contraction of the second cycle (right).

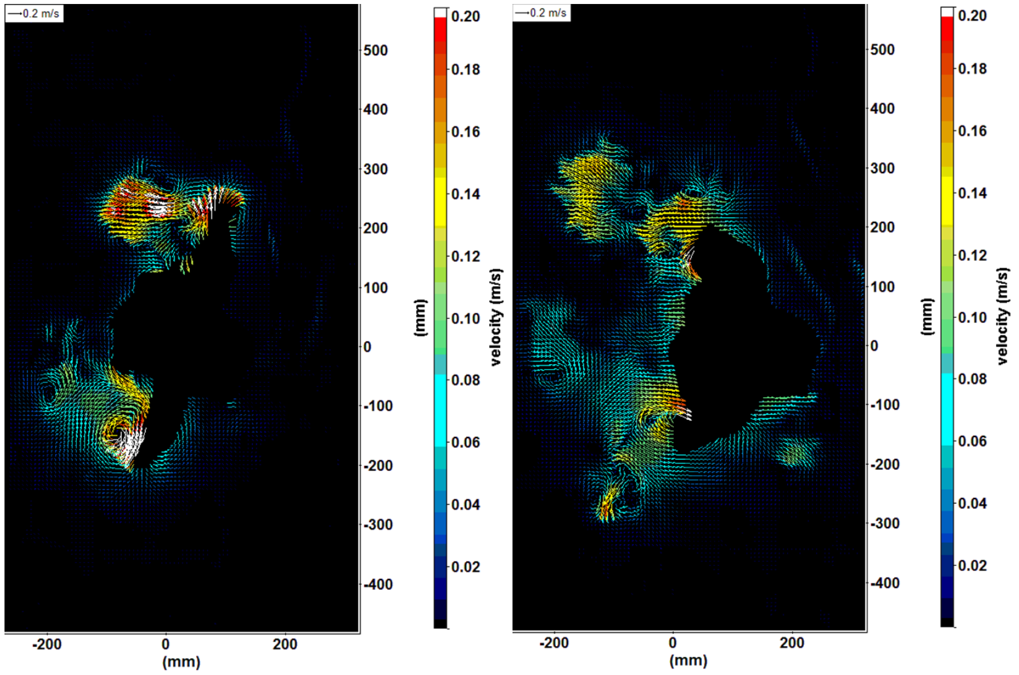

Figure 51 – Velocity field of Cyro 3 during asymmetric contraction timing (50% delay), asymmetric relaxation timing (25% delay), and symmetric marginal flap stiffness. Images show end of first cycle at fully relaxed (left) and full contraction of the second cycle (right).

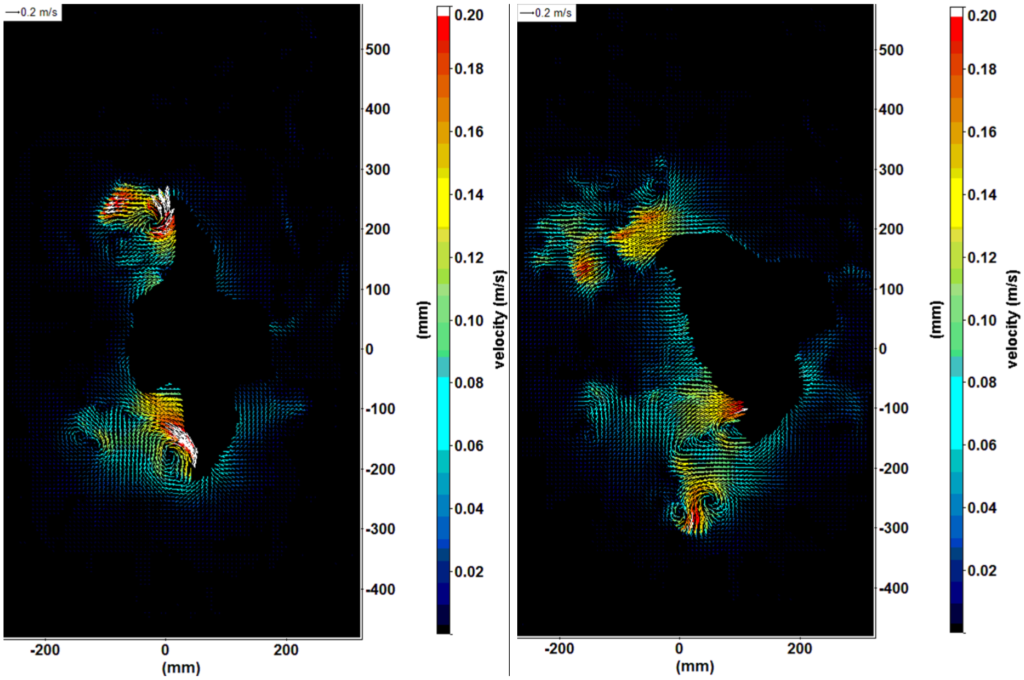

Figure 52 – Velocity field of Cyro 3 during asymmetric contraction timing (50% delay), symmetric relaxation timing, and a stiffened internal quadrant marginal flap. Images show end of first cycle at fully relaxed (left) and full contraction of the second cycle (right).

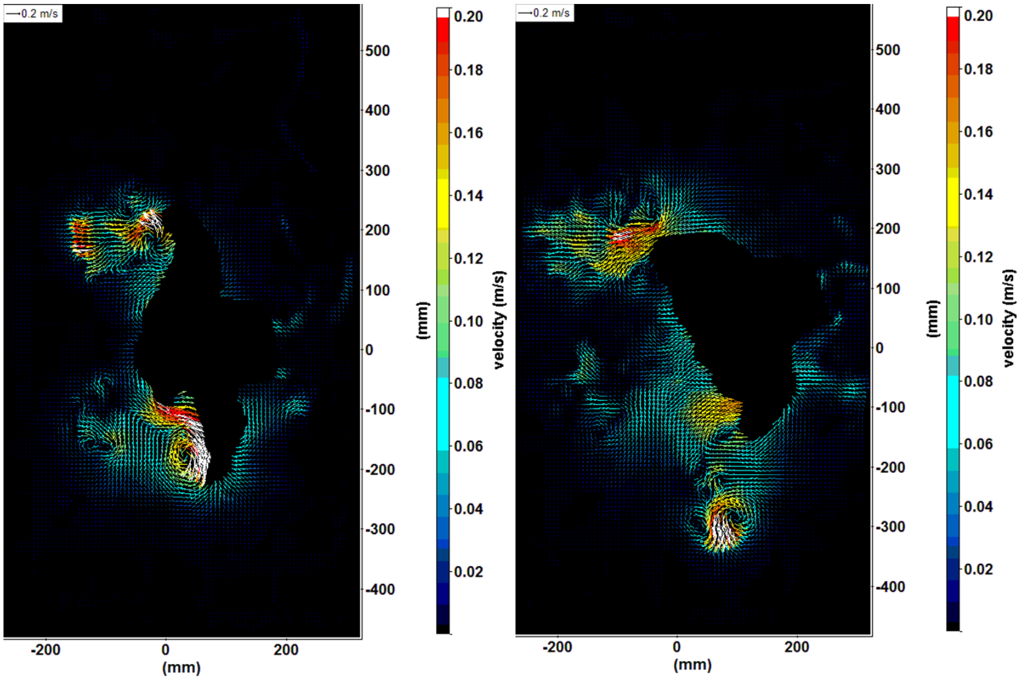

Figure 53 – Velocity field of Cyro 3 during asymmetric contraction timing (50% delay), asymmetric relaxation timing (25% delay), and a stiffened internal quadrant marginal flap. Images show end of first cycle at fully relaxed (left) and full contraction of the second cycle (right).

These fluid phenomena represented two primary forms of momentum flux to produce thrust, the impingement under the bell and the momentum ejected from the bell. The flow field under the bell during the first two cycles was captured, with varying distances depending on blocked views from masking of the robot body. In order to capture the most of the flow field for the first two cycles, a 4cm downstream transect from the underside of the bell margin tips was used for all data. The flow directed upward to impinge on the bell towards the proximal portion of the bell, then the vortex ring and co-flow around the bell directed fluid backwards towards the marginal tips. A proxy measurement of moment on the body, the velocity of the impinging fluid multiplied by the normalized bell radius, was taken across the underside of the bell, averaged for each side, and then added to find the total moment contribution. It can be seen that the delayed relaxation augmented the moment from impingement, while the even relaxation cases were consistently lower in value. The loose straight swimming had a large deviation from the expectation of no moment, but it was observed that most gaits stabilized during cycle three, including any angular motion reduced during straight swimming cycle three, and both relaxation cases were prior to cycle 3. This can be seen in how the 0% cases trended to lower values in the second cycle, while the delayed turning gaits trended to higher values and the even turning cases trended to near zero impingement effect. This showed that impingement was a primary factor for delayed relaxation impacting the turning amount, and could be the factor that boosted the turning rate even further for each case.

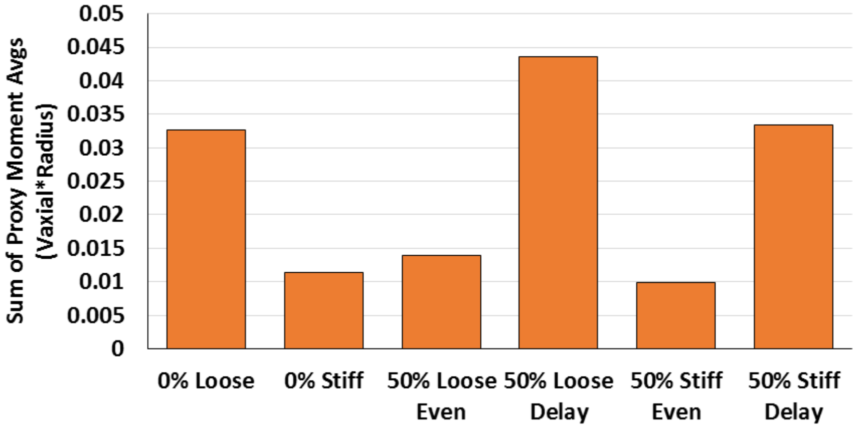

Figure 54 – Proxy moment from impingement under the bell of Cyro 3 during varied gaits, averaged over Cycle 1 and 2. Percentage represents turning amount, stiff and loose represent the flexibility of the inner marginal flap, and even or delay represents the symmetry of the relaxation.

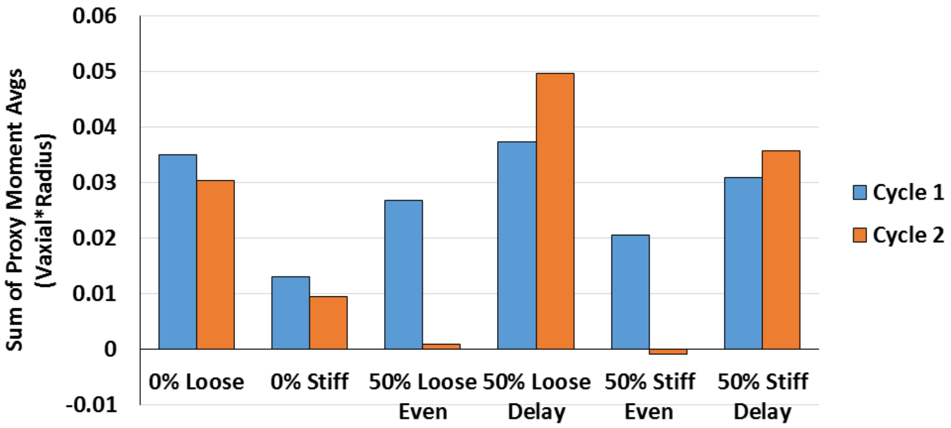

Figure 55 – Proxy moment from impingement under the bell of Cyro 3 during varied gaits, separated between Cycle 1 and 2. Percentage represents turning amount, stiff and loose represent the flexibility of the inner marginal flap, and even or delay represents the symmetry of the relaxation.

The momentum flux produced from the vortex rings had three primary components, the vorticity magnitude, entrainment diameter, and ejection speed. The maximum vorticity on each side in the starting vortex when the outside ejected the stopping and starting vortex was found for cycle 2 and 3. These were averaged on each side, and the difference found between inside and outside vorticity. The result was a large difference for any case not intended to swim straight, with once again the delayed relaxation boosting the vorticity difference relative to the related even relaxation cases. The stiff 0% case produced a large portion of vorticity difference, similar to the loose even turning case, which was similar in proportion to the amount of turning produced during the kinematic tracking.

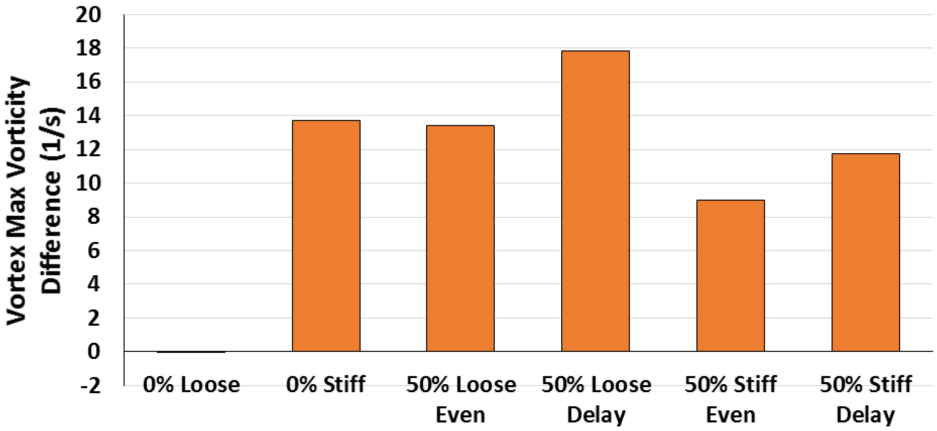

Figure 56 – Difference between vorticity of each side during varied gaits. Values represent difference of vorticity averages for each side over second and third cycles for each gait.

With the peak vorticity in each starting vortex, the vortex size was estimated with boundary contours defined as 20% of the peak vorticity for each side for each maneuver. A circular bound was drawn manually over the threshold regions, and the area of the resulting circle was recorded. It can be seen that the loose case once again exhibited differential vortex sizes. The loose even turning gait had a larger vortex on the inside lobe of the turn, and while turning was better with a delayed relaxation the vortex size was maximum for the stiff even turning gait.

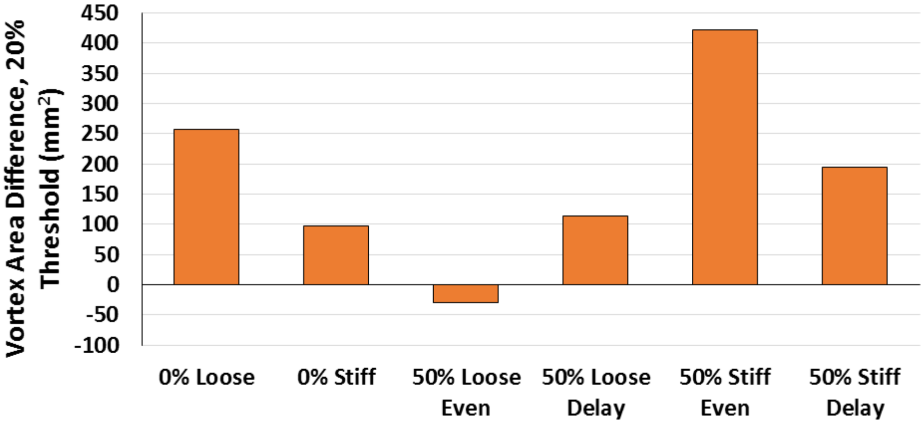

Figure 57 – Difference between vortex area of each side during varied gaits. Values represent difference of vorticity area averages for each side over second and third cycles for each gait, with a 20% peak threshold for vortex boundary.

In order to create another proxy for entrained energy, the vortex area was multiplied by the vortex peak vorticity and the difference of the mean values between the second and third cycle for each side was found. The high size differential caused the straight loose swimming case to still obtain a differential rotational energy volume on each side, but the stiff 0% and other turning cases still showed an increased differential result. The size difference also caused the stiff even case to exhibit higher results, with the stiff delayed case exhibiting a lower value due to smaller size but still higher vorticity difference. In order to get a complete representation of the flow results that cause the turning result seen in the kinematic tracking, the ejection speed and the transient vortex size and vorticity magnitude should be tracked. This can be combined with existing methods for reconstructing asymmetric vortex rings and previous analysis methods for axisymmetric vortex ring thrust production.

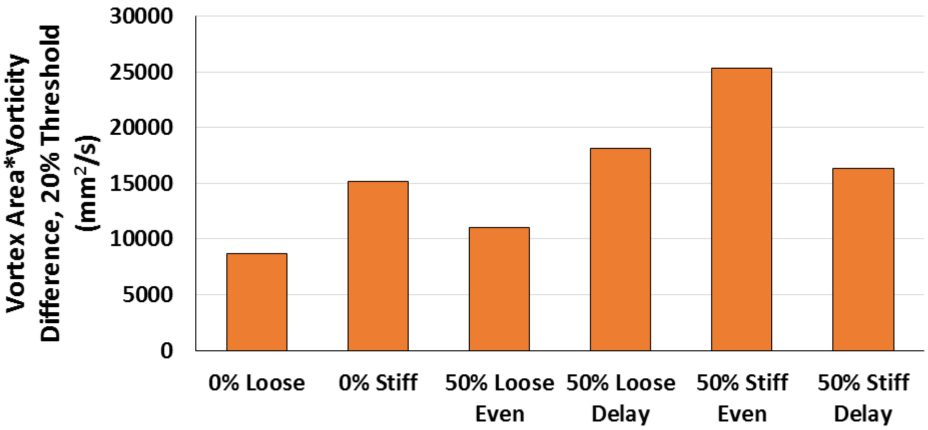

Figure 58 – Difference between product of vortex peak vorticity and area of each side during varied gaits. Values represent difference of vortex area averages for each side multiplied by vortex peak vorticity averages over second and third cycles for each gait, with a 20% peak threshold for vortex boundary.

3.4. *Conclusion*

Throughout the development of the Cyro 3 robot platform, the knowledge gathered on jellyfish locomotion in our lab and the scientific community as a whole has been culminated into a comprehensive, fully capable jellyfish robot with the degrees of freedom expected for bio-inspired propulsion and mimicry for inquiries into biological locomotion and fluid dynamics. The study of the fluid interactions and resultant turning kinematics from decoupled and coupled effects of stiffened inner lobes and asymmetric contraction timing has exposed the fact that these individual factors contribute significantly to turning performance for rowing jellyfish. In addition, the ability to further boost turning with asymmetric relaxation timing was seen to significantly exist, although to a lesser degree than the former two factors that were clearly observable in nature. These results of muscular and cognitive effort in relation to propulsive benefit clearly answer that marginal flap stiffness is not needed but worth the additional cost for benefit, asymmetric contraction allows a tunable control space for graded turning proportional to muscular effort in a coordinated maneuver, and relaxation does significantly impact rowing propulsion and directional control.

Additional studies on these phenomena would further elucidate the isolated and coupled effects of material and kinematic asymmetry. Pressure measurements under the bell to back out torque from impingement, as well as on top of the bell to determine asymmetric co-flow and thus drag, would help fully characterize the flow field around rowing jellyfish during turning. More trials would help smooth the trends discovered in this study, since near unstable systems introduce variability in turning performance due to physical and environmental factors. These additional trials could include graded stiffness and relaxation timing studies, since these could expose a continuous or bi-modal trend of the impact of these factors on performance. Partial stiffening, or a transient stiffness change during contraction and relaxation, could be present in natural swimming to reduce metabolic effort and induce a more efficient fluid interaction to maximize torque. In addition, the previous studies have looked at radially bound fluid rotation in asymmetric rings via 3D PIV, while this study has indicated the possibility of vortex tubes and later forming weak rings due to the different positions and vorticity magnitudes on each side of the ring. This would necessitate consideration of out of plane motion, since synchronizing out of plane quadrants was seen to produce strong turning while a cascading contraction around the bell did not produce reliable turning. Both of these are neurologically possible, but difficult to discern in video footage of rowing jellyfish and thus equally possible in natural behavior.

4. Biological research into the anatomy and biomechanics of Siphonophores

4.1. *Introduction*

Jellyfish locomotion has been explored in our research group in the past due to their relative structural, neural, and muscular simplicity while still achieving continuous swimming, operational proficiency in terms of low energetic cost and specialized feeding, and significant ecological diversity and biomass (Dabiri et al., 2007; Dabiri et al., 2010; Gemmell et al., 2013; Satterlie, 2011). However, this low energetic cost and simplicity sacrifices the degree of maneuverability and controllability typically seen in larger, more complex systems. In order to explore similar systems with related features and design elegance while exhibiting higher levels of control and locomotory proficiency, the broad phylum of Cnidaria can be explored.

One closely related yet unique part of Cnidaria is the order Siphonophora, which consists of colonial organisms that achieve higher levels of complexity through redundant and specialized collaborative units known as zooids (Dunn, 2009). One particular body form present within siphonophores is known as Physonects, which utilize this redundant specialized colonial architecture to generate thrust along an axial central stem. The thrusting units, known as nectophores, produce a directed jet of water that induces thrust vectors onto the body at specific times and positions. By the organization of these thrust producing bodies spatially, temporally, and by thrust magnitude, the potential space of achievable and controllable maneuvers is greatly increased over that of single jetting or rowing units utilized by jellyfish.

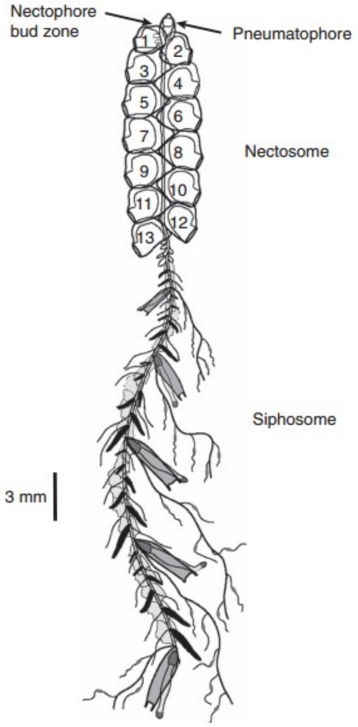

Figure 59 - Diagram of a typical *Nanomia* sp. specimen with its functional units labeled. The pneumatophore is a gas filled sac used for buoyancy control, the nectosome consists of nectophores that create propulsive thrust by jetting, and the siphosome is used for feeding and reproduction. Image courtesy of Jack Costello.

The physonect siphonophores *Nanomia* have been observed and documented in literature on the basis of their general anatomy and proficiency of locomotion and maneuverability (Costello et al., 2015; Mackie, 1964). *Nanomia* includes two species, but since the field is starting to believe that they are not distinct species this research will consider them as one slightly diverse classification (Barham, 1963). This collection of features and interest in the locomotive capabilities of the species made it an ideal candidate for a basis species of bio-inspired design and research. However, quantitative measurements of their anatomy and specific locomotion capabilities have not been explored in sufficient detail. The largest study by Mackie broadly explored the capabilities of *Nanomia*, particularly in their locomotive modes, ability to direct thrust using a muscular velum nozzle, and overall organization based on zooids and currently understood neural structures (Mackie, 1964). While some additional neural studies have been completed as analysis methods have advanced, the details of control and anatomy are still greatly unexplored (Grimmelikhuijzen et al., 1986; Mackie, 1973; Mackie, 1978). Costello et. al.

released a study on the anatomy-based thrust production for maneuvering, but the maneuvers explored were either static cases that did not represent the dynamic capabilities that make physonect siphonophores unique or axial cases that exhibited limited further knowledge over the study by Mackie (Costello et al., 2015). Therefore, to correctly establish a baseline quantitative and more advanced qualitative data set on the behavior of *Nanomia*, this chapter details a broad study of the detailed nectophore anatomy, kinematics of the velum and contraction cycle over time, and the colony-wide performance characteristics during axial swimming in two cycle modes. Since the physonect siphonophores form serial chains of nectophores in a region consisting only of nectophores, known as the nectosome, the length-based and thus nectophore count-based performance variation is of great interest for determining the performance variation over the life cycle of siphonophores and possible size scales that may be implemented on multi-jet bio-inspired robots.

4.2. ***Video Analysis for Kinematics and Local Morphology***

The design of a new biologically inspired system requires the identification of key morphological and functional features, characterization of the impact of each feature on the desired performance parameters, and the reduction of order from the animal's fully featured system with interacting complex functions to the robot's simplified but still fully functional electromechanical design. The identified features of interest for the propulsion of the animal, as with the organization of the physonect body plan, is focused on the individual nectophores. The formation of a fluid jet requires a displacement of volume, a controlled or passive outlet diameter, and a controlled or passive outlet direction. Therefore, the data collected from videos of biological nectophores in natural motion focused on these three primary parameters, as well as the resultant whole-colony kinematics. Videos of a siphonophore swimming straight in a synchronous escape response were obtained by Dr. Jack Costello, including a single video of a shadowgraph revealing the cross section of the nectophore for forward escape swimming, one video of a shadowgraph revealing the cross section of the nectophore for reverse swimming in an escape response, one video of a collated light imaging showing the colony plane cross section at higher magnification, and one video of a seeded tank with a laser light illuminating the center plane of a specimen as it swims forward in the tank. These videos were collected of specimens starting at rest in a fully relaxed state, and a rod was touched to the siphosome for forward swimming and the anterior end of the nectosome for reverse swimming to induce escape behavior from the tactile feedback pathways for synchronous escape responses. Three shadowgraph videos of non-axial maneuvers illuminated to show the cross section in the plane of the colony were also provided, including one video of a specimen jetting from its anterior-most nectophore for a static-body turn, and two videos of a four-nectophore specimen asynchronously jetting for planar motion. Finally, two backlit collated light videos looking normal to the symmetric plane of the body to obtain a frontal view of the nectophores were provided, with one video showing a single-nectophore static body turn and one video showing synchronous straight swimming. The body plane normal video of the single-nectophore turn, seeded and laser-illuminated video, and two symmetric plane normal videos were provided with single frame images of scale bars for the videos. Since other shadowgraph videos appeared to be the same specimen, but may have been taken at slightly different magnifications, the resting ostium diameter of the second nectophore (numbered by convention from anterior to posterior) was used to normalize and rescale the measurements back to the known scale videos' second nectophore ostium diameter. The ostium diameter of nectophore two was chosen since it is always in the frame of the video, it is always being a tracked feature for all analyses, and it is invariant to body rotations due to a cylindrical shape. Many of these videos were provided in the supplementary information in a published paper by Dr. Costello and his colleagues, and the remaining videos were shared privately between our group, Dr. Costello, and Dr. Brad Gemmell (Costello et al., 2015).

Video analysis of key features was completed using pixel measurements of key features in a single frame, manually selected points at fixed intervals throughout the video and recorded using a custom MATLAB script (keyframing), automatically tracked point locations using Adobe After Effects motion tracking tools, and the Mocha AE contour tracking for area measurements. Image measurements of stills from the videos, as well as validation and combination with database and published images and sketches, provided a baseline morphology scaling that allowed a 3D model to be created for the robot nectophore designs. Video keyframing tracking provided single frame and coarse temporal measurements of data that is difficult to track via automated methods, once again informing for more design-based characterizations. The video contour tracking, combined with the data from previous methods, provides a finer data set of full colony and local nectophore morphological changes during swimming.

High speed shadowgraph videos of a *Nanomia* specimen were adjusted to improve contrast and detail after collection in Adobe Premiere. The analysis for each required data set is detailed below. Data that was not available due to the *Nanomia* specimen extending outside the viewing area was completed with static measurements of the specimen from additional videos. The compiled data for nectophore and velum metrics were averaged for nectophore 4 through 6 and interpolated using a cubic spline constrained for periodic form over the contraction cycle.

The duration of the contraction and relaxation phases were assumed to be equal on average, and were not significantly different between synchronous and asynchronous gaits (Mackie, 1964). This assumption was verified by collecting contraction times and relaxation times from turning, forward, and reverse shadowgraph videos. Timing was found using position data of the point where the nectosac muscle pulls in to contract, as well as the final measured volume data. The data and the derivative was plotted, and the point where the slope of the data or the sign of the derivative changed was seen as when contraction and relaxation started and ended. The ratio between the duration of the contraction and relaxation phases was found for the single nectophore static turn video, averaging three contractions and two relaxations, to be 0.624:1 for a mean contraction time of 0.1272 seconds and a mean relaxation time of 0.2038 seconds. However, the relaxation exhibited a clear reduction of relaxation rate at a point near the equal ratio relaxation time. This could be due to the stored elastic energy released for relaxation reducing in magnitude, where a longer duration relaxation would return to the passive relaxed state while consecutive contractions relaxed to a sub-peak volume in part due to the reduced contraction magnitude for consecutive cycles. The volume at the equal timing point was 92.6% and 95.7% of the starting volume, and 96.1% and 94.8% of the ending volume of the cycle, respectfully for the first and second cycles. Therefore, this equal timing volume was within 10% of the starting volume, and nearly within 5% of the peak relaxation volume. Therefore, the assumption of equal contraction and relaxation time was reasonable, and used as a reasonable simplifying assumption in future calculations.

The excluded nectophores were not a component of the average due to deviating behavior attributed to immaturity (nectophores 1-3) or growth early in the colony's formation (nectophores 7-9). Nectosome and siphosome length were assumed to be approximately equal during swimming due to siphosomal contraction. While siphosome length varies widely from specimen to specimen, several images of specimens were measured and the assumption of a 1:1 length between nectosome and siphosome was a reasonable middle ground between variation and thus a reasonable simplifying assumption. Future data collection of contraction times and siphosome to nectosome length, to find the mean and variation of length ratios in different specimens from different growth zones, would be the best route for finding a true population value without simplifying assumptions of equality in values.

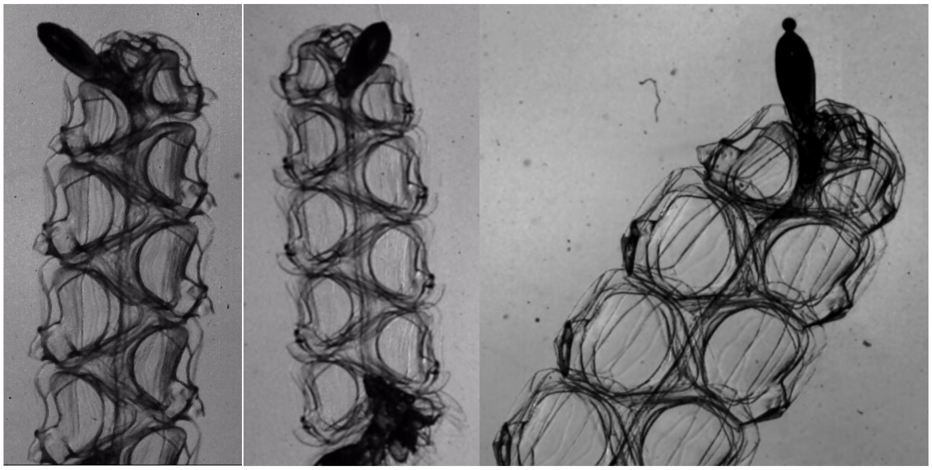

Figure 60 - Shadowgraph videos of *Nanomia* during forward acceleration (left), reverse acceleration (middle), and static turning (right). Images courtesy of Jack Costello.

4.2.1. Body Kinematics

The body velocity and orientation measurements were collected in Adobe After Effects by motion tracking the dark intersection points of the nectophore axial wings' border shadows and the stem. These motion tracks were compiled and low pass filtered with a cutoff at 100 Hz to compensate for sharp variations in the mean as tracking points entered and exited the frame.

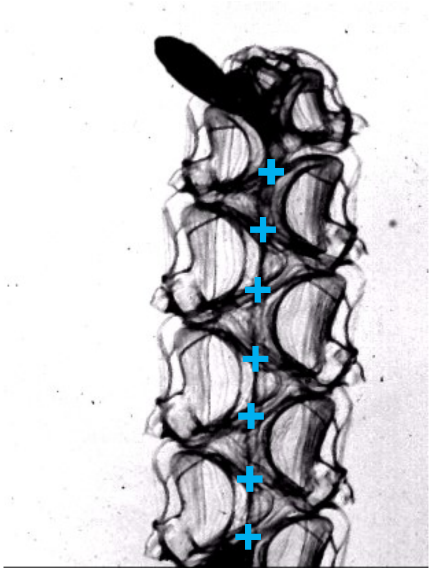

Figure 61 – Tracking points along the nectosome stem axis, spaced roughly evenly at the intersection of the periphery of the axial wings of the nectophores.

4.2.2. Nectophore Volume

The main nectosac's and pre-ostium nectosac chamber's cross sectional areas were contour tracked in Mocha AE, with the automated tracking forming the bulk estimation while manual adjustment was used to fine tune when the tracking failed to resolve points correctly. Manually adjusted points were then interpolated by the software to smooth the track, or the automatic tracking was run between the corrected points until the tracking was back on the correct profile for the entire video. This spline bounded region was converted from a contour mask to separately colored regions in After Effects. Mocha AE does not provide time-varying contour data for sub-pixel reconstruction, so the colored regions allowed for area and corner extraction in MATLAB with the same pixel resolution as the videos. The main nectosac region is approximately an oblate ellipsoid with an arced major axis, so side and top views were used to reconstruct an equivalent straight oblate ellipsoid with one circular cross section. The circular cross section was determined by finding the cross sectional area of the main nectosac region and determining the radius of a circle with equivalent area. The major axis was determined from the nectosac centerline length of a top-down image of a representative *Nanomia cara* nectophore, with the axis length normalized and scaled relative to ostium diameter to account for variation based on nectophore maturity (*Nanomia cara* nectophore). While the axis would slightly shorten during contraction, the endpoints are fixed to the stem and thus the only change in axis length would be from the moving center of area. There is no time-varying top-down view of the nectophore during contraction, so we assume this change is not significant and any attempt to correct for this change may induce comparable or more error relative to error from assuming a constant axis length. The pre-ostium nectosac chamber was determined to be a tapered cylinder, with the end diameters and depth measured directly from the cross sectional area corners. The final formula for volume can be solved as

$$\begin{aligned} \boldsymbol{V_{nect}} &= \frac{4}{3}\pi abc + \frac{\pi}{3}(r_1^2 + r_1 r_2 + r_2^2)h \\ &= \frac{4}{3}\pi \frac{l_{cl}}{2} r^2 + \frac{\pi}{3}\left(\left(\frac{d_{in}}{2}\right)^2 + \left(\frac{d_{in}}{2}\right)\left(\frac{d_{out}}{2}\right) + \left(\frac{d_{out}}{2}\right)^2\right) l_{ost} \\ &= \frac{2}{3} l_{cl} A_{cs} + \frac{\pi}{12}(d_{in}^2 + d_{in} d_{out} + d_{out}^2) l_{ost} \end{aligned}$$

with the variables represented in Figure 62.

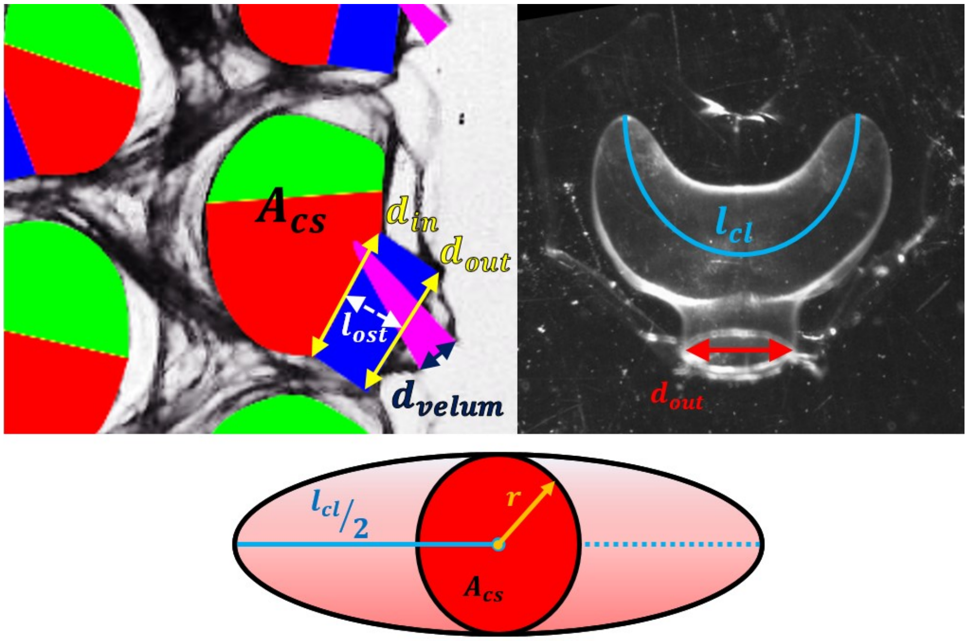

Figure 62 – Composite video and colored regions image from After Effects, with the nectosac cross sectional area and dimensions measurements (top), as well as velar diameter measurement. The bottom ellipsoid shows the constructed volume used to represent the nectosac internal geometry. Top view courtesy of ZIMNES database (Nanomia cara nectophore).

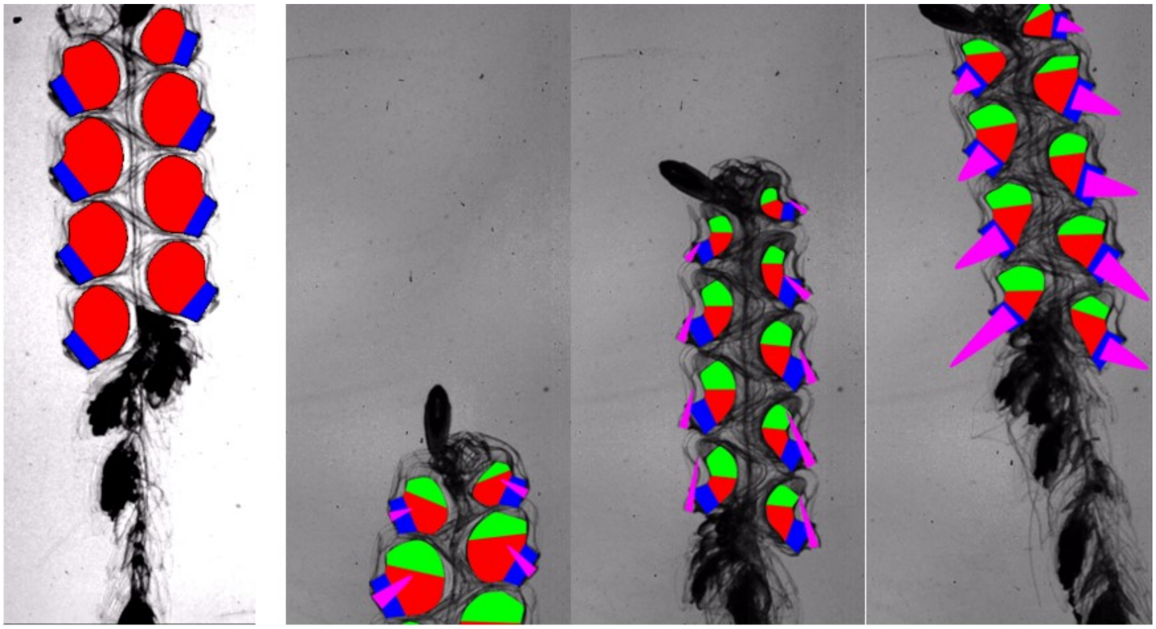

Figure 63 – Left: Initial resting volume for all nectophores from reverse swimming video. Right: Area tracking of *Nanomia* nectosac cross sectional area (green and red, bisected at contraction axis), pre-ostium nectosac chamber cross sectional area (blue), and velar diameter and angle (magenta).

This method opens the question of whether the nectosac wing contributes significant volume to the ejected volume, as well as whether the nectosac deforms in the plane of the ostium opening, subsequently referred to as the ‘front view’ of the nectophore. Frontal views of the nectophores, aligned normal to the symmetric plane of the nectosome, were obtained from Jack Costello and Brad Gemmell, as well as static views from Jackie Sones at UC Davis. These videos were contour tracked in Mocha AE, as were the side views tracked to include the wing and additional main cavity features, and the data was acquired similar to the original footage. To match the scaling of the nectophores, the height of the nectosac main cavity in the side and front views were scaled to match that of the side view. This scaling was then used to adjust the width measurement, which was then multiplied by the area of the nectosac main chamber to get the main chamber volume. Wing volume was taken as starting with a proportion of the measured resting width, determined to be 25.62 percent width per wing, and the projection depth of the wing area was determined as the initial width minus the change in width total at each time instant. This preserves that the inside of the wings are static as they mesh around the stem and other nectophores, while the outside area follows the projection seen from the nectophore front view. These two projected volumes, plus the revolved volume of the ostium as determined above, were combined to estimate the total volume through time from all contraction motions.

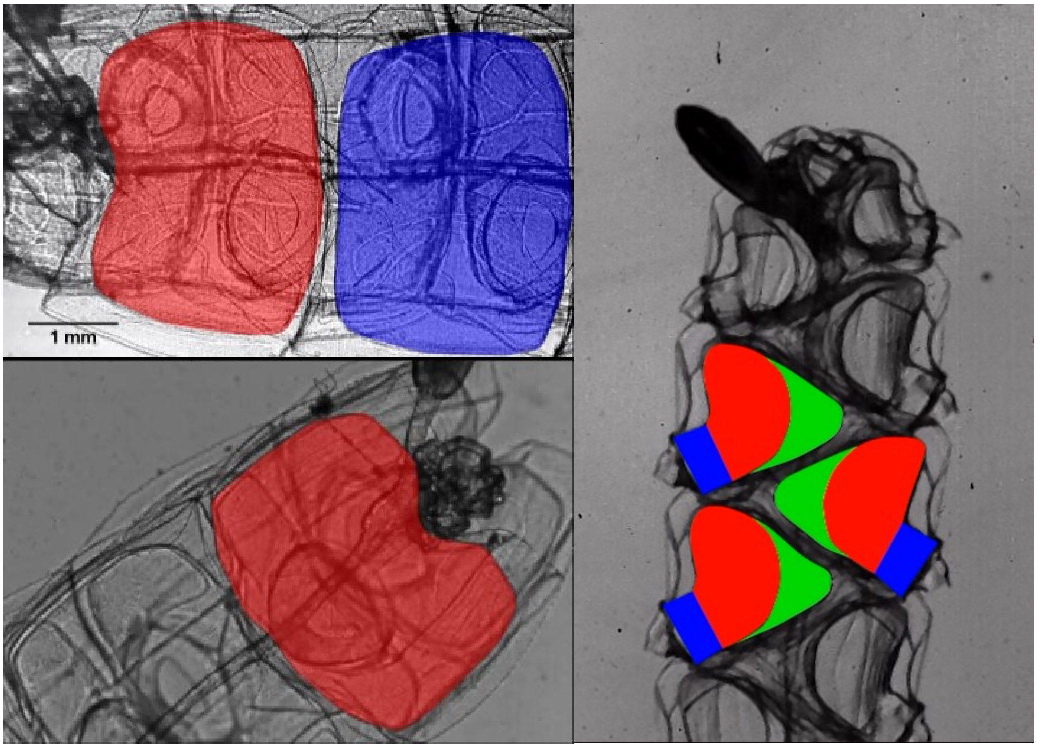

Figure 64 - Updated tracking of the front and side views. Footage views provided courtesy of Brad Gemmell (upper left) and Jack Costello (bottom left and right)

4.2.3. Velum Diameter and Angle

The linear planar projection of the velum opening cannot be tracked via contour tracking used for nectophore volume, and traditional motion tracking in After Effects would have not reliably tracked the velum due to limited image resolution, morphing landmark shapes, and obscuring of the velum during the refilling phase that required human judgement of the final location of the velar tips. Therefore, two methods were used to resolve the velar opening diameter and angle. The first method used a script that stepped from frame to frame at a fixed interval of 5 frames (0.005s in real time) in MATLAB, with the user keyframing the points of the velum upper and lower opening extremes. These points were resolved to find the diameter and angle through time. The stem angle and the ostium opening angle were both tracked the same way, and when combined the angle of the nozzle and ostium relative to each other as well as the stem axis could be calculated.

To automate this process and form consistent data for model development with fine temporal resolution, the contour tracking was used to form a shape that consisted of a linear region, representing the projection of the velar tip opening, and a parabolic region that would represent velar direction and not register on corner detection in MATLAB. The masks were then brought into MATLAB to extract the shape using thresholding on the color channels and the built-in MATLAB corner detection. This provided time-varying data of the points at the upper and lower bounds of the velum opening. This data was iterated through to reject any faulty point values that deviated from previous and following data values. This cleaned data was then used to calculate the velum diameter, as the distance between the two points, and angle, as the angle between a line connecting the points and the normal vector of the colony, for an approximation of jet direction and form. PIV video has shown that the mixing in the nectophore, a short velar region, and an asymmetric nectophore and velar shape causes the true jet direction to deviate from the velum output, but the approximation is appropriate for a physical model without significant three dimensional fluid calculations, new non-traditional modeling of asymmetric jetting systems, and additional measurements.

4.2.4. Axial Swimming and Maneuvering Gait Patterns

The multi-jet control of thrust and torque utilized by *Nanomia* and other physonect siphonophores is a major improvement in potential controllability over single bell propulsion of jetting and rowing jellyfish. Therefore, understanding the jetting patterns used during swimming, in terms of temporal and spatial variation of the jetting propulsion and the resulting effects on colony kinematics, is critical for characterization of the animal's propulsive capabilities as well as the development of the control space possible for an engineered or bio-inspired multi jet vehicle. Mackie had qualitatively described the axial swimming gaits of *Nanomia*, both in terms of synchronous escape swimming and asynchronous general swimming, and Costello had discussed the static turning case with one anterior nectophore firing more normal to the colony axis to induce a pivoting moment on the colony (Costello et al., 2015; Mackie, 1964). However, the unique dynamic maneuverability has been widely ignored for locomotion studies due to difficulty of inducing constant swimming in limited captivity durations, space, and imaging window size and resolution.

For gait analysis of steady-state swimming, frame-by-frame timing measurements of the jet production relative to nectophore position along the chain were collected from a fluorescein dye trail video of a *Nanomia* specimen swimming in open water. In addition, a blackwater diving video of a physonect similar to *Nanomia* was characterized to obtain additional gait data in open water swimming (UnderH20, 2013). The temporal and spatial resolution of the videos were limited due to frame rate and a broad frame to capture full-body locomotion, but relative jetting patterns were resolved and combined with published gait patterns in literature. This timing relative to the intended maneuver, such as steady state forward swimming or varying radii of turning, was tabulated and represented in indexed and gait-dependent notation.

4.2.5. Development of Physical Model Representation

Using the videos provided by Jack Costello, Brad Gemmell, Jackie Sones, and additional views and sketches present in published work, measurements of the morphological landmarks of mature representative *Nanomia* nectophores were collected. These dimensions were normalized to the ostium opening internal diameter, which could be visible in all projections and is expected to be circular in shape and easy to identify. An initial 3D model was formed from these projections, which is critical for the consideration of true internal volume and the biomimetic design of a flexible jetting body. The axial wings allow the nectophore to interlock along the stem, and while the nectosome is comprised of flexible elements the combination of interlocking zooids and contractile tension in the stem during swimming leads to a rigid constraint on the nectosome (Mackie, 1986). Some slight flexion has been seen during turning maneuvers, and while significant flexion in the stem has been observed during extreme turning maneuvers, it cannot be ruled out that the flexion is out of plane of the serial chain or an unpowered flexion, and hence not constrained by nectophore form. Additional footage with three dimensional tracking at multiple magnifications is needed to further establish the chain flexibility and the movement capabilities out of plane.

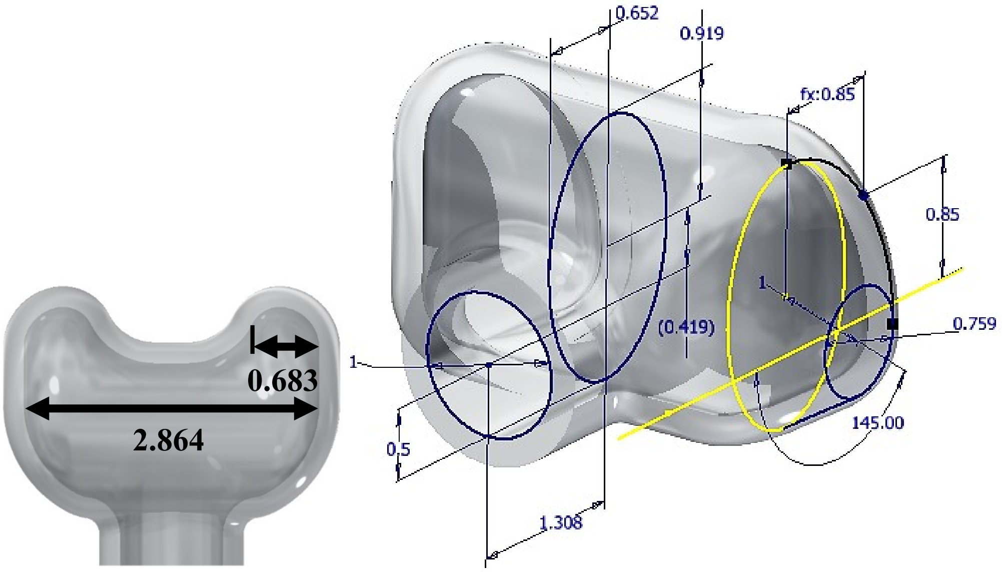

Figure 65 – Diagram of the measured dimensions and resulting values from multiple views across multiple sources. Dimensions are normalized to ostium diameter.

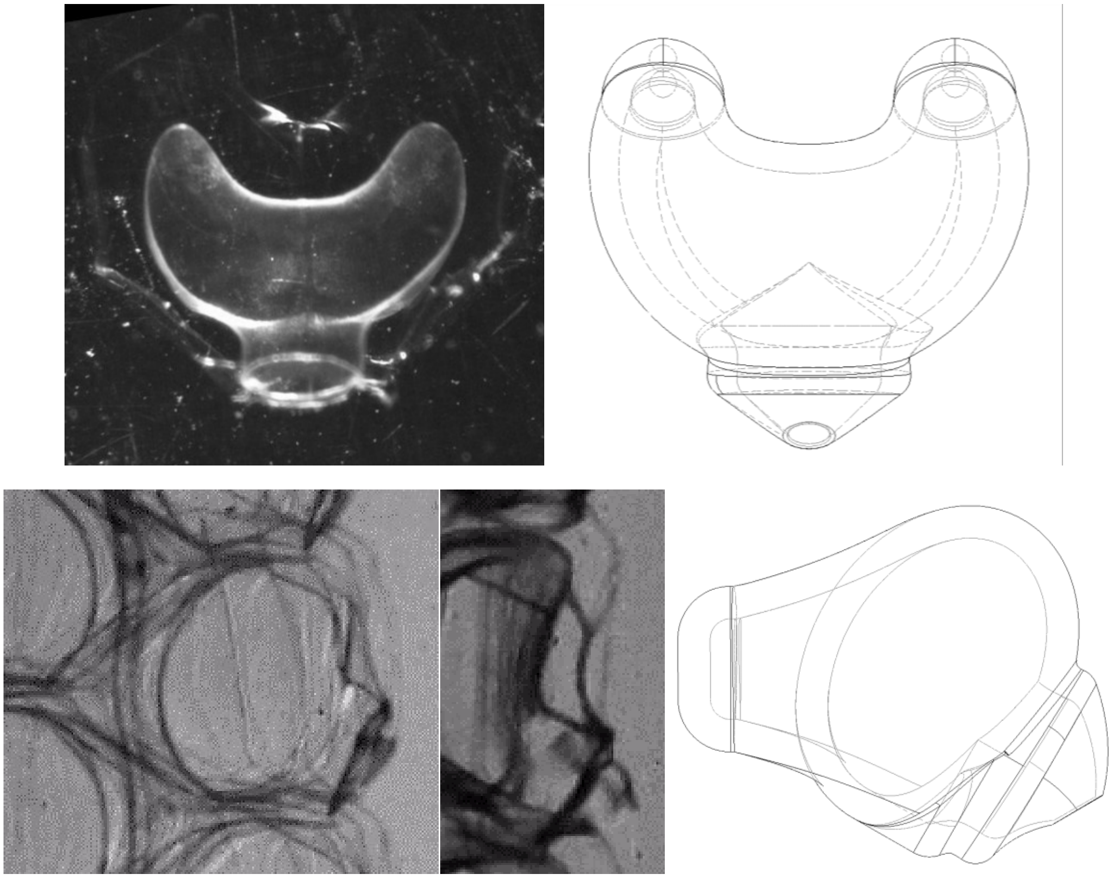

Figure 66 – Initial nectophore model design with projected views. Top view courtesy of ZIMNES database (*Nanomia cara* nectophore). Side views courtesy of videos from Jack Costello.

However, upon further inspection with additional sketches from Totton, review of the videos where the specimen rotates out of plane, and repeated inspections of the original source material, the original model fell under scrutiny. From the top views of nectophores available the rounding around the nectosac apical wings was more exaggerated in the model than in the specimen nectophores. In addition the frontal view of the model was more elliptical than the correct rounded rectangular projection. This rounding is hard to resolve from the video views of only side projections, and the amount of rounding and planar flattening has been previously documented as part of the differences between species of supposedly different specimens (Totton, 1956). As mentioned before, these split classifications are likely the same actual species and rounding of the nectosac may be part of the morphological variation (Barham, 1963). These observed features were reconsidered and included in a revised design. This served as the framework for the final model for the design of future biomimetic jetting bodies. This brings into question the bent ellipsoid model used for approximation of the internal volume, which agreed with the previous model that is now considered inaccurate. It can be considered that the front section of the cavity still deforms in cross section, any corner features do not deform and hence are out of the changing volume of water, and the axial wings do not contribute a large amount of biological volume change as with the ellipsoidal approximation. Therefore, the ellipsoidal approximation can be considered appropriate for an initial approximation without reliable data on 3D deformation profiles through time. In addition, the biological form would be more organically rounded and continuous than the closest design approximation using existing geometric tools, so a rounded approximate is less inaccurate than our 3D model would lead one to expect. Although views of the front during contraction were provided and used in conjunction with the side views to form a more comprehensive model, calculating the true change in volume would require additional concurrent views during swimming of specific specimens, as well as a study on a deformable model beyond the capabilities of the software in which this CAD model was developed.

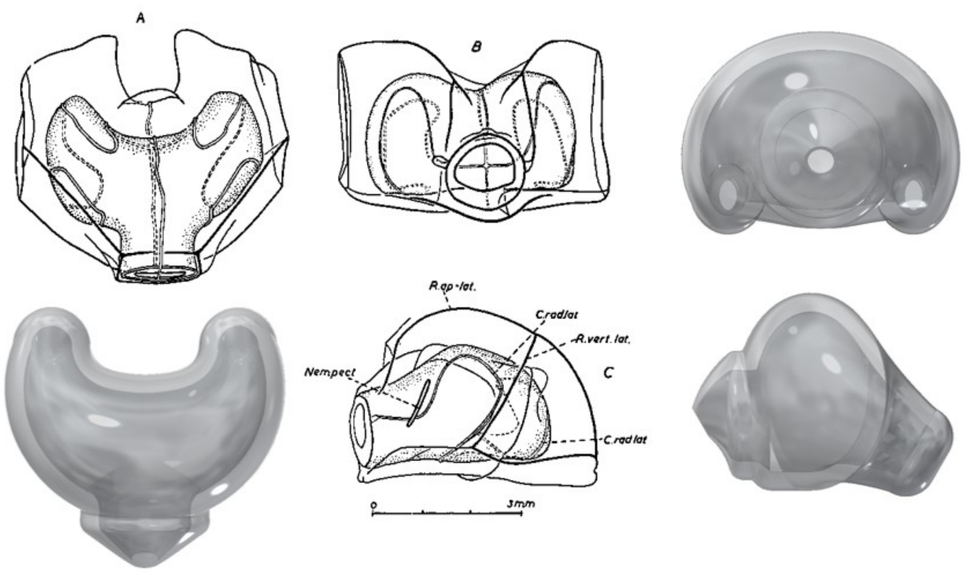

Figure 67 – Proof of form inaccuracies for projection. Top view (left) appears accurate, but the rounding at the front of the wings is more rectangular in the biological observations. The front view (upper right) further shows the excessive rounding to an actually more rectangular cavity. The side view (bottom right) shows that the other morphology differs – while this appears to be a height-flattened and potentially immature nectophore, other features can be considered for the shape of the final nectophore model. Sketches of *Nanomia cara* nectophores extracted with no known copyright restrictions (Totton, 1956).

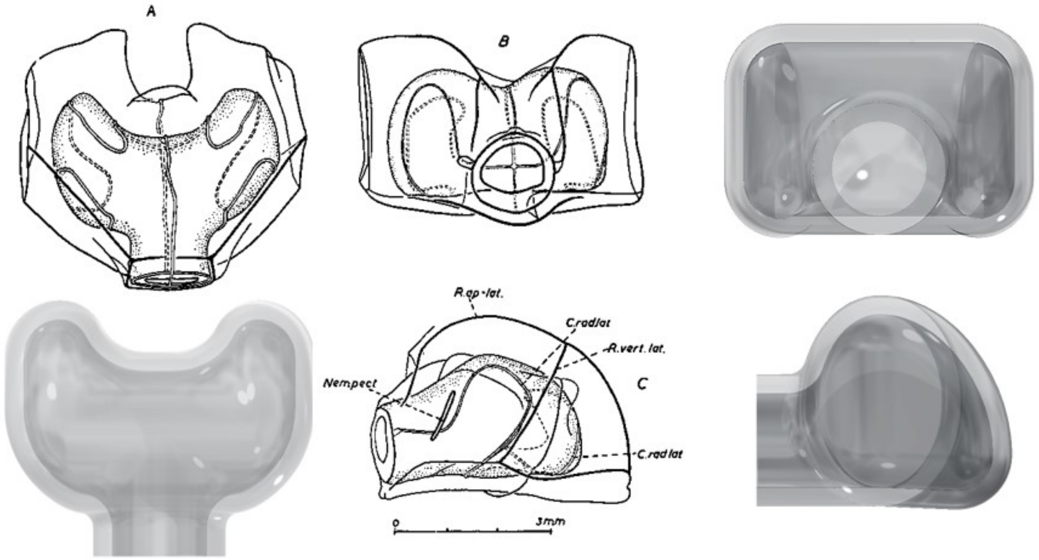

Figure 68 – Final form corrections for inaccuracies. These three views agree with the forms presented by Totton (with some exceptions), as well as video evidence. Sketches extracted with no known copyright restrictions (Totton, 1956).

4.3. ***Conclusions***

4.3.1. Body Kinematics

For reference of the body kinematics, the nectosome length for this specimen was determined to be 21.61mm, and the nectosome diameter was 9.12 mm. This diameter was measured from the extremes in plane of the colony, and the out of plane depth was not known for the specimen in the straight swimming video. A still image of one specimen from Jackie Sones showed that for a single specimen the ratio of the diameter in the plane of the colony versus the depth in the plane of the colony symmetry was about 1.32:1. Therefore, assuming a circular colony cross section in a top down view with the major diameter is larger in area by at least 32.8% relative to an ellipsoidal cross sectional area, and thus conservative for drag, added mass, and total mass calculations. Since the siphosome was not completely visible in the shadowgraph videos that were tracked, for simplicity and from published reports the length of the siphosome was assumed to be roughly equal to the length of the nectosome, resulting in a full body length of 43.22mm. From purely forward swimming, the peak velocity of 221.8 mm/s, or 5.13 body lengths per second, is impressive for the animal, especially since it is achieved in about 0.099 seconds resulting in an acceleration of 2.21 m/s^2. In comparison to the peak velocity of 255 mm/s for Cyro 2, which has a much larger mass but also a much larger thrust capacity, this amount of swimming acceleration at a scale reduced by over an order of magnitude is even more impressive performance for such a small organism. Therefore, this validates the aptitude in high speed swimming ability for siphonophores relative to their scale, and necessitates further exploration into their anatomy and locomotion.

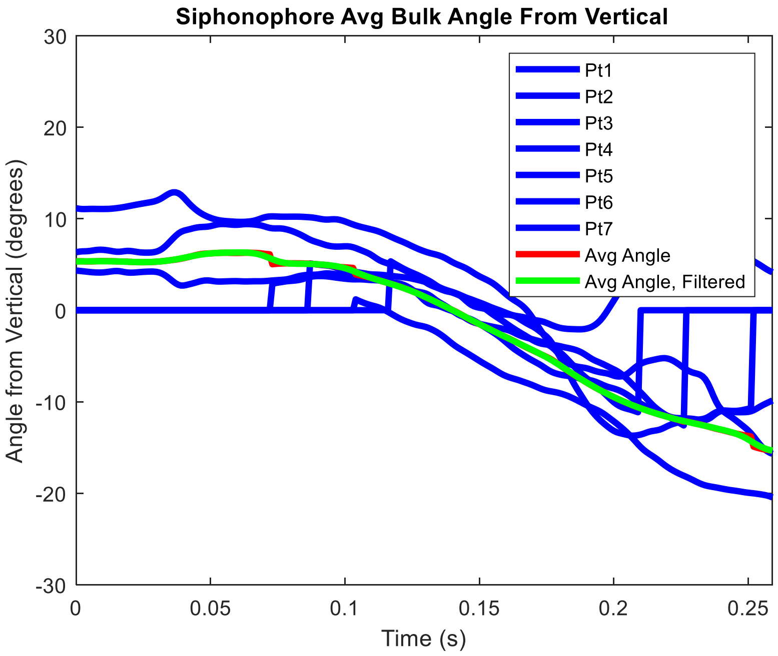

Figure 69 – Measured angle of nectosome angle during synchronous forward swimming, using points along axis at axial wing intersections with the stem. Angles found from between point and following point along stem, then averaged and filtered at 100Hz to eliminate jumping in value as the points enter and leave the frame of the video.

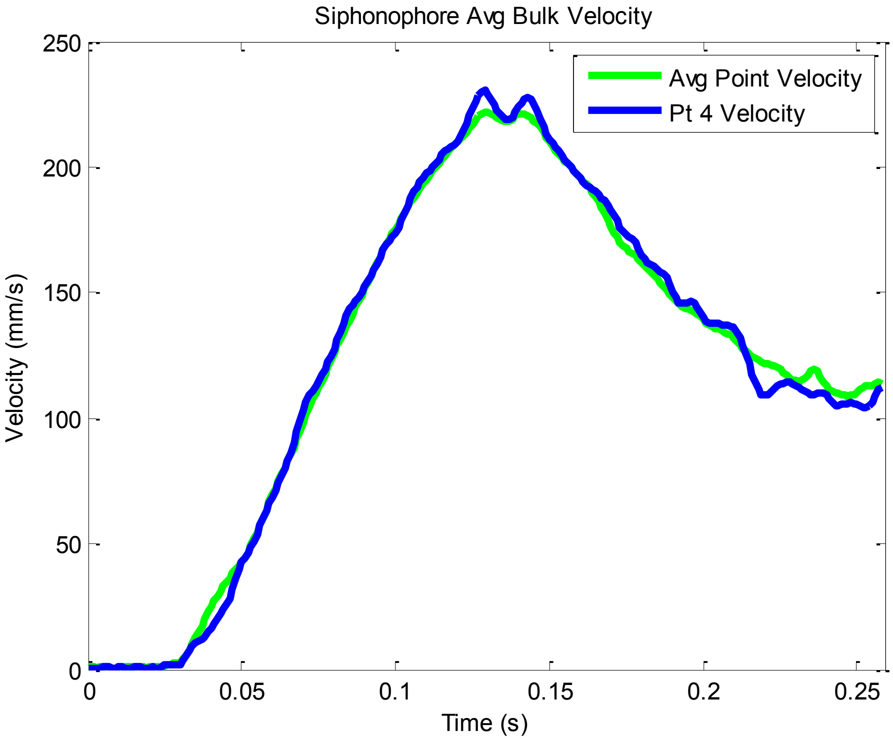

Figure 70 - Temporal average of the nectosome velocity, as well as measurement of the velocity of a point in frame for the duration of the forward swimming video

4.3.2. Nectophore Volume

From the tracking of nectophore volume, it can be found that while the nectophores scale up in size and internal volume as they mature and move down the axial chain, their percent volume change remains close to the average normalized volume change of 67.72%. Therefore it can be expected that the muscular layout and performance scales with size, but does not exhibit losses or gains in performance relative to size over maturity. This establishes a baseline for the expected performance of the nectophores in the design, and eliminates any change of effort-based functional specialization. The temporal volume change of each nectophore was roughly V-shaped with gradual acceleration and deceleration near full volume but rapid changes at reduced volume full contraction. This can be evidence of shape-based nonlinearity during contraction as opposed to muscular effort, especially since the video of this specimen was an escape based response that was of utmost importance to exhibit rapid motion that was globally controlled.

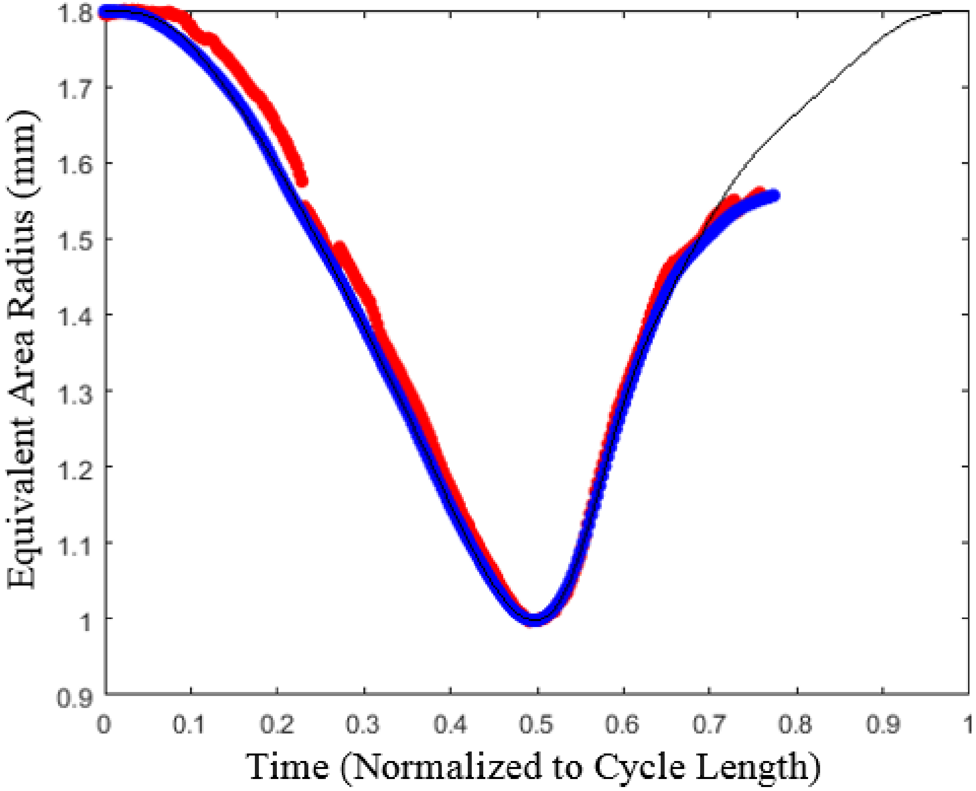

Figure 71 – Time history of the radius of a circle with equal area to the cross sectional area of a nectophore

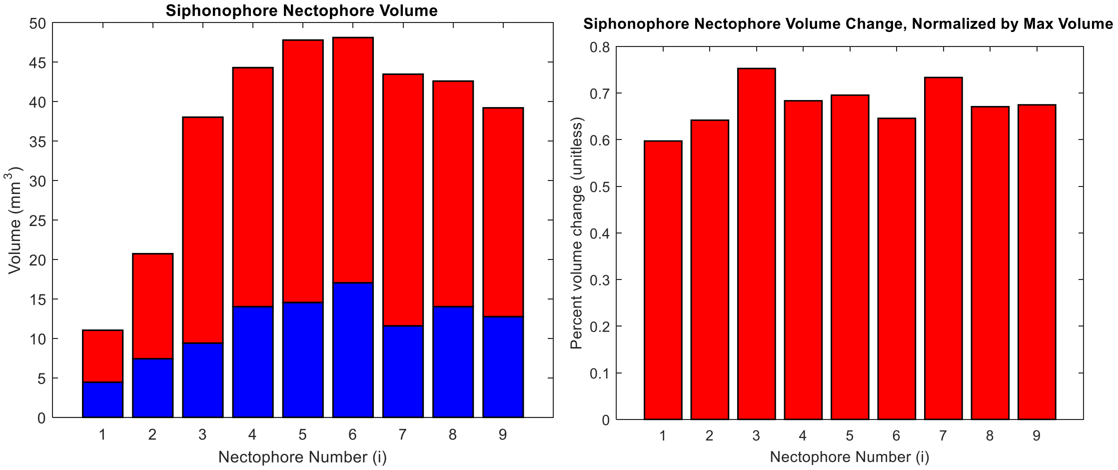

Figure 72 – Left: Nectophore volume change relative to position along chain. Although nectophores at the beginning of the chain are smaller, they exhibit a percent volume change that is insignificantly different than that of more mature in the chain. The blue bar shows the minimum volume at maximum contraction, while the red bar shows the range of volume change and peaks at the maximum volume at pre-contraction. Right: Percent nectophore volume change from fully relaxed to fully contracted, normalized by the maximum volume of the nectophore at the fully relaxed position

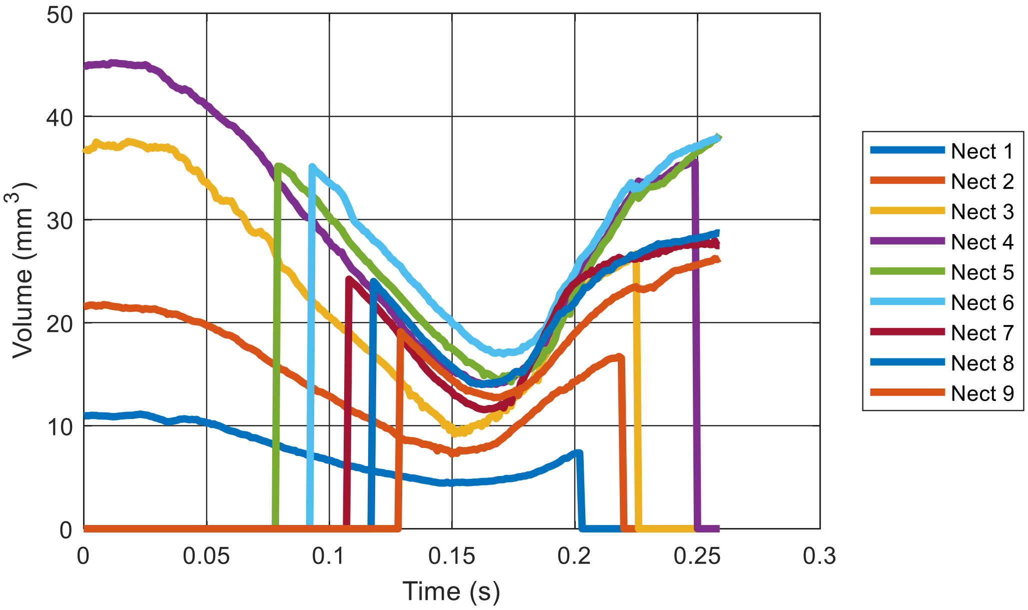

Figure 73 – Raw total nectophore volume data from all nine nectophores in the forward synchronous swimming video.

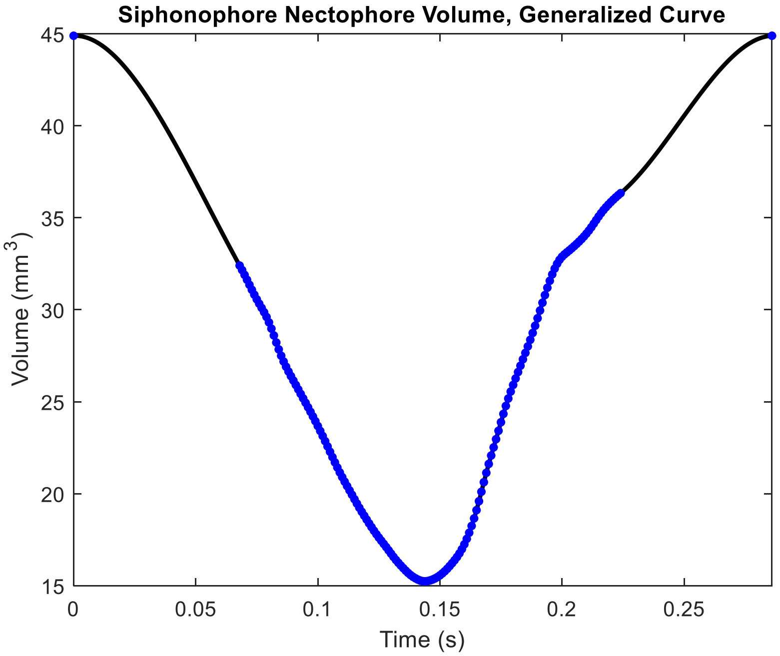

Figure 74 - Temporal average of the nectophore volume over the duration of the nectophore jetting cycle. Data from initial portion of curve eliminated to remove 'jump' in data when nectophore data begins for nectophores 5 and 6, data missing for end of cycle due to end of video before full relaxation. However, form of curve matches expected volume profile from other video nectophore data for ending points, and nectophore 4 data for starting points.

The additional tracking of the wings and contraction normal to the plane of symmetry, combined with the ostium and contraction in the plane of symmetry refined from the previous results, yielded the following values. It can be seen that while the total volume starts at a resting peak of 75.78 cubic mm, the main cavity contributes 63.80 cubic mm (84.2%), the wings 7.98 cubic mm (10.5%), and the ostium 4.10 cubic mm (5.4%). The total volume reduction is from the peak to 27.30 cubic mm, a change in volume of 48.48 cubic mm (64.0%). This percent change matches the original analysis across nectophores of all ages (within 3.72 cubic mm). However, this absolute volume for a generalized mature nectophore is nearly 170% the original curve resting values. This could have been caused by the scaling steps in the analysis to match the height and width to the different views. Most front views were about three quarters to a half of the side view heights, which required uniform scaling of the data magnitude to match the height values and temporal scaling to match the start and end of contraction. These highly variant scales and timing parameters, as well as the unknown true ratio of a single specimen of all views, highlights that errors are inevitable from differing datasets from different specimens of *Nanomia*. This could be in part due to aspect ratio variability shown in the sketches of *Nanomia* nectophores in previous literature (Totton, 1956). Therefore, the scaling could have been smaller instead of to the larger height from the side view. Ultimately two conclusions can be determined. Additional high speed shadowgraph footage of multiple specimens, each stimulated to swim with cameras imaging the three orthogonal views in unison, will be needed to fully profile the change in form factor and contraction across multiple specimen sizes. In addition, the original data for volume using the bent ellipsoid matched the expected slug flow velocity out of the velum, which was measured using PIV footage and particle streak velocimetry. The updated volume from multiple views results in exceedingly high jet velocity relative to the PSV and published results of directly measured specimens. Therefore, this analysis was a more comprehensive method but required more simultaneous data to truly reconstruct the volume. Additional methods to compensate for volume loss during contraction that was underestimated using an external bounding box estimation of height and width, such as using the average of the inscribed and external bounding boxes, were tested but not utilized since the contraction causes a creasing in the middle of the nectophore near the plane of symmetry, as well as along the band of circular muscle aligned approximately horizontally. This creasing heavily reduces the inscribed bounding box, and some forms result in multiple solutions for the internal bounding box. This results in an unreliable average, so the external bounding box was determined to be rapid to calculate, easy to match between views, and stable during creasing during contraction. Side view height was taken as what would be the peaks of the nectophore, so the external bounding box of the front matches the same structural peaks.

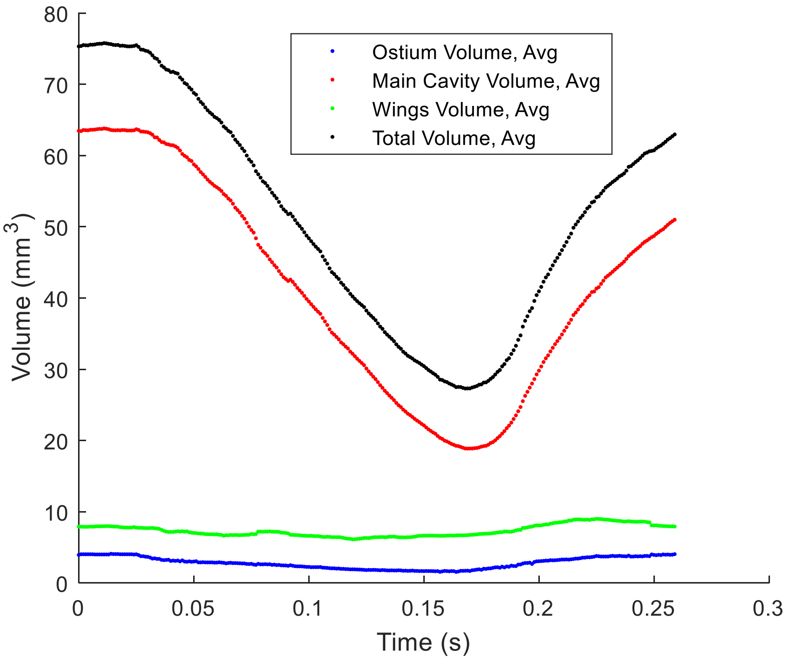

Figure 75 - Volume components through time for a generalized mature nectophore, using the projection method for volume estimation

4.3.3. Velar Kinematics

Since *Nanomia* exhibits the ability to muscularly control their velar direction for different escape behaviors, at least in axial forward or reverse directions, and the muscular presence and control of velar shape was generally mentioned in previous studies but not verified or discussed further, the study of velum angle and diameter and their effect on performance was of utmost importance (Mackie, 1964). The angle of the nectophore, and thus the ostium opening at the base of the velum, has been cited as a potential specialization method for thrust directionality, and the local velar direction across nectophores was critical for actuation characterization (Costello et al., 2015). Therefore, the angle of the nectophore was studied first to form a baseline understanding of colony form regardless of swimming. As expected from visual inspection and the study by Costello, the anterior nectophores consistently exhibit an orientation more normal to the stem axis (Costello et al., 2015). As the nectophores mature they tilt to point more backwards than anterior nectophores, with the most posterior nectophores pointing even further back past the nearly uniform mature nectophore angle across nectophores 3 through 8.

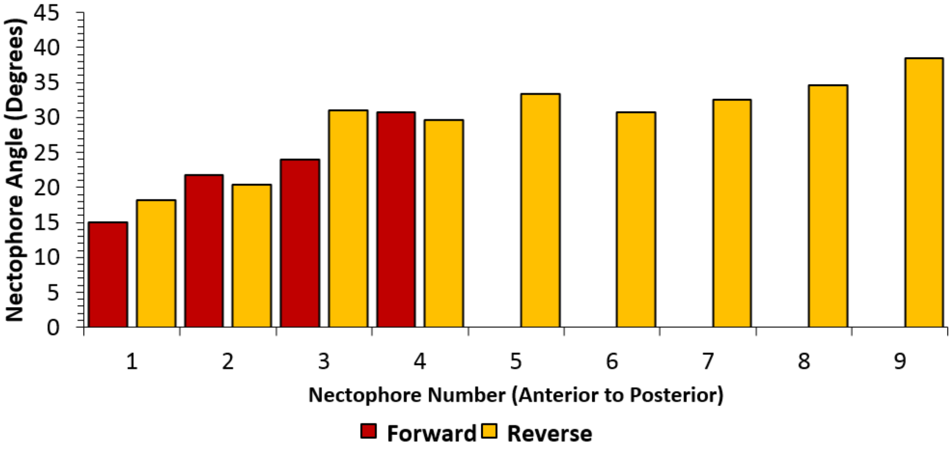

Figure 76 - Angle of nectophore ostium opening prior to flexible velum at rest for *Nanomia* in shadowgraph videos. The angle represents the downwards deviation from horizontal and normal to the colony, where lower angle represents a nectophore outlet angled normal to the stem and higher angle represents a more backwards orientation.

Once the general form was understood, the velum deflection represented the component of velar ‘effort’ to extend backwards and send the jet even further back relative to the nectophore orientation. This angle was found to be relatively consistent across all nectophores at full deployment, with an abnormally high value for the most anterior nectophore and a slight increase in angle as the nectophores mature. Therefore, it can be assumed that the phenomena driving the velar angle, whether purely fluid force on the thin velar flap or some muscular contribution to control or stabilize the velar deployment, was a relatively stable and regular absolute magnitude phenomena and should not be a varied parameter in a design.

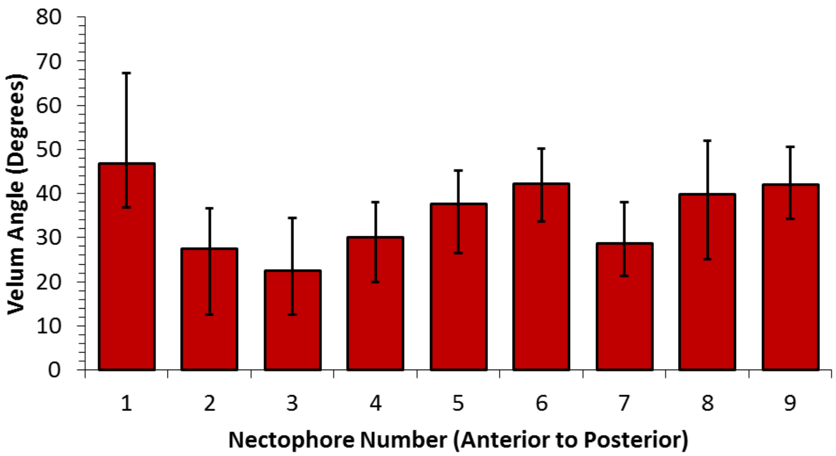

Figure 77 - Angle of velum outlet relative to nectophore ostium opening during full deployment during contraction for *Nanomia* in shadowgraph videos. The angle represents the downwards deviation from the normal vector of the nectophore ostium opening. Error bars represent the absolute range of the data for each nectophore measurement.

Velar dynamics during backwards deflection and normal contraction were observed further using close-up collated light imaging videos, as well as the tracked velar angle during high flow and low flow periods of the cycle. These observations revealed that the velar nozzle changed from a passive relaxed state at no flow to a restricted diameter at full deployment, which then was followed by the nozzle inverting and increasing in diameter during refilling. A completely passive velar nozzle with passive flexibility that returned to the aligned angle under no flow, as well as has differential stiffness to increase the velar diameter in the inverted position during inflow versus the deployed position during outflow, would be the best explanation for the physical system's characteristics. This flow-based passive and differentially stiff velar flexibility was representative of the velar mechanics of jetting jellyfish, and this closeness in form and function was viable considering how closely related, in taxonomy and functional roles in actuation and ecology, jetting jellyfish and physonect siphonophores are observed (Sahin et al., 2009).

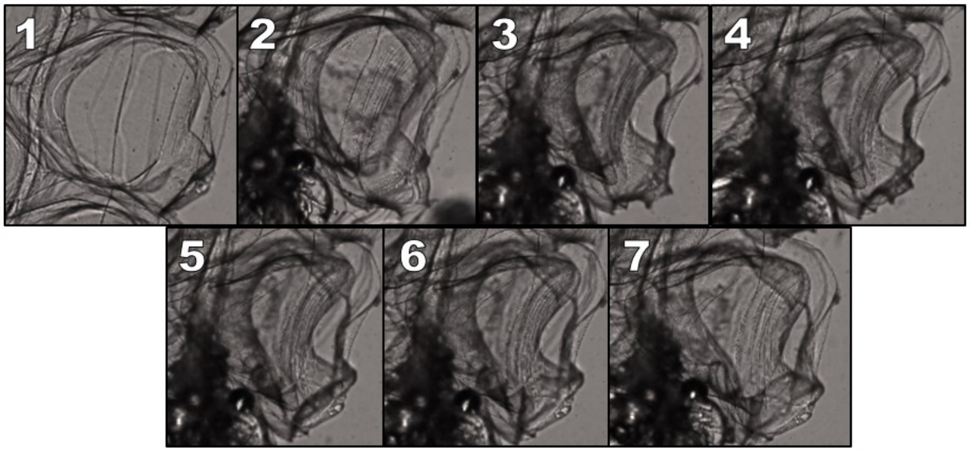

Figure 78 – Velum deflection and inversion during cycle start static (1), contraction and full velar deployment (2), and relaxation with velar inversion (3-7). This was similar to jetting jellyfish velar deflection (Sahin et al., 2009).

The sensitivity of this angle has been explored in a collaborative study with Colin Stewart, and it was found that jet angle would reduce thrust production if they were held at the aligned angle with the nectophore ostium opening, due to a more normal jet vector. However, holding the velum angle at the fully deployed position or allowing the velum to flex during the cycle approximately equally improved thrust production and hence the expectation of muscular changes to the velum angle during the cycle can be considered unnecessary. This implies that the design of a mechanical system would not need an actively actuated velum angle, with the flap either left as a fixed form or a passively flexing membrane. This would eliminate reverse swimming, but this behavior was observed as purely for escape and not a common enough occurrence to warrant additional design complexity (Costello et al., 2015; Mackie, 1964).

By forming a composite of these measurements, the full angle of the velum versus the colony can be formed. This angle for a design basis was measured as the velar deviation at full deployment added to the static full-volume form of the nectophore. This was how a physical representation would be cast out of flexible materials, and thus this was the most important for a mechanical device. However, this form was not ensured during actuation of a mechanical or a biological system since the muscle deformed the nectophore near the ostium and thus near the velum base, causing some anterior motion of the ostium downwards and towards the axis of the colony. This can pull the velum angle slightly more towards normal during full contraction, and thus there was a tapered steady-state full deployment angle. When this idealized angle was converted from this mechanical convention, where angle was proportional to the contribution to thrust, to the convention used by Costello, where angle represents the alignment with the backwards axial direction of the colony, the jet angles by Costello showed a more normal alignment of the jet relative to the colony axis (Costello et al., 2015). In addition, Costello tracked seeding particles in a planar laser illuminated flow during swimming, and the particles showed the true flow angle versus our proxy measurement of the morphology. Additional normal-biased deviation was expected since the fluid flowed around the cavity of the nectophore, through the more-normal ostium, and through a relatively short velar region that had only physically deviated a little from the ostium height. Therefore, this ostium-aligned momentum, as well as the short velum deviation that could have acted more as an ovular tilted aperture as opposed to a long flow-directing nozzle, caused the true jet flow to be more normal to the colony axis. While our data showed variation over a roughly flat velar angle, with a slightly more backwards angle as the nectophores mature, the true jet angle was considered by Costello to have a strong downward trend as the nectophores matured and were positioned further down the chain. This was the basis for his argument of the functional specialization of anterior nectophores contributing more to imparting a moment to the body while the posterior nectophores contributed more of a thrust force aligned with the body axis. This was partially claimed to validate a static case, and has not been proven to functionally matter on a dynamic case. In a qualitative assessment, the contribution of the nectophores during dynamic turning appears to be more based on position along the chain relative to the center of mass, with anterior nectophores providing an opposite moment around the roughly rigid nectosome as anterior nectophores on the same side, as well as based on temporal variation where an entire side will contract asynchronously or synchronously out of phase of the opposing side to produce temporally differential thrust and time for momentum to impart an angular change in colony heading. Therefore, this affect can only be settled with more observations and quantifications without a previously expected performance, and it may very well be a case-wise and specimen-wise dependency. It was likely that the immature nectophores are aligned due to the close packing body structure, growth orientation at the non-linear anterior end of the stem, and deviation during motion due to the angling of the pneumatophore. These factors are more likely to passively affect the anterior nectophore orientation and this as a result the performance, and not be an active strategy for actuation.

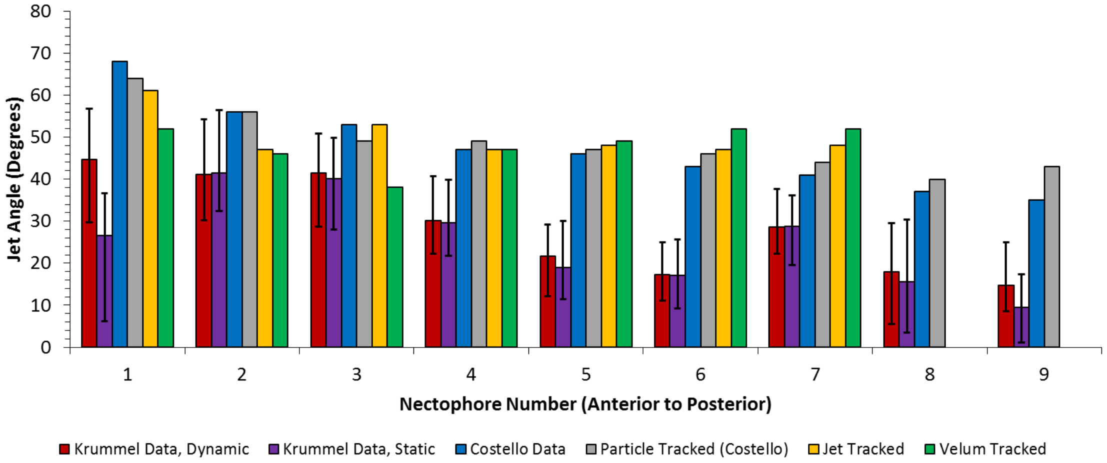

Figure 79 – Comparison of jet angle measurement methods. Dynamic case takes average of velum angle at full deployment relative to stem angle during forward swimming shadowgraph video. Static case takes average of velum angle relative to ostium opening during the shadowgraph video, added to the relaxed angle of ostium from the reverse swimming shadowgraph video relative to the stem angle. Costello data represents the data reported in the siphonophore locomotion paper (Costello et al., 2015). Particle tracked used a static frame of the colony with overlaid vectors provided in the supplementary data of the Costello study. Jet tracked found a mean vector of the full length jet direction relative to the colony axis at the static Frame 182 of the tracer particle video. Velum tracked found the velum angle relative to the colony axis at the static Frame 182 of the tracer particle video. The frame provided with the paper roughly agreed with the more robustly collected measurements plotted in the paper. Jet angle re-measured from a single frame showed on average the same angles as Costello, while the static frame velum agreed with jet angle on even nectophores and deviated more on the anterior odd nectophores. Velum angles in shadowgraph videos were typically lower than the angles found in the tracer video of another specimen, with posterior nectophores deviating the most. Static shadowgraph approximation fits dynamic velum angle data well for all nectophores except the most immature nectophore. Error bars show range of data.

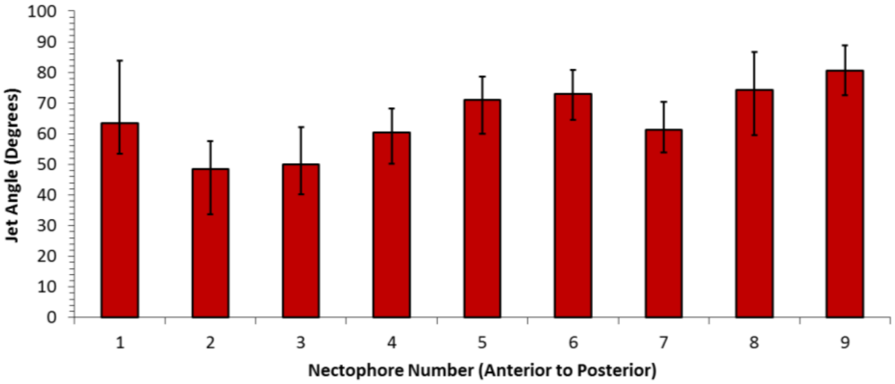

Figure 80 - Expected outlet jet angle of nectophores, which was the sum of the nectophore angle at rest and the velum angle at full deployment. This was the baseline design expectation for the robot jet angle, although contraction deflected the jet due to flexion of the nectophore. The angle represented the downwards deviation from horizontal and normal to the colony, where higher angle represented more thrust contribution from the jet. Error bars show range of data.

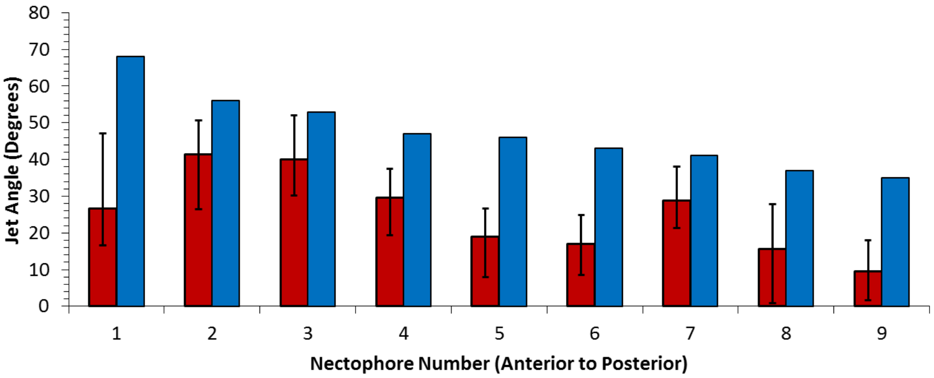

Figure 81 – Jet angle from Costello et. al. compared to measured jet angles derived from velum angle relative to the stem at full deployment. The angle represents deviation outwards from the backwards axial direction. Red bars indicate the jet angle measured by the keyframing data, while the blue bars represent data by Costello. Error bars show range of data.

As seen in the tracking of the velum diameter over time the diameter reduces during contraction due to the velar deployment, and thus the jet was smaller and hence faster with more momentum. As the nectophore relaxes the observed inversion and subsequent widening of the velum, likely due to differential stiffness, increases the velar diameter to a peak diameter roughly the full internal diameter of the ostium minus the velar wall thickness on each side. As the flow was reduced at the end of the relaxation, the velum was not forced open as much and relaxed more towards a neutral form with a reduced diameter. This drastic change in diameter was critical to refining the jet to maximize momentum by reducing the opening area and increasing the jet velocity for a determined change in volume, while also reducing the refilling momentum velocity for a known roughly symmetric volume rate of change. At a peak diameter, the refilling diameter is about 3.4 times the contraction diameter, resulting in about an 11.56 times change in outlet area. For the same volume displacement, this change in inlet area also reduces the jet speed by 11.56 times, reducing the thrust for pure slug flow by 11.56 times. Since the refilling jet was still angled slightly downward, even after the reduction in angle due to inversion, reducing this refilling momentum was critical to minimizing the negative thrust on the body of the colony and hence inertial fluctuation during any gait. This diameter change with a dynamic angle was explored in a collaborative study, and it was shown that any fixed diameter resulted in either reduced positive thrust or increased negative thrust during the cycle, and hence a dynamic diameter was critical to the asymmetric thrust production that results in forward swimming. Dynamic jet angle was not found to be significantly impactful over simply angling the jet backwards with a dynamic diameter, although changing angle does reduce the heavily reduced negative thrust by another factor of nearly half. It cannot be ruled out that an active muscular constriction of the velum was present in addition to the differentially stiff velum material, as seen in jetting jellyfish, and hence further studies are suggested for the isolation of these passive and muscular mechanisms (Sahin et al., 2009). This could be achieved by blocking nervous connections to the velum but allowing contractile muscles to function normally, thus reducing the action to purely passive flexure based on the flow through the velum initiated by nectosac muscular force. Regardless of the biological mechanism, implementing either an asymmetrically stiff material for the velum, an active velum diameter change, or both in a biomimetic design was critical to achieving forward progress during swimming of any gait.

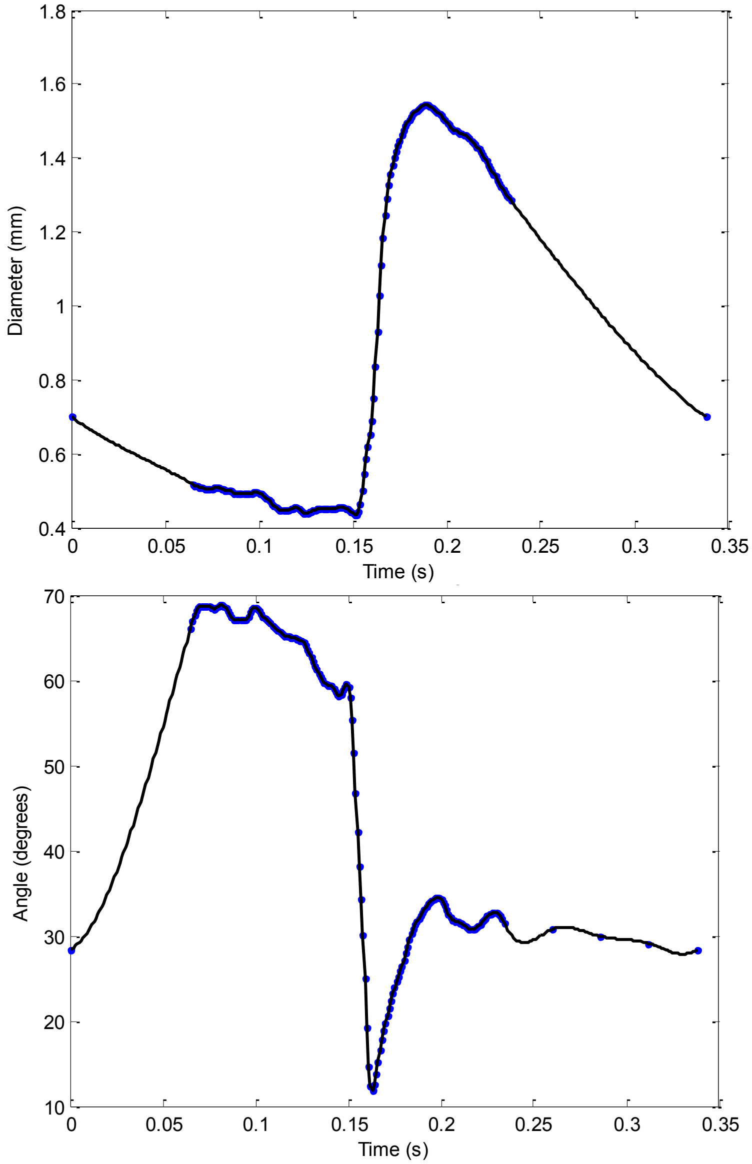

Figure 82 – Temporal average of the velum diameter (top) and jet angle relative to the orientation of the stem (bottom) over the duration of the nectophore jetting cycle

4.3.4. Neural Control and Swimming Gait

The nectophore contraction timing was determined in previous studies to be controlled by two distinct mechanisms. The stem generated a pattern signal along two giant axons, which was connected to each nectophore (Grimmelikhuijzen et al., 1986; Mackie, 1973). The nectophores generated a control signal via a neural network local to the nectophore near the thrust block, with limited spatial sensing and minimal if any cross-communication between nectophores. This distributed control with central pattern generation isolated global gait generation to central control and all individual timing parameters to each individual nectophore. As long as the nectophore was aware of its position along the stem it was able to correlate the gait pattern and current phase to nectophore muscle action without definite stem axon coordination control. Therefore, as the number of nectophores increased the computational time of the gait was invariant, resulting in constant time computational complexity invariant to scale. This was a significant improvement over the complexity of organisms with central nervous systems, which would take at best linear computational time relative to size and potentially introduce delay artifacts that would affect coordination integrity.

During synchronous forward and reverse swimming for escape, the nectophores along the length of the stem contract and relax at the same time, with slight variation in relaxation timing. Steady state swimming generally utilizes a cascading asynchronous pattern with contraction propagating from anterior to posterior nectophores (Mackie, 1964). The contraction of the anterior-most nectophore starts after the posterior-most contracts, with approximately equal timing between consecutive nectophores in the sequence. During gradual turning, the nectophores on the inside of the turn contract first, followed by contraction of the outside nectophores. The turning amount is expected to be proportional to the wait time between outside contraction at the end of a cycle and the inside contraction at the start of the consecutive cycle, as observed with jellyfish differential timing. This form of turning can be seen utilized both with synchronous and cascading form, thus inferring that the timing of this gait based on side relative phasing was critical to the turning and not the single side pattern during the turn. As can be expected and has been validated in the collaborative simulation study, the cascading motion smooths the time history of thrust during the cycle, reducing inertial fluctuations during the swimming and smoothing the overall colony motion. This has been observed by Mackie and in our source videos when forward swimming with gradual turning was with alternating side-synchronous contraction, which imparts a side-to-side oscillation in the body due to lateral fluctuations in momentum and inertia (Mackie, 1964). For sharp turns, the outside nectophores contract only on one side on the outside of the turn. This behavior has only been seen in limited capacity, since the sharp turning was performed when the fluorescein dye was mostly depleted in the nectophores and the specimen was out of plane and out of focus. However, the inertial control of angular rate with temporal organization of thrusting then cruising has been seen with the side-wise phase lagging, and this extreme was not outside the variation space since the side-to-side delay between contractions on the disabled side can be considered as infinite. In addition, the specimen imaged in the PBS black water dive shows a progression of synchronous swimming for the first two cycles, then a cascading outside-only turn, then a cascading straight swimming gait for steady slower swimming (UnderH20, 2013). This confirms our previous observations of gait use and progression.

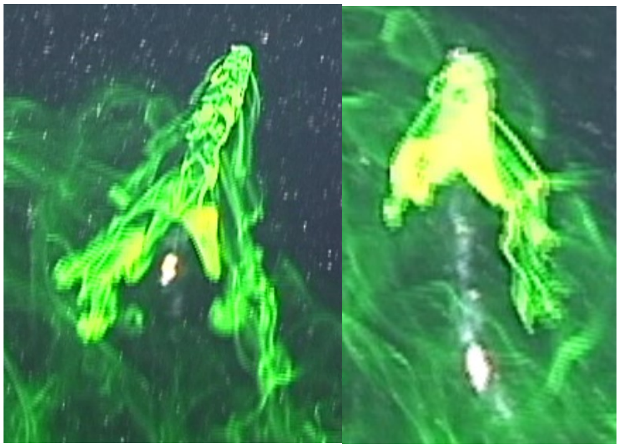

Figure 83. *Nanomia* swimming through fluorescent dye at a constant velocity while using a cascading gait. Propulsive jets emanating from the body are marked by dye and are seen as streaks. Left: Purely forward swimming with a symmetrically cascading gait. Right: Slight right turning using a left-firing immediately following a right-firing pattern, with side synchronization. Images courtesy of Jack Costello.

Table 3 – Gait cycle timing for nectophores. N represents total nectophore count, i represents the index of the nectophore (numbered anterior-most to posterior-most), and t_{cycle} represents the contraction and relaxation cycle period

Bulk Movement	**Odd Nectophore Index (i) Delay Time**	**Even Nectophore Index (i) Delay Time**
Synchronous forward *Synchronous reverse*	0	0
Cascading forward	$\frac{(i-1)t_{cycle}}{N}$	$\frac{(i-1)t_{cycle}}{N}$
Alternating forward	*0*	$\frac{t_{cycle}}{2}$
Gradual turn towards odd nectophores side, cascading $t_{inc} = \frac{t_{cycle} - t_{stall}}{N}$ $t_{stall} \approx 2t_{inc} = \frac{t_{cycle}}{\frac{N}{2}+1}$	$\left(\frac{i}{2}\right) t_{inc}$	$\left(\frac{N}{2} + N\%2 + \frac{i}{2} - 1\right) t_{inc}$
Gradual turn towards even nectophores side, cascading	$\left(\frac{\mathrm{N}}{2} + \frac{\mathrm{i}}{2}\right) \mathrm{t}_{\mathrm{inc}}$	$\left(\frac{\mathrm{i}}{2} - 1\right) \mathrm{t}_{\mathrm{inc}}$
Gradual turn towards odd nectophores side, alternating	*0*	$\frac{t_{cycle}}{2} - t_{stall}$
Gradual turn towards even nectophores side, alternating	$\frac{t_{cycle}}{2} - t_{stall}$	0
Sharp turn towards odd nectophores side, cascading	∞	$\frac{\left(\frac{i}{2} - 1\right) t_{cycle}}{\frac{N}{2}}$
Sharp turn towards even nectophores side, cascading	$\frac{\left(\frac{i}{2}\right) t_{cycle}}{\frac{N}{2} + N\%2}$	∞
Sharp turn towards odd nectophores side, synchronous	∞	0
Sharp turn towards even nectophores side, synchronous	*0*	∞

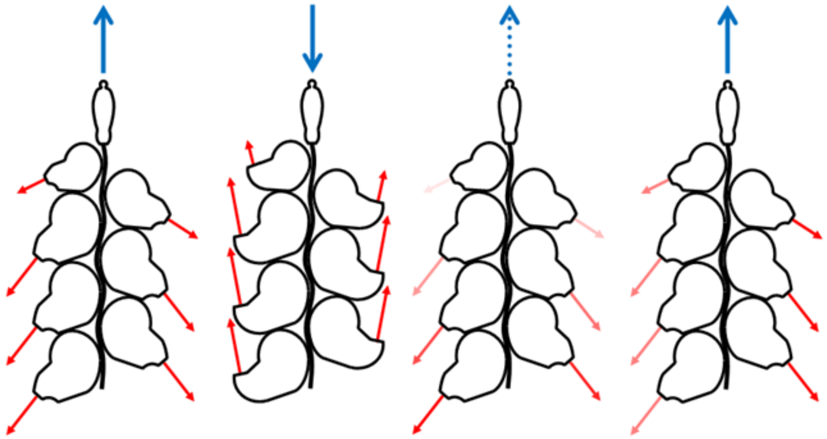

(1) Synchronous Forward

(2) Synchronous Backward

(3) Cascading Forward

(4) Alternating Forward

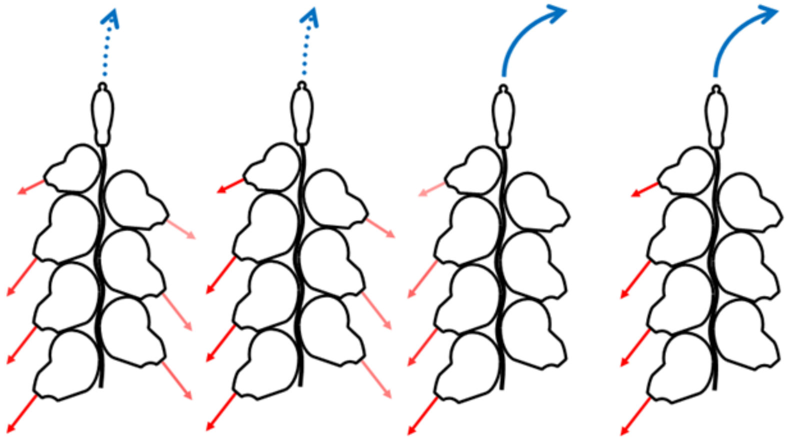

(5) Gradual Turn Cascading

(6) Gradual Turn Synchronous

(7) Sharp Turn Cascading

(8) Sharp Turn Synchronous

Figure 84 - Preliminarily identified distinct gait patterns of *Nanomia*. The synchronous gaits require firing of all nectophores at the same time, with the velum directed to achieve forward or backward motion. This movement was used for escape behavior and rapid acceleration. Once accelerated, the cascading gait was used for maintaining forward motion. The contraction occurs from anterior to posterior nectophores, and the anterior nectophores relax before the cycle was completed. The turning gaits utilize nectophores on the outside of the turn, where the anterior nectophore fires to produce a moment and the posterior nectophores produce translation thrust. The inside nectophores contract first to reduce the moment and increase translation. After the outside nectophores contract, the inside nectophores fire again after a delay.

5. Design, control, and simulation of a Siphonophore-inspired model

5.1. *Introduction*

As established in the biological study of the morphology and locomotory function of physonect siphonophores, the streamlined multi-jetter body form was of particular interest for the design of a biomimetic multi-jet robot. In particular, the species classified under *Nanomia* was a prime basis for a robot design due to the broad understanding of its swimming capabilities and additional anatomical specialization for maneuvering. The spatial and temporal distribution of thrust enables significant propulsive control capabilities and swimming power for a small organism, while the amount of neural control and interconnectivity over the colony was minimal (Mackie, 1964). The nervous system of the siphonophore consists of the distributed zooids and the central stem. The stem consists of some muscular tissue and a giant axon pair, which conducts global signals for escape responses as well as gait coordination via combined activation potentials (Mackie, 1973). The stem connects to each nectophore via a neural network, which contributes local control (Mackie, 1978). This local control primarily drives the muscles of each nectophore, and can initiate asynchronous contraction during slow travel during migration (Grimmelikhuijzen et al., 1986). Although some sensory feedback to the colony was necessary for stimulating the escape response, the interconnectivity between nectophores for collaborative control was not well understood and was expected to be very limited (Mackie, 1964). This central connectivity for synchronization but local neural network control for the mechanics of each zooid for a colony-wide motion was very similar to the distributed neural ring with neural networks at each lobe of jellyfish (Satterlie, 2011). Therefore, the electrical design, actuation, and control implemented on Cyro 3 to functionally distribute and specialize functions but synchronize the system with pattern generation communicated to each node was expanded into the colonial architecture for a siphonophore mimetic robot.

The control system of a siphonophore, and hence a siphonophore mimetic robot, was a unique approach to high level control with physical coupling but minimal feedback coupling between the system units. One control system design typically used for higher order systems is a centralized processing unit developed on a model of the bulk dynamics of the system. While this would allow for a high degree of predictable prescribed operations with discrete coupling, the complexity of a system like this with flexibility and fluid dynamics included would require significant computational power on a small mobile robot. In addition, as the long chains typically seen in Physonects scale in complexity due to increased numbers of propulsion units and increased size and flexibility of the system, the algorithms would scale at exponential form rates and quickly exceed the speed and power of small scale microcontrollers traditionally used on modern small aquatic robots.

In order to solve this multi-unit system organization problem, we can look to swarm robotics methods (Barca and Sekercioglu, 2013). Swarm architectures typically divide multi-unit system control into either centralized or distributed control. Centralized systems exhibit high levels of control on the whole system performance, and the performance of each unit as a component of the composite system would be prescribed and highly predictable. However, for multi-agent systems the loss of the central control and the necessity of high-bandwidth feedback to a single unit inherently causes a vulnerability of the composite system that reduces robustness in hazardous live environments. Therefore, purely distributed control is commonly used on multi-agent systems to improve reliability with redundant agents that are capable of filling in operational roles if a unit was lost. However, this redundancy and more independent performance with on-board planning reduces the predictability of the agent performance and thus overall system performance. These strengths and weaknesses have driven the development of hybrid control systems for multi-agent collaboration. This typically introduces a central agent that handles bulk pattern control, while individual units can work locally to complete components of swarm objectives. If the central unit is lost the individual units collaborate and reorganize the system hierarchy, including re-assigning key nodes that are lost or compromised, to adapt to active environments and unit functional challenges in order to maximize reliability and ensure swarm goal completion.

Siphonophores are one of the few organic examples of a collaborative multi-agent system, and they further simplify the system dynamics with physical constraints on the overall colony. Each nectophore was constrained to move together in a semi-rigid body, and the thrust of a single unit compounds with the thrust of the multiple colonial units to produce bulk colony moments and vector forces (Mackie, 1986). For general pattern generation, the stem provides a rapid pulse for immediate motions such as synchronous forward swimming, while the individual units can perform asynchronously with limited to no feedback as long as individual outputs collaboratively contributes to the overall system goal (Grimmelikhuijzen et al., 1986). This spectrum can include central patterns that individual units interpret via their local mechanics and neural network, requiring only central sensing feedback control and peripheral motion control. This greatly reduces the complexity of the control system because feedback lines can be minimized or even eliminated and the same signal can be sent from the central stem to the entire colony. While purely centralized high-complexity systems for this level of control would scale at the order of exponential or polynomial form at best with additional thrust units, this distribution and uniform signaling theoretically causes computational complexity to stay on the order of constant time. This was due to an additional unit not adding to the central control complexity, and the other units are completely isolated except for basic sensing. Therefore additional units do not change system computational time in proportion to the number of units. This promotes a loosely connected modular system.

The development of a colonial robot with minimal hybrid distributed-central control and a serial chain of modular actuators was highly complex and interconnected. The design of the actuation, electronics architecture and interfacing, and scale enables the control system to function properly, while the control system decides the functionality of these physical components. Therefore, the following chapter divides the physical system and control software development, but the development of each will persistently reference the functional requirements of the entire system.

5.2. ***System Design and Characterization***

5.2.1. Biomimetic Electrical and Interfacing Design

In the case of bi-serial chain colonial architectures seen in physonect siphonophores, four primary control and electrical connectivity architectures are possible. The most common implementation would be a single central controller, which was connected to all jetting unit motion control boards. While this was the simplest system to program and troubleshoot, the number of I/O ports needed on the board with the appropriate motion control output capabilities required a large board with a significant number of wires running to the board. This made modularity extremely difficult, since adding or removing units changed the computation time of the control system and required temporary hardware connections for power and control signals. The second method, which was implementing one microcontroller per side, reduced the I/O ports needed for each microcontroller to half and thus to a more reasonable requirement for two small microcontrollers. However, this only divided the computation time in half, and inherently included the same number of wires trailing through the body and the same constraints on modularity. In addition, the two units needed to synchronize the signals to operate correctly, introducing the possibility of temporal errors from computation time and synchronization delays.

The alternative to a centralized or semi-centralized architecture was levels of a hybrid distributed-centralized architecture. The third form integrated a microcontroller unit for pairs or four-unit blocks, while the fourth form used a single microcontroller for each single jetting unit. These forms drastically improved the computation time to constant time, and localized all wiring to a few I/O ports while reducing the number of wires running to the central controller. The central controller sent clocking and gait requirement signals, and each module or unit controller identified the requirement of actuation to achieve these timing and gait parameters in the assigned position in the chain. Each unit or nectophore could have a programmed position in the chain, but an initial routine to measure the position in the chain would be more robust and allow for modular arrangements that change in size but do not require significant reprogramming.

The mixed central coordination, distributed motion control scheme was used by *Nanomia* and thus adapted for the control of the siphonophore robot motion. To represent the central stem synchronization and central pattern generation seen in *Nanomia*, the central stem of the robot included a microcontroller that generated a gait characteristic signal over a digital clock and serial data line, which controlled the actuation frequency based on the clock frequency and bulk colony heading based on the serial encoded data. The clock signal was consistently driven, and the heading encoded data was only sent when a change was desired and held when the gait should persist as previously defined. This encoded signal included two bits, which held the cycle frequency, turn direction, and turn amount. The nectophores each knew the number of nectophores in the colony and their position in the chain by a resistor along an auxiliary power line. When the unit was attached to the colony stem, the unit resistors connected in series and formed a voltage divider driven by the I/O level of 5 V. This divider circuit provided a distinct voltage drop and starting voltage at each unit that indicated the number of series resistors and number of previous resistors based on Ohm's laws of series resistor voltage dividers. These parameters, as well as the measured position within the chain, were combined with the closed-form pattern and timing solutions on each individual unit microcontroller to efficiently generate local solutions to actuation control. The central microcontroller dictated the heading control based on sensor feedback, though the heading control law will detailed in a later section. With this modular structure and control network, the nectophore modules were able to be attached in chains of any length within the bounds of less than 30 nectophores found in nature (Totton, 1965). The colony form maintained the closely packed and streamlined structural organization as seen with *Nanomia* colonies. This interconnectivity architecture was reduced to one clock wire, one serial data wire, one ground wire, one power wire, and one position sense wire. The siphosome contained the power storage and regulation elements, as well as the central microcontroller, that generated the power and signal lines up through the colony.

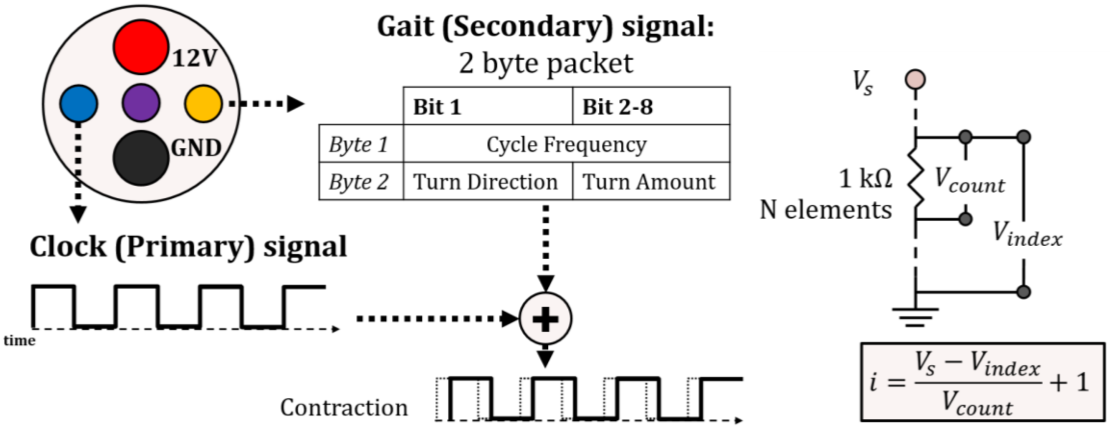

	Bit 1	Bit 2-8
Byte 1	Cycle Frequency	
Byte 2	Turn Direction	Turn Amount

$$i = \frac{V_s - V_{index}}{V_{count}} + 1$$

Figure 85 - Control system and signal scheme for central pattern generation for colonial gaits, as well as how each jetting unit microcontroller will process these signals to generate local actuation control.

For this design, the AT-Tiny85 was selected due to its broad array of functional features in a small package. A circuit for positive polarity PWM control of a solenoid was designed for a custom PCB or free wire design. The position sense resistor is integrated between the pre and post resistor analog inputs, and a 1 kΩ value was chosen so a chain length of up to 12 units would not exceed the current output of a digital pin from the central microcontroller. Digital inputs via a software serial library and digital interrupt pin were used for central control inputs, with a 10 kΩ pull-down resistor to induce a load and eliminate floating state input. The transistor and flyback diode was selected for the voltage and current requirements of the solenoid as well as the need for a 5 V digital line gate control. A resistor in line with the gate and digital output reduced current between the gate and microcontroller I/O, and an additional drop down resistor was added to hold the pin state at ground to reduce the risk of high power delivery in case of a fault. The input to the microcontroller was a regulated 5 Volts, but a positive temperature coefficient resettable polyfuse was selected for overcurrent protection and a 0.1 µF capacitor was added for power line noise rejection. While these protection components were not necessary, it improved the robustness of the system and prevented burning out the microcontroller from voltage or current spikes from a switching power supply without low level overcurrent protection.

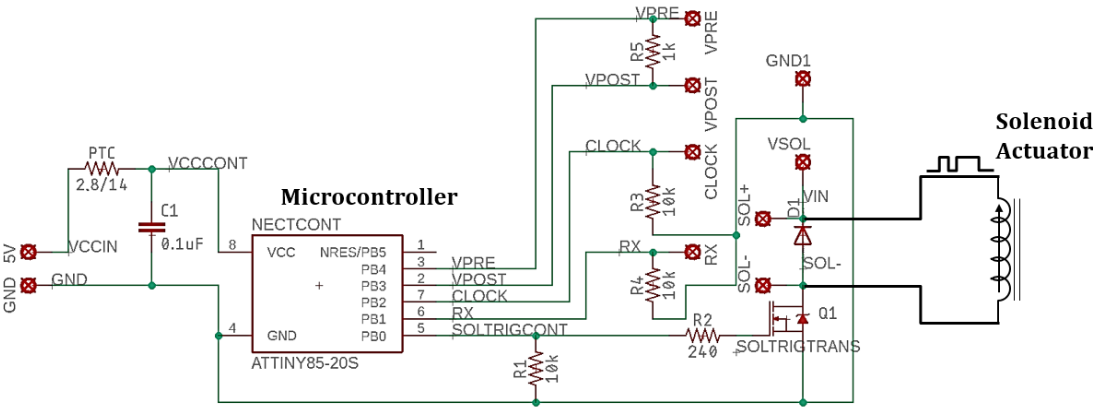

Figure 86 - Transistor circuit design for custom PCB board

When the control scheme was changed to utilize a reversible polarity H-bridge motor controller, an additional digital line was needed for directional control via a digital state. Since the operating frequency of the actuators was reduced to maintain the fluid properties of the jet and stay within the actuation speed bounds of the coils, the clock line was transferred into a single-bit signal on the serial line. The serial line updated at every half second or less, with the first bit dictating the clock signal, the next three bits indicating frequency as a normalized value between 0 to 4, then a bit indicating turn direction, then a three bit value indicating the turning amount. While this reduced the resolution of control, the reduced actuation frequency band and turning control range allowed for a compromise of signal read and write speed to overall performance. A control law using this new architecture, with selection bits of whether a synchronous or asynchronous methodology would be used for turning or straight swimming motions, was implemented on the AT-Tiny85 chip, with a clock rate adjusted to 8 MHz for improved processing speed and thus temporal resolution.

5.2.2. Manufacturing of Nectophore Units

The primary nectophore shape, consisting of an interlocking thin-membrane cavity that deforms to change volume and produce a jet thrust, an outlet to the cavity, and a nozzle that angles back to produce more posterior thrust, was modeled relative to anatomical analyses in Chapter 4. This resulting model required manufacturing that could produce a consistent thin membrane with a complex shape, with the material sufficiently flexible to allow easy actuation, durability in live environments, and passive elastic energy storage to return to a fully relaxed shape.

The first method for manufacturing the nectophores was a 3D printed model, consisting of the Stratasys TangoPlus printable elastomer. This process was highly repeatable and provided high-accuracy parts without significant manufacturing complexity. However, this elastomer was low strength and stiff, thus requiring a thin shell to allow deformation that resultantly did not store enough elastic energy to return to its original shape. Even as the model was reduced to 0.25mm wall thickness, the solenoid actuator at the time could not deform the shell to create a jet. However, this material performed better for an accordion-type nozzle since the shape inherently allowed controlled flexure, yet the low tear resistance still proved undesirable when the material was easily damaged when removing support material or under repeated use once the material dried.

Figure 87 - 3D printed nectophore, showing thin wall structure and stress fractures along the shell periphery.

The second attempted manufacturing method used in industry for casting thin parts was rotocasting. This method consists of manufacturing an external mold, partially filling the mold with enough casting material to form the desired end shape, and rotating the mold with a two degree of freedom motorized frame to evenly coat the mold walls with a thin layer of material. This molded part would then be removed after curing time is complete and trimmed as needed. This requires a dual axis motorized frame, which can be purchased commercially but was sufficiently simple to build out of 80/20 slotted aluminum extrusions and basic mechanical parts. A DC motor with a high torque gearbox was chosen to reduce the spin speed for the viscous silicone material, and additional gearing was manufactured and added to the motor drive to further slow the spinning without sacrificing power from the motor to spin the frame.

Figure 88 - Custom built rotocasting frame with two degree of freedom motion

However, this method proved to be inconsistent in quality, completeness, and wall thickness consistency. The casting material tended to collect near the ends of the mold, and the viscosity of the silicone did not allow it sufficient movement to move around the mold during the spinning cycle. Additional mold designs to extend the ends of the shape and include material-holding cavities were attempted, but this resulted in further wall thickness inconsistencies due to material collecting in the extended cavities and not moving into the mold. Thinning of the casting silicone was also attempted to improve flow in the mold, but the tear resistance of the resulting part was reduced and the quality of the part was similar to non-thinned samples.

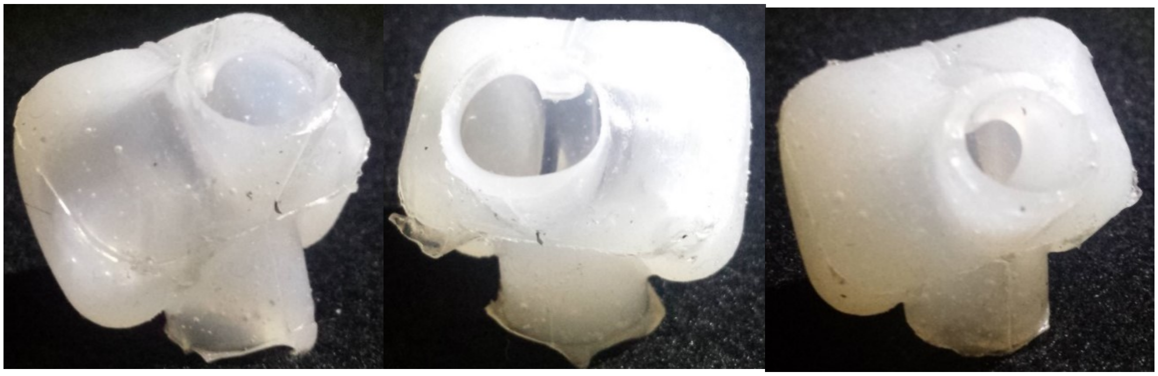

Figure 89 - Rotocast silicone models of nectophore with defects. Visible in each model is inconsistent wall thickness, all with the same casting parameters.

The final casting method consisted of two refined stages for consistent, quality casting without mechanical defects. The first stage was to properly mix and degas the mixture with a vacuum chamber pumped to -27inHg. This silicone was then poured into a multi-part mold that was 3D printed out of Stratasys VeroClear. This mold had both external and internal forms, with the two locking together on integral indexing features. The external mold was assembled separately in two halves, each half was filled with silicone, and then they were brought together with the internal form inside to perform what is commonly known as 'squish casting.' This method ensures that no air pockets are formed, the mold has sufficient silicone material and flow, and that excess is quickly removed via the seams to reduce trimming after casting. This final form was then released by peeling off the external mold halves and rolling the thin silicone form off the internal mold. Any voids in the part were repaired with silicone applied on the finish part, or by re-inserting the part into the mold with additional silicone to flow into and fill the voids. While this process worked well for highly flexible silicone casting rubbers such as Ecoflex, the stiffer silicones that were explored for improved durability and elastic energy storage and rebound, such as DragonSkin, had some additional difficulty in flowing throughout the mold, curing completely without cure inhibition reactions, and removing from the internal mold. Therefore, Ecoflex was chosen for this design.

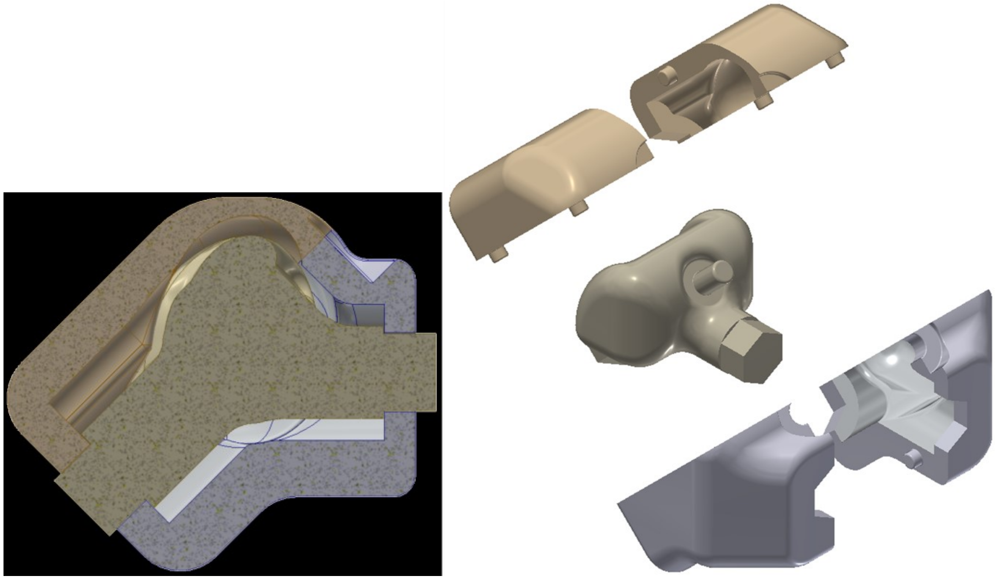

Figure 90 – Mold form for properly casting the nectophore shape. This form was for the solenoid design, and integrates additional features for this actuator.

Figure 91 – Squish-cast nectophore with solenoid channel integral to the form.

5.2.3. Biomimetic Mechanical Design

The video measurements presented in the previous chapter have informed the design of the modules for the siphonophore robot. The presented nectophore models were adapted and integrated with actuators and mechanical assemblies. The contraction of the nectophore for *Nanomia* is initiated by circular muscles around the internal cavity of the nectophore (Mackie, 1964). This contraction resulted in the front face of the nectophore being pulled towards the back of the nectophore, with the rear portion held static by the attachment to the stem and the interlocking support of the axial wings. This motion resulted in a roughly linear motion in plane with the center plane of symmetry for the nectophore.

Therefore, the analogue of linear repeated motion can be actuated typically with a few classical methods, which have been explored and critically reviewed.

The simplest linear repeated motion, with an absolute start and end point with a roughly linear response, can be controlled by a solenoid. Solenoids consist of an electromagnetic coil wrapped around a cylindrical cavity, which holds a cylindrical ferromagnetic core. As the electromagnetic field is turned on in each direction, a force is imparted on the core and it moves out of the coil in a direction relative to the voltage polarity. This simple actuator can be inherently waterproof as long as the coil is insulated, typically with a resin coating on the magnet wire. Since the amount of travel for a small commercial solenoid (SparkFun ROB-11015) was found to be small but resulted in a large impulse force output, the first design used mechanical advantage to push a plate against the nectophore at the correct angle and form to mimic the contraction profiles seen in the video. This mechanical linkage was 3D printed in Stratasys VeroClear rigid plastic on an ObJet Eden 260V high resolution printer, with the printed model as a single integral assembly with multiple moving parts to improve durability and eliminate the assembly of small parts. The nozzle was designed to have an accordion-type shape, inspired by various flexible nozzles and straws that are commercially available. The nozzle and nectophore were printed out of Stratasys TangoPlus flexible printable material to ease manufacture of the complicated shape.

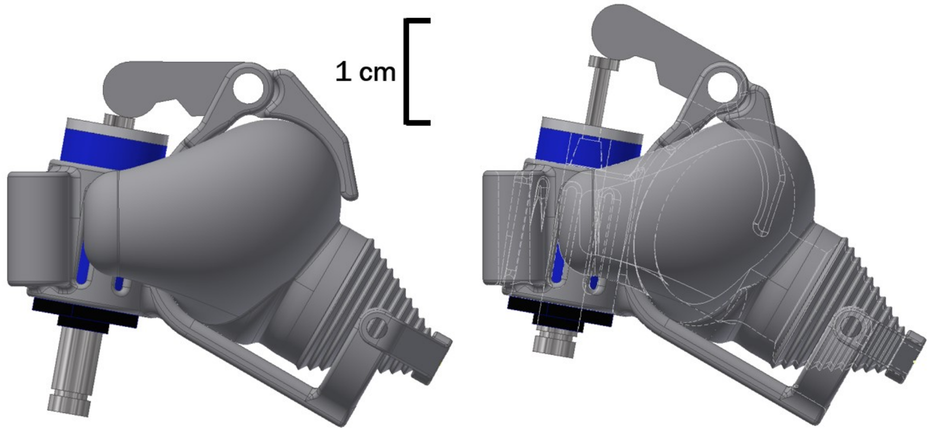

Figure 92 – First modular unit design. The solenoid (blue) was held in a frame rigidly affixed to a cradle around the nectophore, and when it was activated it moved a moment arm that forced the linkage to initiate contraction with a conforming plate. The nozzle top is affixed to a pivoting link to rotate up or down for different directions of swimming. The nectophore is increased in scale by 3.88 times the biological nectophores.

However, this design presented some problems that further eliminated once promising directions. While the solenoid produced an impulsive force and rapid speeds, the actual force when met with a mechanical resistance was extremely low. This was coupled with the fact that the TangoPlus material was relatively stiff and did not flex and rebound back into the original shape, but rather folded and held the deformed shape. The nectophore was iterated in wall thickness to balance the stiffness and ease of flexure, and the mechanical advantage of the contraction linkage was varied to balance stroke length and force output, but the linkage experienced very little movement during attempts at actuation. Therefore, the printing of models using TangoPlus was tried for a few designs but was quickly ruled out as a viable manufacturing option. In addition, it was determined that the small travel that was part of the stock solenoid design needed to be increased while also increasing force production. The large space of the solenoid behind the nectophore and the large space needed to clear the linkage and core movement where the nectophore should be nesting closely with the adjacent units resulted in large gaps between units, thus increasing frontal and surface area and unnecessarily increasing potential drag.

The improvement in the stroke length and force production was resolved by replacing the core with a 4mm low carbon steel machined and lubricated rod. To further increase the electromagnetic forces on the core, various arrangements of small neodymium magnets attached to the ends of the core were used. This was intended to provide a repulsive and attractive force for the coil to react with, thus imparting magnetic forces as opposed to purely ferromagnetic-induced directional ejection. The first iteration of this design was still a rigid cradle for the solenoid and nectophore, with the solenoid directly acting on the contraction motion of the nectophore cavity. A single neodymium magnet was attached to the core and the front of the nectophore, creating a single pole to repel and attract with the electromagnet.

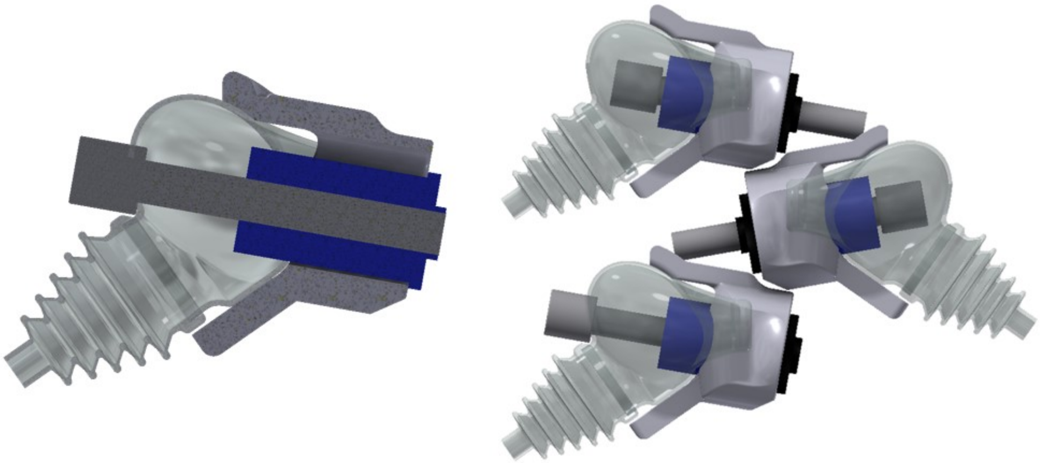

Figure 93 – Second modular unit design. The solenoid (blue) was held in a frame rigidly affixed to a cradle around the nectophore, and when it was activated it directly actuated the nectophore. The nozzle remained affixed to the opening of the nectophore model ostium, but actuation of the nozzle was not as important as improving contraction and hence was not actuated.

While the single magnet caused an augmented contraction force for the core, the stroke force was non-uniform. As the magnet was close to the core, the forces were high enough to move the core. However, as the magnet was further away during the actuation cycle, especially at the start of contraction with a high force requirement, the forces dropped due to the separation of the two magnetic fields. This is due to the inverse-square law of Coulomb's Law, whereas distance increases the attraction or decays repulsion force inverse quadratically. To reduce this loss at a distance, an additional magnet was added at the back of the core and the core was elongated. As the one magnet moved away from the coil the opposing magnet would move closer, causing a more uniform force response. The first version of the twin magnet core used magnets aligned to create a strong magnetic field around the core, which would be thought to react the most with the magnetic field of the coils. However, this caused the solenoid to just evenly push or attract at each end, resulting in a zero net force with only minimal force at the extremes of the stroke where one magnet dominated. The final design reversed the poles to create two ends that had like poles attached to the core. While the core wasn't magnetized except locally, the poles would always provide additive forces when the electromagnet was activated and polarized. During contraction the rear magnet would repulse strongly and the front magnet would attract weakly, eventually swapping strength but maintaining overall magnitude as the coil moved to the fully contracted position and subsequently relaxed when the electromagnet switched polarity.

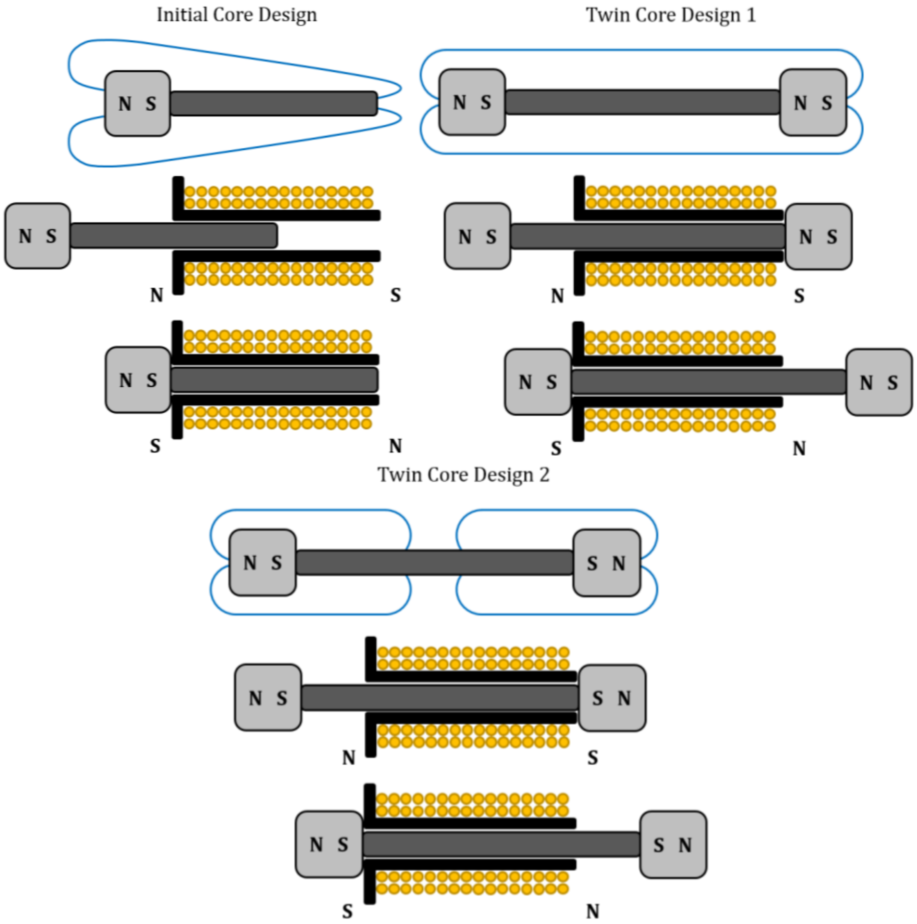

Figure 94 – Iterations of core design. The initial design (top left) consisted of a single front magnet, magnetizing the entire core as a weak magnet. The first twin magnet core design (top right) had poles aligned to form a uniform magnetic field, but received no force. The final twin magnet core design (bottom) aligned the magnets to form uniform force using a dual magnetic field.

The resultant jet production is shown in stills in Figure 95 with fluorescein dye showing the jet flow, where the single magnet even with stacked magnets formed a vortex ring with clear pinch off due to minimal movement and volume ejection. This performance was present at both 1Hz, a regular pace for a mechanical system, and 4Hz, the frequency at which siphonophores contract and relax. Although vortex rings are expected, the jet of *Nanomia* is clearly a strong, fast, low-diameter jet to maximize momentum flux. The dual magnet actuation resulted in a strong full contraction, which caused a visibly turbulent jet.

The reference video has provided a full deployment representative velum diameter of 0.434mm, and with a 1 m/s jet velocity the Reynolds number of the jet was expected to be

$$Re = \frac{uL}{\nu} = \frac{\left(1\frac{m}{s}\right)(0.000434\ m)}{1.004 * 10^{-6}\frac{m^2}{s}} = 432.27$$

which was very much laminar flow, which was as observed in PIV footage of the specimens. This design had a higher diameter of 2.5mm, the same kinematic viscosity, and an exit velocity of approximately 1 cm in 0.1 second (0.1 m/s) near the beginning of the cycle. Thus the improved jet had a Reynolds number of

$$Re = \frac{uL}{\nu} = \frac{\left(0.1\frac{m}{s}\right)(0.0025\ m)}{1.004 * 10^{-6}\frac{m^2}{s}} = 249.00$$

which was even more within the laminar regime. Therefore this jet was not turbulent in nature by the flow characteristics, but the stepped features of the nozzle induced tripping and mixing to add additional motion in the flow that prevented the typical laminar jet flow visualization.

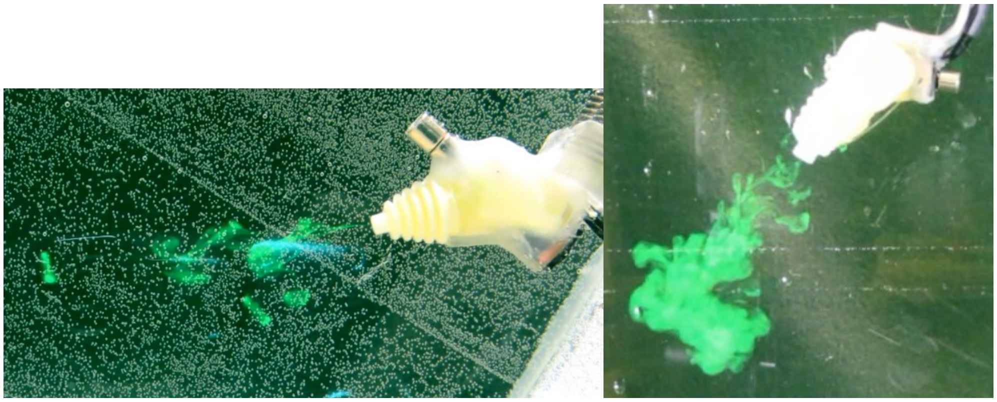

Figure 95 - Preliminary nectophore design with a single magnet (left) and new nectophore design with dual magnet (right), with morphology, orientation, and mechanics mimicking that of *Nanomia*. The trailing jet from the nectophores are shown with fluorescein dye, with the early design showing clear vortex ring formation due to low volume displacement and the new design showing a high volume but apparently turbulent jet.

The final frontal solenoid design with the commercial solenoid coil had a fixed jet diameter and angle that was set at the fully deployed orientation and size seen in the shadowgraph videos. The thin casting could allow the velum to flip inside the opening of the nectophore during relaxation, and hence mimic *Nanomia*'s velum motion to impart a differential thrust direction to minimize deceleration during refilling. However, some problems still remain with the solenoid design. The stroke length of the solenoid relative to the size of the nectophore, as well as the profile of the solenoid out the rear of the nectophore housing, still required spacing to clear neighboring actuators of moving parts and thus prohibitively limited the compactness of the colony. Since compactness is part of the drag-reducing elements of the colonial design, this should be considered a paramount goal for the final design.

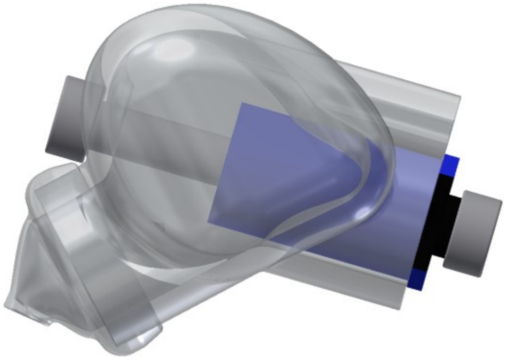

Figure 96 - Most recent nectophore design with a direct solenoid core, with biomimetic nectophore chamber, thin passive velar nozzle, and magnetically-forced bidirectional solenoid actuator. The solenoid is aligned to the contraction axis measured from *Nanomia*.

Therefore, fixed profile designs were explored to maintain the performance of the nectophore unit while reducing the space needed for the actuation stroke. This included two more traditional methods of actuation, starting with a crankshaft on an electromagnetic motor. While this design is simpler and has well established requirements for implementation, the motor required significant space to the back of the nectophore for the swing of the crank and to the side for the motor body. Small motors were still large relative to the nectophore, with was already significantly large relative to the animal, and did not have the position feedback used on larger motors and necessary for the proper indexing of the actuator for timing control of the cycle. Miniature stepper motors with a cable winch design were implemented, but the low stepping torque of the motors led to stalling under contraction loads. The next two solutions, using the PneuNet pneumatic actuator concept from Harvard and a novel design based on the iron lung machines, utilized pressurized air to inflate a chamber to reduce the nectosac volume. The PneuNet design used specifically shaped chambers to exhibit fast and high force responses of an already parametrically studied form (Mosadegh et al., 2014). The PneuNet had only been manufactured for linear starting shapes, so this curved form was completely new to the design methodology. The iron lung form utilized a rigid shape around a flexible cast membrane, and the space between the membrane and the shape either increased in pressure to bring the nectosac inwards to contract and the velum diameter inwards, or reduced in pressure with venting or vacuum to restore the nectophore shape and expand the velum diameter to the relaxed diameter to maximize refilling with reduced momentum flux. However, manufacturing the pneumatics with extra soft casting materials resulted in leaks and ruptures even at low pressure, and manual assembly of the multi-part pneumatics to form a proper seal without errors was difficult and at times impossible to complete.

Figure 97 – Iterations of low-profile actuator design. The crankshaft on a small motor design (top left) increases mixing inside of the nectophore and extends behind and to the side of the nectophore. The PneuNet nectophore (top right) and Iron Lung nectophore (bottom left) reduced the profile significantly by using air, but increased manufacturing complexity and reliability issues. A cable winch combined with a miniature stepper motor (bottom right) was attempted, but could not produce sufficient torque.

Thus, the design and actuation of the nectophore was changed back to the clearly promising form of the solenoid coil and augmenting magnets on a ferrous core. Multi magnet designs were attempted to improve stroke length with a reduced core length, but the interference of the magnets (especially at close proximity at full contraction) caused the fields of the coil and the magnets to redirect and dissipate to an unusable level. Therefore, a custom coil wound around a 3D printed resin spindle with an epoxy-coated magnet wire on a wire winding machine was formulated. An initial measurement of the contraction force needed to move the front of the nectophore inward found that the required coil-magnet system needed to produce more than 30 grams of retraction force. Analytical modeling of coil force production based on current and wire parameters of the original commercial coil was used to find a starting point for the custom coil, and iterations from this modeled design isolated a design that worked. The final coil was constructed with 30 gauge wire with 5.7 Watts of consumption and 228 Ampere-turns. The magnetic field strength of the coil, attraction neodymium magnet, and each with a ferrous core were measured at a 3 Volt activation with a Gauss meter. This combination of field strength to coil design was then modeled using classical magnetic attraction force equations to find the curve of attraction across the full stroke length.

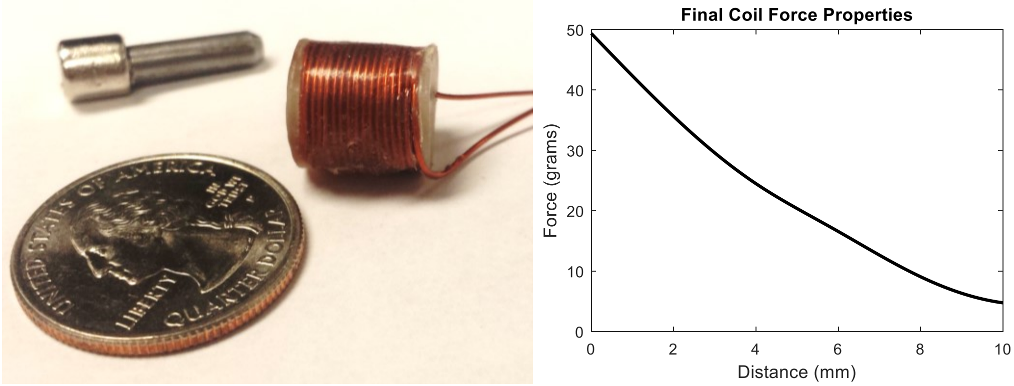

Figure 98 – New solenoid coil design (left) and the resulting force characteristics at varying distances through the stroke length.

This new coil was then implemented on the most recent nectophore design. A new nozzle design that accounted for the changing diameter found in biological specimens was designed, with inspiration from the control vanes of a jet engine. The vanes were actuated by a linkage attached to a sliding ring that only needed a short stroke to change diameter rapidly. Actuation was designed to utilize miniature electromagnetic coils on a static backing plate behind the ring and a combination of miniature magnets and ferrous cores that were attached to the ring. Although this design was elegant and functional at a large scale, producing sufficient force to slide the control ring with miniature electromagnets proved to be ineffective. An additional design with paddles that held magnets over the coils and attached to the vanes to directly actuate the radial displacement was attempted, but again the low force production of the miniature electromagnets and neodymium magnets restricted the applicability of this design at millimeter scale.

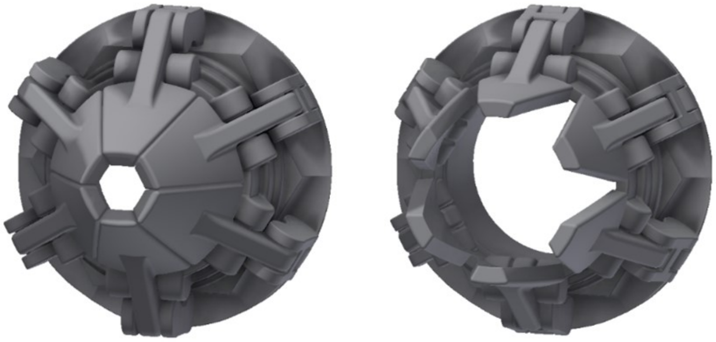

Figure 99 – Multi-vane nozzle with a sliding ring linkage that opens and closes the nozzle diameter with embedded electromagnetic coils and miniature neodymium magnets.

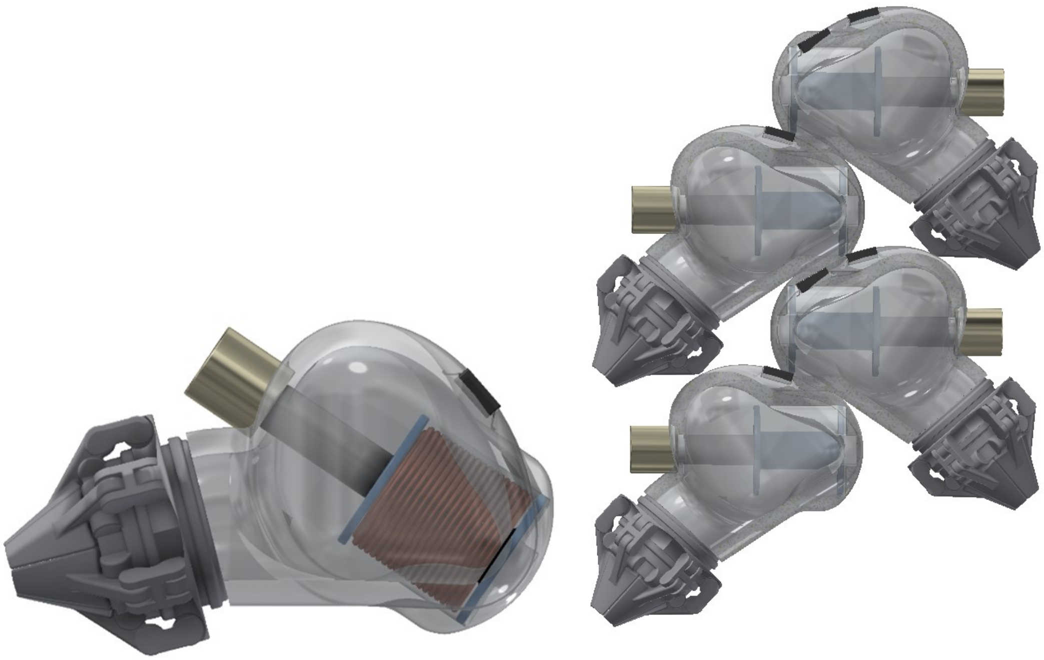

Figure 100 – New solenoid coil design implemented into the most recent nectophore model after adjustments for coil integration (left) and the full colony design using the coil actuator (right).

Therefore, a passive nozzle design was formulated to reduce actuator requirements at the millimeter scale. The nozzle consisted of three main sections. A rear tube section attached to the front of the nectophore and directed the flow to the correct angle. A frontal section then snapped into this rear portion to form cylindrical sliding bar and a hollow cavity. The front had two main openings – a 2.5mm central tube that was always open, and openings arranged radially around the central column. A slider slipped on the central column and caught the flow to control which openings were active. When the nectophore contracted and fluid flowed through the nozzle, the cupped back end of the slider caught the flow and quickly moved forward to block the radial openings. When the nectophore relaxed, the low pressure inside the nozzle pulled flow through the radial openings and thus pushed the slider back. The central jet bore was tapered following tabulated radius values to minimize head loss on entry or exit, and the hollow cavity was dimensioned such that when the slider was in the back position during refilling the cross sectional area along the flow path was equal to or greater than the opening cross sectional area.

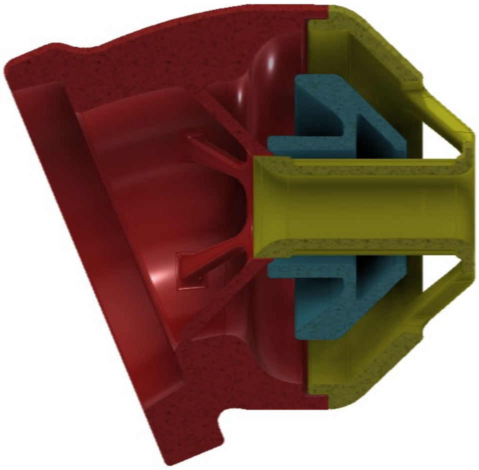

Figure 101 – Final passive nozzle design with rear attachment and redirect section (red), front open cavity with multiple openings and a central column (yellow), and a flow control slider (blue).

The prior presented study of nectophore motion obtained additional views that indicated a symmetric lateral contraction from the circular muscles in addition to the front deflection inward. Rear-directed solenoid actuation for the front deflection only brought in the center of the nectophore, consumed significant space between units that thus reduced the close packing of the nectophore units, and introduced potential interacting magnetic fields with proximal electromagnets and moving magnetized cores. Additional designs with gear, linkage, and cable driven couplings that brought a larger front surface inward and also contracted the side walls of the nectophores were designed and tested, but none of the designs were capable of producing the force for all components of contraction. Increasing the magnet or coil design would only increase the problems present with the centerline actuation method. Therefore, the lateral contraction was targeted to allow integration of actuators into the cavity of the nectophore without external protrusions to contain the coils. The lateral arrangement also allowed space for the nectophore to fold along the symmetric centerline at full contraction to passively eject more fluid from the cavity. The design originally included either a central electromagnet with magnets and ferrous cores on each side wall or an electromagnet on one side wall and a single ferrous core and electromagnet on the opposite side wall. However, the dual magnet design had interactions between the two strongly concentrated magnetic fields, especially when the magnetized cores attracted to each other at close proximity at peak contraction. This high strength attraction at the end of contraction also reduced the ability of the electromagnet to separate the polarized cores for passive or active relaxation. The single core design found similar limitations that were encountered with the centerline actuation, including excessively long stroke length that caused a limited field interaction strength for contraction and required protrusions out of the side wall to enclose the moving core.

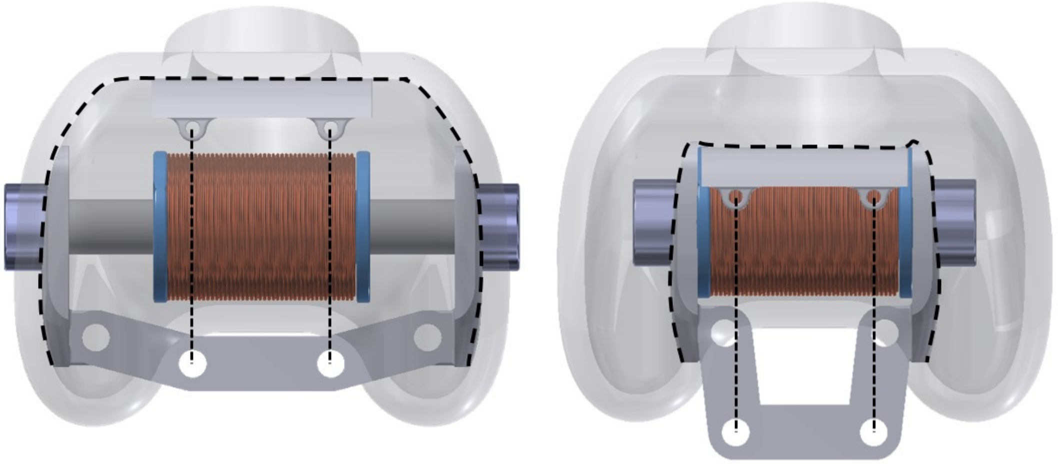

Figure 102 – Combined single central coil, dual lateral magnetically polarized cores with linkage and cable driven frontal contraction concurrent with lateral contraction.

Therefore, the reverse design was attempted and found to be the best solution. A 1/2 inch diameter and 1/4 inch depth neodymium magnet was adhered to the back wall of the nectophore cavity at the centerline with cyanoacrylate adhesive. Two ferrous cores were attached to the magnet and extend laterally in the cavity. Electromagnetic coils were then form fit to the side walls of the cavity, wound with copper wire, and adhered using cyanoacrylate glue to the side wall. This produced a dual coil design that, when activated, contracted the nectophore laterally without significant field interaction. There was some interaction since the cavity transmitted stress, and thus contraction required higher forces as the coils synchronously moved inward and relaxation was passively forced open from residual stresses. The coils had protrusions upwards and rearwards to locally reduce flexion and thus force the cavity along the center walls to bend under stress. While a PTFE coil pair has been machined to improve dimensional stability as the coil heats and reduce friction, the mass production of the coils was completed with the VeroClear 3D printing resin. A future design should use the PTFE coils due to superior performance. The wings could be cut by hand or milled after a simple spindle shaping on a lathe, and then bent to match the nectophore curvature with simple pressure to induce yielding. The final core was actuated at 12 Volts and 1A, with 360 ampere turns for additional strength. The coil wire was reduced in diameter to 34 gauge to increase the voltage and reduce the current. Since the colony chain included multiple units, power transmission at high current and low voltage was undesirable due to losses from resistive heating. In addition, power regulation and control at low voltage and high current requires larger and more costly components, which was unacceptable for a small scale compact design with duplicate power and control components. This new nectophore design was then attached to a rigid 3D printed resin central column that was hollow to allow the routing of cables. Control electronics for each nectophore, the motor controller and AT-Tiny85 with additional resistive and regulation elements, were adhered to the column and under the nectophore to enable close packing only proportionally different than the animal by 1 mm. The cast nectophore was derived from the final biological form, with small additional features to improve electromagnet clearance when moving inward as the thin walls concurrently folded into the cavity. The biological nectophores, and thus the cast nectophores, had a centerline notch that localized lateral folding to the centerline to further constrict the nectosac volume.

Figure 103 – Final cast nectophore design with additional features for solenoid coil and ferrous core clearance.

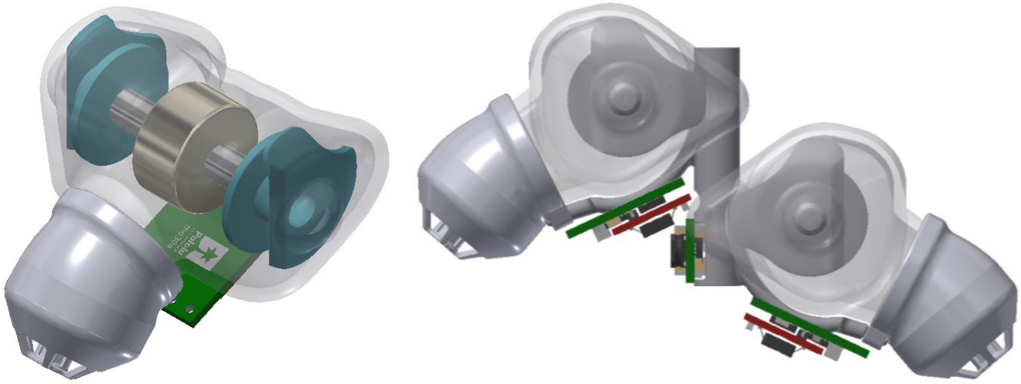

Figure 104 – Final nectophore design with lateral solenoid coil and magnet arrangement, passive nozzles, and control electronics arranged around the nectophore. Each nectophore pair is attached to a central rigid column with cradles around the nectophores.

5.3. ***Biomimetic Maneuvering and Control***

5.3.1. LQR Optimal Control Framework

For the practical implementation of an optimal trajectory planner, especially one that can rapidly compute trajectory and control inputs, the system dynamics and control limitations must be understood and handled appropriately. As with any underwater locomotion, the motion of these robots is highly nonlinear due to state-dependent drag, inertia, and thrust vectoring. This locomotion method also requires the pulsation of thrust, with the refilling phase needed after each ejection to collect fluid for ejection in the subsequent cycle. This level of complexity, including the time-variant waveform of the thrust, has been simulated in detail and controlled in one study in our research group using a complex sliding mode controller in discrete and continuous time (Faria et al., 2013).

However, implementation on a small physical platform driven by only digital microcontrollers requires the algorithms to be simple but effective. This would require the true dynamical complexities to be reduced, lending the solution to an adaptation of proven linear optimal control methods. The optimization would prioritize reducing energy expenditure for locomotion, establishing time variant requirements for the jetting chain on each side of the planar bi-serial body. These time varying requirements for the control forces can then be interpreted by a predetermined library of possible motions, and then into individual actuator control using PID position control or simple open loop voltage control. This distributed multi-stage control system, driven by a reduced order optimal control algorithm, would provide robust but efficient and rapidly computed control of efficient locomotion for future long mission duration robot platforms.

Since this system will have limited possible control inputs from the predetermined gait library, as well as execute discrete point-to-point trajectory controls, a dynamic programming algorithm would lend itself to solving the nonlinear system by using constraints to reduce problem complexity (Lewis et al., 2012). However, the near infinite possible intermediate states, long total operation durations, and limited computational power for establishing a path possibility graph and searching for the optimal control framework would make this approach infeasible for small robot implementation. The nonlinearity of the fluid and thrust production dynamics makes traditional linear optimal control approaches less than feasible, and initial linearization of the problem severely underestimates the nonlinear effects since the system velocity and orientation can rapidly change over several orders of magnitude. Nonlinear control is in general an unsolved, highly variable field with system-specific solutions available in literature, usually for submersibles with sufficient room for computing power.

For this study, the system is characterized completely in its full complexity nonlinear form to accurately establish the fundamental system dynamics and forcing input responses. This system is then locally linearized at each time interval, and the local solution for the state space matrices is subsequently discretized for the duration of each cycle to lock in inter-cycle fluctuation during propulsion. This locally linear, discrete model is then implemented with the State-Dependent Riccati Equation (SDARE) to generate a near-optimal path while approximately accounting for global nonlinear dynamics.

This section will discuss the formulation of the fundamental system dynamics in the context of expected system design and use. This fundamental model will be specialized for two cases, linear and planar motion, where the simplification, linearization, and solving process for the SDARE algorithm will be outlined. The resulting performance of these two discrete cases in simulated examples, as well as the performance and algorithm details and limitations, will be detailed. Finally, the resulting conclusions and future expected work in the context of robot implementation on a physical aquatic autonomous robot will be discussed.

5.3.1.1. Problem Formulation

For this study, the control of a siphonophore-inspired robot is primarily studied. The general dynamics, with changes in control inputs from different propulsion mechanics and known shape factors for drag, can be applied to jellyfish inspired robots as well. In both cases, the control architecture of the robot is based on the neural framework of the basis species. The control can be split into three primary and unique stages that are independent but functionally connected. The central stimuli response (Stage 1a) takes sensory input to establish a goal position relative to the current position based on mission objectives. This goal position, as with the animal, can be based on daily migration, a gradient of a key criteria requiring more inspection, surfacing for communication and recharging using solar energy harvesting, or returning to a station position after an external disturbance. These control requirements are then converted, via a natural neural network (abstracted into a clever closed-form algorithm or an Artificial Neural Network) aware of system capabilities via a library of gaits, into global frequency, timing, and patterning inputs (Stage 1b). Combined with proprioception of each unit and actuator dynamics, this signal is interpreted by localized microcontrollers into local jetting unit output (Stage 2). A local PID controller commands the actuator dynamics based on tuned controller gains. Stage 1b and 2 are correlations learned or prescribed offline, and are impractical to combine into a large comprehensive system model due to the complexity and variety of possible system behaviors. In addition, observations of the animal locomotion methods, combined with the system response characteristics obtained from system identification, provides a discrete set of known classes of gaits that can be hard-coded and varied in an interpretive step. These extra steps are either already implemented on microcontrollers, or require additional system identification for each version of the robot system for each application.

Therefore, the goal of this study is to complete the sensing and path planning stage of the algorithm after the sensor signal preprocessing. To minimize energy expenditure to extend the potential operational duration, the trajectory will be optimized to minimize control effort while simultaneously minimizing positional error at the end of the maneuver to a goal position. The trajectory will account for the position and orientation throughout time, although final velocity and orientation are not the priority and are given a wider acceptable error threshold. Orientation can be adjusted by an inflatable float on the robot and fine control at the target position. As described, the system input will be discretized to an aggregate cycle-averaged force input from each side of the serial chain of jetting units. Lateral forces from the jetting bodies are present in the system due to the angled orientation of the individual jets, but significant broad profile drag and balanced nectophore numbers approximately cancel or dampen out any lateral impacts on the kinematics. Since the robot control is purely planar, as with the animal, the system dynamics and motion are only considered in a planar constrained motion where out of plane motion is uncontrolled and dampened out by drag. Considerable out of plane motion can later be corrected with an orthogonal optimal path planning for a jellyfish robot, and the siphonophore robot is incapable of out of plane control and thus the effects are inconsequential.

5.3.1.1.1. Fundamental Dynamics

To appropriately characterize this planar motion, the six states of interest are horizontal position of the center of mass (X), vertical position of the center of mass (Y), angular orientation of the body major axis (θ), horizontal velocity of the center of mass ($\dot{X}$), vertical velocity of the center of mass ($\dot{Y}$), and angular velocity of the body major axis ($\dot{\theta}$). The two inputs into the system (F_{left} and F_{right}) represent the axial force vectors at the periphery of the left and right side of the body, respectively. These vectors are separated by the diameter of the body measured at the opposite outlets of the jets on each side. These force vectors each impart a forward thrust force and opposing moments, with the relationship:

$$\begin{bmatrix} \dot{X} \\ \dot{Y} \\ \dot{\theta} \\ \ddot{X} \\ \ddot{Y} \\ \ddot{\theta} \end{bmatrix} = \begin{bmatrix} 0 & 0 \\ 0 & 0 \\ 0 & 0 \\ \frac{cos(\theta)}{(1+\alpha)m_c} & \frac{cos(\theta)}{(1+\alpha)m_c} \\ \frac{sin(\theta)}{(1+\alpha)m_c} & \frac{sin(\theta)}{(1+\alpha)m_c} \\ \frac{-d/2}{I_{rot}} & \frac{d/2}{I_{rot}} \end{bmatrix} \begin{bmatrix} F_L \\ F_R \end{bmatrix}$$

The $(1 + \alpha)m_c$ term represents the mass plus the added mass coefficient. Added mass represents the mass of fluid moved with the body as the body moves through the fluid, and it was estimated for a long streamlined body of diameter d and length L as $0.541\left(\frac{L}{d}\right)^{-1.4}$ (Munk, 1922). These dimensions were estimated using the current CAD model of the robot. The mass and rotational inertia of the body was estimated as a cylindrical body with a geometrically centered Center of Mass about which the body rotates and is tracked in this study. The density characteristics are assumed with equivalent average density of that of water (necessary for neutral buoyancy) and half spatial infill (to account for scalloped and hollow components). It should be noted that the resulting forcing term is nonlinear due to the angular dependence of global Cartesian frame linear acceleration to the locally axial thrust force. The system dynamics matrix was established as a linking of the equivalent states and state derivatives, and the deceleration due to velocity-based drag:

$$\ddot{X} = -\frac{\dot{X}abs(\dot{X})\rho S(C_{D,a}abs(cos(\theta)) + C_{D,l}abs(sin(\theta)))}{2(1+\alpha)m}$$

$$\ddot{Y} = -\frac{\dot{Y}abs(\dot{Y})\rho S(C_{D,a}abs(sin(\theta)) + C_{D,l}abs(cos(\theta)))}{2(1+\alpha)m}$$

$$\ddot{\theta} = -\frac{\dot{\theta}abs(\dot{\theta})(\frac{L}{2})^2\rho S(C_{D,l})}{2 * 2I}$$

The linear drag components were derived from S (the surface area of a cylinder of equivalent diameter and length), $C_{D,a}$ (the drag coefficient of an equivalent aspect ratio streamlined body in axial flow from $Re = (10^4, 10^5)$), $C_{D,l}$ (the sum of the skin and pressure drag coefficients for an equivalent cylinder in axis normal flow from $Re =$

$(10^4, 10^5)$), and inertial properties. The drag was scaled to the proportion of flow in the axial and lateral directions (i.e. axial motion is pure streamlined drag, and sideways drift is lateral broadside drag) (Hoerner, 1965). Rotational drag was estimated as a triangular tangential velocity of a cylinder, reduced to a uniform average velocity, in the lateral direction, with the mass normalization completed with the rotational inertia. Note that the true angular velocity for the tip of half of the body is $\dot{\theta}\,\frac{L}{2}$, where the average velocity is that measurement divided in half. The square of this velocity, and then multiplied by two for the two ends on each side of the center of mass, results in an additional 1/2 drag multiplier. Once again, these dynamics include an angular dependence to resolve the 2D global motion into the Cartesian component velocities, as well as the square of the velocity states to determine drag. This results in nonlinear dynamics, which coupled with the nonlinear input response indicates a completely nonlinear, state-dependent system.

5.3.1.1.2. Temporal Representation

Previous attempts to control this nonlinear system, particularly for a rowing jellyfish inspired robot (Faria et al., 2013), accounts for the time-varying pulsed dynamics of the ejection and refilling phases. In addition, the multi-jet nature of the siphonophore includes multiple fluctuations combined as a net system response in continuous time. In order to reduce the input complexity to time invariant dynamics for implementation and collapse the rapid and small magnitude fluctuations, the system is represented in continuous time differential equations, combined into a continuous time state space model, and discretized at the cycle frequency (4 Hz) to take the cycle average forcing and dynamics change for each step. This update frequency is rapid enough to account for full robot changes in dynamics and have minimal losses in resolution. Future work on the jellyfish model, since the cycle time is close to 5 seconds, may need to reconsider the discretization in terms of losses of resolution that compound into control-response error.

5.3.1.1.3. Control Output Limitations

Since the cycle average output of each jetting thruster is limited to positive thrust only (negative thrust during jetting is only possible in very specific biological cases that are not implemented on the robot, and negative thrust during refilling is part of the cycle average and reduced based on nozzle kinematics to a negligible magnitude). There are methods for constraining the control output for optimal control, but the limitation was implemented in the framework of the LQR controller (Heemels et al., 1998). First, the biological limit of about 0.9 mN per jetting unit was found in recent modeling in our group, and this was estimated for the robot by scaling the thrust proportional to the cubic increase in scale (therefore scaling thrust with mass). The true force of the jet is equal to the density of the media times the area of the outlet nozzle opening times the squared velocity of the jet. Density of the jet held as that of water, the area is increased by a squared rate, and jet velocity increased (volume change increased cubically, jet duration time was held constant, and the outlet area increased at a square rate, resulting in a linear increase in jet velocity, and thus a squared increase in the velocity squared term), and thus true force would increase at an approximate quartic rate. Since a faster jet could have efficiency losses due to turbulence or jet mixing, the cubic increase in thrust is kept in the model as a conservative estimate.

This thrust limit is then multiplied by the number of jetting units on each side of the chain, providing an absolute maximum for each side's input. The limit was enforced by clipping any input less than zero and larger than this limit. The tuning of the R term was then used to reduce the input magnitude to the system to provide the position response accuracy desired while also minimizing or eliminating clipping. Since the system is updated each iteration (described in later sections), any clipping should be inconsequential except for some loss in optimality due to artificially lowered input relative to the absolute optimal solution and thus minor imperfections in regards to performance.

5.3.1.1.4. 1D Axial Motion Control

The simplified case of one dimensional, purely axial motion has been significantly studied in the biological motion of siphonophores (Mackie, 1964). Therefore it is logical to start the exploration of optimal control in this one dimensional, reduced complexity case. The dynamics follow the second order differential equation for just the X direction, with the drag term only accounting for axial motion and thus removing a thrust and drag dependency on orientation. The quadratic drag was then computed for the velocity range from still (zero velocity) to the maximum simulated velocity (0.5 m/s for a timeframe of

30 seconds), and linearly regressed to a first order drag term based on the velocity. This resulted in a model of:

$$\begin{bmatrix} \dot{X} \\ \ddot{X} \end{bmatrix} = \begin{bmatrix} 0 & 1 \\ 0 & F_D \end{bmatrix} \begin{bmatrix} X \\ \dot{X} \end{bmatrix} + \begin{bmatrix} 0 \\ \frac{1}{(1+\alpha)m} \end{bmatrix} \begin{bmatrix} F_{Thrust} \end{bmatrix}$$

This linearized model was then discretized at 0.25 second steps and controlled using a state feedback controller via a Linear Quadratic Regulator (LQR) framework for a nonzero fixed final state at a fixed final time (Lewis et al., 2012). The Q matrix (2x2 matrix) was set to zero and the R matrix to 1 (1x1 matrix) to purely optimize the control based on a cost function of the square of the input, which is an analog for optimizing energy. This was then simulated with higher control cost gains and various time spans to estimate the starting conditions of the 2D case and understand the cost relative to the tuning parameters.

5.3.1.1.5. 2D Planar Motion Control

The full case of planar motion was also studied using the fundamental system dynamics. Since the system in the planar frame has additional nonlinearities due to local orientation relative to the Cartesian coordinates (which are used for position determination), simple linear regression was not sufficient for this problem. Therefore, the components of the constraining dynamics matrices were locally linearized using finite differences, and subsequently implemented in combination with the State Dependent Discrete Time Riccati Equation (SDRE) algorithm to accurately represent a simplified subset of the system (Cloutier, 1997). At each time step, the B matrix terms for linear components were evaluated for the current angular orientation of the system. Since the linear and angular acceleration terms for the system dynamics matrix A were velocity and orientation dependent, the elements of the matrix were assessed as the local partial derivative of the acceleration differential equations with respect to the multiplying term to determine the locally linear dynamics (Beeler, 2004). At the beginning of each time step, the partial derivatives were updated based on finite differences around the current state, keeping the nonlinear effects in the system with time evolution of the dynamics while enabling classical linear optimal control methods. The step size for the finite differences were tuned to appropriately estimate a reasonable bounds without over or under estimating with large or small bounds ($\delta\dot{X} = 0.03\frac{m}{s}, \delta\dot{Y} = 0.15\frac{m}{s}, \delta\dot{\theta} = 0.1\frac{rad}{s}, \delta\theta = 10°$). For the drag matrix coefficient terms relative to velocity, a maximum of -0.01 for linear translation and -0.0001 for rotational rate were implemented to eliminate instability at low velocities. A constant term to represent the solution for the drag, added mass, and inertial resistive forces induced deceleration at the current state was added to the system dynamics matrix to add a center point that each partial derivative would augment to introduce deviation. This linearized continuous time model was then discretized using a zero order hold method, which was then fed into the discrete time algebraic Riccati equation solver DARE to find the state feedback gain terms for the current inputs to the system. The continuous time algebraic Riccati and a post-discretization method was also tried, and no noticeable difference was found. In order to clip the force inputs, the calculated control input term was calculated and compared to the bounds. Any negative inputs were set to zero gain, and any large inputs were clipped by assigning the gains as the max input limit times the pseudoinverse of the current state vector to result in a max input force when re-multiplied by the current state vector. The gains of the R and Q matrices were tuned to improve the accuracy of the final results, as well as reduce the input magnitudes below the limits. Long time frames with low input provided a smoother response with a generally lower cost.

In order to make this approach applicable to any form of the algebraic Riccati equation solution, the initial and final target states were transformed so the final state is moved to the origin with an orientation of zero degrees. The initial position was translated by the difference between the states, and the translated points are rotated around the origin using the planar rotational transformation matrix. In the plotted example, the initial position is at $\left[0\ m;\ 0\ m; \frac{\pi}{2}\ rad\right]$ and the final position is located at $[-2\ m;\ 5\ m; \pi\ rad]$ (with zero initial and final velocities), so the initial position was moved to $[2\ m; -5m]$ and rotated to $[-2\ m;\ 5\ m; -\frac{\pi}{2}\ rad]$.

5.3.1.2. Results and Discussion

5.3.1.2.1. 1D Axial Motion Control

The quality of fit factor R^2 for the linearization of the drag was assessed as 0.949, which is considered to be a very good fit for a linear estimation and within acceptable error bounds. For a 30 second operation time simulation, the optimal control produced a cost of about $J_{0,30s} = 0.2778$. The control inputs were only clipped at the end due to a low magnitude deceleration required when the goal was reached, but residual orientation velocity error is of less concern than position error. This response is exactly as expected for this type of motion - a throttled acceleration to a steady state speed to eliminate inertial effects and maximize the effects of momentum, and then prior to the goal decelerate and allow drag to slow down the system by gradually removing thrust in a controlled stop. This simulation can be accelerated with acceptable thrust magnitude down to a 12.5 second maneuver, but the increase in cost to $J_{0,12.5s} = 0.7198\,(2.59 * J_{0,30s})$ should be considered when balancing operational expediency to lifetime of the limited power supplies and fatigue on the actuators. This suggests that a longer time frame, within reason, is overall more optimal and energy efficient. This particular simulation of the robot traveling 10 meters in under 30 seconds, for a robot less than 0.12 meters in total length, is surprisingly effective and still a very reasonable performance expectation.

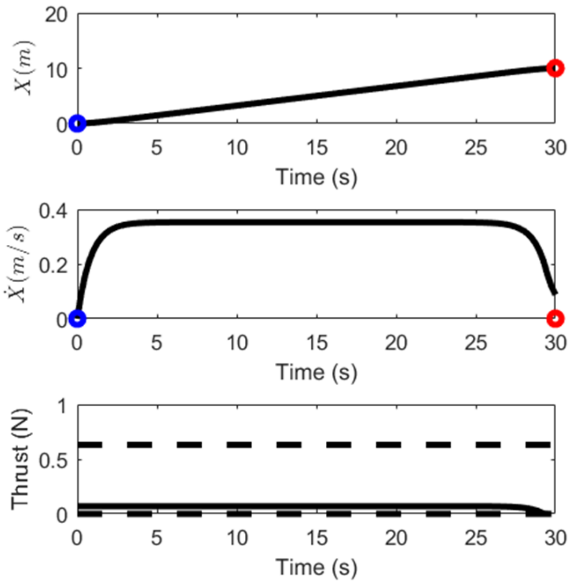

Figure 105 -30 second response time position, velocity, and thrust profile

5.3.1.2.2. 2D Planar Motion Control

The 2D case of the trajectory control was finely tuned to ensure the completion of the trajectory, the reduction of the magnitude of the control inputs, the accuracy of the drag estimation with a Reynolds number less than 10^5, and improve the accuracy of the final and closest passing point. The final weights for the Q state weighting matrix were set initially as an identity matrix (even unity weighting for all states) and the position and orientation states on the upper half of the matrix were weighted with an additional 10 times the normalized magnitudes of the initial condition before transformation. This made the furthest distances penalize the most to drive fast towards those states, and relatively weight less aggressively states that were closer to the initial condition. The first three states were then weighted with a multiplier of 2, 15, and 2, in that order. While the intended target of this optimization is to minimize energetic cost, a pure identity or zero matrix affects stability for the algebraic Riccati equation solution and allows an efficient path with significant and unacceptable levels of position error. The cost weighting matrix R was weighted as 30×10^5 on the diagonal to drive control effort down. The resulting control achieves 0.16 meters X error, 0.04 meters Y error, and -21.50 degrees orientation error at the final step relative to the desired final state. These are achieved at 0.00 m/s, 0.00 m/s, and 0.04 deg/s velocities, respectively, which is accepted as a near still state. At the closest point to the final point during the trajectory, the X error was only 0.02 meters, the Y error was only 0.10 meters, and the angular error was only -13.37 degrees (with a 0.02 m/s, 0.00 m/s, and -0.93 deg/s velocity state, respectively).

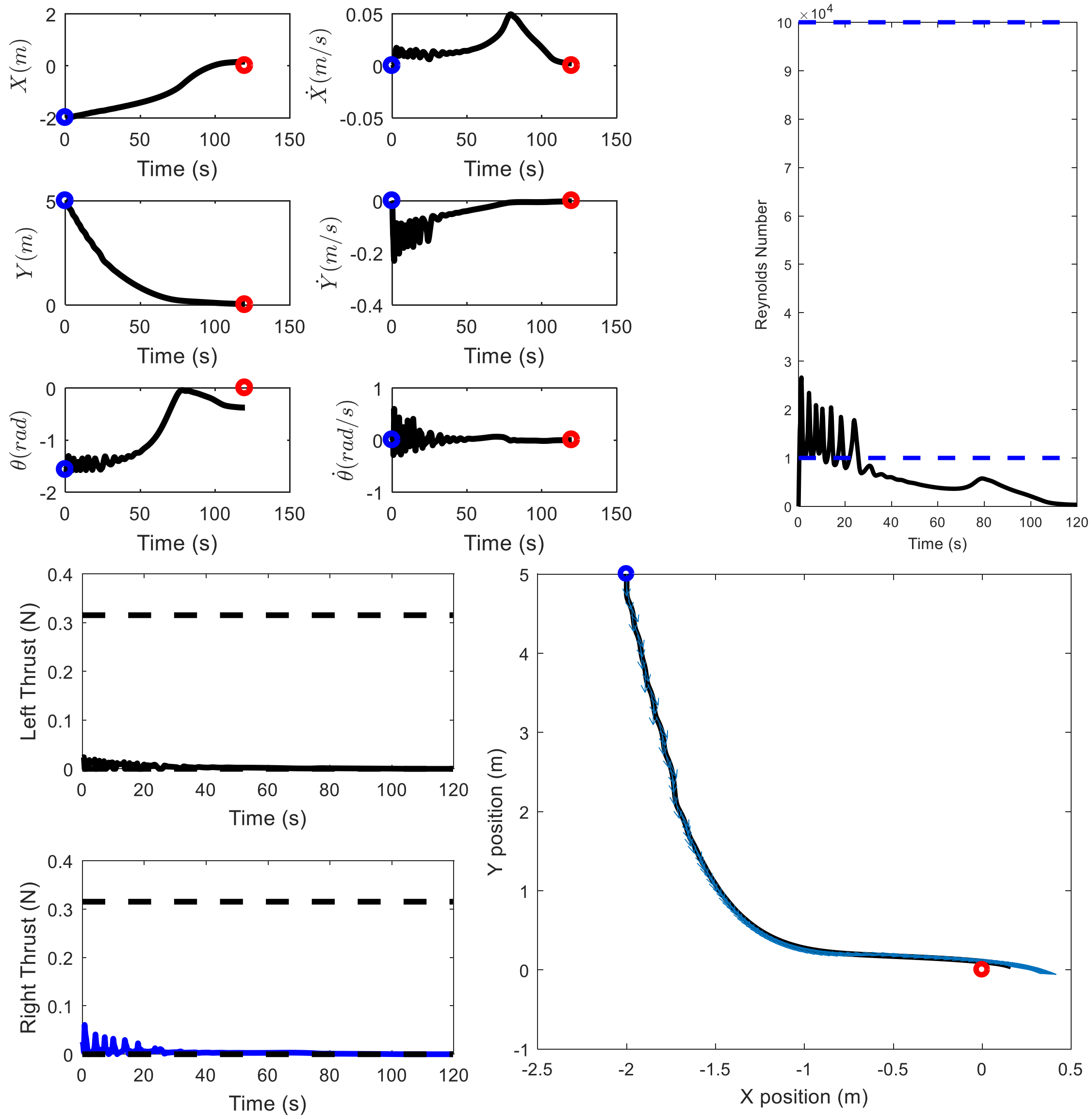

Figure 106 – Time histories of state vectors (upper left), Reynolds number (upper right), left and right thrust (lower left), and trajectory path (lower right)

This trajectory path is actually indicative of the patterns seen with natural siphonophore motion. From rest the initial acceleration has been observed to slightly oscillate laterally as speed is picked up and asymmetries are balanced (many siphonophores start by high forward thrust and then uncontrolled drift forward and sideways) (Mackie, 1964). As momentum is built up during the acceleration phase, these oscillations and asymmetries are added with the momentum of the system and generate smoother, broader curves with damped out oscillations due to increased drag at a higher speed. Another interesting feature of this trajectory is how the X-translation is achieved. For the beginning of the trajectory both control inputs are working to approximately achieve forward motion in the Y-direction. However, at the 20 second mark the control inputs drop in magnitude, halt in oscillation, and decay towards zero input. This, in addition to the initially higher right thruster output, uses the momentum of the system to initiate an almost negligible energy smooth glide towards the target in the X direction.

5.3.1.2.3. Conclusions and Future Work

This control scheme produces a near-optimal trajectory, with room to improve with extensive tuning, for guiding a siphonophore inspired robot from an initial position, orientation, and velocity to a final state within a specified amount of time. The commonly studied 1D axial case, as well as the more interesting and applicable 2D planar trajectory control, are constructed using the state dependent, locally linearized version of the discrete time algebraic Riccati equation for suboptimal control.

It should be noted that while video footage of siphonophores shows rapid and quickly controlled locomotion, this study has supported the hypothesis that low speed and static fine control and dynamic slow heading control (due to forward momentum, the small separation of the jetting bodies laterally across the body, and reduction in turning capacity at high speeds due to high drag) need to be studied separately with the understanding that fast motion results in smooth motion that is constrained to a mostly axial path. On the contrary, broad rowing jellyfish never reach high velocities and can turn sharply as needed, providing a counter-case in terms of maneuverability and speed over multiple body plans. The representation of this system to enable the application of linear control methods does inherently limit the accuracy of the solution. By locally linearizing and driving the control law, significantly rapid and high magnitude changes over time can be limited and this method has been proven to work. In addition, the slow and long duration performance has been proven to help lower cost. However, since the control is below the maximum and may be able to drive faster to the goal, the system may be able to be tuned to change kinematics faster at the expense of continuity between local linearization between steps. The full parameter space across values is quadratic with respect to speed for drag, and is periodic in nature with respect to the angle due to the decomposition to direct the inputs and external forces. This is highly nonlinear in nature, and full range linearization is not likely to be possible. The fine tuning of speed of movement, final position accuracy, and the cost of the total path should be fine-tuned as the control system is adapted for and implemented on the physical robot. The limitations of this system with a pulsed input represented as a cycle-averaged signal, as well as the lack of negative thrust for braking operations, limits the ability of this system to ever perfectly arrive at a goal and stop. The non-smooth external structure of the robot would likely increase drag-induced braking and improve true stability, but this has yet to be conclusively determined. When the signal is not clipped to positive only values, the robot model tended to approach the point, overshoot, and zig-zag towards the point with a broad angle to allow an approach without having to heavily brake a high speed driven, direct approach. True system identification of the true system behavior in a water tank with high speed cameras and variable input code, or at least better characterization of the components going into the model, would help improve model fidelity and close the gap between expected modeled performance and true physical system performance. In addition, the positive-only with an upper bound limitation is still solvable, but a more specialized method for avoiding the extremes and optimizing with the prior knowledge of the control constraints would make the motion solution more practical and better than the current restricted suboptimal solution (Chang and Bentsman, 2013; Heemels et al., 1998). In addition, this methodology is general enough that the adaptation of the model and optimized control for a jellyfish robot would be possible. This would require redefining physical dimensions, adjusting the shape-factor of the drag coefficients and curves to a more oblate and non-streamlined circular shape, and characterization of the effects of vortex ring momentum asymmetries on turning dynamics as well as how to represent that turning technique as a forcing matrix of inputs. This would still be less complicated and quicker to compute than the sliding mode controller previously made in our research group. However, the cycle average method may become less feasible due to the 5 second cycle time, allowing the cycle-averaged dynamics to cause further inaccuracies in that cycle time span. Further physical characterization, implementation on a microcontroller architecture with shared overhead for other system-wide routines, and testing with the SDRE method is needed to ensure that the generalized method would work in this other critical low-energy system developed in our research group.

5.3.2. Biomimetic Maneuvering Gait Implementation

As mentioned in the connection architecture of the robot and the gait patterns identified from the biological reference videos, the gait can be established as a closed-form series of patterns. The core of each pattern was a central timing, global establishment of the gait by an additional signal to form a twin giant axon inspired control form, and gait-based delays of a contraction pattern from the central timing based on the known position along the chain.

The initial system design started with a setup on the system boot which read in the resistor drop voltage and input voltage, which in a closed form provided the position of the robot in a calculated chain length. This provided the basis for gait delays. The solenoid output was an expedited digital signal output. Whenever the clock square waveform changed state, the time of the state change was recorded in a buffer queue. Every cycle of the runtime loop checked if a state change had happened and if the state change was urgently needed at the time due to the calculated delay for the nectophore position and gait. The timing parameters were also checked to see if the clock overflowed or was about to overflow, and handled the timing corrections accordingly. This included verifying that current time did not roll over since the buffered previous change time and, regardless, that the true rollover-compensated time was necessitating a state change. If a state change was needed, it was triggered and the buffered time was removed from the queue. Time was sampled before each decision. In the case that a serial update was needed, the serial line was read and the gait delay was changed accordingly. Since serial communication was time-intensive, this check allowed the code to quickly loop and lose minimal cycles with communication by only accessing urgent updates. This time-optimized code allowed rapid gait changes and minimal lost cycles, while also being fault-tolerant against missed actuated or input clock cycles. This architecture of the prescribed gaits and response to the clock cycles and serial inputs has been validated on the A-Star Micro microcontroller using an oscilloscope to monitor the digital outputs under varied conditions without reprogramming.

Since the A-Star Micro was too large for the individual units, the AT-Tiny85 was selected for a small scale microcontroller that can be embedded or placed around the nectophore. The initial iteration with a positive-only control using PWM through a transistor with a fly-back diode for the solenoid coils was adopted from the code verified for the A-Star. The primary changes were streamlining of the code for a smaller memory capacity on the Tiny microcontroller, removal of native libraries and inclusion of a software serial library, and the use of different clock architectures on the chip for Fast PWM instead of phase- and frequency-corrected PWM output. This output was still possible, but had limited controllability with the adjustable parameter registers available on the chip. Once the bi-directional control was needed for the coils, the pin arrangement was moved to allow for a digital output and a serial clock bit instead of a dedicated interrupt line for the digital input. It should be noted that the timing was changed from a microsecond scale to a millisecond scale due to the reduced actuation frequencies, so the clock roll over was no longer a short-term concern and thus the roll over compensation was removed. This code was once again verified to function for varied gaits and desired outputs.

For the robot testing performed, the architecture with one microcontroller for each side of the robot was utilized. The A-Star Micro was once again used due to the additional I/O ports, and the two boards were synchronized using a master digital output each cycle. An interrupt-driven comparison to add or subtract a bias time on the secondary controller adjusted for positive or negative clock drift. Instead of a square wave output for power into the nectophore coils, a triangle wave was more desirable for controlled contraction. Although feedback and position control of the solenoid was not currently possible, an open loop voltage control has shown to be reliable as long as the friction of the moving coils was eliminated. The triangle wave also matched the form of the volume change of biological specimens, though the curve had a smooth transition at the peaks and troughs. Therefore, the Fourier series of the triangle wave was taken and the dual-sine function approximation was utilized for its linearity on the ramp portion and curved transition at the peaks and troughs. The Fourier series was adjusted to normalize the curve magnitude to peak at a unity value at the positive and negative end. This simplified the definition of the wave amplitude and bias in the code. Using a phase-synchronized periodic waveform with phase lags of each nectophore determined by the previous rules, this elegantly provided an analog curve that was used to generate a smoothly varying PWM waveform into the H-bridge controller. This variation and resulting PWM output has been verified when implemented on the A-Star Micro microcontroller.

5.3.3. Jetting Scaling Similarity from Biological to Robot Scale

The scale of the robot nectophore was determined by normalizing each measurement of the biological nectophore by the ostium opening diameter. This diameter was then scaled to be 1cm, maintaining the normalized measurement values in centimeter scale. This resulted in an average of 5.58 times increase in size when compared to multiple specimen measurements. This called into question the similarity of the robot to the biological animal.

The uniform scaling of all dimensions has maintained a geometric similarity to the animal. In order to achieve dynamic similarity of the robot to the animals, the Reynolds and Strouhal numbers have to match that of the animal. The Reynolds number of the body would not be of utmost importance to match between scales. However, the Reynolds number of the jet should match to achieve the same flow characteristics assuming no additional induced flow or mixing. For a scaling factor $\beta = 5.58$, the Reynolds number of the jet holds

$$Re_{animal} = \frac{U_{jet,animal} l_{animal}}{\nu} = Re_{robot} = \frac{U_{jet,robot} l_{robot}}{\nu}$$

$$U_{jet,animal} l_{animal} = U_{jet,robot}(\beta * l_{animal}) \rightarrow U_{jet,robot} = \frac{U_{jet,animal}}{\beta}$$

$$U_{jet,robot} = \frac{dV_{robot}}{A_{robot} T_{robot}} = \frac{dV_{animal}}{\beta A_{animal} T_{animal}}$$

For a volume change not matched by scaling due to contraction errors and limitations, the volume change can be estimated as $dV_{robot} = \eta \beta^3 dV_{animal}$. Also, the period of contraction is the inverse of frequency of contraction.

$$\frac{dV_{animal} f_{animal}}{\beta A_{animal}} = \frac{\eta \beta^3 dV_{animal} f_{robot}}{A_{animal} \beta^2} \rightarrow f_{robot} = \frac{f_{animal}}{\eta \beta^2} = \frac{4\,Hz}{\eta (5.58^2)} = \frac{0.1285\,Hz}{\eta}$$

With the Reynolds number (proportional to jet diameter and velocity) matched at a reduced actuation frequency, the jet force was expected to match since the force was proportional to the square of the product of jet diameter and velocity. If the jet has a different formation number, shape, or additional induced dynamics, the thrust may be changed relative to the animal.

$$F_{robot} = \left(\frac{dm}{dt}U\right)_{robot} = \rho dV_{robot} f_{robot} U_{robot} = \rho(\eta\beta^3 dV_{animal})\left(\frac{f_{animal}}{\eta\beta^2}\right)\left(\frac{U_{animal}}{\beta}\right) = F_{animal}$$

To assess the similarity of the formation number, which dictates the form of the jet and vortex ring ejected from the animal and robot,

$$T^*_{robot} = \frac{U_{robot}}{f_{robot}D_{robot}} = \frac{\left(\frac{U_{animal}}{\beta}\right)}{\left(\frac{f_{animal}}{\eta\beta^2}\right)(\beta D_{animal})} = \frac{\frac{1}{\beta}}{\frac{1}{\eta\beta}}T^*_{animal} = \eta T^*_{animal}$$

Therefore, for a perfect change in volume the formation time will be the same. For a sub-optimal contraction, the robot formation time will be lower. For a nearly pure jet formation without considerations of pressure differentials, the formation number must be much larger than 4 (Dabiri, 2009). The animal formation number was found in a modeling study in our group to be about 70, so the minimum possible volume reduction with a good formation number would be $\eta = \frac{T^*_{robot}}{T^*_{animal}} = \frac{4}{40} = 10\%$, where a much larger result is desirable for non-marginal jet formation. The volume displacement of the robot has been found to be $1200\ mm^3$ for passive relaxation and full contraction, and up to $1875\ mm^3$ for a powered relaxation. This resulted in 22.98% and 35.91% fully scaled contraction volume displacement, respectively, which was acceptable but could use some improvement. In order to match closer to the volume displacement of the animal, the forced relaxation was implemented using a bipolar voltage controller that can force the coil open more after passive relaxation.

For full colony scaling, the Strouhal number should match between the animal and robot.

$$St_{robot} = \frac{f_{robot}L_{robot}}{U_{robot}} = \frac{f_{animal}L_{animal}}{U_{animal}}$$

We can assume a uniform length scaling, neglecting the minor increase in space between nectophores since additional tissue is not included on the robot and thus should average out to similar length.

$$\frac{f_{animal}L_{animal}}{U_{animal}} = \frac{f_{robot}L_{robot}}{U_{robot}} = \frac{\left(\frac{f_{animal}}{\eta\beta^2}\right)(\beta L_{animal})}{U_{robot}} = \frac{f_{animal}L_{animal}}{\eta\beta U_{robot}}$$

$$\rightarrow U_{robot} = \frac{U_{animal}}{\eta\beta}$$

Therefore, the robot speed should be reduced by the scaling factor and sub-contraction factor to match the Strouhal number. This would result in fluid similarity at the larger scale, but a reduction in proficiency since

$$Proficiency_{robot} = \frac{U_{robot}}{L_{robot}} = \frac{\frac{U_{animal}}{\eta\beta}}{\beta L_{animal}} == \frac{U_{animal}}{\eta\beta^2 L_{animal}} = \frac{Proficiency_{animal}}{\eta\beta^2}$$

Therefore, it should be understood that as a vehicle the robot can pulse faster than these similarity results, but the fluid motion will not be similar to that of a siphonophore and may exhibit different swimming performance. While matching the fluid scaling is important for a comparative study, this will result in a reduction in actual performance. It was previously found that *Nanomia* achieves 221.8 mm/s, or 5.13 body lengths per second. Therefore, the robot proficiency at peak would be

$$Proficiency_{robot} = \frac{5.13}{5.58^2\eta} = \frac{0.16}{\eta}$$

At perfect contraction the proficiency would peak at just under 0.16 body lengths per second (about 6 seconds to travel one body length), which would be further reduced to about one body length per second, which is relatively fast. However, sub-contracting requiring an increase in contraction frequency would lead to an increase to 0.46 body lengths per second of allowed proficiency. This may show some merits of sub-contracting and contracting faster.

5.4. ***Robot Control Space Modeling***

5.4.1. Modeling Formulation

The existing 2D dynamic model used for the LQR control simulation was adapted for the current robot design and the input of a time-varying thrust profile for each nectophore. Since 2D rotational motion is not just a result of the off-center thrust on each side of the chain at the nozzle, the additional factor of an off-center thrust in the lateral direction of each nectophore was included. The nectophore distance was based on the robot's staggered nesting, so each nectophore was staggered down the bi-serial planar chain. This allowed any unbalanced forces around the center of mass to contribute to the rotation of the colony.

The thrust of each nectophore was generated through two methods. The thrust of the nectophore of a siphonophore was found to scale to about a peak of 0.5 mN at a cycle frequency of 0.357 Hz. The measured value of the nectophore thrust was found in a study to vary up to 0.45 mN using particle streak velocimetry, so the 0.5 mN peak was a reliable estimate for a mature nectophore (Costello et al., 2015). The waveform was found to generally ramp up and down from the peak during the jetting phase and generate a near zero thrust during refilling. Therefore, for the majority of the comparative studies a positive half-sine wave with a peak of 0.5 mN was used, and filtered at a cutoff frequency of ten times the cycle frequency (3.57 Hz) using a 3rd order Butterworth low pass filter to smooth the sharp discontinuities without adding substantial ripple to the zero thrust refilling phase. This thrust was purely in the axial direction, so the angle of the nozzle and axial thrust was used to resolve the total jet thrust and then the lateral thrust. For a more accurate representation of the actual thrust output of the robot, load cells on a thrust stand were used to directly measure X and Y thrust. The first thrust stand used linear bearings to isolate the X and Y axes, with a 5 lb load cell (Futek LSB200 with CSG110 amplifier) on each axis. However, the measurement showed a pure oscillatory system without a clear thrust magnitude on the signal. The 0.5 mN thrust output was below the noise floor of the sensor, so it was found that 10 mN would produce a 20dB signal to noise ratio for the sensor. The second measurement stand utilized a 200:1 lever constructed of a 1 inch, 1/8 inch wall thickness aluminum tube. 3D printed pivots and mounts were constructed to mount the load cell and nectophore at the correct distance, as well as mount the complete setup to the edge of a workbench to hang into an acrylic water tank. Any flexure points in the mounts were laminated with metallic strips with high stiffness to reduce the loss or drift in the measurement. The resulting thrust measurement was then scaled to the true value and resolved from the lateral direction to the axial direction complement in the modeling software. Once corrected, a 50-node piecewise polynomial spline interpolation was used to force a periodic waveform, force a zero derivative of thrust at the beginning and end of the cycle, and eliminate most noise in the system that could introduce instability in the model. The nectophore thrust was collected at 0.357 Hz, 0.5 Hz, 1 Hz, 2 Hz, and 4 Hz to cover the range from the fluid dynamic scaling matching frequency to the frequency of jetting for the animal (Mackie, 1964).

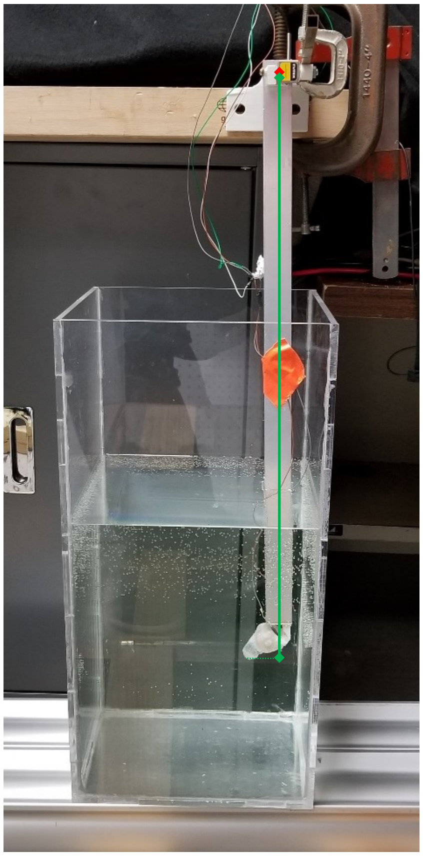

Figure 107 – Load cell amplification lever arm with short moment arm (red) attached to load cell, and long moment arm (green) attached to nectophore.

The drag and added mass calculations were also updated in this model due to additional features in the final design and refinement of the accuracy of the model. The axial motion drag and added mass remained the same as the model, using a streamlined ellipsoid approximation for the primary portion of the body. Since mostly axial flow was present, but a Reynolds number of the flow in the axial direction could be resolved, the drag on the streamlined body for axial movement was resolved from X and Y velocities. Instead of assuming a similar added mass when moving in the lateral direction, the complementary added mass for a streamlined ellipsoid was resolved from the same work. The lateral and streamlined added mass coefficients were curve fit using two-term functions in the MATLAB Curve Fitting Toolbox, finding

$$\alpha_{axial}, K_1 = 0.5141\left(\frac{L}{d}\right)^{-1.212} - 001284\ (R^2 = 0.9999, SSE = 2.63 \times 10^{-5})$$

$$\alpha_{lateral}, K_2 = 0.8807e^{\left(0.00899*\left(\frac{L}{d}\right)\right)} - 0.7643 * e^{\left(-0.6815*\left(\frac{L}{d}\right)\right)}$$

$$(R^2 = 0.9998, SSE = 4.15 \times 10^{-5})$$

from empirical tabulated data (Munk, 1922). Since the nozzles of the siphonophore robot extended outside of the central column of the nectophores, unlike the biological nozzles remaining within the profile of the external nectophore tissue during full deployment, an additional drag term for the additional features and tripped flow was added to the axial drag term. The drag of a cylindrical stud of approximately equal diameter to height was found to be about a drag coefficient of 0.8. The nozzle section was also angled down, so a cubic sine reduction in drag was included in the term to appropriately scale the induced drag of each nozzle (Hoerner, 1965). Since the nozzles were angled between 27.07 degrees at the ostium opening to the 49.6 degree nozzle opening, an average angle of the two was used to represent the smooth sweep of the nozzle between these angles. The wetted area of the nozzle was used in the drag calculation, and the drag of one nozzle was multiplied to include the multiple drag features similar to cylindrical studs on sheet metal joints along the flow. Mixing and additional drag from the complex form and the voids behind the nozzles were not included, but would represent additional drag in the real robot. For lateral drag, the drag on an elliptical cylinder circumscribing the whole colony was used, with a sine function resolution of the flow into the elliptical cylinder. As with before, the additional tripping and void induced drag forces in the design increases the lateral drag force. A tow tank measurement of a 3D printed rigid representation of the robot would be able to resolve the drag coefficient of the robot in each direction.

The resultant Reynolds number, as well as the lateral and axial Reynolds number, of the swimming quickly rose to around 10^3 to 10^4, with almost all of the forward Reynolds numbers above 10^2, depending on the gait and colony size. The axial drag was a function of Reynold's number and the ratio of length to diameter, so the full range drag coefficient across all body forms and Reynolds numbers was valid. The lateral drag was a fixed value based on experimental wind tunnel data for a circular or elliptical cylinder between two walls, which was flat from a Reynolds number of 10^4 to 10^5 and relatively constant back to about 2×10^2. The protruding stud drag of the nozzles in the boundary layer was also given as a single value for a turbulent-induced boundary layer from tripped flow, which was appropriate for this case. It can be assumed that for lower Reynolds numbers, the flow was slow enough to reduce drag faster than the increase of the drag coefficient, was quickly exceeded in time to the expected range, and was not well established for slow movement but rather for more viscous flows such as an oil bearing system (Hoerner, 1965).

5.4.2. Straight Swimming Performance

5.4.2.1. Baseline Straight Swimming

The first modeled result was the variation in performance across the three straight swimming gaits (synchronous, alternating side to side, and cascading down the chain) and across the considered body lengths from 2 nectophores to 10 nectophores. Any larger nectosome lengths have been found in previous modeling to have diminishing returns, and most specimens had around 9 near- or completely matured nectophores active for the full chain. It was found that while peak velocity did increase for more nectophores, it was roughly consistent especially past 4 nectophores. This increase was more steady and seen across all gaits for the average speed, showing that while synchronous reaches the highest speeds and cascading peaks at a lower speed, the cascading gait reduced acceleration during the cycle while other gaits have cycles where the robot lunges forward and then glides on either one side or both sides. Odd numbers of nectophores exhibited higher velocities than the even bounding numbers, although for synchronous swimming this trend varied in magnitude more than the other smoother gaits.

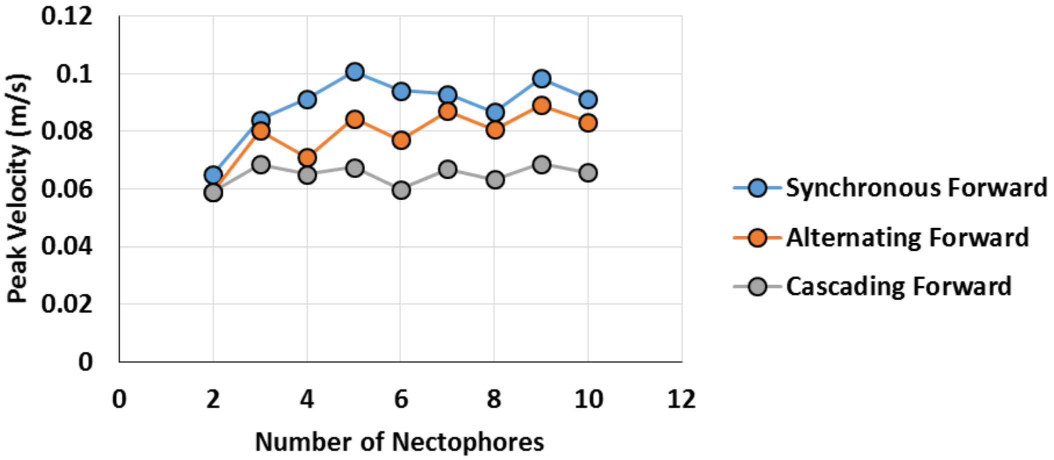

Figure 108 – Peak velocity for 2 to 10 nectophores, across varied forward swimming gaits.

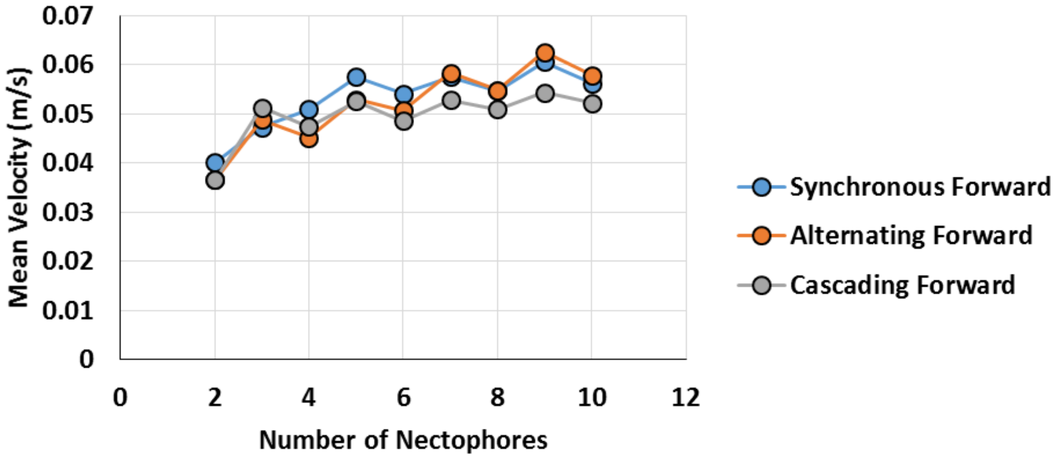

Figure 109 - Average velocity for 2 to 10 nectophores, across varied forward swimming gaits.

One unexpected result that was found was that, despite exhibiting a straight swimming gait that has been observed in nature and previous work, the straight swimming was causing an arcing turn towards the side of the even numbered nectophores. In this model, the nectophores are front-most and thus odd on the left side, and even on the right side, hence resulting in a negative angular velocity. While this violates the current understanding of how siphonophores move underwater, this was a real physical phenomena. In videos of longer chains in laboratory environments with a synchronous escape response, the animal arced toward the even nectophores side. A specimen used for the straight swimming tracking from the colony plane normal view was found to exhibit an average turning rate of -1.3874 radians per second (about -79.5 degrees per second). This was due to the nesting arrangement of the nectophores in an effort to reduce axial drag. While this streamlined the body, reduced cavities in the body surface, and reduced frontal area, it meant that the odd nectophores side had a resultant lateral thrust positioned slightly forward of the center of mass for an even number of nectophores and the even side had a resultant lateral thrust behind the nectosome center of mass. This induced a torque on the body, and thus an induced turn. According to the modeling data, synchronous swimming was the strongest turning gait, with an angular rate of about -0.18 rad/s (about -10.3 degrees/s) for 2 and 3 nectophores. A chain with 4 nectophores obtained a moderate turning rate, while 5 to 10 nectophores using a synchronous gait roughly linearly reduced in turning rate. Alternating gaits reduced this turning rate, while cascading remained similar to the higher synchronous values from 7 to 10 nectophores and similar to alternating gaits at 2 to 3 nectophores. This reduction in turning, although the moment arm of the nectophores was increased, was in part due to the increased lateral drag that resisted turning due to a longer body length. It should be noted that odd numbers of nectophores reduce turning because of the centered lateral thrust resultant on each side. However, a torque still existed since the thrust vector of the jet was still distal from the centerline of the colony, resulting in a small moment that had a larger contribution with an uneven number of nectophores on the odd side. This can also induce a lateral drift due to an unbalanced lateral thrust towards the even side of the colony.

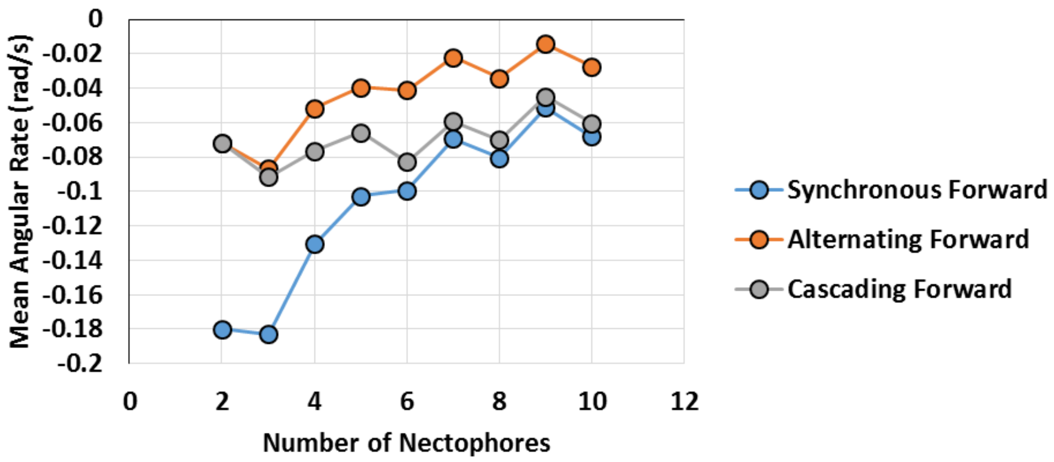

Figure 110 – Average angular velocity for 2 to 10 nectophores, across varied forward swimming gaits.

5.4.2.2. Straight Swimming Sub-contraction Tuning

In order to correct for this lateral arcing during forward swimming, several factors can be considered. While changing the gait to an alternating forward gait and reducing the number of nectophores to an odd number can help, it does induce a lateral drift and does not eliminate the turning amount entirely. Therefore, subcontracting the nectophores to reduce thrust on the side on the outside of the turn can help straighten the swimming trajectory to the orientation before swimming. Depending on the number of nectophores and the number of synchronous cycles used to start the straight swimming, different scaling factors can be used to result in straight swimming. For a low number of nectophores, this scaling factor was relatively consistent despite the number of synchronous cycles used to get up to full speed. However, as the colony grew the contraction amount needed to maintain straight was reduced with increasing numbers of synchronous cycles at the beginning of the maneuver. This resulted in a reduced turning rate, which was easier to achieve with less nectophores than with a longer nectosome chain. This can also reduce the lateral deviation from the starting position, although oscillation away and back towards this centerline was observed and the initial movement in the straight swimming did result in a lateral shift towards the odd nectophores side due to unbalanced lateral forces. It should be noted that while sub-contraction did modify the trajectory during synchronous and cascading motion, the temporal coupling of the left and right side contractions still induced an arc in the trajectory path.

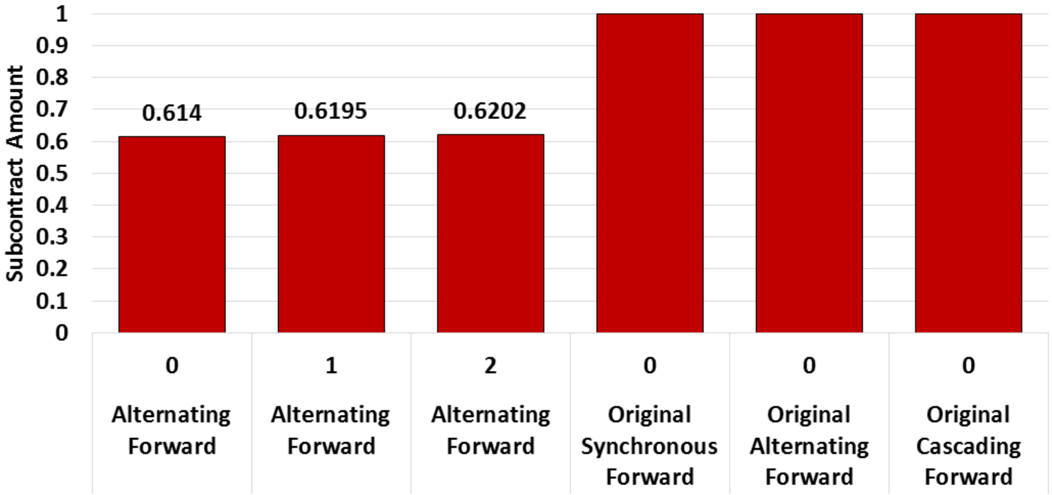

Figure 111 – Sub-contraction amount for tuned forward swimming of 2 nectophores with 0-2 synchronous swimming cycles followed by alternating forward swimming. 100% contraction used for original three straight swimming gaits.

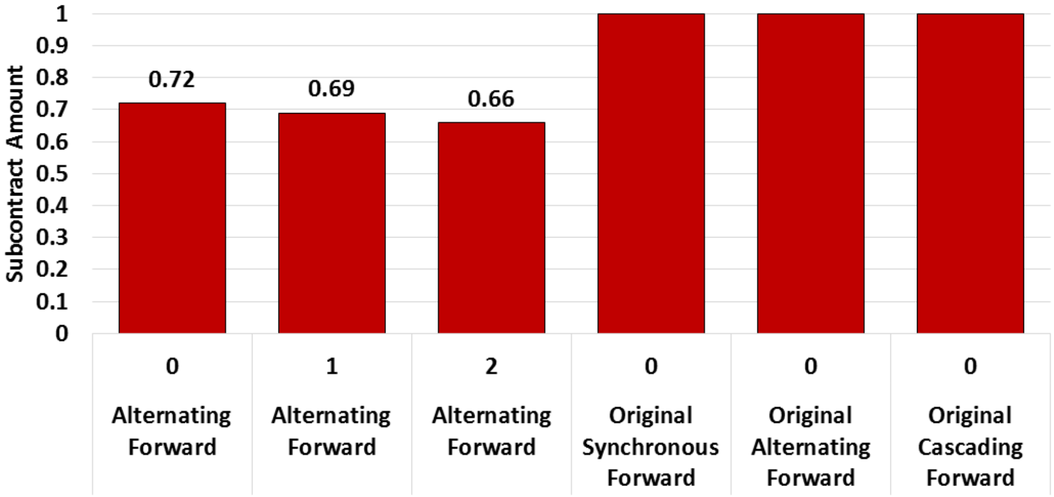

Figure 112 – Sub-contraction amount for tuned forward swimming of 10 nectophores with 0-2 synchronous swimming cycles followed by alternating forward swimming. 100% contraction used for original three straight swimming gaits.

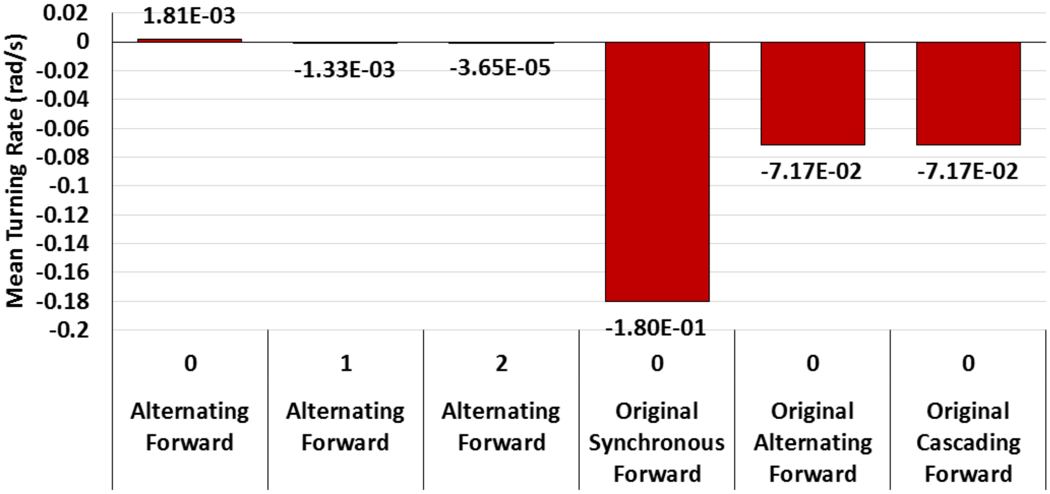

Figure 113 – Mean turning rate during tuned straight swimming of 2 nectophores, with original fully contracting gaits and subcontracted gaits with 0-2 cycles of synchronous swimming followed by alternating forward swimming.

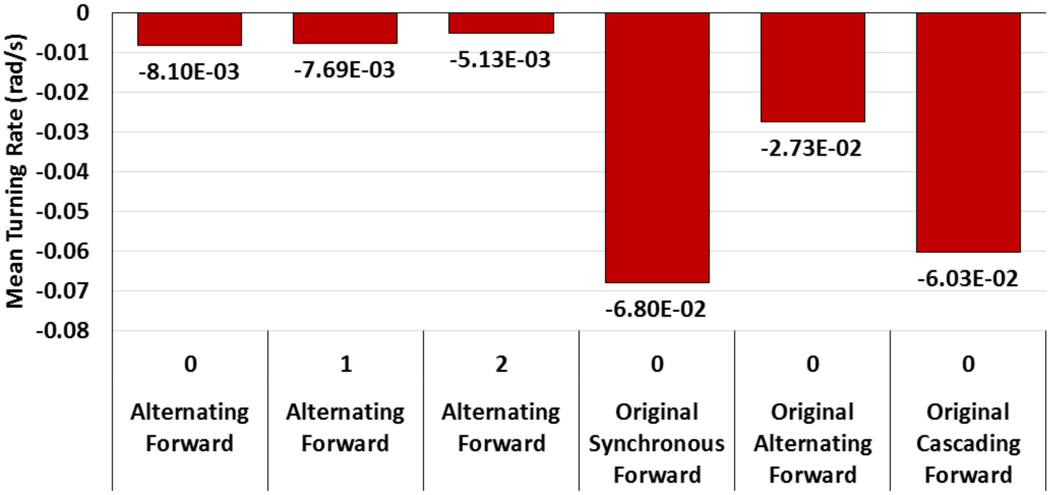

Figure 114 – Mean turning rate during tuned straight swimming of 10 nectophores, with original fully contracting gaits and subcontracted gaits with 0-2 cycles of synchronous swimming followed by alternating forward swimming.

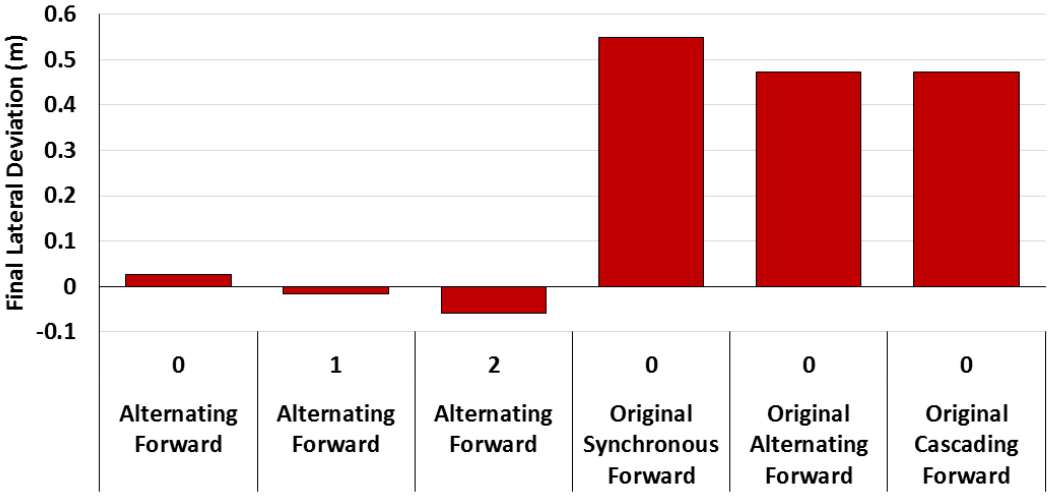

Figure 115 – Final lateral deviation of straight swimming of 2 nectophores from starting axial direction, with original fully contracting gaits and subcontracted gaits with 0-2 cycles of synchronous swimming followed by alternating forward swimming.

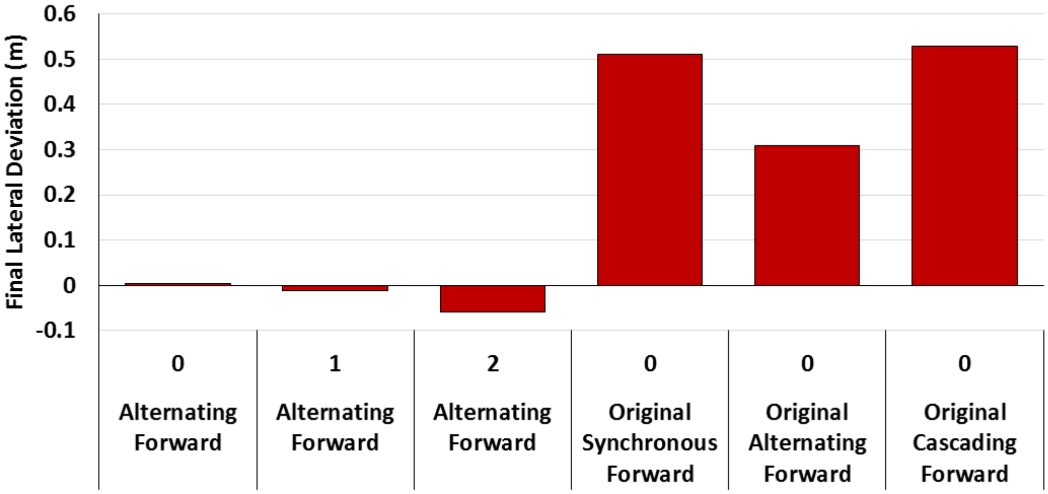

Figure 116 – Final lateral deviation of straight swimming of 10 nectophores from starting axial direction, with original fully contracting gaits and subcontracted gaits with 0-2 cycles of synchronous swimming followed by alternating forward swimming.

5.4.3. Tuned Turning Performance

One key aspect of having a colony of jetting bodies is the ability to spatially and temporally vary jetting parameters at each nectophore to change colony swimming behavior. This variation was seen in the described gaits for turning, and additional variation was expected for longer and shorter chains of nectophores. Therefore, turning capacity for different gaits, sub-contraction amounts, and colony sizes were characterized in detail.

5.4.3.1. Sharp Turning Performance

The sharp turning gaits utilize contraction on a single side of the colony, which will represent the outside of the turn. This style of turning can either utilize a synchronous pulsing for a fast pulse of turning with a drifting period, or a cascading pattern to smoothly turn. Variation of these two gaits for each side across 2 to 10 nectophores has shown that as the colony grows in size, the ability to turn was reduced due to the additional moment of inertia and drag on the system. It should be noted that the turning towards the even nectophores was larger in magnitude since the shifted forward thrust relative to the center of mass on the odd side still induced a moment in the negative angular direction. On the contrary case, turning towards the odd side was reduced since while the even nectophores induce a turn, their thrust shift behind the center of mass also induced a negative angular moment.

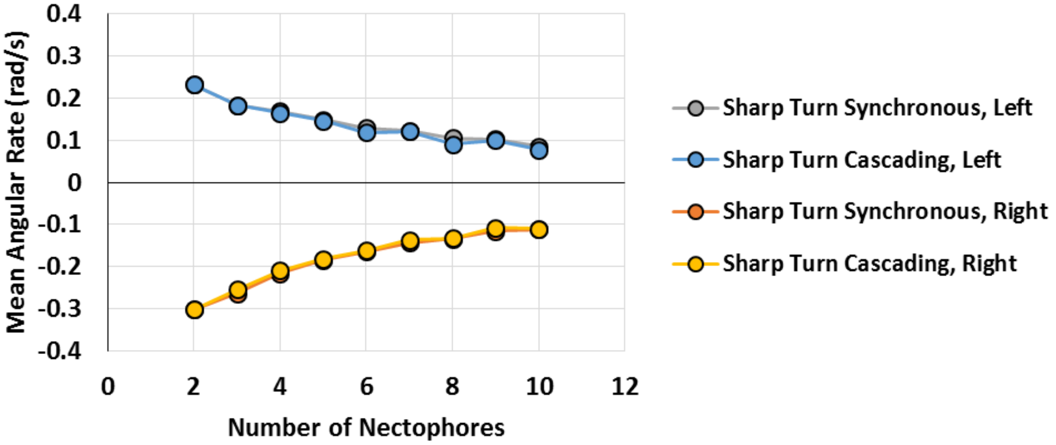

Figure 117 - Angular turning rate during synchronous and cascading strong turning (side-isolated pulsing) in the odd (left) and even (right) turning orientations across multiple nectophore chain lengths.

However, a notable result was noted in the varied turning gaits. Although synchronous was more impulsive turning and cascading created a smooth turning rate, both gaits produced very similar turning rates for both sides. This thus created a dual possibility for the same turning, where if a quick turn was needed the impulsive synchronous gait could be used while smooth continuous turning could use a cascading gait to reduce instantaneous current draw and minimize voltage losses to each nectophore.

5.4.3.2. Timing-Graded Performance

Tunability of graded synchronous and cascading turning, where one side pulses or cascades jetting, the other side pulses or cascades, and then a delay is introduced to prolong the momentum of the last thrust input into a cruising turn, was tried due to its possible observation in nature and similarity to the turning gaits of rowing jellyfish. Turning rate increased in magnitude for smaller colonies, as found before, and synchronous turning did exhibit larger turning rates with stall time. However, the difference between left and right turning for each cycle was negligible, restricting this turning gait to only turning towards the even nectophores which was already experienced during the straight swimming. Turning variability at larger colony sizes near 10 nectophores for synchronous swimming, and all sizes for cascading turning, was nearly constant, but smaller colonies did experience about a two-fold increase in the right turning rate for synchronous swimming. Therefore, this is an option for right turning in the synchronous cases for small colonies, but is restricted in its general applicability.

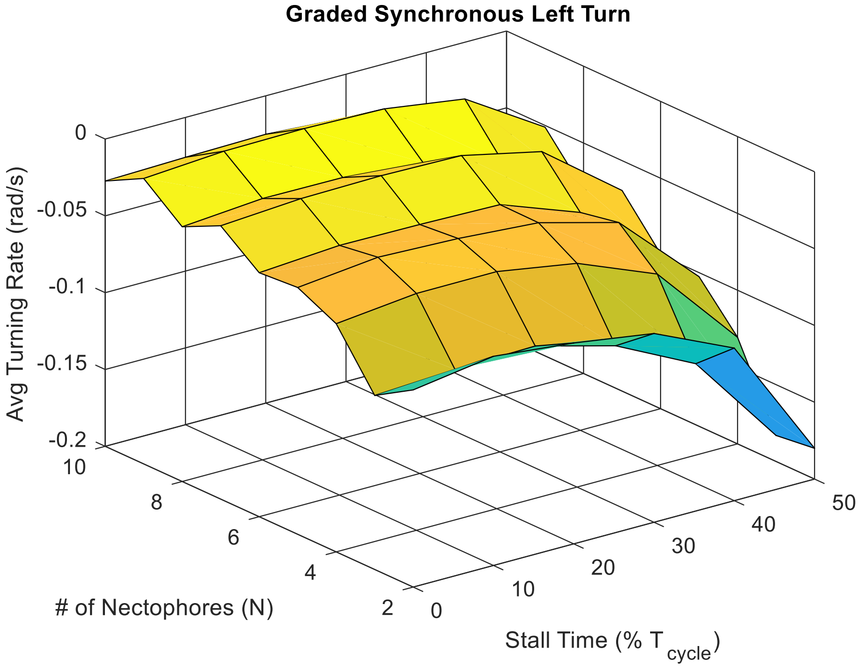

Figure 118 - Turning rate across 2-10 nectophores and 0%-50% cycle length for stall time, for a synchronous left turn.

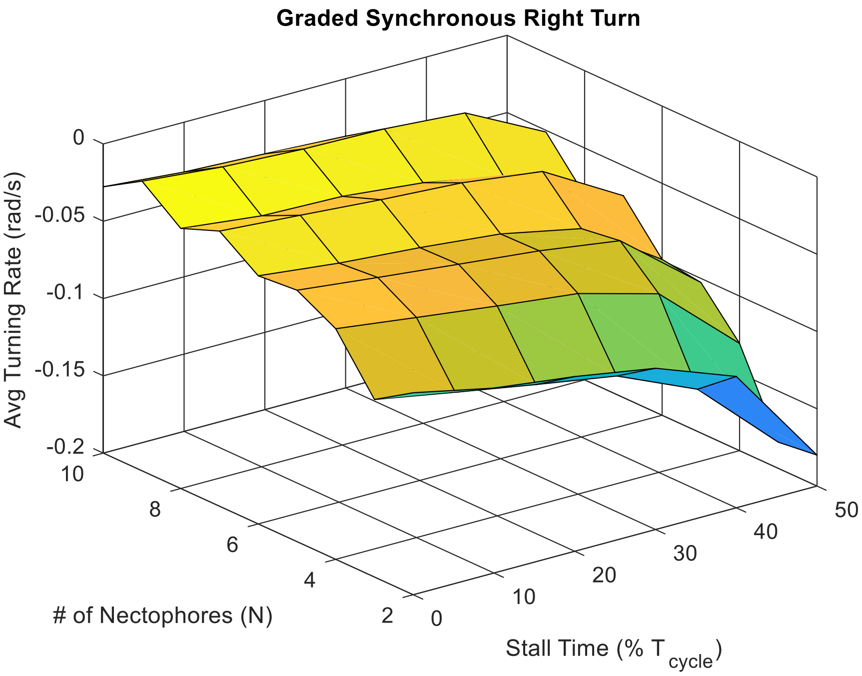

Figure 119- Turning rate across 2-10 nectophores and 0%-50% cycle length for stall time, for a synchronous right turn.

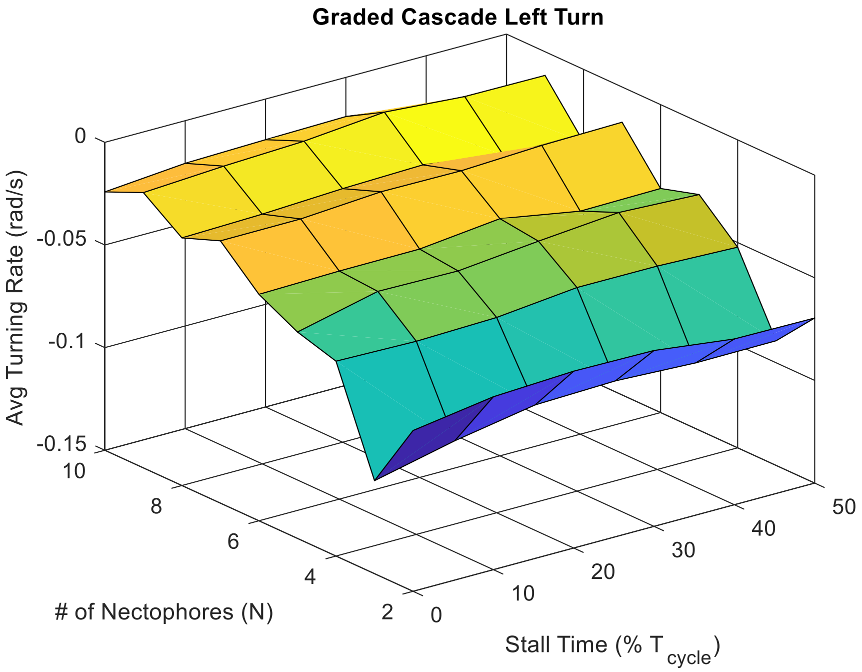

Figure 120 - Turning rate across 2-10 nectophores and 0%-50% cycle length for stall time, for a cascading left turn.

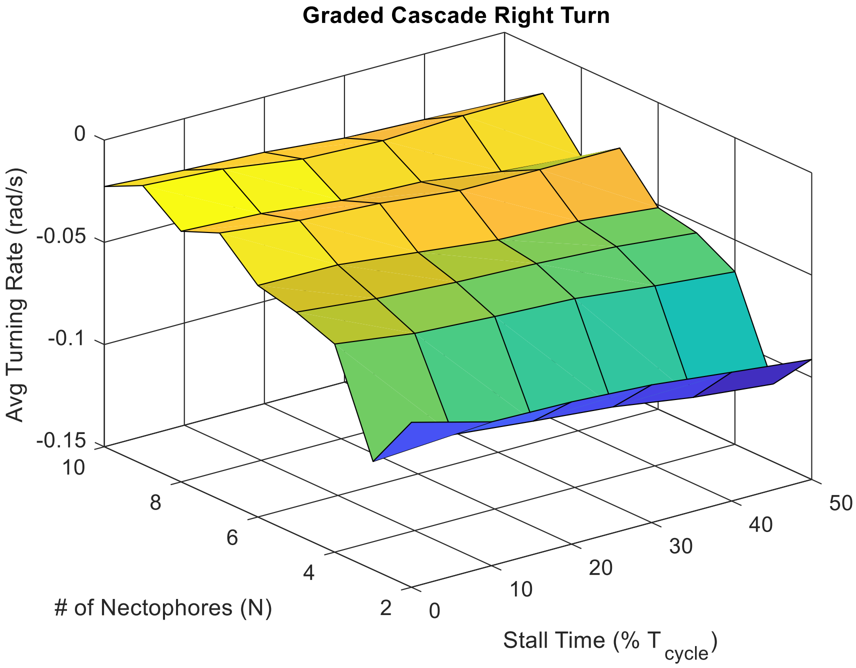

Figure 121 - Turning rate across 2-10 nectophores and 0%-50% cycle length for stall time, for a cascading right turn.

5.4.3.3. Sub-contraction-Graded Performance

While a graded timing gait for turning was not generalizable for all turning maneuvers, the sharp turning gaits with single side jetting was found to be successful for all nectophore chain lengths. Therefore, the nectophore sub-contraction from full contraction to 20% contraction was varied for the sharp turning cases of even and odd side turning, synchronous and cascading turning, and multiple nectophore chain lengths. This resulted in a generalizable turning gait that successfully produced odd side and even side turning despite the natural even-sided bias, with variability in magnitude present for all chain lengths. Therefore, this methodology of sub-contraction for the correction of straight swimming, as well as the modulation of turning gaits, is recommended for robot control due to its reliability, general applicability, and simplicity in iteration. It should be stated that, depending on an active or passive relaxation, the graded sub-contraction could result in changes in power consumption, and it is expected to reduce power consumption but also potentially place increased load on the microcontroller and motor driver chipsets to modulate power at this reduced level. Further system level characterization for each configuration is recommended.

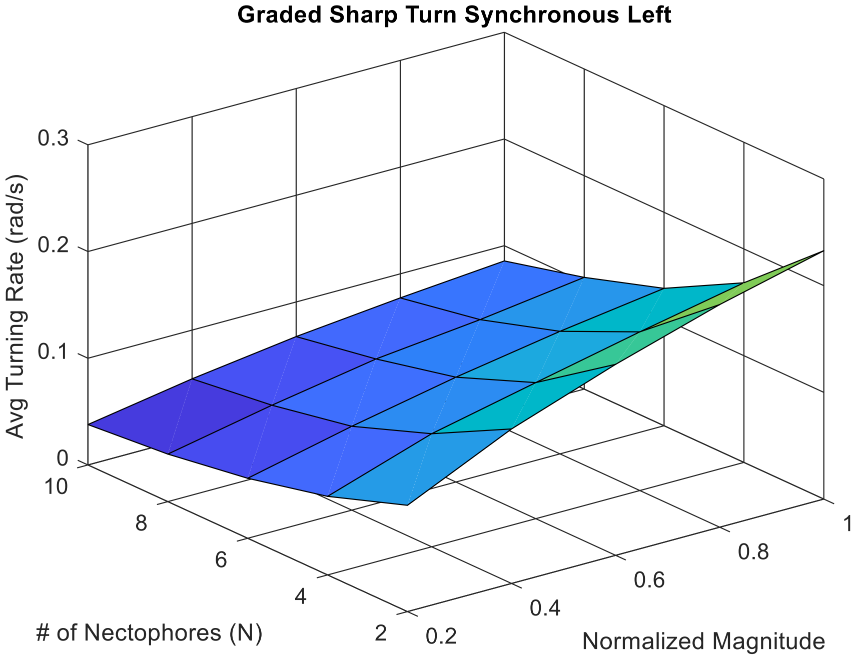

Figure 122 - Turning rate across 2-10 nectophores and 20%-100% contraction magnitude for a synchronous left turn modulated from the sharp turn gait.

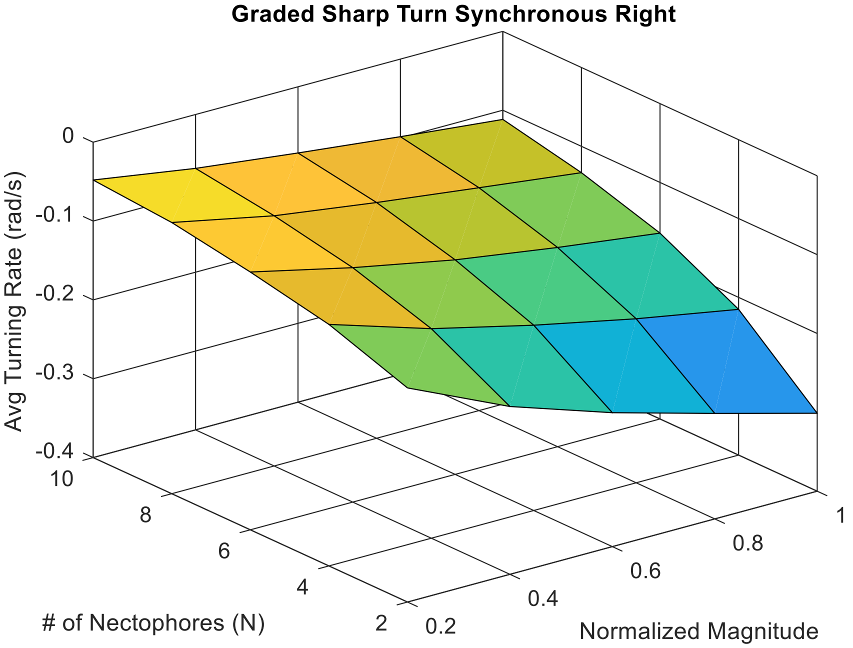

Figure 123 - Turning rate across 2-10 nectophores and 20%-100% contraction magnitude for a synchronous right turn modulated from the sharp turn gait.

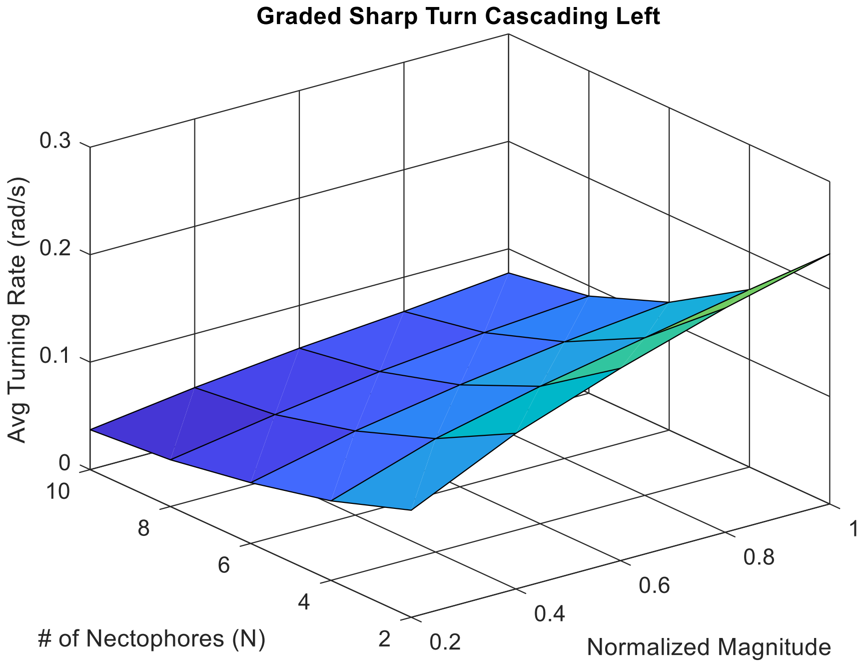

Figure 124 - Turning rate across 2-10 nectophores and 20%-100% contraction magnitude for a cascading left turn modulated from the sharp turn gait.

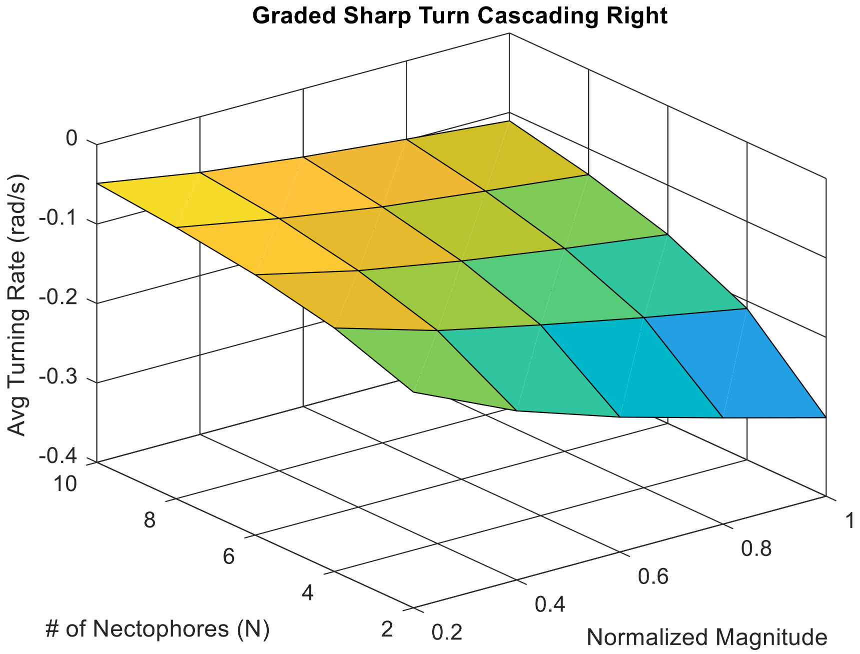

Figure 125 - Turning rate across 2-10 nectophores and 20%-100% contraction magnitude for a cascading right turn modulated from the sharp turn gait.

5.4.4. Robot Performance

Initial benchtop testing of the robot was performed to characterize the systems necessary for overall performance. Actuation of the electromagnetic coils using PWM variation in voltage at a high frequency was effective, but not all of the I/O ports on the microcontroller chips were able to produce the PWM waveform shape or frequency. While the frequency of the PWM was set to 30 kHz to minimize audible signatures of the system, the I/O pins able to produce the smooth variation in position produced an audible frequency sweep as duty cycle was changed. Therefore, to reduce microcontroller I/O requirements and eliminate the audible signature of the modulation signal, a simple digital form was selected for pure contraction and pure powered relaxation. Positive voltage was applied for half of the cycle to contract the nectophore, and then a negative voltage powered the coils to open the nectophore volume. This powered relaxation was more consistent than passive relaxation due to the low strain energy stored in the thin wall cavities. Power consumption of each coil was found to be at about 12 V at 1 A, resulting in a 24 W power consumption per nectophore and 240 Watts for a ten-nectophore colony. A series configuration of the coils was used to reduce the current draw of the total system, as well as reduce the inductance of the coil pairs to reduce response time. Gait timing parameters found for the animal for synchronous and asynchronous contractions were validated for a ten nectophore chain.

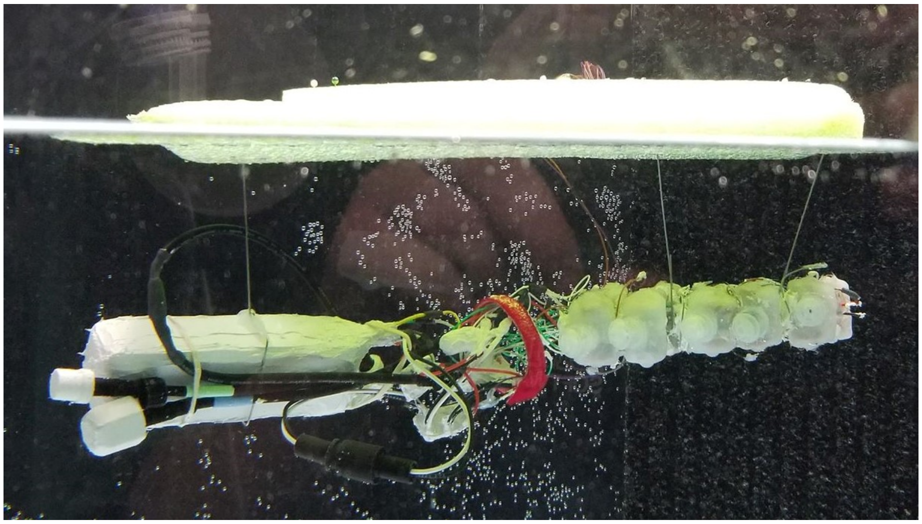

Figure 126 – 10-Module robot with waterproofed battery and flotation device for gravity and buoyancy neutral measurements

To test the robot kinematics in the water, a floating sting apparatus was utilized. A foam board with stainless steel spring wire extending below the surface hooked around the battery and robot body. This allowed the robot to move in the plane of the surface of the water without assistance or negative effects from gravity, tether cables, or buoyancy. Since the robot, as with the animal, was a planar body plan, this constrained setup allowed the robot to move freely in one plane without significant drifting out of plane. Tracking balls were added to the foam board to optically locate the centerline of the robot from side and top views. The tracking elements were analyzed in Adobe After Effects, and calibrated using a metric ruler in plane with the robot position in the centerline of the tank.

The robot velocity using synchronous swimming and six active nectophores was recorded across a frequency sweep of 0.5 to 4 Hz. The lower end of the frequency range represented the scaled frequency to match the jet Reynolds number, while the upper end at 4Hz represented the biological actuation frequency. It can be seen that there was a tapering effect but improvement in movement velocity with increased frequency. It should be noted that with digital actuation the contraction speed was constant, so this increasing effect was a balance of reduced non-jetting time and possibly a resulting limitation in the nozzle actuation speed on jet diameter constraints. It was found in benchtop testing of the nozzle that it worked well at least up to 1Hz, and the response time should only depend on the jetting speed and thus the drag and pressure on the nozzle slider. If the Strouhal number is plotted relative to body length or jet diameter, frequencies that generate a positive forward velocity maintain an approximately constant Strouhal number. Additional measurements of the jetting volume displacement to generate an equivalent stroke length for the correct Strouhal number in comparisons with jellyfish metrics is of future interest.

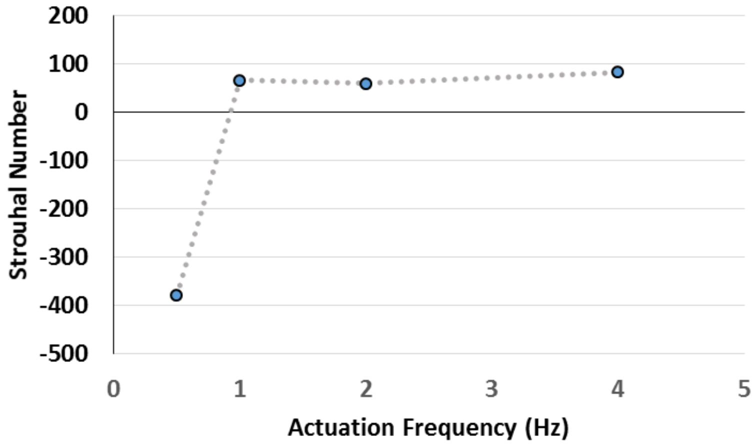

Figure 127 – Robot Strouhal number relative to body length (170mm) across a frequency sweep

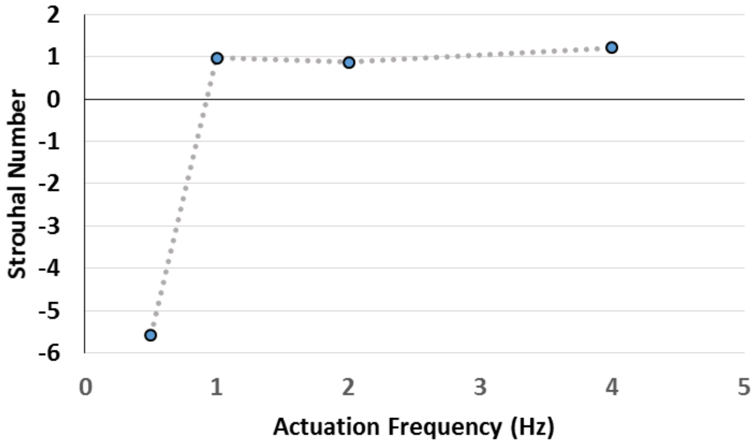

Figure 128 – Robot Strouhal number relative to jet diameter (2.5mm) across a frequency sweep

Thrust measurement across multiple actuation frequencies for a single nectophore was expanded to observe the change in velocity, turning rate, and proficiency for multiple frequencies of actuation. It was found that low frequency was the best case for velocity and displacement, although turning rate was increased for higher velocity output. The 1Hz case was found to be lower, likely due to changes in the jet speed that induced additional mixing in the jet and thus reduced thrust capacity. Higher frequencies likely increased the average thrust over time, thus slowly improving speed and displacement despite reduced thrust in the jet. When compared with the swimming performance of the robot, the robot performance was higher than the modeled performance. However, this scale was relatively consistent across all moving values for the physical robot, and was expected due to the digital pulsing (all relaxed or all contracted, no analog variation between points) used for full robot testing due to the limited number of ports with pseudo-analog voltage modulation. Therefore, it can be assumed that digital pulsing, as with a pure transistor driven motor control without pulse width modulation, will increase velocity by about 2.5 to 3 times. Proficiency also increased by about 1.5 to 2 times. It should be noted that the robot colony was 10 nectophores long but pulsed only 6 nectophores, with 3 on each side, so the simulated results on the plots were for 6 nectophores, while the robot proficiency was for a 10 nectophore length versus a 6 nectophore length simulation result.

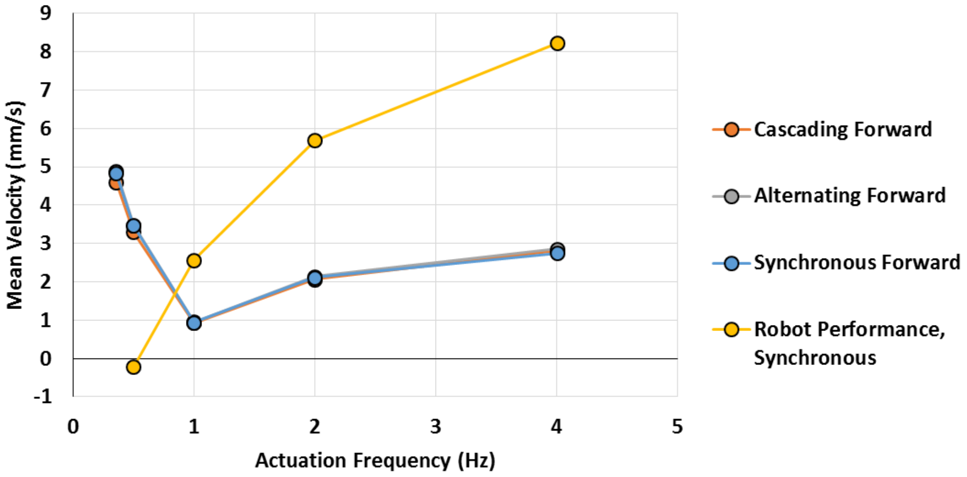

Figure 129 – Mean velocity across 0.357Hz to 4Hz actuation frequencies, for the real robot performance as well as the modeled performance from single nectophore thrust measurements.

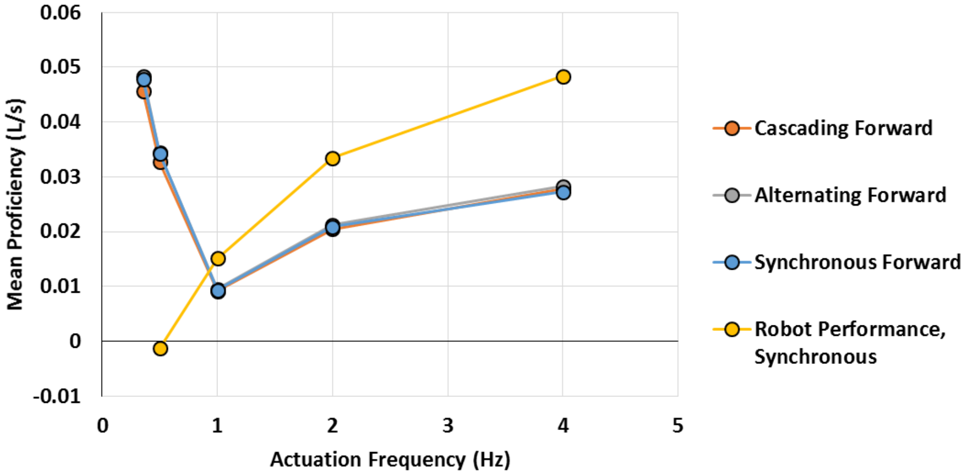

Figure 130 – Mean proficiency across 0.357Hz to 4Hz actuation frequencies, for the real robot performance as well as the modeled performance from single nectophore thrust measurements.

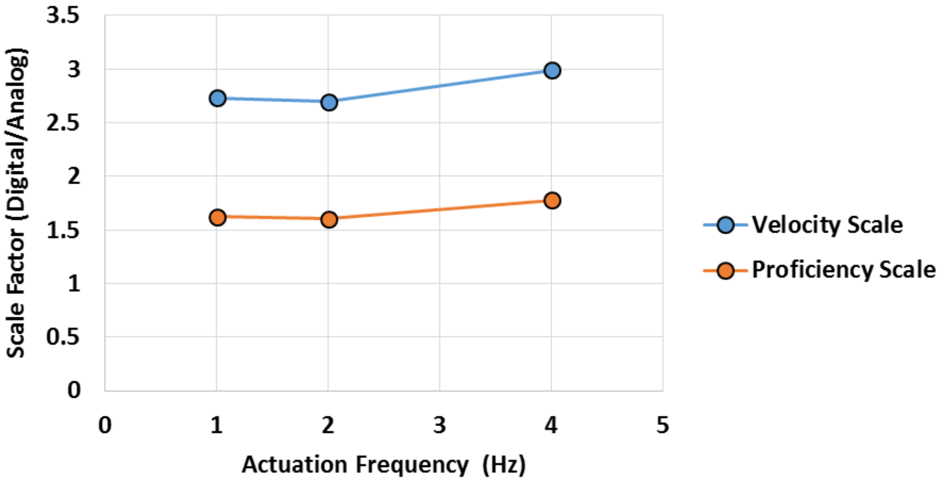

Figure 131 – Mean velocity and proficiency scaling for 1 Hz, 2 Hz, and 4 Hz for the robot performance using digital jetting vs analog modeled jetting.

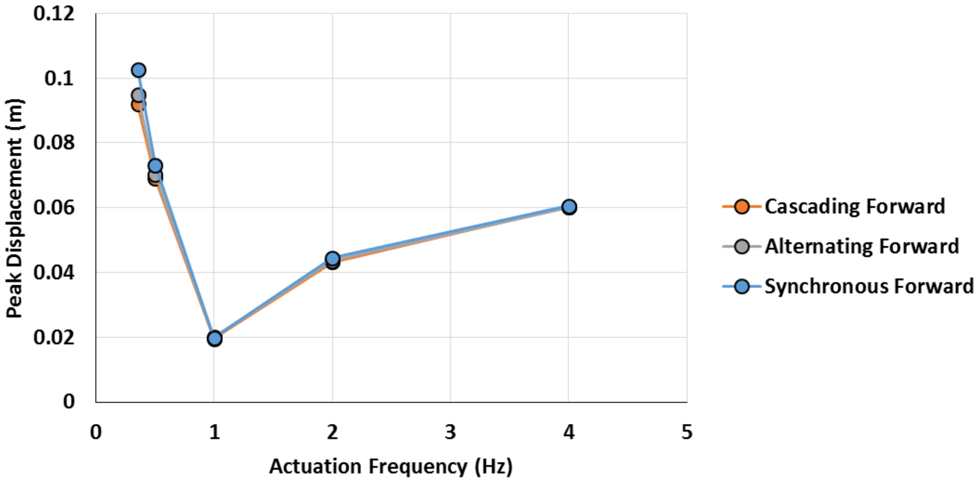

Figure 132 – Peak displacement across 0.357Hz to 4Hz actuation frequencies, for the modeled performance from single nectophore thrust measurements.

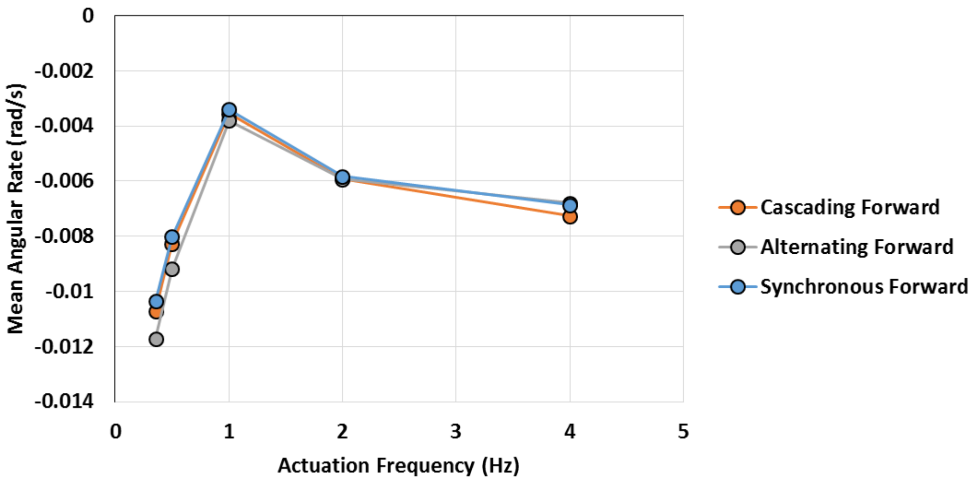

Figure 133 – Mean angular rate across 0.357Hz to 4Hz actuation frequencies, for the modeled performance from single nectophore thrust measurements.

5.5. ***Conclusions***

The complex body plan combined with a simple yet effective control architecture has proven to be a viable vehicle design for multi-jet propulsion. Additional studies of the complicated system dynamics with a modular multi-input system would greatly advance the control space possibilities for underwater robots. While single bell jellyfish have been proven to be effective swimming body plans, they are better suited for limited maneuvering goals such as station keeping. However, the new capabilities of a multi jet system will allow the rapid deployment, operation, and retrieval of a sensing package with the large siphosomal capacity for position awareness and environmental sensing and computation packages. In addition, other modular systems would benefit from the implementation of a control algorithm structure without the increase in computational complexity with additional modular units while maintaining control integrity. Future designs could use this modularity for deployment of clusters of modules for sensing with larger spatial coverage, with the siphonophore colony form as a rapid deployment and retrieval form with additional computational and power capabilities over the individual units.

6. Technical Limitations and Conclusions

6.1. *Jellyfish Inspired Propulsion Technology Limitations and Future*

As seen in the work laid out in this dissertation, the development of biomimetic mid-size robots enables further advancements in robotic design and biological research. This size of robot utilizes a balance of thrust production for payload capacity, maneuverability for directional and positional changes, and implementation cost for larger collections of robots for more advanced goals. Smaller robots can be useful for goals that would benefit from swarming and maneuvering in small spaces, but they are both prohibitively difficult and expensive to make with inherently less capabilities and payload capacity, especially in the case of power source payload. These reduced size robots typically utilize smart materials for smaller scale actuation, but these actuators are inherently limited in capabilities and draw proportionally more power for similar motions by slightly larger electromagnetic actuators (Marut, 2014; Marut et al., 2013; Villanueva et al., 2011; Villanueva et al., 2014). On the other side of the spectrum, as seen on Cyro 1, this method of locomotion can be limited in maneuvering and operational capabilities due to the large scale inherently increasing necessary power consumption for swimming and resistive forces that complicate straight and curved path swimming (Villanueva et al., 2013). As noted in the comparison with other animals, oblate jellyfish are inherently stiff swimmers due to the broad body shape in the direction of travel, so turning and overall operation must consider a balance between scale and ability to change direction for full navigation capabilities. The development of a simple axial swimming robot Cyro 2 and a more complicated but fully featured and navigationally capable robot Cyro 3 has proven the performance capabilities of mid-range jellyfish robots for tasks such as environmental monitoring and station keeping in active environments. In addition, the experiments completed with these robots has helped to complete the picture of how rowing jellyfish swim using different control space parameters. Future improvements to enable the designs for final implementation would be to design and implement an automatically stiffening marginal flap material that can grade the silicone substrate resistance to flexion and thus the augmentation of turning. This could be achieved using a clever cable driven system paired with the current control scheme, as well as localized or proximal driven, peripherally transmitted actuators with interlocking plates for digital stiffness control.

The primary limitation of jellyfish inspired robots is the actuation methods available for implementation, especially in aquatic environments. The requirement of large rotary motors, often in pre-engineered waterproof housings with pre-tuned controls and gear systems, for effective motion of cable systems peripherally is biomimetic and low profile, but then requires significant mass and space in the central column of the robot to house and seal the components. While jellyfish like *Cyanea* carry significant trailing mass along their central column, the inclusions of stiff elements with high density is a source of significant problems for balancing and buoyancy control over a neutrally buoyant nearly homogenous material such as mesoglea. These rigid, high-mass structures do not deflect when the robot moves and thus does not strain-relieve or find a low-resistance position as in the densely packed yet highly flexible trailing structures of *Cyanea*. This mass is continually trailed behind the robot, while biological oral arms and tentacles may be passively deployed in the water and only jerked forward briefly during swimming. Integration of electronics and power storage into the center of the bell profile would reduce resistive forces during swimming and improve robustness by being sealed and cushioned from the outside environment. This would be representative of the Robojelly form, but with an integral cable system and onboard power instead of high power smart material actuators(Villanueva et al., 2011; Villanueva et al., 2014). The cable system could also be integrated internally with more complicated casting techniques and the inclusion of inextensible layers to force the neutral axis of the bell to a known position (Mosadegh et al., 2014). To aid in control and improve autonomy in future robots that are more application-based, automatic buoyancy control using accelerometers and inflatable bladders distributed within the bell would help balance on startup as well as adjust periodically for changes in water and robot density at changing depths of operation. This is especially useful since the current robots require manual adjustment of this balance, especially as the robot saturates in the water for up to two hours of constant changes in density. Reducing the profile of the actuators and required electronics would enable smaller and more accurate designs, such as a biomimetic robot of *Aurelia*. This species was attempted in Robojelly, but the robot had to be tethered to power the high-current smart material actuators (Villanueva et al., 2011). Modern MEMS actuation, electronics, and fluid control devices are further enabling iterations of our current robot designs, and advancements in these technologies could enable the reduction in profile of these types of robots.

As with any underwater robot, another primary problem is the waterproofing of electronics. While our method has been refined greatly over the development of Cyro 2 and Cyro 3, these improvements are still questionably reliable and require a persistent 'check, repair if needed, test until broken' strategy that slows down testing and development due to unforeseen delays. This could be improved with injection molded parts with no potential for leaking due to layer delamination or inaccuracies in the frame and seal dimensioning during manufacturing and assembly. High tolerance, high strength assemblies with industrially designed and implemented labyrinth and gasket seals would greatly improve maintenance and reliability. More controlled potting methods combined with enclosures for electronics that need consistent maintenance or reconfiguration would result in a final product that is more capable of application based operations.

In addition to the physical design of the robot, the materials and stiffness refinement of the bell has been a persistent goal that could use further improvement. Mesoglea is a finely refined multi-layer organic structure that can allow fine tuning in buoyancy by changing saturation and can exhibit differential tension in areas that could reduce actuator or muscular need by clever changes in form or directional material properties (Zhu et al., 2012). While silicone rubber of varying low-end durometers are appropriate analogues for the stiffness and density of the mesoglea, it saturates slowly to eventually cause buoyancy problems, requires clever profile design for localized stiffness control, and can be problematic to cast since silicone is meant as more of a mold material or high-durability stiff rubber, not as a low-stiffness flap casting material. Further design refinement for localized stiffness and bending control, methods for changing density of the bell such as a fluid-filled ballast cavity where the mesoglea matrix would exist, and improved but more costly casting protocols with machined molds and pressurized flow control could all improve the performance of this material for more realistic and passively capable jellyfish bells, and thus jellyfish robot performance.

6.2. ***Multi-Jet Propulsion Technology Limitations and Future***

As seen in the development of a multi-jet colonial biomimetic robot with soft structures, this robot enables an additional option for the design of mission-capable robots in between swarm systems with high-level networking and planning complexity and the large robots with centralized control that is limited in operational range and maneuvering capabilities. By eliminating the scaling of a control system and thrust production for different size systems, this robot architecture allows mission-specific robot scale and performance without significant development changes and considerations of control and power requirements.

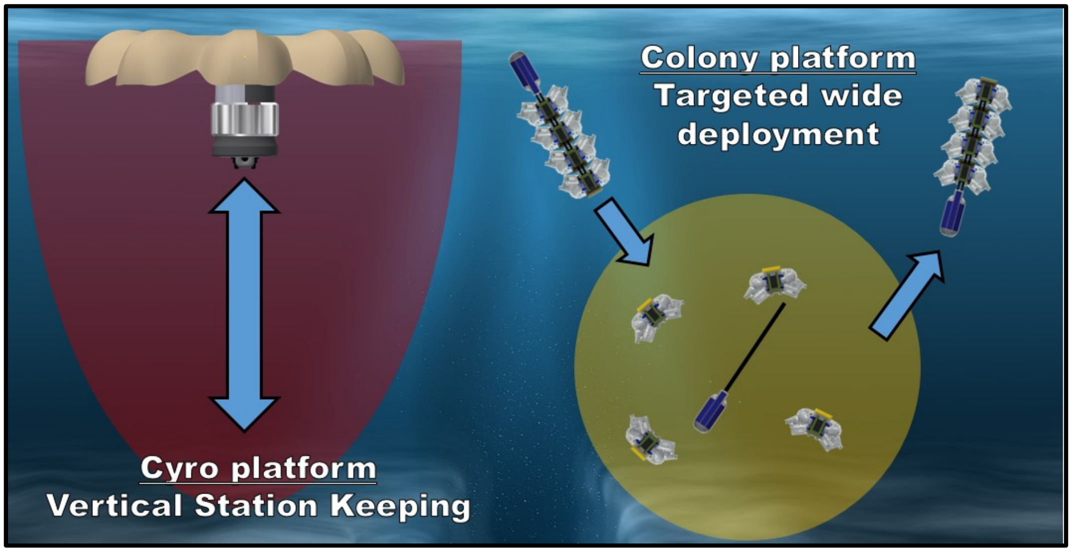

Figure 134 – Concept of use of the jellyfish and colonial robot in underwater missions. Jellyfish robots would be able to monitor a limited area with disturbance rejection and a large payload capacity, while the colonial robot would rapidly reach a target, collect data in a broad area, and recombine for rapid extraction.

The development of jellyfish inspired and mimetic robots has a wide range of options for scale and form, and our lab has implemented these robots on multiple scales with success, although with limitations primarily due to actuation and manufacturing of the bell. However, for a centimeter-scale and smaller siphonophore like *Nanomia*, mimicking this animal with technical limitations and fluid performance restrictions is of much greater concern.

As with any small robot, the actuation methods are extremely limited. The first primary issue is that the actuators need to be waterproofed, which adds space and mass from seals and housings as well as reliability concerns, or need to operate in open water, which is usually only rated for short term and shallow depths. This is further limited by the actuator scale and required performance relative to the nectophore size. Electromagnetic motors can commercially go down in size to slightly below a centimeter, which are commonly used for vibration-inducing motors found in portable communication devices. However, these motors are inherently high speed and low on torque, and even with a gearbox is not typically powerful enough to actuate the flexible nectophores, especially on the true 1:1 scale. This is especially true since small scale electromagnetic motors rely on miniature cast gears, typically with very small teeth formed in Nylon, that cannot support the torque requirements of the nectophores, and position control of small motors is uncommon in commercial components. Electromagnetic actuators such as solenoids can be scaled down, but the stroke length needed relative to the size of the nectophore unit is extremely restrictive on the scale of the colony and the degree of close-packing to reduce drag of the serial chain. In addition, the requirement of a strong magnetic field at a distance necessitates a large solenoid coil relative to the nectophore size. Miniature coil and magnet systems were attempted with the robot designs, but negligible contraction force was able to be produced. This close packing limitation is also present in rotary crank systems, where the crank stroke size needed to achieve full contraction travel is large relative to the colony. The drag forces on the colony during axial swimming are primarily skin friction with a small pressure drag, and any loose nectophore packing potentially doubles the skin friction and pressure drag terms by exposing new areas for circulation and more frontal area. Protruding and recessed features add serially to the drag coefficient and magnitude of the colony, and thus as close an approximation of a smooth form is required to reduce these tripping features in the boundary layer or open flow around the colony (Hoerner, 1965). This actuation scheme can be simplified by picking the ideal gaits and reducing the number of motors to do colony-wide pattern generation and phasing via mechanical means. This could be done with a crankshaft on each side of the robot powered by a rotary actuator, with phasing achieved by a torsional displacement of the shaft at flexible interfacial elements between the crank elements for each nectophore. This has been utilized for phased control of crankshafts in cars over multiple commercial packages from each major car manufacturer. However, for a system such as siphonophores where modularity and simple control is a focus, simplifying mechanics unnecessarily reduces the control and loses the interesting aspects of a colonial robot. In a limited sense, purely cascading or synchronous thrust production with timing control on each side could enable turning and axial motion with extremely simple actuation and control requirements, although miniaturized systems still require significant power storage and delivery capacity.

Figure 135 – Example of a multi-jet colonial robot with deployable units, constructed by a senior design class team in conjunction with the siphonophore robot project. Lower power pumps forced water through frontal scoops to jet out of nozzles that could be vectored for 3D motion. The units were designed to reduce drag, stabilize roll, and attach and reattach with a central stem.

In addition to the actuation input, power supplies for small robotic systems are exceedingly difficult to balance and implement. On a robot the scale of Cyro 3, the batteries available on the market are capable of high current, high capacity, and low mass due to modern cell chemistries. These batteries are also of appropriate size to include power monitoring and safety circuitry to protect the powered system from power problems and potential fire or chemical hazards. However, scaled-down cells for a smaller system are typically low-current, low-capacity, and unprotected to a degree that even if an actuator was chosen for appropriate mechanical operation the powering of the actuator, as well as the protection and power switching circuitry, can be expected to be insufficient. Modern research on battery technology, supplementary energy harvesting, and more efficient actuators on the small scale will make the implementation of small scale robot power and motion more practical and thus enable smaller biomimetic designs.

Additional measurements of the gait performance for the robot is of significant interest for future design characterization and relation with the control space of siphonophores. It was found that the PTFE coil spindles performed consistently over heavy use, but the 3D printed resin increased the possibility of overheating and binding due to deformation. The robot design in the enclosed study uses the printed resins for rapid prototyping, but after long term testing the resin spindles posed problems that caused the nectophores to cease from actuating. Therefore, only PTFE coil spindles are recommended, and additional studies with these coil designs would be imperative for long term reliability. In addition, the cyanoacrylate adhesive and primer for the coils and magnet to the silicone was effective over other adhesive options, but this method did not hold up for all cases when the coils heated and introduced high heat to the adhesives at the coil and magnet attachment points. Specialized heat and moisture resistant adhesives were preliminarily tested and found to improve reliability, and thus will be necessary for appropriate bonding strength and durability under repeated load and heat generation.

Control of the siphonophore robot posed multiple difficulties due to the high number of required I/O for detailed control and the limited reliability of PWM pattern generation across multiple I/O ports. Dedicated electronics boards with power management, control through analog approximation using PWM, isolation of high power I/O from the board I/O ports, and switching H-bridge elements should be developed for a refined robot design with optimized space. As with any large systems with multiple units, cable routing and management, especially for modular elements, will be a factor of reducing wire breakage and excess drag from loose wires under motion and repeated manual placement in the water.

Since power and actuation are critical systems for robot implementation, the current option for using these technologies is to scale the system up to the smallest possible design for actuator integration. Small animals such as *Nanomia* operate at a size scale where their inertia is near insignificant relative to their thrust production, making their motion easier for a small profile. By scaling up the design for a new system, the cubic increase in mass and quadratic increase in drag directly hinder the performance of the mimetic robotic system. The jet production Reynolds number can be scaled accordingly, but whether this scaled jetting body with cubically increased volume and linearly increased jet diameter will form a laminar jet with sufficient force to overcome the drastically increased resistive forces is difficult to theoretically determine and plan for in the design. Dimensional analysis can provide some indication and consistency in key performance characteristics, and modeling of the system similar to the modeling of the animal could provide expected dynamic performance. However, changing structural parameters such as close packing and density for the robot makes correlations between robot and animal performance more difficult since the performance is often constrained to stay within bounds of fluid parameters and actuation. As with Cyro 3, improvements in the soft cavities of the robot, as well as additional soft features such as a differentially stiff directed nozzle and a central column with included stiffness and wiring enclosures, would improve possible performance at each scale. Additive manufacturing of multiple materials of variable stiffness, as well as potentially printing in electrical pathways using conductive filament or resin as is available commercially in other forms, would enable the printing of a small scale robot with actuators and flexible elements. Further improvements in battery chemistry and computational hardware over existing lithium polymer and silicon microchips will revolutionize the capabilities of robot design and manufacturing, and a combination of additive manufacturing and automated parts assembly during the printing process will allow for integration of control circuits and jetting methods proposed in this dissertation without the limitations of human error and dexterity.

References

Acuna, J. L., Lopez-Urrutia, A. and Colin, S. (2011). Faking Giants: The Evolution of High Prey Clearance Rates in Jellyfishes. *Science (80-.).* **333**, 1627–1629.

Arduino Board Uno *Arduino Website*.

Arduino Playground - ArduinoReset *Arduino Play.*

Barca, J. C. and Sekercioglu, Y. A. (2013). Swarm robotics reviewed. *Robotica* **31**, 345–359.

Barham, E. G. (1963). Siphonophores and the deep scattering layer. *Science (80-.).* **140**, 826–828.

Beeler, S. C. (2004). State-Dependent Riccati Equation Regulation of Systems with State and Control Nonlinearities. *Contract*.

Chang, I. and Bentsman, J. (2013). Constrained discrete-time state-dependent Riccati equation technique : A model predictive control approach. *Proc. IEEE Conf. Decis. Control* 5125–5130.

Cloutier, J. R. (1997). State-dependent Riccati equation techniques: an overview. *Proc. 1997 Am. Control Conf. (Cat. No.97CH36041)* 932–936 vol.2.

Costello, J. H., Colin, S. P. and Dabiri, J. O. (2008). Medusan morphospace: Phylogenetic constraints, biomechanical solutions, and ecological consequences. *Invertebr. Biol.* **127**, 265–290.

Costello, J. H., Colin, S. P., Gemmell, B. J., Dabiri, J. O. and Sutherland, K. R. (2015). Multi-jet propulsion organized by clonal development in a colonial siphonophore. *Nat. Commun.* **6**, 1–6.

Dabiri, J. O. (2009). Optimal Vortex Formation as a Unifying Principle in Biological Propulsion. *Annu. Rev. Fluid Mech.* **41**, 17–33.

Dabiri, J. O., Colin, S. P., Costello, J. H. and Gharib, M. (2005). Flow patterns generated by oblate medusan jellyfish: field measurements and laboratory analyses. *J. Exp. Biol.* **208**, 1257–1265.

Dabiri, J. O., Colin, S. P. and Costello, J. H. (2007). Morphological diversity of medusan lineages constrained by animal-fluid interactions. *J. Exp. Biol.* **210**, 1868–1873.

Dabiri, J. O., Colin, S. P., Katija, K. and Costello, J. H. (2010). A wake-based correlate of swimming performance and foraging behavior in seven co-occurring jellyfish species. *J. Exp. Biol.* **213**, 1217–1225.

Daniel, T. L. (1983). Mechanics and energetics of medusan jet propulsion. *Can. J. Zool.* **61**, 1406–1420.

Dunn, C. (2009). Siphonophores. *Curr. Biol.* **19**, R233–R234.

Faria, C. T., Priya, S. and Inman, D. J. (2013). Modeling and control of a jellyfish-inspired AUV. In *SPIE Smart Structures and Materials+ Nondestructive Evaluation and Health Monitoring*, p. 86880P–1–86880P–14.

Fish, F. E., Kolpas, A., Crossett, A., Dudas, M. A., Moored, K. W. and Bart-Smith, H. (2018). Kinematics of swimming of the manta ray: three-dimensional analysis of open-water maneuverability. *J. Exp. Biol.* **221**, jeb166041.

Fried, L. (2015). Bluefruit EZ-Link Tutorial. *Adafruit.*

Gemmell, B. J., Costello, J. H., Colin, S. P., Stewart, C. J., Dabiri, J. O., Tafti, D. and Priya, S. (2013). Passive energy recapture in jellyfish contributes to propulsive advantage over other metazoans. *Proc. Natl. Acad. Sci. U. S. A.* **110**, 17904–17909.

Gemmell, B. J., Troolin, D. R., Costello, J. H., Colin, S. P. and Satterlie, R. A. (2015). Control of vortex rings for manoeuvrability. *J. R. Soc. Interface* **12**, 20150389.

Gladfelter, W. B. (1972). Structure and function of the locomotory system of the Scyphomedusa Cyanea capillata. *Mar. Biol.* **14**, 150–160.

Grimmelikhuijzen, C. J. P., Spencer, a N. and Carr�, D. (1986). Organization of the nervous system of physonectid siphonophores. *Cell Tissue Res.* **246**, 463–479.

He, Z.-H., Bottinelli, R., Pellegrino, M. A., Ferenczi, M. A. and Reggiani, C. (2000). ATP Consumption and Efficiency of Human Single Muscle Fibers with Different Myosin Isoform Composition. *Biophys. J.* **79**, 945–961.

Heemels, W. P. M. H., Van Eijndhoven, S. J. L. and Stoorvogel, A. A. (1998). Linear quadratic regulator problem with positive controls. *Int. J. Control* **70**, 551–578.

Higgins, A. J. E., Ford, M. D. and Costello, J. H. (2008). Transitions in Morphology, Nematocyst Distribution, Fluid Motions, and Prey Capture During Development of the Scyphomedusa Cyanea capillata. *Biol. Bull.* **214**, 29–41.

Hoerner, S. F. (1965). *Fluid-Dynamic Drag*.

Koerhuis, C. L., van der Heide, F. M. and Hof, A. L. (2003). Energy consumption in static muscle contraction. *Eur. J. Appl. Physiol.* **88**, 588–592.

Lewis, F. L., Vrabie, D. L. and Syrmos, V. L. (2012). *Optimal Control: Third Edition*. John Wiley & Sons, Inc.

Lortie, A. (2012). Arduino Remote Programming with the Bluetooth Mate RN42. *blogs.gnome.org*.

Mackie, G. O. (1964). Analysis of Locomotion in a Siphonophore Colony. *Proc. R. Soc. B Biol. Sci.* **159**, 366–391.

Mackie, G. O. (1973). Report on giant nerve fibres in Nanomia. *Publ. Seto Mar. Biol. Lab.* **20**, 745–756.

Mackie, G. O. (1978). Coordination in physonectid siphonophores. *Mar. Behav. Physiol.* **5**, 325–346.

Mackie, G. O. (1986). From aggregates to integrates: physiological aspects of modularity in colonial animals. *Philos. Trans. R. Soc. London* **313**, 175–196.

Mackie, G. O., Pugh, P. R. and Purcell, J. E. (1988). Siphonophore Biology. *Adv. Mar. Biol.* **Volume 24**, 97–262.

Mapstone, G. M. (2014). Global diversity and review of Siphonophorae (Cnidaria: Hydrozoa). *PLoS One* **9**, e87737.

Marut, K. J. (2014). Underwater Robotic Propulsors Inspired by Jetting Jellyfish Underwater Robotic Propulsors Inspired by Jetting Jellyfish.

Marut, K., Stewart, C., Michael, T., Villanueva, A. and Priya, S. (2013). A jellyfish-inspired jet propulsion robot actuated by an iris mechanism. *Smart Mater. Struct.* **22**, 094021.

Mosadegh, B., Polygerinos, P., Keplinger, C., Wennstedt, S., Shepherd, R. F., Gupta, U., Shim, J., Bertoldi, K., Walsh, C. J. and Whitesides, G. M. (2014). Pneumatic networks for soft robotics that actuate rapidly. *Adv. Funct. Mater.* **24**, 2163–2170.

Munk, M. M. (1922). *Notes on Aerodynamic Forces - I. Rectilinear Motion*.

Nanomia cara nectophore *Zooplankt. Identif. Man. North Eur. Seas*.

Nanomia cara nectophore *Zooplankt. Identif. Man. North Eur. Seas*.

ON Semiconductor (2017). *1 . 0 A Low-Dropout Positive Fixed and Adjustable Voltage Regulators*.

Sahin, M., Mohseni, K. and Colin, S. P. (2009). The numerical comparison of flow patterns and propulsive performances for the hydromedusae Sarsia tubulosa and Aequorea victoria. *J. Exp. Biol.* **212**, 2656–2667.

Satterlie, R. A. (2011). Do jellyfish have central nervous systems? *J. Exp. Biol.* **214**, 1215–1223.

Totton, A. K. (1956). Siphonophora of the Indian Ocean together with systematics and biological notes on related species from other oceans. In *Discovery Reports, Vol 27*, p. Institute of Oceanographic Sciences (Great Britain).

Totton, A. K. (1965). *A synopsis of the siphonophora*. Natural History Museum Publications.

UnderH20 (2013). Blackwater Drift Dive. *PBS Digit. Stud.*

Villanueva, A. A. and Priya, S. (2014). Cyanea capillata Bell Kinematics Analysis through Corrected In Situ Imaging and Modeling Using Strategic Discretization Techniques. *PLoS One* **9**, e115220.

Villanueva, A., Smith, C. and Priya, S. (2011). A biomimetic robotic jellyfish (Robojelly) actuated by shape memory alloy composite actuators. *Bioinspir. Biomim.* **6**, 036004.

Villanueva, A. a, Marut, K. J., Michael, T. and Priya, S. (2013). Biomimetic autonomous robot inspired by the Cyanea capillata (Cyro). *Bioinspir. Biomim.* **8**, 046005.

Villanueva, A., Vlachos, P. and Priya, S. (2014). Flexible margin kinematics and vortex formation of Aurelia aurita and Robojelly. *PLoS One* **9**,.

Zhu, J., Wang, X., He, C. and Wang, H. (2012). Mechanical properties, anisotropic swelling behaviours and structures of jellyfish mesogloea. *J. Mech. Behav. Biomed. Mater.* **6**, 63–73.